



Universidade do Minho
Escola de Engenharia

Ana Carolina Quintela Alves Vilares da Silva

A bio-inspired computational
model for motion detection.

Ana Carolina Quintela Alves Vilares da Silva A bio-inspired computational model for motion detection.

UMinho | 2015

junho de 2015



Universidade do Minho
Escola de Engenharia

Ana Carolina Quintela Alves Vilares da Silva

A bio-inspired computational
model for motion detection.

Tese de Doutoramento
Programa Doutoral em Engenharia Biomédica

Trabalho efectuado sob a orientação de
Professora Doutora Cristina Manuela Peixotos dos
Santos
Professor Doutor John Richard Gray

STATEMENT OF INTEGRITY

I hereby declare having conducted my thesis with integrity. I confirm that I have not used plagiarism or any form of falsification of results in the process of the thesis elaboration.

I further declare that I have fully acknowledged the Code of Ethical Conduct of the University of Minho.

University of Minho, 29 de Junho de 2015

Full name: Ana Carolina Quintela Alves Vilares da Silva

Signature: _____

Acknowledgements

*"To make a prairie it takes a clover and one bee,
One clover, and a bee, And revery.
The revery alone will do,
If bees are few."*

Emily Dickinson

In life, one may be given a few tools to get where we need to go, but if something is missing, anything can be achieved with a dream. Imagination holds the power to overcome the scarcity of the actual.

My family, in particular my parents, my brother and my sister have been the responsible for nurturing my dream since the very beginning. Without them, their encouragement, I could never have pursued my academic and professional goals.

I am also deeply grateful to my best friend, my shadow and my lucky clover, Nelson. I am thankful for your understanding of the passion for what I do. I am very fortunate and deeply grateful to have you in my life.

I need to further thank all my friends. Specially, to each element of the “ninth group”, for all the good moments we lived together over ten years. I would also like to thank Inês, Elsa and Zélia who have always listened and supported me over the years.

I would like to express my sincere gratitude to my advisor Cristina Santos by allowing me to integrate this research group, for the continuous support of my Ph.D research, for her patience, motivation, enthusiasm, knowledge and friendship. The help and advice provided by her were invaluable in the execution of the present work and during the writing of this dissertation.

A great number of others have contributed to this work in many ways. I am specially grateful to Miguel, Vitor, Jorge, Carlos, Maria and Cesar for the friendship, companionship and for the stimulating discussions in the lab.

Besides, I would like to thank my co-advisor, Jack Gray, by the opportunity to learn new topics about biology, visual stimulation and neural recordings. I am deeply

grateful for the opportunity of spending four months in his lab, where I was received with open arms. I would like to thank Glyn and Dennis for initiating and training me in the mysteries of electrophysiology.

Rose Mary and Christina Kwon, thank you for making Saskatoon feel a little more like home.

I am also deeply grateful to Marie Dacke and Emily Baird for accepting to collaborate with us, for receiving me on Lund Vision Group and for all their continual encouragement and invaluable advices about behavioral experiments. I would like to thank all members of the group, specially Therese, for her friendship, her guidance and for being the best roommate I could ever ask for, and Nicola, for all the trips we made together discovering Sweden.

The present work was possible thanks to the support by the Portuguese Science and Technology Foundation through the Ph.D grant SFRH/BD/70396/2010.

Abstract

Last years have witnessed a considerable interest in research dedicated to show that solutions to challenges in autonomous robot navigation can be found by taking inspiration from biology.

Despite their small size and relatively simple nervous systems, insects have evolved vision systems able to perform the computations required for a safe navigation in dynamic and unstructured environments, by using simple, elegant and computationally efficient strategies. Thus, invertebrate neuroscience provides engineers with many neural circuit diagrams that can potentially be used to solve complicated engineering control problems.

One major and yet unsolved problem encountered by visually guided robotic platforms is collision avoidance in complex, dynamic and inconstant light environments.

In this dissertation, the main aim is to draw inspiration from recent and future findings on insect's collision avoidance in dynamic environments and on visual strategies of light adaptation applied by diurnal insects, to develop a computationally efficient model for robotic control, able to work even in adverse light conditions.

We first present a comparative analysis of three leading collision avoidance models based on a neural pathway responsible for signing collisions, the Lobula Giant Movement Detector/Descending Contralateral Movement Detector (LGMD/DCMD), found in the locust visual system. Models are described, simulated and results are compared with biological data from literature.

Due to the lack of information related to the way this collision detection neuron deals with dynamic environments, new visual stimuli were developed. Locusts *Locusta Migratoria* were stimulated with computer-generated discs that traveled along a combination of non-colliding and colliding trajectories, placed over a static and two distinct moving backgrounds, while simultaneously recording the DCMD activity extracellularly.

Based on these results, an innovative model was developed. This model was tested in specially designed computer simulations, replicating the same visual conditions used for the biological recordings. The proposed model is shown to be sufficient to give rise

to experimentally observed neural insect responses.

Using a different approach, and based on recent findings, we present a direct approach to estimate potential collisions through a sequential computation of the image's power spectra. This approach has been implemented in a real robotic platform, showing that distant dependent variations on image statistics are likely to be functional significant.

Maintaining the collision detection performance at lower light levels is not a trivial task. Nevertheless, some insect visual systems have developed several strategies to help them to optimize visual performance over a wide range of light intensities. In this dissertation we address the neural adaptation mechanisms responsible to improve light capture on a day active insect, the bumblebee *Bombus Terrestris*. Behavioral analyses enabled us to investigate and infer about the spatial and temporal neural summation extent applied by those insects to improve image reliability at the different light levels.

As future work, the collision avoidance model may be coupled with a bio-inspired light adaptation mechanism and used for robotic autonomous navigation.

Resumo

Os últimos anos têm testemunhado um aumento progressivo da investigação dedicada a demonstrar que possíveis soluções, para problemas existentes na navegação autónoma de robôs, podem ser encontradas buscando inspiração na biologia.

Apesar do reduzido tamanho e da simplicidade do seu sistema nervoso, os insectos possuem sistemas de visão capazes de realizar os cálculos necessários para uma navegação segura em ambientes dinâmicos e não estruturados, por meio de estratégias simples, elegantes e computacionalmente eficientes. Assim, a área da neurociência que se debruça sobre o estudo dos invertebrados fornece, à área da engenharia, uma vasta gama de diagramas de circuitos neurais, que podem ser usados como base para a resolução de problemas complexos.

Um atual e notável problema, cujas plataformas robóticas baseadas em sistemas de visão estão sujeitas, é o problema de deteção de colisões em ambientes complexos, dinâmicos e de intensidade luminosa variável.

Assim, o objetivo principal do trabalho aqui apresentado é o de procurar inspiração em recentes e futuras descobertas relacionadas com os mecanismos que possibilitam a deteção de colisões em ambientes dinâmicos, bem como nas estratégias visuais de adaptação à luz, aplicadas por insectos diurnos.

Numa primeira abordagem é feita uma análise comparativa dos três principais modelos, propostos na literatura, de deteção de colisões, que têm por base o funcionamento dos neurónios Lobular Gigante Detector de Movimento/ Detector de Movimento Descendente Contralateral (LGMD / DCMD), que fazem parte do sistema visual do gafanhoto. Os modelos são descritos, simulados e os resultados são comparados com os dados biológicos existentes, descritos na literatura.

Devido à falta de informação relacionada com a forma como estes neurónios detetores de colisões lidam com ambientes dinâmicos, foram desenvolvidos novos estímulos visuais. A estimulação de gafanhotos *Locusta Migratoria* foi realizada usando-se estímulos controlados, gerados por computador, efectuando diferentes combinações de trajectórias de não-colisão e colisão, colocados sobre um fundo estático e dois fundos dinâmicos.

extracelulares do neurónio DCMD.

Com base nos resultados obtidos foi possível desenvolver um modelo inovador. Este foi testado sob estímulos visuais desenvolvidos computacionalmente, recriando as mesmas condições visuais usadas aquando dos registos neuronais biológicos. O modelo proposto mostrou ser capaz de reproduzir os resultados neuronais dos gafanhotos, experimentalmente obtidos.

Usando uma abordagem diferente, e com base em descobertas recentes, apresentamos uma metodologia mais direta, que possibilita estimar possíveis colisões através de cálculos sequenciais dos espectros de potência das imagens captadas. Esta abordagem foi implementada numa plataforma robótica real, mostrando que, variações estatísticas nas imagens captadas, são susceptíveis de serem funcionalmente significativas.

Manter o desempenho da deteção de colisões, em níveis de luz reduzida, não é uma tarefa trivial. No entanto, alguns sistemas visuais de insectos desenvolveram estratégias de forma a otimizar o seu desempenho visual numa larga gama de intensidades luminosas. Nesta dissertação, os mecanismos de adaptação neuronais, responsáveis pela melhoria de captação de luz num inseto diurno, a abelha *Bombus Terrestris*, serviram como uma base de estudo. Adaptando análises comportamentais, foi-nos permitido investigar e inferir acerca da extensão dos somatórios neuronais, espaciais e temporais, aplicados por estes insectos, por forma a melhorar a qualidade das imagens captadas a diferentes níveis de luz.

Como trabalho futuro, o modelo de deteção de colisões deverá ser acoplado com um mecanismo de adaptação à luz, sendo ambos bio-inspirados, e que possam ser utilizados na navegação robótica autónoma.

Contents

Contents	ix
1 Introduction	1
1.1 Motivations, scope and problem statement	1
1.2 Overview of the research	2
1.2.1 Goals and research questions	4
1.3 Contributions to knowledge	6
1.4 Publications	7
1.5 Thesis outline	8
2 Collision Avoidance: a systematic review	11
2.1 Introduction	11
2.2 Collision-warning responses: the LGMD neuron	13
2.2.1 Behavioral implications of the LGMD neural response	16
2.2.2 Biological basis of LGMD neural selectivity	19
2.2.2.1 The critical race hypothesis: feed-forward excitation versus lateral inhibition (H1)	20
2.2.2.2 The feed-forward excitation versus feed-forward inhi- bition hypothesis (H2)	21
2.2.2.3 Integration of distributed computation hypothesis (H3)	24
2.3 LGMD models: Mathematical formulation and description	25
2.3.1 LGMD modeled as a η -function	27
2.3.2 LGMD modeled as an artificial neural network	28
2.3.2.1 LGMD model 1	29
2.3.2.2 LGMD model 2	32
2.3.2.3 LGMD model 3	36
2.3.3 LGMD connective model	40
2.3.4 LGMD models: qualitative evaluation and predicted results . .	45

2.4	Methods	45
2.4.1	Stimulation Protocols	47
2.5	LGMD models: computational implementation and results	51
2.5.1	LGMD η -function: model validation in comparison to biology and a robotic perspective analysis	51
2.5.1.1	LGMD η -function: <i>model evaluation in terms of descriptive adequacy</i>	51
2.5.1.2	LGMD η -function: <i>biological and robotic model performance evaluation</i>	52
2.5.2	LGMD model 1: model validation in comparison to biology and a robotic perspective analysis	55
2.5.2.1	LGMD model 1: <i>model evaluation in terms of descriptive adequacy</i>	55
2.5.2.2	LGMD model 1: <i>biological and robotic model performance evaluation</i>	58
2.5.2.3	LGMD model 2: <i>model evaluation in terms of descriptive adequacy</i>	63
2.5.2.4	LGMD model 2: <i>biological and robotic model performance evaluation</i>	64
2.5.2.5	LGMD model 3: <i>model evaluation in terms of descriptive adequacy</i>	68
2.5.2.6	LGMD model 3: <i>biological and robotic model performance evaluation</i>	69
2.5.2.7	LGMD connective model: <i>model evaluation in terms of descriptive adequacy</i>	74
2.5.2.8	LGMD connective model: <i>biological and robotic model performance evaluation</i>	74
2.6	Model Comparison and Discussion	77
2.7	Conclusion	79
3	LGMD neural responses to complex visual motion with increasing background complexity	85
3.1	Introduction	86
3.2	Materials and Methods	88
3.3	Results	93
3.4	Discussion	105

4	LGMD model development and responses to complex object motion in increasing complex backgrounds	113
4.1	Introduction	113
4.2	Methods and Materials	116
4.2.1	The LGMD model	117
4.2.2	Materials	126
4.3	Results	128
4.4	Discussion	135
5	Statistics of Motion	137
5.1	Introduction	137
5.2	Related work	139
5.3	Methods and Materials	142
5.3.1	Part I: Power spectrum estimation through polynomial curve fitting	144
5.3.2	Part II: Processing α -value and Information Extraction	145
5.3.3	Experimental setup	146
5.4	Results and Discussion	150
5.5	Conclusions	157
6	Vision at low light intensity	159
6.1	Introduction	160
6.2	Materials and Methods	162
6.3	Results	165
6.4	Discussion	179
7	Conclusions	185
7.1	Summary of contributions	186
7.2	Future directions	189
7.2.1	Electrophysiological investigation of the collision avoidance behavior	189
7.2.2	Behavioral studies	190
7.2.3	Modeling strategies and hardware development	191
7.2.4	Image statistics	191
	References	193

Chapter 1

Introduction

This thesis presents the work developed during the past four years in the Control, Automation and Robotics (CAR) group of the ALGORITMI Center from University of Minho, with the additional collaboration of two foreign research groups: the Gray Lab (at University of Saskatchewan, Canada) and the Lund Vision Group (Lund University, Sweden).

This work addresses the field of collision detection and light adaptation through the analysis and implementation of bio-inspired concepts. The ultimate goal of this work is to develop a biologically-inspired, comprehensive computational model of complex motion detection that could be used for motor control.

1.1 Motivations, scope and problem statement

Vision is an extraordinarily powerful sense. The ability to perceive the surroundings allows for movement to be regulated by the world. Many researchers, from psychologists to engineers, have been working on this complex problem of visual perception. Unfortunately, the understanding of how perception works remains unclear.

Due to their relatively simple nervous system, insects are an excellent way through which we can investigate how visual information is acquired and processed in order to trigger specific behaviours, as collision avoidance responses. These behaviors are, by necessity, fast and robust, making them excellent systems to study the neural basis of behavior.

On the other hand, extraction and throughput of critical information required to local maneuvering is a fundamental challenge for vision-based navigation on miniaturized, compact and agile platforms. Current research in autonomous visual navigation has been focused on several useful, but complex algorithms that, not being limited

to, involve feature selection, extraction and classification.

Thus, one can seek bio-inspiration in nature, using simple vision systems to exploit effective machine implementations. Effectively, the fundamental principles inherent to insect navigation are both elusive and promising candidates for closing the considerably large gap in performance and robustness that exists between biological systems and their robotic counterparts. These visual systems has survived and evolved over hundreds of millions of years and provides us with highly optimized neuronal algorithms that can be used as an inspiration to design new architectures for autonomous navigation.

As the important details of the biology are uncovered through neurophysiological and behavioral studies, the challenge is not only to develop appropriate mathematical models of these processes but also to understand how information is processed at the vision system level, in order to control behavior. This thesis, through neurophysiological and behavioral studies, coupled with modeling tools, is a dedicated effort to unravel some of the mechanisms behind insect visual processing, more specifically those responsible for collision detection in complex and dynamic environments and for light intensity adaptation strategies.

1.2 Overview of the research

The choice of a model system for study is often difficult, as the complexity of a behavior is quite often related to the complexity of an animal's nervous system. Nevertheless, some animals have been pressured by natural selection to obtain very complex behaviors, while maintaining a relatively simple nervous system. Insects are a perfect example. They are able to display many complex behaviors, yet their nervous systems are relatively simple and understood. One advantage of studying the nervous system of insects is based on the fact that they have fewer neurons than other animals such as vertebrates. In addition, the properties of a single identified neuron can often yield general properties and mechanisms that are applicable to other systems.

One insect in particular, the locust, has evolved a dedicated and well-studied collision avoidance neural pathway that is responsible for generating collision avoidance behaviors to avoid predation and continual inflight collisions with conspecifics[77]. The visual system of the locust is paramount to its survival, and acts as a great model system for study.

Therefore, this thesis aims, in a first stage, to study and model visually evoked escape responses in locusts. These are natural, robust, probabilistic, and often mul-

tistaged planned behaviors, providing an excellent context for studying the neural mechanisms of sensory-motor integration, leading to the development of more natural, flexible and computationally efficient solutions [59]. In locusts, the corresponding escape behavior correlates with the activity of the Lobula Giant Movement Detector (LGMD) neuron, which responds selectively to approaching threats.

The first bio-inspired model for the Lobula Giant Movement Detector (LGMD) neural network was developed in [150]. The model continued to evolve [16, 195, 229, 234] and was used in mobile robots and automobiles for collision detection. These models have shown the LGMD neuron looming sensitivity and selectivity when stimulated with approaching, translating or receding objects. However, further work is needed to develop models that can account for complex aspects of visual motion and to increase the final robustness to cluttered environments. Recent findings have shown that stimulus properties of single or paired objects approaching from different regions of the visual field [77, 80] and objects that change its course during an approach [119] are manifested in modulation of the LGMD firing rate. Combining information based on LGMD responses to complex motion with analytical tools will permit the development of a more appropriate model that could be implemented for devices that require flexible responses to visual information in real time.

Additionally, many animal species, such as dung beetles, locusts and bees [213, 214], have also developed efficient night vision systems able to work well in low light conditions. Unfortunately, not so much is known about how these insects are able to extend their visual capabilities to lower light levels. Therefore, in a second stage of this thesis, by using a behavioral approach, we expect to infer about the neural adaptations applied by these insects to optimize sensitivity at low light intensities. On literature, there is already described a multitude of sensitivity optimization techniques that apply spatio-temporal filtering processes for noise reduction purposes [116]. However, none have addressed the shaping of visual input dynamics through a behavioral action, thus enabling different extents of neural summation. This strategy is innovative and relevant, involving behavioral experiments with bees to establish a computational paradigm for the light adaptation mechanism.

In fact, the research here described lies at the intersection of several scientific disciplines, such as biology, computer vision and robotics. Therefore, one of the main challenges lies in the integration of the knowledge from various disciplines in order to develop an efficient system that will eventually be capable of autonomous collision avoidance in the presence of obstacles in dynamic environments, even at low light conditions.

The main motivation relies on the number of possible applications in service tasks, ranging from the automobile industry, personal transportation devices for physically impaired humans or motor control of prosthetic devices.

The expected impact on science and engineering is significant and wide-ranging. The proposed computational model built on the principles of information processing in nature can be expected to enable processing applications for which conventional computers are reaching their limits. Results will lead to significant advances in robotic active-security and other similar applications in many diverse fields where performance and cost are critical. Applications areas include service tasks, ranging from automobile industry, co-manipulation systems in medicine (as minimally invasive surgical interventions, which would highly benefit from a navigation system able to work under low light conditions found inside the body), autonomous robot navigation, robot engineering, real-time autonomous processing, embedded systems, and many more.

1.2.1 Goals and research questions

The ultimate goal of this thesis is the development of a collision detection mechanism that combines two relevant biological concepts: collision detection and light adaptation.

To achieve this final goal, new ideas related with biological concepts in insect vision have to be learned, several goals will be achieved and research questions will be answered.

Goal 1: The first step is to conduct an extensive survey on the state of the art related with the biological basis of collision detection, with particular focus in the locust visual system. Specifically, by adopting a systematic review approach, we expect to describe the different hypothesis and subsequent mathematical models, existent on literature, that explain the main working principles of the locust's collision detection system. This goal will enable us to identify the principles behind each model, the robustness and aspects that require modification.

Existent LGMD models will be submitted to standard stimulation protocols, in order to compare and validate each model's plausibility. For that, the development and implementation of a Matlab® [118] simulator will enable to challenge the models with the same controlled visual inputs, repeatedly. The output of each model will be directly compared to data obtained from experiments with real animals, already documented on literature.

Chapter 2 addresses this first goal, which led to a book chapter publication [180].

Goal 2: The second goal is to extract input-output knowledge, relating dynamic visual stimulus parameters with modulation of the LGMD neuron's firing rate. Several visual stimuli will be created, including different background complexities combined with distinct trajectory complexities. Neurophysiological techniques will be applied to access and record the LGMD neural activity when stimulated with those visual stimuli. In order to understand how complex motion parameters shape LGMD response profiles, statistical analysis will be used.

Chapter 3 addresses this second goal, which led to a journal paper publication [178].

Goal 3: The development of a new LGMD model is the next step. This model has to be capable of generating similar responses as the ones recorded in the experiments performed with the real locusts in goal 2. An improved neural network, consistent with the physiology and anatomy of the insect visual processing hierarchy, will be proposed.

Chapter 4 addresses the third goal of this dissertation.

Goal 4: In order to understand, in a more complete way, how the locust brain estimates collisions, it is also important to understand the statistics of the environment relevant to this task.

Characterizing the statistics of motion that occur when navigating in distinct environments and exploring the implications of those statistics for collision detection is the fifth goal of this thesis. A deep analysis of image statistics, using both artificial and real video recordings showing collision scenarios, will be performed.

Chapter 5 addresses the fourth goal of this dissertation, which led to a conference paper publication [179].

Goal 5: The new goal is to analyze how bumblebees modify their flight characteristics at decreasing light intensity levels so that, in the future, the collision detection model could be coupled with a bio-inspired light adaptation mechanism, enabling a reliable detection of potential collisions even in low light levels. In a first stage, bumblebees flying in different conditions of spatial frequency and light intensity will be video recorded. The main effects of light intensity and spatial frequency on the centering position and flying speed of bumblebees will be deeply analyzed. In a second stage, by merging the behavioral results with modeling strategies, we will be able to infer about the optimal neural summation strategies applied by these flying bumblebees to improve image reliability at each condition tested.

Chapter 6 addresses this fourth goal.

The following research questions (RQ) are expected to be answered:

RQ1: Is the LGMD neuronal response affected by different levels of background complexity?

RQ2: How does the LGMD neuron code trajectory changes?

RQ3: It is possible to design a LGMD neural model capable of generating similar responses to the ones obtained with the biological LGMD neuron?

RQ4: What can the spatiotemporal statistics of the image sequences tell us about the proximity of obstacles on a scene?

RQ5: Does the bumblebee's behavioral adaptations reflect neural adaptations applied to improve image reliability at low light conditions?

1.3 Contributions to knowledge

This thesis approaches two distinct but complementary studies: collision avoidance and light adaptation. New knowledge was obtained from either neurophysiological, behavioral and modeling experiments.

The following statements point out the main contributions of this work:

- Findings predicting that the LGMD/DCMD neural circuitry in locusts encodes changes in trajectories (described on Chapter 3);
- Findings verifying that background complexity affects the response of a looming-sensitive neuron to object motion (described on Chapter 3);
- An innovative LGMD model able to detect potential collisions even in highly dynamic environments. This model showed a way of combining and evolving directionally and non-directionally selective neurons, proving that inhibition has a predominant role in eliminating non-colliding objects (described on Chapter 4);
- An innovative methodology to detect potential collisions using a direct evaluation of variations on the image's power spectra (described on Chapter 5);
- Findings showing that day-active bumblebee's flying speed is affected both by the spatial frequency and by the light intensity available in the environment (described on Chapter 6);

- Findings concluding that day-active bumblebees are able to extend their vision into dim light conditions, possibly by applying adaptive spatial and temporal neural summation strategies. This could be the basis of the development of a new algorithm for image noise reduction purposes (described on Chapter 6);

Generally, the main outcomes of this work include a more dynamic and flexible model for collision avoidance in artificial systems. Using this approach one obtains a more robust, flexible, effective, efficient and simple in implementation model, considering collision detection for devices moving in dynamic environments.

In the long run, the acquired insights could be used to develop high-performance intelligent sensors, focusing on adding sensing and actuation to the devices and networks.

1.4 Publications

The work here described allowed the publication of one journal articles, two book chapters and conference papers.

Journal Articles

- Ana C. Silva, G. A. McMillan, Cristina P. Santos and J. R. Gray, *Background complexity affects the response of a looming-sensitive neuron to object motion*, Journal of Neurophysiology, 2014.

Book Chapters

- Ana C. Silva and Cristina P. Santos, *A bio-inspired model reliably predicts the collision of approaching objects under different light conditions*, From Animals to Animats 12, Lecture Notes in Computer Science, Vol. 7426, pp. 85-95, 2012.
- Ana C. Silva, Jorge B. Silva and Cristina P. Santos. *A Modified LGMD Based Neural Network for Automatic Collision Detection*. Informatics in Control, Automation and Robotics. Lecture Notes in Electrical Engineering, Vol. 283, pp. 217-233, 2014.

Conference Papers

- Ana C. Silva, Jorge B. Silva and Cristina P. Santos. *LGMD Based Neural Network For Automatic Collision Detection*, 9th International Conference on Infor-

matics in Control, Automation and Robotics (ICINCO 2012), Rome, Italy, July 28th-31th, 2012.

- Ana C. Silva and Cristina P. Santos, *A bio-inspired model reliably predicts the collision of approaching objects under different light conditions*, 12th International Conference on Adaptive Behaviour, Odense, Denmark, August 27th-30th, 2012.
- Ana C. Silva and Cristina P. Santos, *Computational model of the LGMD neuron for automatic collision detection*, 3rd Portuguese BioEngineering Meeting, Braga, Portugal, February 20th-23th, 2013.
- Ana C. Silva and Cristina P. Santos, *Modeling disinhibition within a layered structure of the LGMD neuron*, The 2013 International Joint Conference on Neural Networks (IJCNN), Dallas, Texas, USA, August 4th-9th, 2013.
- Ana C. Silva and Cristina P. Santos, *A Time-analysis of the Spatial Power Spectra Indicates the Proximity and Complexity of the Surrounding Environment*, 11th International Conference on Informatics in Control, Automation and Robotics (ICINCO 2014), Vienna, Austria, September 1st-3rd, 2014.

Poster communications

- *Robot Vision based on the Locust Visual System*, International Workshop on Bio-inspired Robots, Ecole des Mines de Nantes, April 6th to April 8th, 2011.

1.5 Thesis outline

The thesis is organized in seven chapters, as illustrated in figure 1.1.

Chapter 1 (current chapter) introduces the topic of this thesis, through the presentation of the insect vision based strategies for robotic applications. The overview of the research work is described together with the goals, main contributions and outline of the thesis.

Chapter 2 presents a systematic review of the main different approaches that have been proposed to explain the LGMD selectivity to approaching objects. A description and critical analysis of selected LGMD model's response to specific stimulation protocols, the convergence or divergence in results obtained with each one of the models, as well as the applicability of each model in the robotic field, are described in detail.

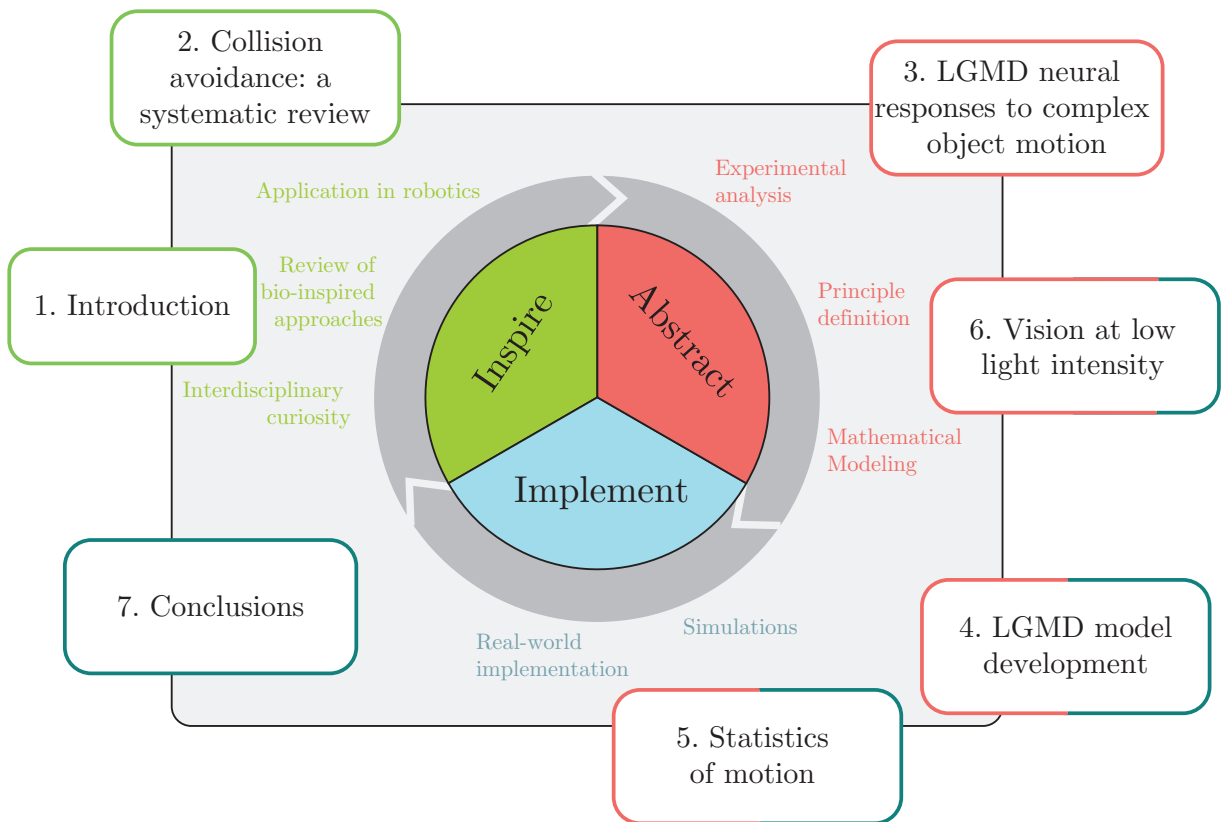


Figure 1.1: Outline of the thesis and chapters.

Chapter 3 presents the neurophysiological experiments performed with real locusts. It is demonstrated how distinct visual patterns' complexities can be directly linked to LGMD neural responses, and how robustly LGMD responses are in different scene's contexts.

Chapter 4 presents an innovative LGMD model, able to account with environments with distinct complexity levels. Results of the technical validation of the model are presented and discussed in detail.

Chapter 5 presents a different approach for the collision detection problem, based on simple motion statistics. The method is described and tested with distinct visual inputs, showing its potential to be used and further developed as a potential collision detection mechanism.

Chapter 6 describes the behavioral experiments performed with bumblebees, showing how flying behavior is affected at different light levels.

Finally, Chapter 7 provides a general conclusion on the achievements of the thesis and the perspectives for future research.

Chapter 2

Collision Avoidance: a systematic review

2.1 Introduction

Based on an improved understanding of the biological basis of adaptive behavior, neurorobotic models may provide a foundation for the development of more effective and autonomous models for robots [47]. These models must be inspired in simple neural systems, requiring a small amount of neural hardware to perform complex behaviors, which also leads to an easier understanding of the mechanisms behind particular behaviors being studied [217, 220]. From an engineering point-of-view, flying insects, as bees, flies, locusts, among others, have been viewed as attractive sources of inspiration due to the complexity and efficiency of their behaviors, allied with the simplicity of a reduced neural system. In particular, invertebrate neuroscience research is, across the last years, providing different neural circuit diagrams that can be easily modeled as sensorimotor controllers for robotic applications [217].

Many insects rely on vision for triggering a range of different behaviors, as flight stabilization [189, 193], collision avoidance[28, 59, 60, 70, 159], regulation of flight speed [147, 192, 194], among others, making their vision system to be highly tuned to perform well these tasks. In particular, the ability to detect and avoid approaching objects is important for survival, serving both to prevent collisions with conspecifics and obstacles as the animal moves, as well as to evade capture by predators[16, 152]. The psychophysics of these visually evoked collision-avoidance responses have been studied in different animal species [28, 29, 59, 126, 130, 142, 146, 148, 174, 184], with particular focus in the locust visual system [4, 58, 59, 70, 78, 79, 150, 156, 159, 170].

The locust visual system has a neural structure called Lobula Giant Movement De-

tector (LGMD) [59, 69, 70, 77–79, 93–95, 131, 155–159, 163] that selectively responds to looming objects approaching on a collision course. The LGMD neuron makes a strong synapse with the Descending Contralateral Movement Detector (DCMD) neuron, whose large axon travels down the animal’s contralateral nerve cord [185] and contacts inter and motor neurons involved in generating jumps and flight steering [37, 59, 82, 120, 184]. Consequently, this neural framework provides an excellent model for studying the sensory-motor transformations that occur during looming evoked collision-avoidance behaviors.

The past two decades have witnessed a growing interest in understanding the molecular and morphological processes underlying the LGMD response’s selectivity [59]. However, making sense of the voluminous data has been a challenging undertaking. A model is a powerful way to combine and summarize data that may be gathering piecemeal [218]. Therefore, theoretical analysis and computational modeling have been viewed as important tools to characterize what this neuron does, determine how it functions and understanding why it operates in a particular way.

In the present chapter, a survey of the three main different approaches [15, 71, 154] that have been proposed to model the LGMD neuron are presented. These approaches use different principles and perspectives to explain the LGMD selective responses to looming objects. Two approaches are focused on having a simple and highly parallelizable architecture [15, 154], which may lead them to be efficiently implemented on hardware. The other LGMD approach [71] proposes biophysical and phenomenological models that can closely describe the LGMD firing rates, experimentally obtained to different visual stimuli.

Unfortunately, the precise projection from photoreceptors to LGMD remains uncharacterized.

Due to the divergence between the different approaches, in this chapter we propose to discuss the behavior of LGMD-based models, with three main objectives in mind:

- (1) To provide a description and critical analysis of selected LGMD model’s response to specific stimulation protocols used in biology to test the LGMD neural response;
- (2) To highlight the convergence or divergence in results obtained with each one of the models;
- (3) To analyze the applicability of each model, in the robotic field.

In the sections that follow, it is firstly surveyed the most important characteristics and properties of the visual neurons that make up the locust visual system, paying a special attention to the LGMD neuron. Following, the principles of selected LGMD

models, as well as its computational formulation are described. The methodology adopted to make a full comparison between selected LGMD models, as well as its implementation and subsequent results are then described and performed. Finally, a comparison between these models is discussed in detail.

2.2 Collision-warning responses: the LGMD neuron

The first and foremost visual interface of the locust with the surrounding world is performed through the compound eyes, which, as the name suggests, have multiple light gathering units called ommatidia. Each ommatidium has its own lens, that forms an image onto the tip of the rhabdom, which is a light guiding structure of the photoreceptor cells [19, 51, 64, 87, 110, 111, 222] (see figure 2.1). In the photoreceptor cells, the visual information is transduced into electrical signals. Following the transduction, the signal is processed by different neuropiles located below the compound eye [108, 185]. These neuropiles are build up by interneurons, responsible for processing the visual information in different ways, showing a very particular hierarchical structure where the receptive fields progressively expand.

The different neuropiles of each optic lobe are disposed in a retinotopic way [19, 20, 137, 165], and the information tends to flow sequentially through the different layers. Nevertheless, some circuits establish lateral connections within a neuropile [133, 144].

Each optic lobe of the locust pair can be divided in four main layers: the first is the photoreceptor layer. The second layer is the Lamina (see figure 2.1). The Lamina is mainly composed by Large Monopolar Cells (LMCs) [10, 86, 97, 111, 209], which are specialized in signaling changes in the luminosity of the captured image. Some axons of the LMCs located in the lamina, project into the next neuropile, the Medulla. The Medulla is mainly characterized by the presence of lateral connections between its neurons. These connections are disposed in particular ways, in order to detect specific movements. By this reason, these neurons are called Elementary Motion Detectors – EMDs [20, 23, 55, 91, 147, 235].

The next layer in the locust optic lobe is the Lobula, where some retinotopic organization is lost due to neuronal convergence [144, 185]. Research studies have concluded that Lobula neurons, excited by movement, can be divided in two distinct categories: directional movement sensitive neurons and non-directional movement sensitive neurons (table 2.1).

Intensive research concerning different neurons located in the third layer of the

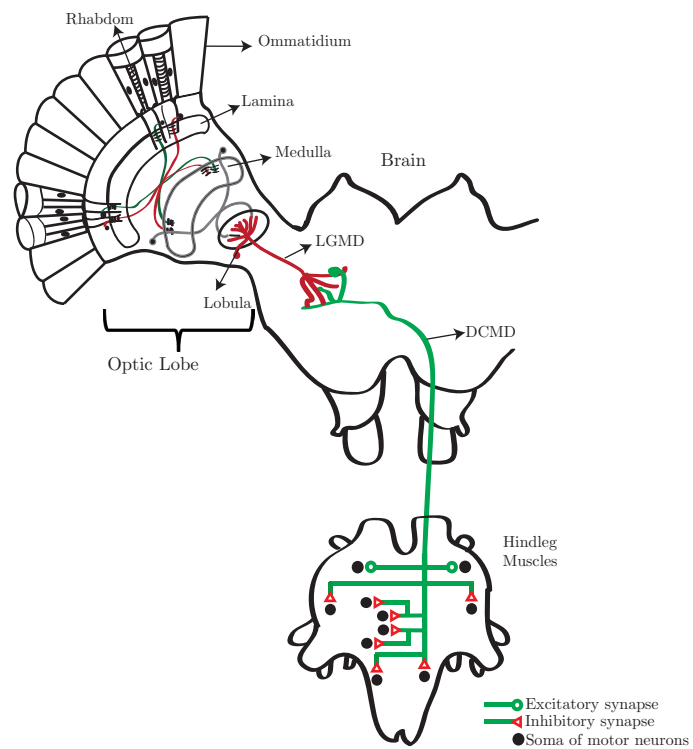


Figure 2.1: Representation of the visual system of a day-active insect. In the optic lobe of the insect, the main regions of organized neuropiles are represented. Additionally, diagrammatic representations of the synaptic connections of the DCMD neuron with motor neurons that control the muscles of the hindleg are shown. Adapted from: [26, 31, 185].

Table 2.1: Different characteristics of two main neuron types present in the Lobula of the Locust visual system [[149, 152]].

	Lobula Neurons excited by movement	
	Directional movement sensitive neuron	Non-directional movement sensitive neuron
Stimuli movement preference	Respond to movements in one preferred direction, at a fixed distance.	Respond to movements in any direction, at a fixed distance.
Stimuli size preference	Stimuli that cover large parts of the neuron receptive field.	Stimuli that cover only a small part of the neuron receptive field.
Neural response	Spontaneous increase of the spike rate when the captured movement occurs in the preferred direction. If movement occurs in the opposite direction, the firing rate decreases.	Production of a burst of action potentials.
Particular observations	Not found	A neuron that responds selectively when the motion is towards the insect, the LGMD.

locust optic lobe, the Lobula, identified a particular neuron that belongs to the non-directional movement sensitive category neuron, showing a selective response to approaching objects: the LGMD neuron (Fig. 2.2). The LGMD neuron is linked to its counter-partner, the DCMD neuron, via a mixed electrochemical synapse in the locust brain, [102, 153]. The spikes produced by the LGMD neuron are sent to the DCMD neuron in an one-to-one way [102, 153]. From the brain, each DCMD axon transports the final commands to the contra-lateral motor centers located in the locust thoracic ganglia, where it excites neurons controlling leg and wing movements [131, 182] (figure 2.1).

The next subchapter gives an overview of the behavioral implications of the LGMD neural response.

2.2.1 Behavioral implications of the LGMD neural response

Flying insects show a degree of behavioral robustness and flexibility that even the most sophisticated robots can not match. The relatively compact nervous system of many invertebrates, as locusts, provides a useful and unique opportunity to investigate and model the contribution of single sensory neurons, as LGMD/DCMD neurons, to natural behaviours, as collision avoidance.

Extensive research has been performed across the last years, in order to relate the LGMD neural responses and the final motor/behaviour modeling. Different escape behaviours have been studied, including: a) flight steering, including climbs and dives; b) gliding and c) jumping.

Past research [25] demonstrated that the DCMD neuron mediates excitatory post-synaptic potentials in the fast motor neuron which innervates the extensor tibiae muscle of each locust hind leg. Following this line of thought, [25] proposed that the DCMD neurons are involved in initiating the jumps that locusts often make when submitted to a dangerous situation.

In 1980, [182] described that each DCMD neuron mediates excitatory postsynaptic potentials in the ipsilateral flight motor neuron (more specifically, the mesothoracic second tergosternal motoneurone, m84), with a comparatively larger amplitude than those evoked in other motor neurons.

Then, following the same line of previous research, [166] shown that tethered flying locusts respond to a side-approaching object by interrupting the flight with a glide, which is characterized by a stereotyped position of the wings, which are elevated and held in a swept back dihedral position above the body, and can be seen as an escape response. This gliding behaviour is consistent with a burst of spikes in the motor

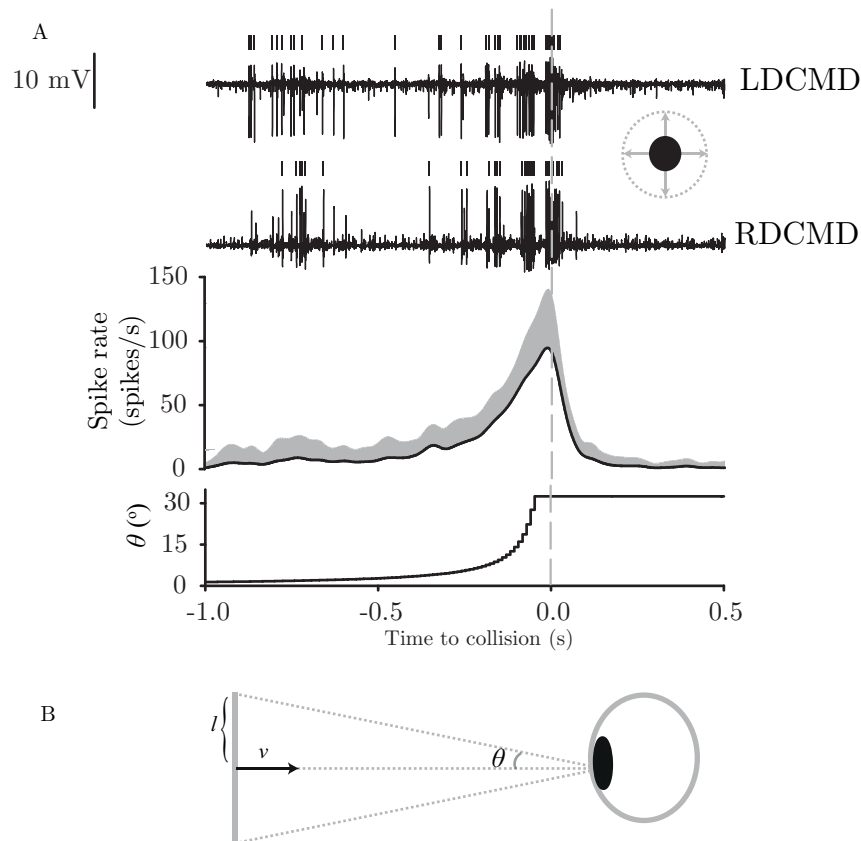


Figure 2.2: Example DCMD response to a looming stimulus. A) A disc with $l/|v| = 12\text{ms}$ was presented to the locust. The Left (L) and Right (R) DCMD activity was recorded (top traces). Pooled mean DCMD responses to a looming black disc approaching is presented in the middle graph (continuous black line). The bottom trace shows the evolution of the stimulus size, on the locust retina, across approaching time. B) In monocular vision, looming stimuli can be described simply by the angle (ϑ) subtended by the object on the retina. For an object approaching at a fixed velocity v ($v < 0$ for approaching) and having a half-size l , the retinal angle at time t ($t < 0$ prior to collision) can be described by $\theta(t) = 2 \cdot \tan^{-1}(l/vt)$.

neuron (m84). However, receding or stimuli expanding at a constant rate, did not elicit glides. Based on these results, it was concluded that the stimuli types that elicit glides are the same ones that are more effective at exciting the LGMD/DCMD neuron. In fact, additional research has found an interesting correlation: the strength of the DCMD response, when evaluated in terms of spike number, highly matches the occurrence of gliding behaviors. Thus, due to the DCMD preference for approaching objects and due to its role in exciting a motor neuron's muscle involved in gliding, the DCMD neuron is a neuron suitable for triggering this escape behavioral response.

In [167], a deeper study was performed in order to unveil the role of the DCMD in triggering escape glides. The work presented in this paper [167] provided evidences that high frequency DCMD spikes (>150 Hz) are involved in triggering glides in tethered flying locusts. Similarly to the research developed in [182], it was shown that the DCMD neuron is the unique looming-excited input to the m84 motor neuron, which is involved in gliding responses. Then, in [168], behavioral responses to simulated bird attacks were characterized and studied. According to the results obtained, the peak DCMD spike rate, as well as gliding responses are strong to stimuli with $l/|v|$ ratios similar to the ones verified in real bird attacks (between 4 and 17 ms).

Focusing its attention in another type of escape responses, the jumping [58], and by comparing electrophysiological and high speed video recordings, interesting relationships between the DCMD spike rate profile and the different phases of the locust leg flexors and extensors activation were obtained. According to the results, the initial preparatory phase of the locust jump occurs, on average, during the rising phase of the DCMD firing rate profile. Additionally, the period used to store the energy required for the jump coincides with the peak firing rate time of the DCMD neuron. Then, the final preparatory phase occurs after the DCMD peak (t_{peak}) and the takeoff happens when the firing rate of the DCMD neuron decays to 10% of its peak. Based on these results, it was concluded that the different preparatory phases and the subsequent takeoff are triggered when the approaching object reaches successive threshold angular sizes on the locust retina, respectively [58, 59].

Additional research [82], conducted through the development of a telemetry system, led to the conclusion that three different features are multiplexed in a single neuron's sensory response in order to prevent collisions: the DCMD firing rate threshold, its peak firing time (t_{peak}) and the number of spikes produced. These different features can be involved on the control of three different motor aspects involved in escaping jumps.

By enlarging the behaviours studied, in [30] a wide range of collision avoidance

behaviours were analyzed in minimally restrained flying locusts, including climbs and dives away and towards the visual stimuli used. According to the results obtained, it was demonstrated that a wide range of different escape strategies were performed by the insects. Taking this into consideration, it was shown that glides may not be used as the last maneuver applied by the insect to escape. Additionally, and based on the fact that the DCMD peak firing rate (f_{peak}), for the $l/|v|$ value used[30], occurs around 100 ms before the time predicted to collision, it seems unlikely that f_{peak} contributes to the collision-avoidance behaviours studied, since those happened substantially earlier during the experiments.

In [120], by using a combination of electromyographic recordings and motion analysis - using video recordings - relationships between forewing depressor muscle activity (m97 - which is often used as a convenient indicator of steering), wing kinematics and 3-dimensional body orientation, when flying locusts were subjected to lateral looming visual stimuli, were extracted. The results obtained for looming discs include cessation of flight, glides and active steering during sustained flight, in addition to a decrease and increase in wing beat frequency prior and during an evasive turn, respectively. The number and relative spike timing, in the forewing depressor muscle (m97), can predict wing kinematics and 3-dimensional body orientation in locusts stimulated with looming visual stimuli, showing its importance at modeling the locust behaviour.

All the research previously described demonstrates that, in fact, LGMD/DCMD neural response's properties are responsible for modeling distinct collision avoidance and escape behaviours.

In the next sub-chapter, previous research efforts related to explain the selective responses of the LGMD neuron to objects in a collision route are described.

2.2.2 Biological basis of LGMD neural selectivity

During the last years, extensive experimental studies have been made in order to find out:

- a) the correlation between stimulus characteristics and the obtained LGMD response (measured in terms of number of spikes, spike frequency, peak time, among other variables) ;
- b) the mechanisms behind the LGMD neural selectivity;
- c) the correlation between the output from a) and the effect on the final behavioral response.

However, the precise computation which is carried out by the LGMD neuron has been and continues to be a matter of research debate. Three distinct hypothesis

proposed in literature, aiming to unveil the LGMD selective response, will be described and analyzed in detail in the following.

2.2.2.1 The critical race hypothesis: feed-forward excitation versus lateral inhibition (H1)

After an extensive and deep study of the LGMD neural response to difference visual stimuli, Rind and her colleagues have found that the LGMD neuron produces its strongest responses, measured as either total spike number or as spike frequency, to objects approaching on a direct collision course. When the presence of a looming stimulus, the LGMD neuron produces a spike train that increases in frequency as the looming stimulus expands over the locust eye [181]. On the other hand, when stimulated with a receding or translating object, the LGMD generates a short and transient spike burst [183].

Based on these results, a research question had emerged: which are the critical image cues used for the LGMD selective response?

In order to answer that research question, new stimulation protocols were applied. When stimulated with an uniformly increasing object (constant angular velocity), the LGMD response consists in a peak followed by a rapid firing rate decrement. If compared to the neural response obtained with looming objects, the response, to an edge expanding at a constant linear rate, is very brief [181].

Object edges must move with an increasing velocity over the locust eye so that the LGMD neural response follows the object movement. Additionally, it was found that an increase in the object's edge amount contributes to an increase in the LGMD spike rate. Thus, the velocity of the boundary edges of the visual stimuli, combined with a rapid increase in object's edge amount, are the most important cues used by the neuron to distinguish approaching from receding or translating objects.

When performing a time analysis of the neural responses obtained, this team [157, 181] has found that, when presented with a looming stimulus, the LGMD spike rate increases throughout the object's approach, and, in the case of small or very fast approaching objects, without peaking prior to collision. Observing that locusts were able to trigger escape behaviors even in these situations, it was considered, by this research team, that the peak in LGMD response is not the essential function variable to trigger these escape responses [155].

After uncovering the correlations between the visual stimulus and the LGMD neural responses, Rind and her colleagues [32, 66, 149, 150, 154–156] proposed a critical race hypothesis: the way through which LGMD neuron extracts an approaching object

can be seen as a pre-synaptic competition between excitation and lateral inhibition [157]. The excitation is produced by the photoreceptor units, which are sequentially excited by the image edges expansion as the object approaches, being transmitted downstream to the neuropiles located below the photoreceptive layer. At the Medulla, each neuron that establishes a synapse with the LGMD neuron, also establishes a synapse with its neighbor neuron, providing a route to the spread of lateral inhibition. As the number of excited medullar units increases as the object approaches, the strength of the lateral inhibition also increases, being temporally limited by the underlying delay of inhibitory synapses [149, 185]. Consequently, the number of excited medulla units should increase across time, so that excitation is sufficiently high to overcome inhibition. In fact, this is verified when there is an increment on the image edges as the object approaches the eye, or when the speed of the edges increases. Both situations will make the excitation to win the race, and the LGMD neuron will respond with an increasing spike rate.

Rind and her colleagues also defends the existence of a second type of inhibition that acts directly on the LGMD neuron, post-synaptically. This type of post-synaptic inhibition (named feed-forward inhibition) is triggered when a high number of photoreceptor units is suddenly activated within a short time interval. This processing step acts to reduce the LGMD neural responses when the whole background moves, when overall light intensity changes, as it happens, for example, during a saccade [48], or at the end of an object approach [154].

According to these findings, the LGMD neuron is seen as a linear summing unit, directly converting inputs from its presynaptic circuitry into a firing rate output.

2.2.2.2 The feed-forward excitation versus feed-forward inhibition hypothesis (H2)

Across the last few years, in order to find out the mechanisms behind the LGMD response selectivity, Gabbiani and his colleagues [59, 67, 68, 70, 71, 83] started to investigate the LGMD neural responses to different visual stimuli trajectories: approaching, receding and translating [70, 83]. The obtained results showed the preference of the LGMD neuron to approaching trajectories, by the production of higher firing rates when compared to receding and/or translating trajectories.

Additionally, electrophysiological recordings from LGMD postsynaptic target's activity, the DCMD neuron, to combined visual stimuli characteristics, showed a very interesting relationship: as the ratio between the looming visual stimuli half-size (l) and velocity (v) - denominated $l/|v|$ - (see equation 5.7) varies over one order of

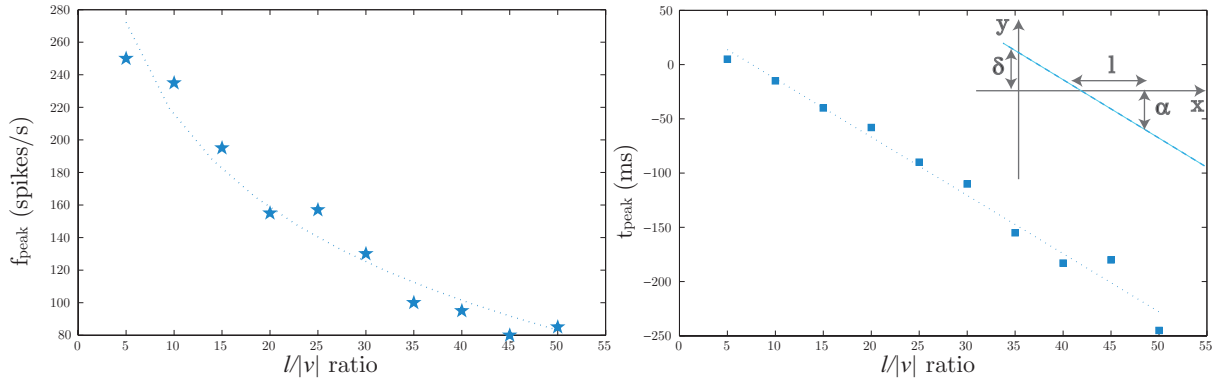


Figure 2.3: Approximation of the LGMD responses to looming stimuli with different $l/|v|$ ratios. *Left panel:* LGMD peak firing rate (f_{peak}) as a function of the stimulus ratio between size and speed (fitted by a logarithmic regression, indicated by the dashed line: $f_{\text{peak}} = -82.14\log(l/|v|) + 404.5$, $r = 0.95$). *Right Panel:* Plot of the LGMD peak time relative to collision (t_{peak}) versus the $l/|v|$ ratio (fitted by a linear regression line: $t_{\text{peak}} = -4.7 \cdot l/|v| + 27$, $r = 0.981$). The values here plotted were extracted from [71].

magnitude (from 5 to 50 milliseconds), the LGMD firing rate profile remains highly unchanged, consisting in a small increase, then a peak and finally a decay towards the end of the approach. However, as $l/|v|$ varies, systematical changes occur.

Firstly, the responses of the DCMD neuron are brisker for lower $l/|v|$ values, leading to a more defined and higher peak in the LGMD firing rate profile (left panel on figure 2.3). Secondly, as shown on the right panel of figure 2.3, the peak time on the LGMD firing rate consistently shifted towards collision as the $l/|v|$ ratio decreased (which corresponds to small and/or fast-moving visual stimuli).

A linear regression analysis between the Time-To-Collision of the peak firing rate (named ast_{peak}) versus $l/|v|$ ratio (see figure 2.3, left panel) [70] revealed that these two variables are linearly related, being represented as:

$$|t_{\text{peak}}| = -\alpha \cdot l/|v| + \delta \quad (2.1)$$

where t_{peak} is the LGMD peak time relative to collision, α represents the regression slope and δ the intercept (see figure 2.3).

Through this regression, it was mathematically shown that it is the angular threshold size ($\theta_{\text{threshold}}$) computation that characterizes the LGMD peak response, which can be determined through the linear regression slope, by:

$$\theta_{\text{threshold}} = 2 \cdot \tan^{-1}(1/\alpha) \quad (2.2)$$

Comparing equations 2.1 and 2.2 with the linear regression values on figure 2.3, we conclude that the LGMD firing rate peak time (t_{peak}) occurs 27 milliseconds after the object reaches an angular size of 24 degrees.

In a behavioral perspective, t_{peak} has been related to a preparatory phase of collision avoidance and escape behaviors triggering [58]. Additionally research, aiming to investigate the dependence of this angular threshold computation - and subsequent behavioral adaptation - on several stimulus parameters, as changes in visual stimuli shape, texture or approaching angle [68, 72], concluded that LGMD is a reliable neuron, because t_{peak} remained invariant to such stimuli variations.

Although the preferential response of LGMD and DCMD to looming objects has been so far recognized, the neural computation performed by the LGMD during approaching remained unclear. Additional experimental and theoretical analysis, aiming to understand the computation and the algorithm used to perform it, were conducted.

Each LGMD neuron receives visual inputs through three different dendritic fields. The biggest one receives excitatory retinotopic inputs from the entire visual field, being named as Field A (Fig. 2.4). Field A receives angular speed signal's inputs from local movement detectors located on the Medulla layer. The other two smaller dendritic fields, named B and C, receive non-retinotopic feed-forward inhibitory inputs, whose activation depends on the visual stimulus's size, being maximally activated by large and transient luminance changes [71] (see Fig. 2.4).

In response to a looming stimuli, the firing rate of the LGMD neuron increases as the stimulus angular size increases, starting to decline at a fixed delay after the stimulus reached a specific angular threshold on the locust compound eye (see equation 2.2). This decline is, according to Gabbiani [71], caused by the feed-forward inhibitory inputs onto the LGMD dendritic fields B and C, which are activated concurrently with the feed-forward excitation from dendritic field A, during the approaching of a looming stimulus, with excitation slightly leading inhibition. Gabbiani also defends the existence of a pre-synaptic lateral inhibitory process, but, unlike the critical race hypothesis previously described, this research defends that it becomes ineffective after the looming stimuli had reached an angular threshold [73]. After reaching this threshold, feed-forward inhibition becomes significantly activated, leading to a fast and pronounced LGMD spike rate decrement [69, 73].

According to the obtained results, it has been proposed that the postsynaptic inhibition has a predominant role in shaping the LGMD neural responses to different stimuli, suggesting the existence of a post-synaptic multiplication, which is implemented within the LGMD neuron itself [71].

In order to discover the processing stream prior to the LGMD neuron, leading to its selectivity for approaching objects, additional morphological, electrophysiological, among others techniques, were required. In [95], it is described that the LGMD's selectivity arises partially from presynaptic mechanisms that synchronize a large population of inputs during a looming stimulus. Further, a decrease in the latency of the excitatory inputs, as the instantaneous angular speed of the edges sweep across individual photoreceptors increases, also contributes to the LGMD neural selectivity [95]. In [69, 138] it is defended that spike frequency adaptation also mediates LGMD looming stimulus selectivity: stimuli with temporal profiles with increasing strength (as the case of looming) are able to overwhelm spike frequency adaptation. Stimuli with temporal profiles of near constant strength (as in the case of a translating stimuli) suffer the effects of spike frequency adaptation, which shuts off synaptic excitation when it is not maximally activated.

A further discussion related to the implications of these findings and its mathematical modeling, will be approached in the current chapter.

2.2.2.3 Integration of distributed computation hypothesis (H3)

Based on the biological results obtained by the two previously described research teams, and due to the divergence between the hypotheses proposed, Sergi and his colleagues [15] proposed an alternative explanation for the LGMD selective response. In a relevant publication [71] it has been defended that the response of the LGMD neuron can not be explained in terms of the interaction between pre and post-synaptic excitation and inhibition, as defended by the critical race hypothesis [154]. On the other hand, unlike the feed-forward excitation versus feed-forward inhibition hypothesis, [15] defend that non-linear responses of the LGMD neuron can be explained in terms of an emergent non-linear operation that results from the integration of distributed computations performed by the neurons of the locust optic lobe processing architecture, as a whole, and not as a multiplicative operation that is local to a single neuron. In other words, the morphology of the optic lobe embeds the overall control.

As a consequence of these three different hypothesis, distinct LGMD models were proposed along the last few years [4, 16, 70]. In the following, it is presented a deep description of the most relevant and representative models of each hypothesis, according to literature.

2.3 LGMD models: Mathematical formulation and description

In order to retain information about modeling of LGMD neurons, multidisciplinary fields, ranging from 1995 until 2012, have been analyzed, including: Computational Biology, Neuroscience, Neurophysiology, Biosystems, Artificial Life, Neurocomputing, Computer Vision and Image Understanding, Neural Networks, Robotics and Automation, Robotic Research.

Table 2.2 summarizes selected papers described in literature where LGMD neuron modeling, based on one of the three previously mentioned hypothesis, was addressed.

One LGMD model proposed by Gabbiani [70], three LGMD models proposed by Rind [121, 176, 233] and one LGMD model proposed by Sergi [15], were the ones that better suited our aims and were in agreement with the three hypothesis. Thus, were chosen to computational implementation and comparison, being highlighted on table 2.2.

Table 2.2: Summary of published LGMD neuron models. P) Photoreceptive layer; L) Lamina layer; M) Medulla layer; LGMD) LGMD neuron.

Dim	Model Reference	Model components				Extra-layers / Processing mechanisms	Robotic implementation
		P	L	M	LGMD		
1D	Gabbiani 1995 [83]				✓	No	No
	Gabbiani 1999 [70]				✓	No	No
	Gabbiani 2002 [71]				✓	No	No
	Gabbiani 2004 [72]				✓	No	No
2D	Rind 1996 [150]	✓	✓	✓	✓	No	No
	Rind 1999 [17]	✓	✓	✓	✓	No	Yes
	Rind 2000 [160]	✓	✓	✓	✓	No	Yes
	Gabbiani 2001[68]	✓			✓	No	No
	Rind 2002 [154]	✓	✓	✓	✓	No	Yes
	Sergi 2004 [4]	✓		✓	✓	Expansion and Prediction	Yes
	Rind 2005 [176]	✓	✓	✓	✓	No	Yes
	Sergi 2005 [14]	✓		✓	✓	Two LGMD models	Yes - UAV
	Rind 2006 a[228]	✓	✓	✓	✓	TSNN	No - Real images of collision scenarios
	Rind 2006 b [229]	✓	✓	✓	✓	G layer/ FFM cell	Yes
	Rind 2006 c [233]	✓	✓	✓	✓	GAs for optimization	No - Real images of collision scenarios
	Gabbiani 2007 [137]				✓	No	No
	Rind 2007 [195]	✓	✓	✓	✓	EMDs	No - Real images of collision scenarios
	Sergi 2007 [13]	✓		✓	✓	Two LGMD models	Yes - UAV
	Gabbiani 2009 a [138]				✓	No	No
	Gabbiani 2009 b [139]				✓	No	No
	Gabbiani 2009 c [136]				✓	No	No
	Rind 2010 a[121]	✓	✓	✓	✓	Additional Depth Movement Feature	No
	Rind 2010 b [234]	✓	✓	✓	✓	Two LGMD models to drive left and right motors	Yes
	Sergi 2010 [15]	✓	✓	✓	✓	Coupled with a stability system based on EMDs	Yes
	Gabbiani 2012 a [94]	✓			✓	No	No
	Gabbiani 2012 b [93]				✓	No	No
	Rind 2012 [231]	✓	✓	✓	✓	Two LGMD models to drive left and right motors	Yes

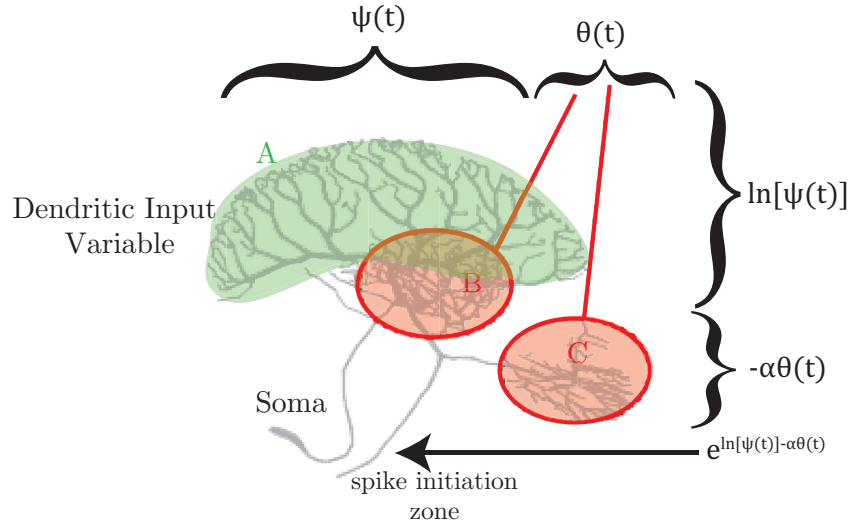


Figure 2.4: Schematic illustration of the LGMD neuron and the core computation performed when the presence of an approaching visual stimuli. Excitatory (A, green) and inhibitory (B and C, red) dendritic fields of the LGMD neuron are highlighted on the image. Adapted from: [35]

2.3.1 LGMD modeled as a η -function

According to the data recorded from the LGMD neuron [70, 71, 83], H1 defends that the responses of this neuron can be explained in terms of the product of two high-level features of the visual stimuli: (1) the object angular size (l) and (2) the object angular speed (v). These two variables are directly conveyed into the LGMD neuron via separated inhibitory and excitatory pathways (see Fig. 2.4) respectively, with excitation undergoing a logarithmic compression in the dendritic tree of the LGMD neuron [94].

The excitatory and inhibitory signals are then combined and power-law transformed by the spike generation mechanism [71], at the spike initiation zone (Fig. 2.4), through a non-linear transfer function of the LGMD neuron, which is close to an exponentiation. The output result signals the angular threshold size through its firing rate peak.

According to this, the LGMD firing rate to a looming object could be fitted by the so-called η -function:

$$\begin{aligned} \eta(t) &= \Psi(t - \delta) \cdot \exp(-\alpha\theta(t - \delta)) \\ \eta(t) &= \exp[\ln(\Psi(t - \delta)) - \alpha\theta(t - \delta)] \end{aligned} \quad (2.3)$$

where,

$$\alpha = \frac{1}{\tan(\theta_{\text{threshold}}/2)} \quad (2.4)$$

and $\theta_{\text{threshold}}$ specifies the angular size subtended by the approaching object (in the simulations, we considered it as 23 degrees, which implies $\alpha = 4.9$) δ milliseconds (here considered as zero) before the LGMD spike rate profile reaches its peak. The angular expansion of the object increases as it is getting closer, leading the LGMD response to increase along with it. Although, when the object's angular size exceeds the threshold value $\theta_{\text{threshold}}$, which is an animal and species dependent parameter, the exponential term of $\eta(t)$ decays fast towards zero, leading to an exponential decay of the firing rate, $\eta(t)$. It was experimentally demonstrated that $\theta_{\text{threshold}}$ is invariant to the actual size, speed, shape, texture or approaching angle of the moving object [68].

Equation 2.3 has already proven to be an excellent fit for the LGMD responses to a looming stimuli [68, 83]. However, this model makes some strong assumptions. For example, it assumes that the insect is able to compute the size and velocity of a looming object. Besides, it overlooks the role of the neurons pre-synaptic to the LGMD.

From an engineering point-of-view, this demands a visual system capable to extract the exact size of the approaching object, as well as its rate of change along the time. This would be computationally expensive.

2.3.2 LGMD modeled as an artificial neural network

Unlike the previous η -function model, LGMD neural network's models [121, 229, 233] are strongly based on the overall morphology of the insect visual system. Highly supported by the anatomy and physiology of the locust optic lobe, the neural network developed by Rind and her colleagues was, initially, composed by three principal layers [17]:

1. The entrance layer (Layer 1 on figure 2.5), also named the photoreceptive layer, representing the ommatidia array and the lamina layer, responding to changes in luminance of the captured image, being able to detect the borders of a moving object.
2. The processing layer (Layer 2 on figure 2.5), where the excitation is transmitted retinotopically through the neural network, while the inhibition is delayed and transmitted laterally between adjacent elements that compose this layer, representing the medulla.
3. The output layer (Layer 3 on figure 2.5), which represents the LGMD neuron,

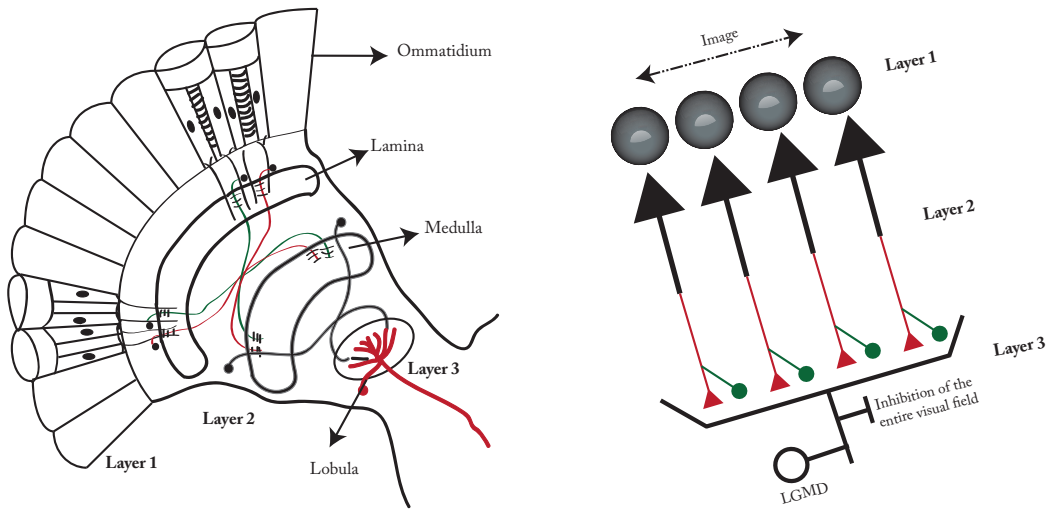


Figure 2.5: Parallelism between the locust visual system and the equivalent neural model.

where the excitation and the inhibition are combined in order to obtain the final response.

Additionally it has been introduced a neural pathway of feed-forward inhibition, in order to inhibit the LGMD output when substantial changes occur in the captured image, such as luminance variations caused by the locust movement in the environment. A graphical representation of the parallelism between the LGMD model based on neural networks and the locust visual system is shown on figure 2.5.

Despite the good results obtained with the first LGMD neural network model [17], the model continued to evolve [16, 154, 160, 176, 229] and it was used in mobile robots and deployed in automobile scenarios for collision detection. These connectionist models have shown that the integration of lateral and feed-forward inhibition can account for aspects of the LGMD neuron looming sensitivity and selectivity when stimulated with approaching, translating and receding objects.

In this section, we will describe three selected relevant LGMD models, all based on the critical race hypothesis, H2 [157]. They were named as LGMD model 1 [233] (table 2.2, Rind 2006 c) , LGMD model 2 [229] (table 2.2, Rind 2006 b) and LGMD model 3 [121] (table 2.2, Rind 2010 a).

The next sub-sections describe in detail the mathematical modeling of each model.

2.3.2.1 LGMD model 1

The LGMD neural network proposed in [233] has the same functional processing structure as the one described in [17]. It is composed by three groups of cells (see figure

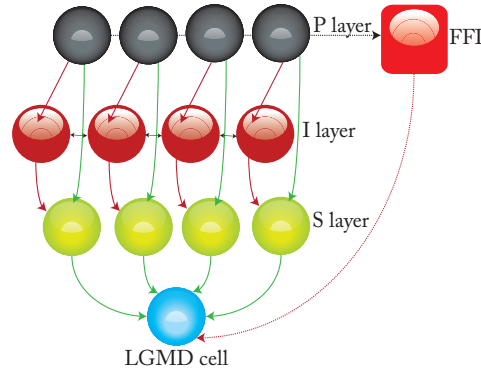


Figure 2.6: Schematic illustration of LGMD model 1. It is composed by three groups of cells (layers) and two single cells: P layer: photoreceptor cells; I layer: inhibitory cells; S layer: summing cells; FFI cell: feed-forward inhibition cell; and LGMD cell: that represents the LGMD biological neuron.

2.6): photoreceptor cells, forming the photoreceptive layer (P layer) , inhibitory cells (I layer) and summing cells (S layer). Additionally, it is composed by two single cells: the feed-forward inhibition cell (FFI cell) and the LGMD cell.

Overall, this model executes an image sequence processing. A grayscale image of the camera current field of view, represented has a matrix of values, is the input, at each time step, to a matrix of photoreceptor units (P layer). The output of each photoreceptor unit is the difference of the pixels' luminance observed in successive time steps. This process tries to mimic the one that happens in the Large Monopolar Cells (LMCs) located in the insects' lamina, which main goal is to eliminate information about mean levels of illumination and enhance changes in illumination, across time. This process can be formally written as:

$$P_{ij}(t) = |L_{ij}(t) - L_{ij}(t - 1)|, \quad (2.5)$$

where L_{ij} is the luminance of pixel at position i, j .

The neural network of the LGMD model detects eminent collisions responding to the edges expansion of the captured image, a computational strategy that substitutes the ones based on object identification. The output excitation that comes from the P cells, passes directly to two different layers of cells retinotopically arranged: the Inhibitory layer (I) and the Summing layer (S).

At the inhibitory layer (I layer), the excitation produced at the photoreceptor layer, at two successive instants of time, is converted into inhibition. The resultant inhibition is laterally transmitted between adjacent units at the inhibitory layer. Thus, the lateral

transmission diffuses the incoming excitation. Mathematically, lateral inhibition is represented by a low-pass filter:

$$I_{ij}(t) = \{\{P_{ij}(t-1) + P_{ij}(t)\} \otimes K_{pq}\}, \quad (2.6)$$

where I_{ij} is the inhibition value at the (i, j) position, \otimes denotes the convolution operation and K_{pq} is a 3 by 3 kernel:

$$K_{pq} = \frac{1}{9} \begin{bmatrix} 1 & 1 & 1 \\ 1 & 1 & 1 \\ 1 & 1 & 1 \end{bmatrix} \quad (2.7)$$

The excitatory (P layer) and inhibitory (I layer) outputs are combined at the Summing layer (S layer). However, based on the conduction delay associated with inhibitory synapses, the output of I layer is delayed one time step before being combined with the actual excitation from the P layer,

$$S_{ij}(t) = P_{ij}(t) - I_{\text{strength}} I_{ij}(t-1) \quad (2.8)$$

where $S_{ij}(t) \geq 0$ and I_{strength} is a tuning parameter of this model. The excitation is only limited by the image expansion rate. Therefore, the S layer combines the excitation of the current time step (t) and the inhibition of the previous time step ($t-1$). I_{strength} represents the inhibition weight over the excitation, which value was chosen such that, if the captured object, between $t-1$ and t , increases only one pixel per side, the produced excitation will be pretty much eliminated by inhibition. Thus, $S_{ij}(t)$ is higher than zero if two successive frames have an object with a minimum expansion rate of two pixels per side. This is the minimum expansion rate to occur excitation.

The excitation resultant of the Summing layer is combined to form the membrane potential of the LGMD cell, which is the output of the neural model:

$$\text{LGMD}(t) = \sum_{i=1}^m \sum_{j=1}^n S_{ij}(t), \quad (2.9)$$

where m and n are the number of columns and rows of the captured image. In order to obtain the LGMD output in terms of spike rate - so that the model output be compared with biological results - the $\text{LGMD}(t)$ value is divided by the number of cells on the S layer (defined by $n \times m$).

At a given time step t , if the LGMD value exceeds a threshold ($\text{LGMD}_{\text{thresh}}$),

Table 2.3: Parameter values of the LGMD model 1. [233]

PARAMETER	VALUE
I_{strenght}	7
$\text{LGMD}_{\text{thresh}}$	5000
$\text{FFI}_{\text{thresh}}$	2.000.000
$\text{FFI}_{\text{delay}}$	3
spike_n	2 or 3
spike_N	5

a spike is produced. If a given number of successive spikes (spike_n), within a pre-specified interval of time steps (spike_N), is observed, a collision detection alarm will be triggered.

The feed-forward inhibition cell (FFI) is very similar to the LGMD cell, but it cell receives the output from the P layer, and is given by:

$$\text{FFI}(t) = \frac{\sum_{i=1}^m \sum_{j=1}^n |P_{ij}(t-1)|}{\text{ncell}}, \quad (2.10)$$

where ncell represents the number of pixels in the captured image. If the value of the FFI cell overcomes a certain threshold ($\text{FFI}_{\text{thresh}}$), it will act over the LGMD cell, inhibiting it. The FFI response is delayed by a number of timesteps (defined by $\text{FFI}_{\text{delay}}$). So, the final response of the LGMD neuron is defined by the following conditions:

$$\text{LGMD}(t) = \begin{cases} \text{LGMD}(t), & \text{if } \text{FFI} \leq \text{FFI}_{\text{thresh}} \\ 0, & \text{otherwise} \end{cases} \quad (2.11)$$

All the LGMD model 1 optimal parameter values were determined through the application of a Genetic Algorithm (GA) described in [233]. Through the mean and the standard deviation of 12 replicate sets of parameters optimized by the GA, the values listed on table 2.3 were used.

2.3.2.2 LGMD model 2

Model 2 [229] surged as an attempt to overcome the limitations observed in the previous models based on neural networks, in what concerns its range of applicability.

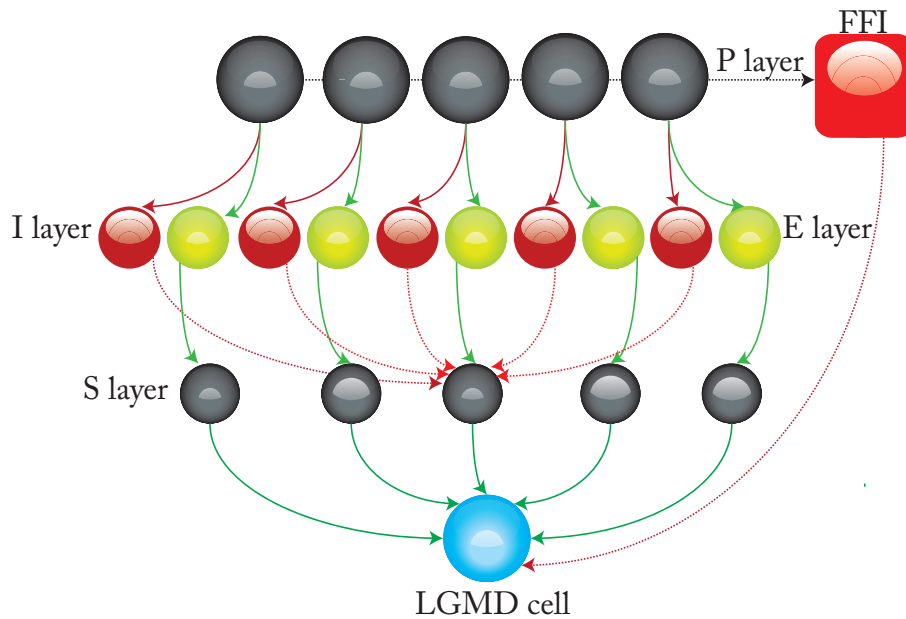


Figure 2.7: Schematic illustration of the proposed LGMD model 2. It is composed by four groups of cells and two single cells: P layer: photoreceptor cells; I layer: inhibitory cells; E layer: excitatory cells; S layer: summing cells; FFI cell: feed-forward inhibition cell. LGMD cell: represents the LGMD biological neuron.

A new mechanism was added to the basic structure of the LGMD neural network, in order to filter out irrelevant visual details, such as noise, aiming to avoid false collision detections.

The new mechanism here introduced makes the excited cells, surrounded by other excited cells, located in the P layer, to have a higher contribution to the membrane potential of the LGMD cell, relatively to isolated excited cells (which would represent noise in the captured image). The isolated excitations will be filtered out by a filter that is able to select the excitation from groups of cells, only enabling image sections with large excited spatial areas to contribute to the LGMD cell final excitation, leading to a reduction on the image noise.

Comparing the structure of the neural network from LGMD model 2 [229] (figure 2.7) to the LGMD model 1 [233] (see figure 2.6), it can be concluded that they are quite similar.

The output of the P layer is the input to two different layers: the excitatory (E) and the inhibitory (I) layer, similarly to model 1. Relatively to the excitatory cells of the E layer, the excitation produced at the P layer is passed directly to the retinotopic counterpart at the S layer. And the inhibition layer (or I layer) receives the output of

the P layer and applies a blur effect on it, using:

$$I_f(x, y) = \sum_{i=-1}^1 \sum_{j=-1}^1 P_{f-1}(x+i, y+j) \cdot w_l(i, j), \quad i, j \neq 0 \quad (2.12)$$

$$[w_l] = \begin{bmatrix} 0.10 & 0.25 & 0.10 \\ 0.25 & 0 & 0.25 \\ 0.10 & 0.25 & 0.10 \end{bmatrix} \quad (2.13)$$

where $I_f(x, y)$ is the inhibition relative to the cell in (x, y) position at frame f , $w_l(i, j)$ represents the local inhibition weight. The main difference to LGMD model 1, is that the inhibition from the (x, y) cell only spreads to the nearest neighbors and does not condition itself (central pixel of kernel w_l is zero, contrary to kernel K_{pq} on equation 2.6).

Analyzing the kernel values (equation 2.13), we conclude that the inhibition value of a particular cell is given by the distance at which a neighboring cell is located. Note that the nearest cells have a higher contribution to the inhibition value of a central cell (0.25), whereas the cells located in the diagonal of the kernel have a smaller contribution to the final inhibitory value of the central cell (0.10). This value's distribution is based on a biological principle: distant neurons inhibit with less intensity a particular neuron than those closer to a neuron, since the strength of a neural signal decreases with increasing distance.

Finally, the excitatory flux from the E cells and the inhibition from the I cells are summed as follows [229]:

$$S_f(x, y) = P_f(x, y) - W_i \cdot I_f(x, y), \quad S_f(x, y) \geq 0, \quad (2.14)$$

where P_f is the output of the P layer at frame f , I_f the output of the I layer at frame f and W_i (a scalar) that represents the final inhibition strength.

Herein, a new mechanism was added to the LGMD_{cell} to filter out background noise. This mechanism allows clusters of excitation in the S units to provide a greater individual input to the membrane potential of the LGMD_{cell} than individual inputs of isolated S units, as in Model 1. At each time step, the excitatory output from each S unit is multiplied by a passing coefficient C_e , calculated by the cell's surrounding neighbors, as:

$$C_{e_f}(x, y) = \sum_{i=-1}^1 \sum_{j=-1}^1 S_f(x+i, y+j) \cdot w_e(i, j), \quad (2.15)$$

where $w_e(i, j)$ represents the influence of the neighboring cells in the central cell coefficient, being simplified as a convolution kernel:

$$[w_e] = \frac{1}{9} \begin{bmatrix} 1 & 1 & 1 \\ 1 & 1 & 1 \\ 1 & 1 & 1 \end{bmatrix}. \quad (2.16)$$

Therefore, if a cell is surrounded by excited neighboring cells, its Ce_f value will be higher.

The final value for each S cell is given by:

$$Se_f(x, y) = |S_f(x, y) \cdot Ce_f(x, y) \cdot w^{-1}|, \quad (2.17)$$

where w is a scalar computed at each frame by:

$$w = \max|Ce_f|C_w^{-1} + \Delta c, \quad (2.18)$$

Cells with higher coefficients will have its excitation raised, relatively to the initial excitation value that particular cell holds. On the other hand, cells with smaller coefficients will have its excitation reduced.

At each time step, the LGMD value is obtained by summing all the excitation that comes from each S cell.

$$\text{LGMD}_f = \sum_{x=1}^n \sum_{y=1}^m Se_f(x, y) \quad (2.19)$$

The membrane potential of the frame, LGMD_f (or Se_f), is normalized with the following sigmoid function, that keeps the output within certain intervals:

$$\text{lgmd}_f = \frac{1}{(1 + e^{-Se_f/\text{ncell}})}, \quad (2.20)$$

where ncell is the total number of summing cells. As Se_f value is always greater than or equal to zero, the normalized membrane potential $\text{lgmd}_f \in [0.5, 1]$. Collision detection is decided by a spiking mechanism, using an adaptable threshold T_s . The threshold is initially set to a predefined value, T_{in} , and is actualized every frame as

follows:

$$T_s = \begin{cases} T_s + \Delta t, & \text{if } \text{lgmd}_{av} > \Pi \text{ and } (T_s + \Delta t) \in [T_{in}, T_{su}] \\ T_s - \Delta t, & \text{if } \text{lgmd}_{av} < \Pi \text{ and } (T_s - \Delta t) \in [T_{in}, T_{su}] \\ T_s, & \text{others} \end{cases} \quad (2.21)$$

$[T_{in}, T_{su}]$ define the upper and lower limits for adaptation process, Δt is the increment value with which T_s is updated; Π , a defined constant value, limits the average membrane potential lgmd_{av} , from frame $f - l$ to frame $f - k$ (l and k specify the average interval size), defined as:

$$\text{lgmd}_{av} = \frac{1}{l - k + 1} \sum_{i=k}^l \text{lgmd}_{f-i} \quad (2.22)$$

If the average membrane potential lgmd_{av} exceeds T_s , a spike is produced. A collision is considered detected when there are four successive neural spikes in five timesteps.

During a deviation maneuver made by a robot, for example, the membrane potential could drastically increase due to the rapid change of the visual scenario caused by the turning movement. This fact could lead to the production of false collision alerts. In order to prevent this particular type of situations, a feed-forward inhibition cell (FFI) was also added to model 2. Its value is computed as:

$$\text{FFI}_f = \sum_{x=1}^m \sum_{y=1}^n P_{f-1}(x, y) \cdot \text{ncell}^{-1} \quad (2.23)$$

If FFI_f exceeds a predefined threshold value (FFI_{thresh}) the LGMD_f is inhibited.

The used LGMD model 2 parameters are based on the ones used in [229], and are listed in table 2.4.

2.3.2.3 LGMD model 3

LGMD model 3 [121], was proposed as an attempt to overcome limitations observed in previous developed models, including the distinction between approaching and receding objects. The model here proposed [121] is able to provide additional depth direction information about the movement captured by the camera.

The LGMD model 3 is composed by the same layers as the two previous models, having three additional cells: two grouping cells (J and H) and one depth movement direction cell (D cell), making up a direction selective system.

Table 2.4: Parameter values of the LGMD model 2.[229]

PARAMETER	VALUE	PARAMETER	VALUE
W_i	0.5	Δt	0.001
C_w	4	Π	0.72
Δc	0.01	l	5
ncell	$n \times m$	k	2
T_{in}	0.88	FFI_{thresh}	75
T_{su}	0.9		

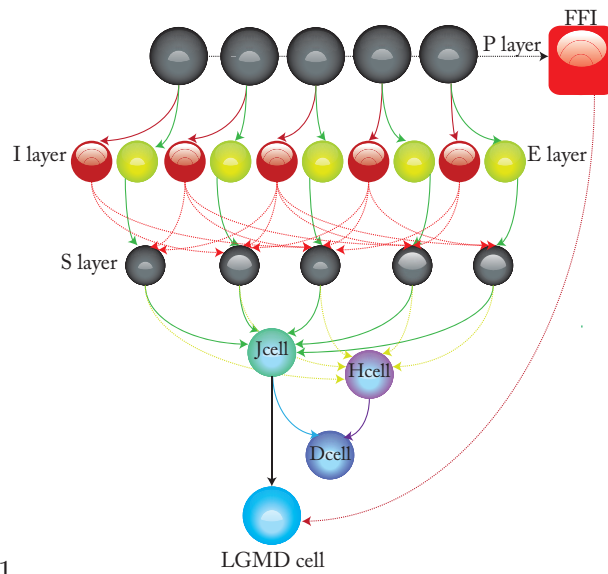


Figure 2.8: Graphical representation of the LGMD model 3.

The first layer in model 3 is the Photoreceptive layer. The output of this layer is given by equation 2.5.

Each excitatory cell from E layer ($E_f(x, y)$) receives directly the excitation value from each photoreceptive cell ($P_f(x, y)$) from P layer.

The inhibitory layer (I layer) works similarly to the one of model 2, being described by equations 2.12 and 2.13.

The output of the I layer is directly sent to the summing layer. The summing layer (or S layer) receives the output from E and I layers, performing the following operation:

$$S_f(x, y) = E_f(x, y) - W_i \cdot I_f(x, y) \quad (2.24)$$

where E_f is the output of the E layer at frame f (see equation 2.14). I_f is the output of the I layer at frame f and W_i (a scalar) represents the inhibition strength. If the excitation of each S cell exceeds a threshold value (T_{thresh}), it is able to reach the LGMD cell. This process is given mathematically by:

$$S_f(x, y) = \begin{cases} S_f(x, y), & \text{if } S_f(x, y) \geq T_{\text{thresh}} \\ 0, & \text{if } S_f(x, y) < T_{\text{thresh}} \end{cases} \quad (2.25)$$

The new mechanism added to this model, introduced in [121], is here described in detail. Two of the new added cells, cell J and H, are used for depth movement recognition. J cell holds the same value as the LGMD cell (equation 2.19), having the same spatio-temporal structure. H cell has the same spatial structure as the LGMD cell, however including a temporal difference.

$$J_f = \sum_{x=1}^n \sum_{y=1}^m S_f(x, y) \quad (2.26)$$

$$H_f = J_{f-1} = \text{LGMD}_{f-1} \quad (2.27)$$

The depth direction movement cell (D cell) is used to calculate the excitation difference between two successive frames, being given by:

$$D_f = |J_f| - |H_f| \quad (2.28)$$

By adding the previously described processing step, model 3 is able to estimate the movement direction in depth, being based on the concept that a looming object gets larger across time and a receding object gets smaller. If an object is approaching, $|J_f|$

is higher than $|H_f|$. If the object is receding, $|J_f|$ is smaller than $|H_f|$. However, in a biological perspective, there is no parallelism between this direction selective system and a correspondence in the insect biology.

Additionally, in order to filter out small movements, a threshold mechanism was added to the depth direction movement cell D (named T_D).

$$D_f = \begin{cases} 1, & \text{if } D_f \geq T_D \\ 0, & \text{if } T_D < D_f < T_D \\ -1, & \text{if } D_f \leq T_D \end{cases} \quad (2.29)$$

Variable D_f can hold three different values: 1 represents an approaching object; 0 represents an object that is moving slowly; -1 represents a receding object. The threshold T_D depends on the image size and it is set *a priori*. Afterward, the membrane potential is transformed into a spiking output using a sigmoid transformation:

$$\text{LGMD}_f = (1 + e^{-J_f \cdot \text{ncell}^{-1}})^{-1}, \quad (2.30)$$

Where ncell is the total number of cells on the S layer and $\text{LGMD}_f \in [0.5, 1]$.

The collision alarm is decided by the LGMD cell spiking. If the membrane potential LGMD_f exceeds the threshold T_s and D is equal to one (denoting an approaching object), a spike is produced.

$$S_f^{\text{spike}} = \begin{cases} 1, & \text{if } \text{LGMD}_f \geq T_s \text{ and } D_f = 1 \\ 0, & \text{others} \end{cases} \quad (2.31)$$

Finally, a collision is detected when there are n_{sp} spikes in n_{ts} time steps ($n_{\text{sp}} \leq n_{\text{ts}}$), as follows:

$$S_{\text{LGMD}} = \begin{cases} 1, & \text{if } \sum_{f-n_{\text{ts}}}^f S_f^{\text{spike}} \geq n_{\text{sp}} \\ 0, & \text{others} \end{cases}, \quad (2.32)$$

where S_{LGMD} is 1 when a collision is detected.

When implemented in a robotic platform, the robot escape behavior would be initialized when a collision is detected. Besides that, the spikes can be suppressed by the FFI cell when whole field movement occurs. If it is not suppressed during the tuning of the animal or the robot, the network may produce spikes and even false collision alerts due to sudden changes in the visual scenario.

The feed-forward inhibition cell (FFI cell) is obtained through the mathematical

Table 2.5: Parameter values of the LGMD model 3.[121]

PARAMETER	VALUE	PARAMETER	VALUE
W_i	0.35	n_{sp}	3
T_{thresh}	3	n_{ts}	5
T_D	0.25·100·100	T_{FO}	10
T_S	0.8	α_{ff}	0.01

computation previously mentioned in equation 2.23.

In the case that FFI_f exceeds a threshold $T_{FFI,spikes}$ produced by the LGMD cell are inhibited. The threshold is given by:

$$T_{FFI} = T_{FO} + \alpha_{ff}T_{FFI_{f-1}} \quad (2.33)$$

where T_{FO} is the initial value of T_{FFI} . As we can observe in the previous equation, the adaptable threshold depends on the previous T_{FFI} and on a coefficient, α_{ff} .

All the parameters used by LGMD model 3 are the ones used on [121] and are listed on table 2.5.

2.3.3 LGMD connective model

An alternative model was proposed in[15].

LGMD connective model (Fig. 2.9) proposes that the non-linear transfer function of the LGMD neuron can be explained by the physiological and anatomical properties of its afferent visual processing hierarchy. Similarly to models 1, 2 and 3, the LGMD connective model [15] is based on the structure of the locust visual system. Figure 2.9 divides the model into three sequential processing steps. Firstly, at the Lamina, a centre-excitation/surround-inhibition connectivity between the signals received by the photoreceptors is proposed, providing an edge enhancement. The second processing step, at the Medulla layer, occurs through neurons interaction, producing onset and offset sensitive responses. The third one, the Lobula, has a specific connectivity mapping that contributes to the transformation of the signals generated in the Medulla into the LGMD neural response.

These processing steps were simplified and modeled through mathematical approaches.

In the Photoreceptor layer (figure 2.9, A), the mean layer activity is obtained

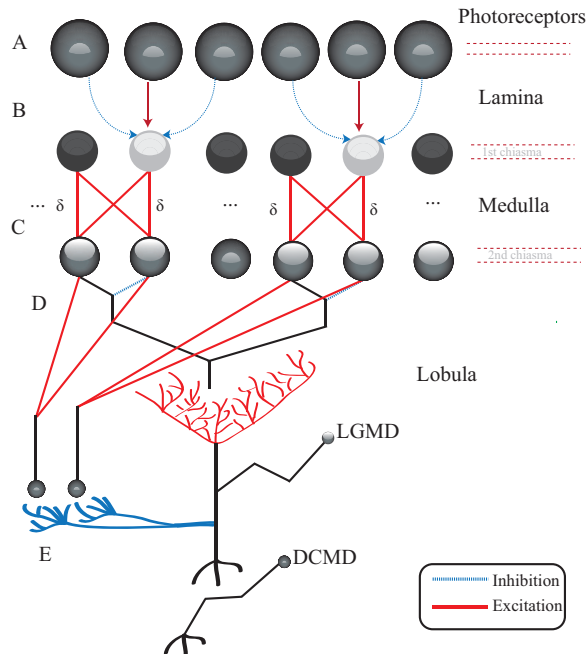


Figure 2.9: LGMD connective model. It is based on the anatomical organization of the LGMD neural pathway. (A) Photoreceptive layer; (B) centre/surround architecture in the Lamina cells; (C) the on-off neurons in the Medulla; (D) neurons connected to the excitatory pathway of the LGMD; (E) LGMD/DCMD output.

Similarly to models 1, 2 and 3, the LGMD connective model [15] is based on the structure of the locust visual system. Figure 2.9 divides the model into three sequential processing steps. Firstly, at the Lamina, a centre-excitation/surround-inhibition connectivity between the signals received by the photoreceptors is proposed, providing an edge enhancement. The second processing step, at the Medulla layer, occurs through neurons interaction, producing onset and offset sensitive responses; The third one, the Lobula, has a specific connectivity mapping that contributes to the transformation of the signals generated in the Medulla into the LGMD neural response.

through the excitation generated by the visual input, being represented as:

$$\text{Mean}_{\text{photoreceptor}}(t) = \frac{1}{n \cdot m} \sum_{x=1}^n \sum_{y=1}^m a_{\text{photoreceptor}}(x, y, t) \quad (2.34)$$

where $a_{\text{photoreceptor}}(x, y, t)$ represents the activity of the photoreceptor unit at position (x, y) , at the time instant t . n and m represent the number of neurons making up this layer, disposed by n rows and m columns. The value of each photoreceptor cell is equal to the value of each pixel in the captured image.

At the Lamina level, a specific configuration on the connectivity between Lamina neurons leads to an edge enhancement of the image captured and transmitted by the photoreceptors. The Lamina neurons have a center-excitation/surround-inhibition disposition. This specific distribution was modeled as a convolution operation of the visual input with a Difference of Gaussians (DoG) kernel:

$$\begin{aligned} a_{\text{lamina}}(x, y, t) &= a_{\text{photoreceptors}} * \text{DoG}_{\text{kernel}} \\ &= \sum_{x=1}^n \sum_{y=1}^m a_{\text{photoreceptor}}(x, y, t) \times \text{DoG}_{\text{kernel}}(i - x, j - y) \end{aligned} \quad (2.35)$$

where $a_{\text{lamina}}(x, y, t)$ represents the activity of the lamina neuron at position (x, y) and at the time instant t . $\text{DoG}_{\text{kernel}}$ is a difference of Gaussians kernel. The result of this mathematical operation corresponds to an edge enhancement and, consequently, the mean activity of the lamina layer is directly proportional to the edges of the visual stimulus:

$$\text{Mean}_{\text{lamina}}(t) = \frac{1}{n \cdot m} \sum_{x=1}^n \sum_{y=1}^m [a_{\text{photoreceptors}} * \text{DoG}] \quad (2.36)$$

Then, the onset/offset responses on the Medulla are obtained through the combination of the activity of one excitatory and one inhibitory neuron, onto a third neuron. The inhibition is time delayed relative to the excitation in the case of the onset detection, and time advanced relative to the excitation in the case of offset detection. The aggregation of on-off neurons will only fire when the motion produced is on the preferred direction (see figure 2.10). In other words, at Medulla, neuron's are modeled as Elementary Motion Detectors (EMDs) [20, 147].

As a consequence, image edges moving in a radial outward fashion will be detected

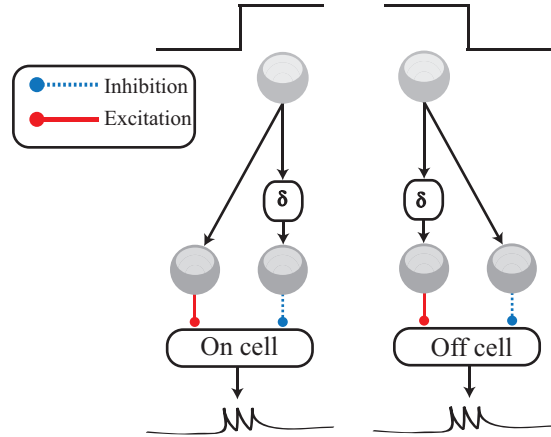


Figure 2.10: Neural connectivity of the neurons responsible for the on-off sensitive responses, which make up the Medulla layer.

in the Medulla, whereas still edges will not elicit responses.

$$\begin{aligned} \text{Mean}_{\text{on-off}}(t) &= \frac{1}{n \cdot m} \sum_{x=1}^n \sum_{y=1}^m [a_{\text{photoreceptors}} * \text{DoG}_{\text{Kernel}}] \\ &= \frac{1}{n \cdot m} \sum_{x=1}^n \sum_{y=1}^m a_{\text{on-off}}(x, y, t) = \begin{cases} \text{(A) } k \cdot \theta(t) & \text{if looming} \\ \text{(B) } 0(t) & \text{if no motion} \end{cases} \end{aligned} \quad (2.37)$$

where k is a constant and $\theta(t)$ is the area of the object in the retina. The computation of the on-off neurons result in a null response (equation 2.37, (B)) when the visual stimulus is not moving (the object can be stopped or it is bigger than the field of view). On the other hand, when the object is approaching, the response directly follows the input (equation 2.37, (A)).

The connectivity mapping of the on-off neurons, allied with the threshold mechanism of their postsynaptic neurons (named Linear Threshold - LT- neurons), have a crucial role in this model, forming the excitatory input to the LGMD neuron. These LT neurons have lateral interactions with their neighboring cells, via a lateral excitation that spreads and smooths their activity over the pre-synaptic excitatory fan of the LGMD neuron.

Consequently, the mean activity of the excitatory pathway to the LGMD neuron, linearly follows the input activity for object sizes up to the angular threshold ($\theta_{\text{threshold}}$). This phenomena only occur for looming stimuli due to the specific connectivity pattern with the on-off aggregations that are tuned to respond to specific oriented motion: radial outward motion. After reaching $\theta_{\text{threshold}}$, the size of the object becomes bigger than the surrounding connectivity pattern, leading to a plateau at the excitatory level, and then to a decaying, when the object covers the whole visual field. This mechanism

Table 2.6: Parameter values of the LGMD connective model.[15]

PARAMETER	VALUE
$m \times n$	10000
Thr	0.3
gain _{Exc}	0.2
gain _{Inh}	0.005
LGMD _{Meanfiringrate} threshold	50

can be modeled as:

$$\text{LGMD}_{\text{Exc}}(t) = \sum_{x=1}^n \sum_{y=1}^m \text{Thr}(a_{\text{on-off}}(x, y, t) * \text{ConneC}_{\text{Kernel}}(x, y)), \quad (2.38)$$

where the excitatory input to the LGMD neuron, named LGMD_{Exc} results from the application of a threshold operation (named Thr) to the convolution of the on-off neurons activity with the connectivity kernel ($\text{ConneC}_{\text{Kernel}}$).

In the last processing stage, the LGMD receives post-synaptic inhibition from the medulla neurons. The role of this inhibition is to bring the LGMD neuron activity back to a baseline, after the looming visual stimuli reaches the angular threshold size.

Therefore, the difference between the excitation and the inhibition will approximate the membrane potential of the LGMD neuron (LGMD_{Vm}), which will be then converted into a firing rate output:

$$\text{LGMD}_{\text{Inh}}(t) = \text{Mean}_{\text{on-off}}(t) \quad (2.39)$$

$$\text{LGMD}_{\text{Vm}}(t) = \text{gain}_{\text{Exc}} \cdot \text{LGMD}_{\text{Exc}}(t) - \text{gain}_{\text{Inh}} \cdot \text{LGMD}_{\text{Inh}}(t) \quad (2.40)$$

$$\text{LGMD}_{\text{Firing}} = \exp(\text{LGMD}_{\text{Vm}}) = \exp(\text{LGMD}_{\text{Exc}} - \text{LGMD}_{\text{Inh}}) \quad (2.41)$$

where gain_{Exc} and gain_{Inh} determine the excitation and inhibition contribution to the final response of the LGMD neuron (see table 2.6).

2.3.4 LGMD models: qualitative evaluation and predicted results

Before performing a quantitative evaluation and validation of the selected LGMD models, and according to the model's description and respective mathematical formulation previously described, the summary of the most important characteristics of each hypothesis formulated are gathered on table 2.7, showing:

- The main properties that explain the selective response of the LGMD neuron to looming objects;
- The models formulated to explain this particular selectivity;
- Model's qualitative evaluation: in terms of explanatory adequacy (*EA* - whether the theoretical account of the model helps make sense of collected LGMD data) and interpretability (*IP* - whether the components of the model, particularly its parameters, are understandable and linked to known processes)[125];
- The predicted responses when stimulating the LGMD models with distinct visual stimuli.



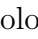
2.4 Methods









































In order to analyze the quality and acceptance of any computation model, evaluation and validation are important and fundamental steps that need to be taken (for a better understanding, see figure 2.11).

Our main interests are to:

1. Compare the results obtained with the models associated with each hypothesis formulated, with the biological results - evaluated in terms of Descriptive Adequacy (*DA*) [125];
2. Show that the hypothesized mechanism can actually perform collision detection, and subsequently investigate how each model behaves under a range of situations/conditions not necessarily foreseen - evaluated in terms of Complexity/Simplicity (*CS*) and Generalizability (*Ge*) [125].

In order to achieve that, a wide range of environmental conditions, conventional and additional stimulation protocols were adopted.

Table 2.7: Summary of the different hypothesis here addressed (H1, H2 and H3), the selective basis of each hypothesis, the described models for each hypothesis and the results expected at each particular situation. LI: Lateral Inhibition; FFE: Feed-forward excitation; FFI: Feed-forward inhibition; *EA*: Explanatory adequacy; *IP*: Interpretability; -N: noise absence; +N: noise presence. Green cell color: model is able to correctly detect an emminent collision . Red color: model wrongly detect a collision. : we expect it to behave in agreement with biology; : we expect it to not behave in agreement with biology; : Not enough information available to predict results;

Hypothesis	H1						H2		H3	
Selectivity basis:	LI versus FFE						FFI versus FFE		Synaptic organization	
Model	Model 1		Model 2		Model 3		η - function model		LGMD Connective model	
Model evaluation:	<i>EA</i>	<i>IP</i>	<i>EA</i>	<i>IP</i>	<i>EA</i>	<i>IP</i>	<i>EA</i>	<i>IP</i>	<i>EA</i>	<i>IP</i>
Qualitative measures										
Expected response to	-N	+N	-N	+N	-N	+N	-N	+N	-N	+N
Approaching										
Receding										
Real images										

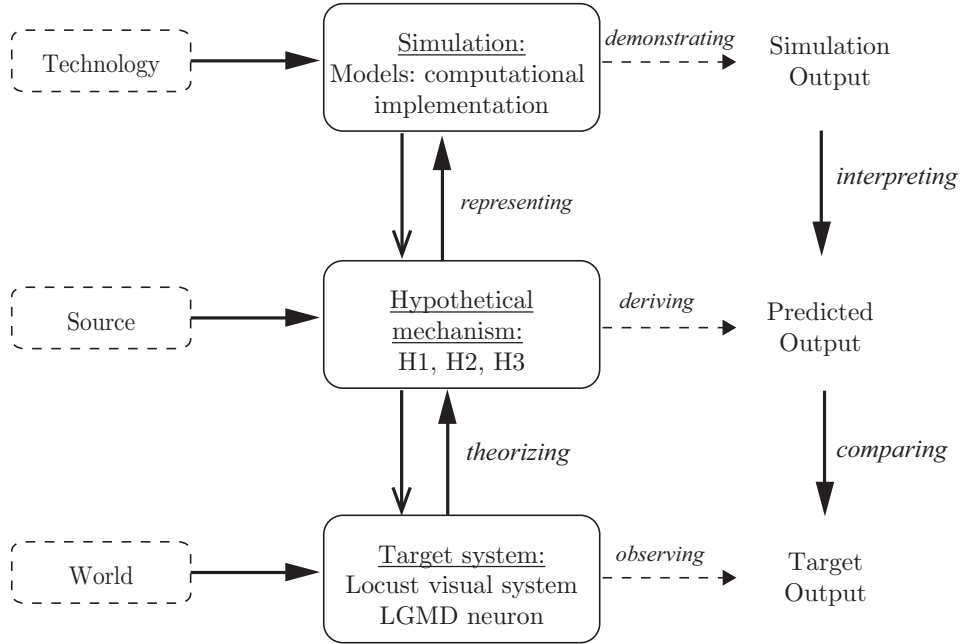


Figure 2.11: Schematic illustration of the process used in the LGMD models evaluation stage. Adapted from: [216, 219]

2.4.1 Stimulation Protocols

A looming object, with a specific half length l and moving at a constant speed v , shows a typical rate of expansion, with a slow initial angular speed that rapidly increases as the object is getting closer to the camera (see figure 2.2, B). The angular size subtended at the retina by an approaching object is given by:

$$\theta(t) = 2 \cdot \tan^{-1}(l/vt) \quad (2.42)$$

t denotes the Time-To-Collision (TTC) of the object in relation to the eye, conventionally chosen to be negative prior to collision. Velocity (v) is negative for an object approaching and positive to a receding object.

In a looming approach, both the angular size ($\theta(t)$) and the angular expansion rate ($d\theta/dt$) are non-linear functions of time (equation 5.7), whose temporal dynamics solely depend on $l/|v|$ ratio.

Taking this into account, and following the stimulation protocols used in biology (see figure 2.3) [70, 71], the first step in model evaluation process, is to analyze the relationship between the responses of each LGMD model and the visual stimulus properties, including the relation between the :

1. DA_f : LGMD model peak firing rate value (named as f_{peak}) and the $l/|v|$ ratio:

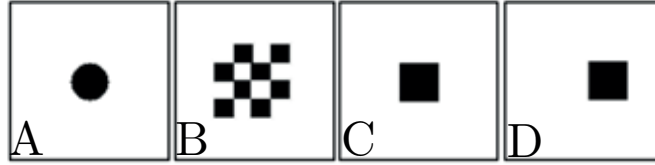


Figure 2.12: Artificial visual stimuli, developed in MATLAB®.

typically on biology, LGMD neural responses are brisker for small or fast-moving objects (corresponding to lower $l/|v|$ values) leading to higher peak firing rates (f_{peak})

2. DA_t : The TTC of the LGMD model peak firing rate (named as t_{peak}) and the $l/|v|$ ratio: [70] defends that the timing of the peak firing rate is independent of the object approaching size or speed, being an indicator of the angular threshold computation. Despite the effective relation of this threshold computation on triggering escape and collision avoidance behaviors not be consensual in literature [30, 58], it is important to analyze the relation between these two variables

For that, looming stimuli with $l/|v|$ ratios ranging from 5 to 95 milliseconds (ms), with a 10 ms step size interval, were created in MATLAB® [118]. Responses will be evaluated in terms of:

Descriptive adequacy (whether the model fits the biological data): measured in terms of f_{peak} mean difference and standard deviation between biological and model data points, as well as t_{peak} function difference between biological and model data.

Further, invariance of neuronal responses is a key aspect of sensory processing and should be guaranteed by its subsequent artificial modeling. Changing parameters of objects directly affect the time course of the spatially distributed excitatory and inhibitory inputs impinging onto the model. Thus, we investigate the extent to which the t_{peak} of LGMD models change as the parameters of the approaching object are modified.

Thus, the invariance of the LGMD model's responses to looming stimulus characteristics, as shape, texture and approaching angle, was tested.

This implied the use of the following visual stimuli (depicted on figure 2.12):

1. S_L : Looming back square, with different $l/|v|$ ratios;
2. $S_L I$: Looming objects, with the same $l/|v|$ ratio's range, owing different

shapes (square (Fig.2.12 C) versus circle (Fig.2.12 A)), textures (without texture (Fig. 2.12 C) and with a checkerboard pattern texture (Fig. 2.12 B), and different approaching angles (0° (Fig. 2.12 C) and 75° (Fig. 2.12 D) deviated from the camera center).

In addition to a biological validation, an analysis relative to the model's suitability from an engineering perspective, was adopted. This neuron behavior could be seen as a novel solution to difficult and persistent problems on the development of collision avoidance algorithms. Consequently, the model's performance/ behaviour was analyzed in more realistic and complex visual scenarios. In order to evaluate the LGMD models response, four different conditions were created and tested:

1. *S_A_R*: Different object motion trajectories: approaching and receding objects, for two different $l/|v|$ ratios. In case of approaching objects, the initial size subtended by the object at the beginning of approach was < 2 degrees in visual angle, and the full final angle subtended at the end of approach was equal to 60 degrees, independently of the $l/|v|$ value. Subsequently, uniquely the time course of the visual stimulation differed as $l/|v|$ changed.
2. *S_U_L*: Model response dependence on different image cues: uniformly increasing object size (approaching visual stimuli with constant angular velocity ($\partial\theta/\partial t$)) versus looming object. This protocol was previously used to stimulate the LGMD neuron in biology, in order to find out critical cues used by LGMD neuron to detect looming objects [136, 151]. The initial size subtended by the object at the beginning of approach was < 2 degrees in visual angle. Then, the angular size increased linearly (one degree at each simulation step), reaching a final subtended angle of 60 degrees. In biology, LGMD firing rate profile consists in a fast increase of the firing rate, followed by a peak and then a slower decrease of the excitation level.
3. *S_N*: Different noise conditions. Attention was focused in verifying if models are capable of correctly detecting a collision, when the images are corrupted by salt-and-pepper noise with increasing noise ratios. Salt-and-pepper noise was chosen due to its intensity spiking characteristic, which may lead to the production of false collision alarms. In a robotic perspective, this is a commonly verified noise form, caused by malfunctioning camera's sensor cells, by memory cell failure or by synchronization errors in the image digitization and transmission. For that, a sequence showing a looming square, approaching at two different $l/|v|$ ratios

(25 and 50ms) was used. Then, increasing percentages of salt-and-pepper noise, ranging from 0.1% to 100% (with an increment step that can be observed on the x -axis of figure 2.21), were added to the images sequence.

4. S_Re : Real environment.

For each of these condition tested, models response will be evaluated in terms of: Firing Rate Profile (FRP - through a visual analysis of graphical displays), Correctly/Missed detected collisions (CD , measured in terms of correct collisions/(correct+missed collisions)), Distance (D - a safety distance is considered, between 3 and 25 cm from the camera) at which a collision was detected.

Finally, according to the results obtained, each model will be evaluated in terms of its:

b) *Complexity/Simplicity* (whether the model's description of observed data is achieved in the simplest possible manner): evaluated in terms of the number of model parameters.

c) *Generalizability* (whether the model provides a good predictor of future observations): the model that provides the best fitting in replications of experiments when noise has changed has a higher generalizability.

A simulation environment was developed in MATLAB® ([118]), in order to assess the response of the chosen models. Objects were simulated according to their movement and corresponding data was acquired by a simulated camera and processed by the respective LGMD model. In order to mimic the locust visual system, the image sequences were generated by a simulated camera, with a field of view of 60° in both x and y axis and with 100×100 pixels of resolution, and a sampling frequency of 100 Hz. Both intrinsic characteristics of the visual stimuli, as the object size, velocity, shape, texture, as well as extrinsic characteristics, such as noise level in the image background, trajectory or object approaching angle, can be specified in real time. This allows the creation of a wide variety of different visual scenarios.

In order to access the effectiveness of the models in a realistic visual scenario, with real-world luminance and contrast values, and environmental complexity, a real video sequence of a black approaching ball, using a Sony Cyber shot digital camera 7.2 megapixels, was recorded. The resolution of the video images is 640×480 pixels, with an acquisition frequency of 30 frames per second. The relation between real ball half size ($l \simeq 3.35\text{cm}$) and approaching speed ($v \simeq 1.7 \text{ m/s}$) was 30 ms.

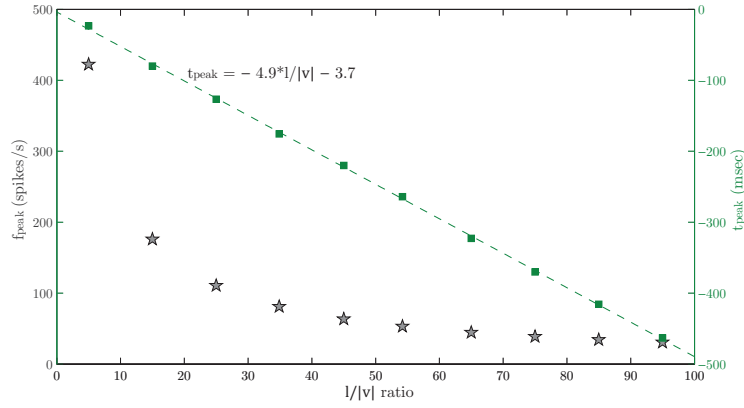


Figure 2.13: Left axis: Relation between the model peak firing rate versus the $l/|v|$ ratio (gray stars, logarithmic regression as $f_{\text{peak}} = -124.2 \log(l/|v|) + 557.2$, $r = 0.90$). Right axis: Relation between the TTC of the peak firing rate versus $l/|v|$ ratio (green squares). Dashed line indicates the linear regression.

2.5 LGMD models: computational implementation and results

2.5.1 LGMD η -function: model validation in comparison to biology and a robotic perspective analysis

2.5.1.1 LGMD η -function: *model evaluation in terms of descriptive adequacy*

Results obtained for S_L protocol are shown on figure 2.13. Note that the relation between the f_{peak} and the $l/|v|$ ratio is near exponential, following the results obtained with biological data (see figure 2.3, right panel) [70, 71]. For $l/|v|$ values between 5 and 50 ms, the mean difference between f_{peak} values obtained in biology and using the η -function model obtained is 55 spikes, with a standard deviation of 67 spikes.

Analyzing the regression line represented on figure 2.13 ($t_{\text{peak}} = -4.9 \cdot l/|v| - 3.7$, $r = 0.99$) and comparing it to the linear regression, represented on the top left panel of figure 2.3 - modeled by equation 2.1 - we conclude that $\alpha = -4.9$ and the $\delta = -3.7$ milliseconds. Consequently, we conclude that the peak on the LGMD model firing rate occurred 3.7 milliseconds before the object had reached a full angular size of 24 degrees on camera, for all $l/|v|$ values tested.

As a next step, the invariance of the LGMD model response, in terms of t_{peak} , to shape, texture and approaching angle of the visual stimuli should be tested (protocol

S_L_I). Although, as it was said before, this model computation only takes into account the angular size and speed of the visual stimuli. Consequently, all the other properties of the visual stimuli are not taken into account by the Gabbiani [70, 71] model and, consequently, will not influence its final response.

2.5.1.2 LGMD η -function: *biological and robotic model performance evaluation*

After the model descriptive adequacy evaluation and in order to perform a deeper analysis about the performance of the LGMD model previously described, and looking at its response as a possible robotic solution perspective, we subject it to different visual stimuli, as described in section 2.4.1.

Protocol: S_A_R

The initial size subtended by the object at the beginning of the approach was < 2 degrees in visual angle. Then, the angular size increased linearly (one degree at each simulation step), reaching a final subtended angle of 60 degrees.

Analyzing figure 2.14, LGMD model here addressed shows a typical biological *FRP* to an approaching stimulus: as the angular size of the retinal projection of the stimulus increases, the firing rate increases, peaks and decays, which, with this model, happens before the time predicted to collision. The response of this model has shown to peak when the angular size of the approaching object reaches a specific angular size, known as the angular threshold, $\theta_{\text{threshold}} = 24$ degrees, whose importance, on timing the escape behaviors in locusts, remains controversial.

In the case of receding objects, the initial size subtended by the object at the beginning of approach was 60 degrees in visual angle, and the full final angle subtended at the end of approach was < 2 degrees.

Figure 2.15 presents the results from the model when stimulated with an object showing a receding trajectory, implying a negative angular speed. When comparing both results, from figure 2.14 and figure 2.15, we verify that the *FPR*, either for $l/|v| = 25$ or 50 ms, are the reverse of the response obtained for approaching trajectories. These responses are not in agreement with the LGMD biological response when stimulated with similar trajectories. For receding trajectories, the biological LGMD neuron response is very brief when compared with the response obtained for the same approaching object.

A possible explanation for the responses obtained is based on the fact that η - function model does not take into account some constraints on the excitation and

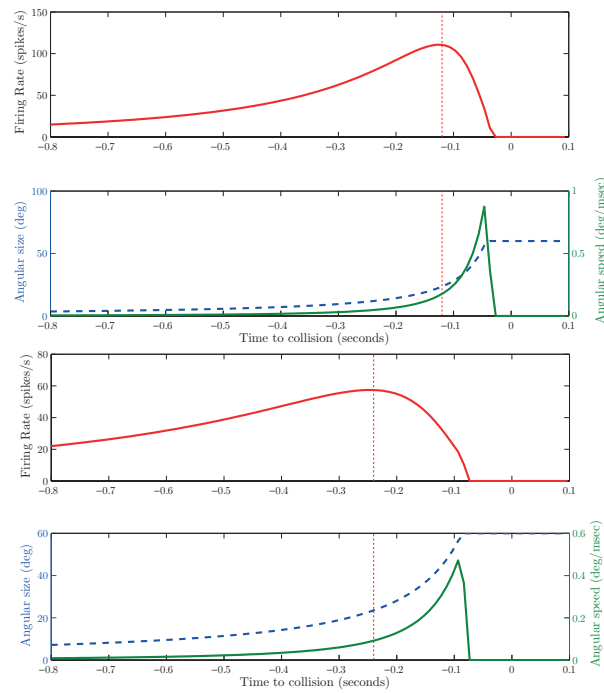


Figure 2.14: Responses of the LGMD model proposed by Gabbiani [70, 71], to an approaching looming stimulus with $l/|v|$ equal to 25 (top) and 50 (bottom) milliseconds. Top graphs: output of the η -function. Bottom graphs: time-course of the angular size (θ , dashed blue line) and angular speed ($\partial\theta/\partial t$, solid green line) of the approaching stimulus. The time predicted to collision is defined as zero. Red vertical dotted line indicates the moment when the object angular size is equal to $\theta_{\text{threshold}} = 24$ degrees.

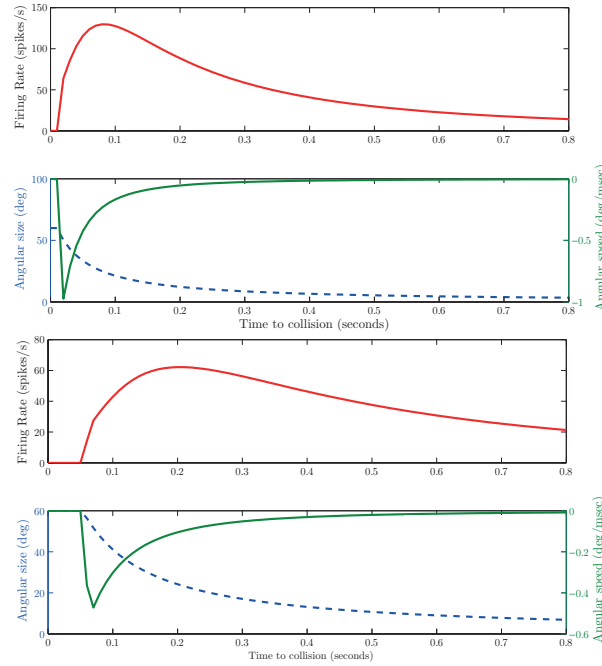


Figure 2.15: Similar to figure 2.14 to a receding stimulus, with $l/|v|$ equal to: Top panel: 25 ms; Bottom: 50 ms.

feed-forward inhibition dynamics across time [136, 139].

This model does not include any processing stage for the production of collision alerts to signal approaching objects. Subsequently, CD and D variables are null for the η - function model.

Protocol: S_U_L

Taking as a term of comparison the biological response to the same simulation protocol [181], and taking into account that η - function output depends on the angular velocity of the approaching object, a completely different response profile when comparing looming and uniformly approaching visual stimuli should be expected. Observing the FPR obtained to an object linearly approaching at 1 degree per time-step (Fig. 2.16, top graph), a peak at the onset of the visual stimuli, followed by an exponential decrease in the firing rate is noticed.

Analyzing the spike rate profile obtained for this model, when stimulated with a looming stimulus (Fig. 2.14) and comparing it to the results obtained for the uniformly approaching object, we notice that the peak at the preferred angular size ($\theta_{\text{threshold}} = 24$ degrees) disappeared under the last stimulation protocol (figure 2.16).

In terms of behavioral transduction of the model response, the absence of a peak

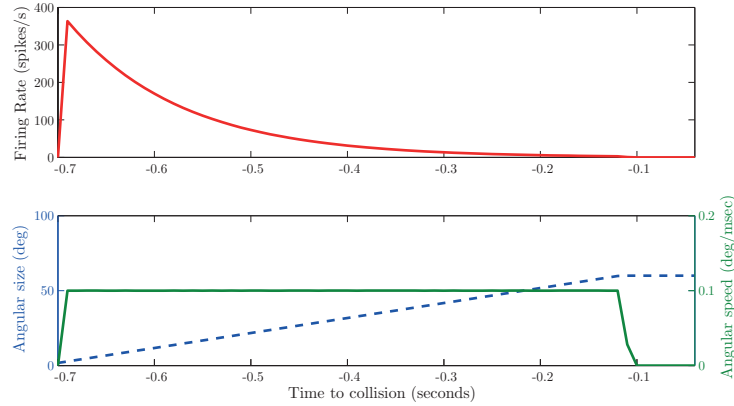


Figure 2.16: Response of the LGMD model to an approaching stimuli under the conditions of a constant angular velocity. $t=-0.7$ at the onset of stimulus

can imply the non existence of an escape response.

Protocol: S_N

As a neural pathway specialized in the detection of potential collisions, the LGMD neuron must be reliable in all the environmental conditions. Thus, it is especially important, for this neuron, to remain undisrupted by noise.

As previously mentioned, the η - function model only depends on the object angular size and velocity. The application of reliable computer vision techniques to extract the object angular size and velocity from the captured video, is needed. Consequently, the noise impact on the final response of this model will depend on the computer vision techniques used to extract the object, and not in the model response *per se*.

Table 2.8 summarizes all the results obtained during the evaluation process of the η - function model.

2.5.2 LGMD model 1: model validation in comparison to biology and a robotic perspective analysis

2.5.2.1 LGMD model 1: *model evaluation in terms of descriptive adequacy*

Figure 2.17 shows, on the top panel, the relation between LGMD model 1 peak firing rate (f_{peak}) and the $l/|v|$ stimulus ratio. Observing the results obtained, we can conclude that they are consistent with the ones observed on the biological systems (see figure 2.3). The mean difference between f_{peak} values obtained with this model,

Table 2.8: Summary of the η - function model evaluation results obtained for each of the simulation protocols tested. The nomenclature here used is described on section 2.4.1. \checkmark : behaves as expected; \times : behaves in an opposite way as expected; \boxtimes : No results were obtained; $\mu(f_{\text{peak}})$: average of the absolute difference value between f_{peak} values obtained with the model and f_{peak} values obtained in biology, for 5-50 ms $l/|v|$ values; std: standard deviation; $\Delta\theta_{\text{threshold}}$: difference between $\theta_{\text{threshold}}$ values obtained with the model and biological data; A: approaching; R: receding; L: looming; U: uniformly approaching.

		Model evaluation: Descriptive Adequacy													
		S_L						S_{L_I}							
η -function		DA_f			DA_t			DA_t							
		$\mu(\Delta f_{\text{peak}})$	std(Δf_{peak})		$\Delta\theta_{\text{threshold}}$			$\Delta\theta_{\text{threshold}}$							
		55	67		0.4°			0.4°							
η -function		Model evaluation: biological (<i>FRP</i>) and behavioral perspective (<i>CD</i> and <i>D</i>)													
		S_{A_R}				S_{U_L}			S_N			S_{Re}			
		<i>FRP</i>	<i>CD</i>	<i>D</i>		<i>FRP</i>	<i>CD</i>	<i>D</i>	<i>FRP</i>	<i>CD</i>	<i>D</i>	<i>FRP</i>	<i>CD</i>	<i>D</i>	
		A: \checkmark R: \times	\boxtimes	\boxtimes		L: \checkmark U: \checkmark	\boxtimes	\boxtimes	\boxtimes	\boxtimes	\boxtimes	\boxtimes	\boxtimes	\boxtimes	\boxtimes

for $l/|v|$ values between 5 and 50 ms, and the results obtained in biology is 42 spikes, with a standard deviation of 39 spikes.

Taking into account the regression line presented on the bottom graph of figure 2.17 ($t_{\text{peak}} = -1.8 \cdot l/|v| + 7.5$, $r \simeq 0.99$) and comparing it to the linear regression represented on figure 2.3, we conclude that, for all $l/|v|$ values, the LGMD model 1 peak firing rate always occurred 7.5 msec after the object reached a final angular size of 60 degrees on the camera. Unlike η -function model, the LGMD model 1 output only reaches its maximum peak when the object reaches its full angular size that is, in this case, 60 degrees.

Tests for S_{L_I} showed that the linear relation between the TTC of peak firing rate and the $l/|v|$ ratio was not affected by the shape, texture or approaching angle of the visual stimuli ($r \approx 0.99$).

According to these results, we conclude that the intrinsic linear dependence between the peak firing time and the $l/|v|$ ratio remains preserved by LGMD model 1. This emphasizes the fact that the feature extraction performed by the LGMD model 1 is independent of the image context.

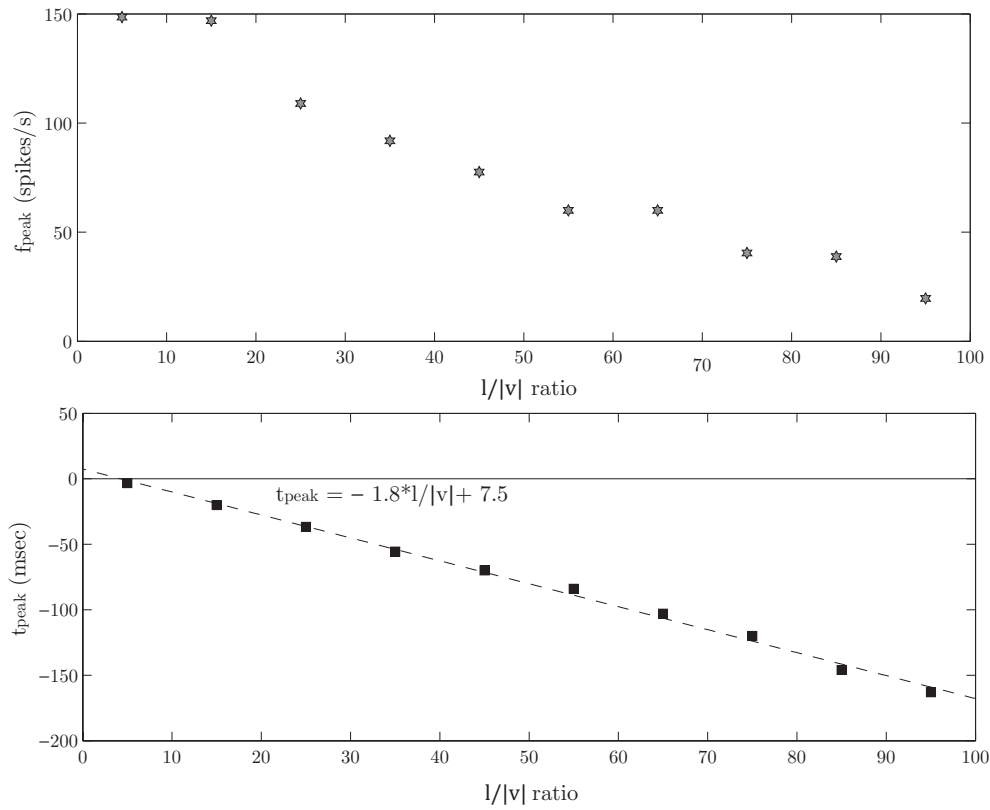


Figure 2.17: Relation between f_{peak} and t_{peak} on the $l/|v|$ ratio, obtained with LGMD model 1. Top panel: The LGMD Peak firing rate (f_{peak}) is plotted as a function of $l/|v|$ (logarithmic regression represented by: $f_{\text{peak}} = -47.26 \log(l/|v|) + 294.4$, $r \simeq 0.89$). Bottom panel: Peak firing time (t_{peak}) is plotted as a function of $l/|v|$ (indicated by black squares). Linear regression line is indicated by the black dashed line.

2.5.2.2 LGMD model 1: *biological and robotic model performance evaluation*

As the LGMD neuron's output from model 1 is given as a membrane potential, the response of this model will be evaluated in amplitude (represented as LGMD membrane potential) and not in frequency (LGMD spike rate).

Protocol: *S_A_R*

A deep and comparative analysis of the model 1 response to for protocol *S_A_R* was done as depicted on figure 2.18 and 2.19. The activity of the LGMD model 1 was analyzed in order to identify the relationship between simulated approaching stimuli and the LGMD *FRP* response.

Figure 2.18 shows the LGMD model 1 *FRP*, which is similar to the typical one of the LGMD neuron to an approaching stimulus: as the retinal projection's angular size of the stimulus increases, the membrane potential increases, peaks and decays before the collision occurs (figure 2.18, top panel of a) and b)).

Analyzing the obtained results, we observed that the time interval (or delay, indicated by δ) between the instant at which the first spike occurred and the time instant at which the membrane potential peaked, was the same for both situations tested, taking a value of 50 ms. However, for $l/|v| = 25$ ms, the first spike (which signals collision) occurred when the object reached an angular size equal to 32 degrees (being the approaching object located at $D = 5.2$ cm from the camera); for $l/|v| = 50$ ms, the spike was produced when the object reached an angular size of 42 degrees (being the approaching object located at $D = 4.2$ cm from the camera). For both $l/|v|$ values, LGMD model 1 was able to correctly detect a collision. Based on these two case studies, we can conclude that this model is able to detect approaching objects in a simple environment.

Figure 2.19 depicts results when a receding object is used as the input to the model. The LGMD membrane potential peaks when the object starts moving and then slowly decreases as the object recedes from the camera. In this situation, no collision alerts should be produced, as there is no risk of collision if the object is receding. However, a spike was produced 0.05 seconds after the object started to recede (Fig. 2.19, middle graph). This represents a limitation of model 1, since it could not be correctly deployed as a collision detector in mobile devices, since it does not respond properly to receding objects.

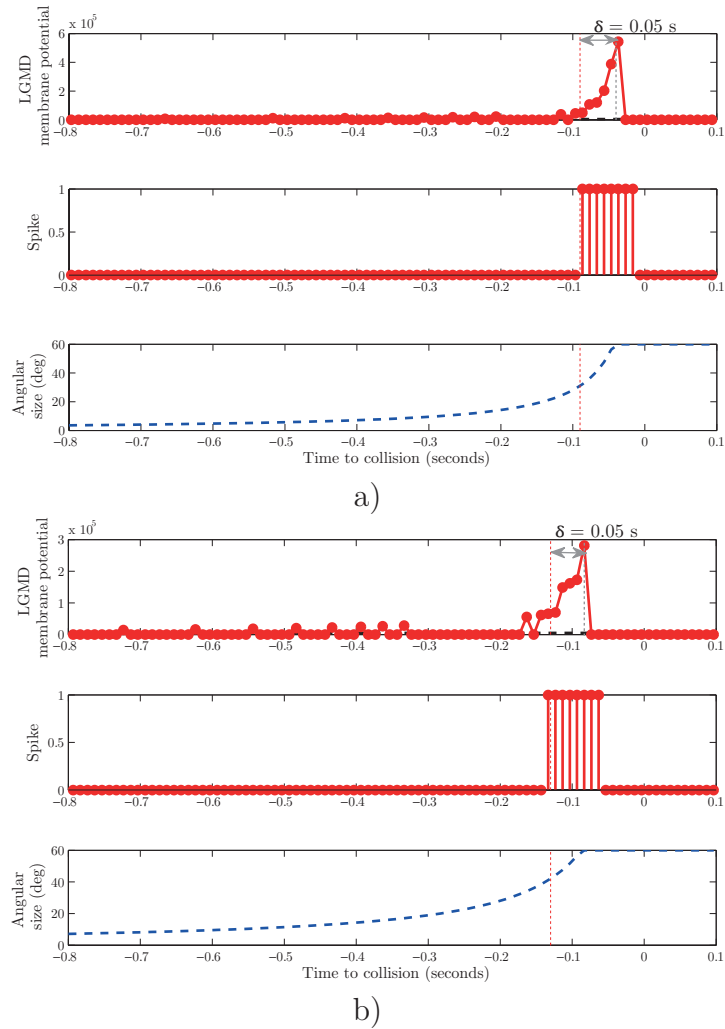


Figure 2.18: LGMD model 1 responses to an approaching looming stimulus with $l/|v|$ equal to: a) 25 ms and b) 50 ms. Top graphs: Red Dots represent the LGMD membrane potential, computed at each timestep. The dashed black line represents the $\text{LGMD}_{\text{thresh}}$ value. Middle graphs: the first spike produced, representing the collision alert, occurred at -0.087 and -0.133 seconds before collision (for $l/|v| = 25$ and 50 ms, respectively). Bottom graphs: time-course of the stimulus angular size (θ). In all graphs, the time predicted to collision is defined as zero.

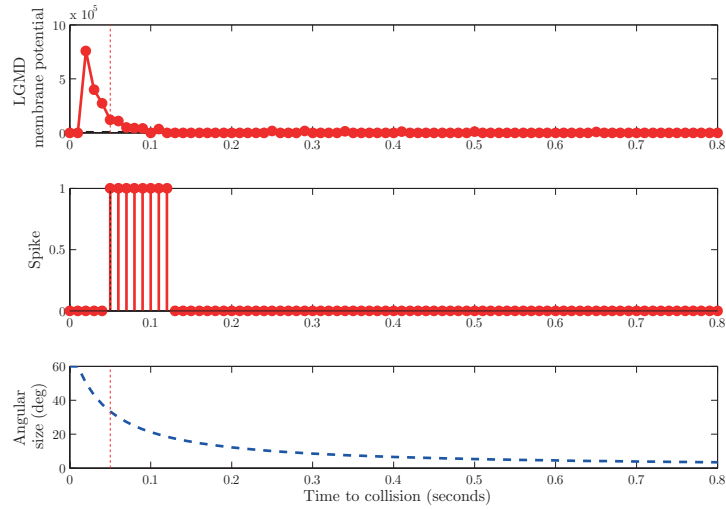


Figure 2.19: Responses of LGMD model 1 to a receding stimulus with $l/|v|$ equal to 25 milliseconds. Legend similar to figure 2.18.

Protocol: S_U_L

To analyze the behavior of the LGMD model 1 to protocol S_U_L , objects simulated show a uniform increase in size. The obtained results are depicted on figure 2.20.

Two objects were considered. One object approaches such that it linearly increases one degree per time-step. In this case, the LGMD membrane output is very low due to the inhibitory layer that spreads its inhibition to the neighboring pixels. As the image increases only one degree per time-step (corresponding to one pixel per side at each time-step), the inhibition wins the competitive race over the excitation and almost all the excitation produced by the photoreceptive layer is canceled out by inhibition. Consequently, and observing the m for this situation (dots), no spikes were produced by the LGMD model 1 in this situation case (see Fig. 2.20, middle graph).

The second simulated object has a higher linear increase (two pixels per side, at each time-step). Observing figure 2.20 (gray solid lines), a great difference is noticed when comparing it to the previous result (dots). There is an almost linear increase in the LGMD membrane potential (Fig.2.20, top graph, gray continuous line), being directly related to the linear increase of the object. As the simulated object increases uniformly at two pixels per side, the inhibitory layer only affects one pixel in each side of the image growth. Therefore, excitation is higher than inhibition, leading to an almost linear increment on the LGMD membrane potential, which follows the increase of the stimulus size. A spike (or collision alert) was produced at 0.05 seconds (Fig.2.20, middle panel), when the object's position was still very distant from the

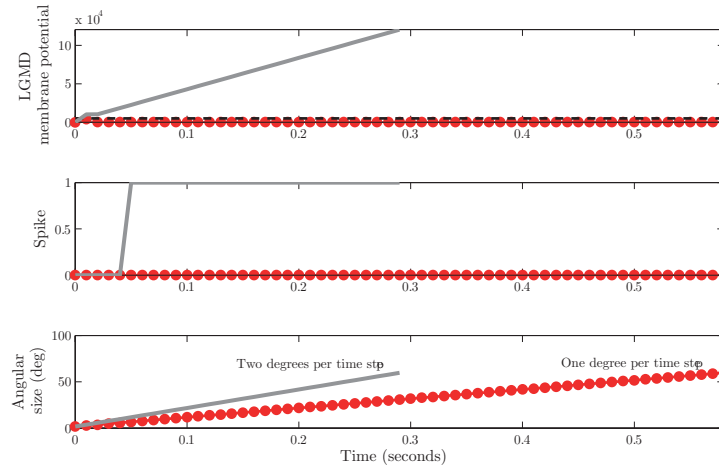


Figure 2.20: LGMD model 1 response to an object that approaches at one pixel per side (red dots) and two pixels per side (red continuous line). The object approaches at one degree and two degrees per time step, respectively. Legend similar to figure 2.18. Zero time represents the stimuli onset instant.

camera.

When compared to the biologic response [181], LGMD model 1 *FRP* is not consistent to the verified in the biological LGMD neuron.

Protocol: S_N

In here, we pretend to verify if LGMD model 1 response remains undisrupted to noise increment. Figure 2.21 summarizes the results obtained for each situation tested.

According to these results, the noise added to the image sequences has a high effect on the obtained results. It could be inferred that, for a percentage equal or higher than 0.25% and lower than 50%, the excitation produced by noise was not eliminated by any form of inhibition (as lateral and feed-forward inhibition). By this reason, noise acts as an “extra” excitation that raises the LGMD membrane potential to a level superior than $LGMD_{thresh}$ value. Thus, for these situations, the first spike was produced prematurely when the object was still far away from the camera (at D ranging from 0.9 to 1 meter). For situations tested in which the noise level was equal or higher than 50%, LGMD model 1 did not spike. That happened due to the activation of feed-forward inhibition (FFI, equation 2.23), which was higher than FFI_{thresh} , eliminating all the excitation produced by the approaching object.

With these results we can conclude that the LGMD model 1 response is not immune to noise. In fact, it’s response is highly affected even by small noise amounts.

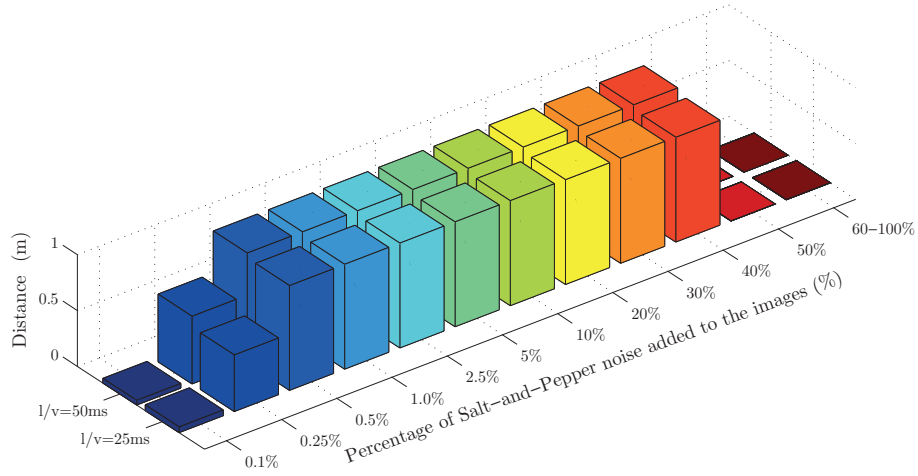


Figure 2.21: Distance (D) at which a collision was detected, by the LGMD model 1, at increasing noise levels for two different $l/|v|$ ratios tested: 25 (front) and 50 ms (rear).

Table 2.9: Summary of the LGMD model 1 evaluation results obtained for each of the simulation protocols tested. Legend is equal to the one on table 2.9.

Model evaluation: descriptive adequacy													
Model 1	S_L						S_L_I						
	DA_f			DA_t			DA_t						
	$\mu(\Delta f_{\text{peak}})$	$\text{std}(\Delta f_{\text{peak}})$		$\Delta\theta_{\text{threshold}}$			$\Delta\theta_{\text{threshold}}$						
	42		39		36°			36°					
	Model evaluation: biological (FRP) and behavioral perspective (CD and D)												
S_A_R			S_U_L			S_N			S_Re				
FRP	CD	D	FRP	CD	D	FRP	CD	D	FRP	CD	D		
A:✓ R:✗	✓✗	✓✗	L:✓ U:✗	✗✗	✗✗	✗	✗	✗	✓	✓	✓		

Protocol: S_Re

Figure 2.22 shows the output of the LGMD model 1 when feeded with a real image sequence. For this situation, LGMD model 1 detected a collision when the ball was located at $D = 19$ cm relatively to the camera, which corresponds to the moment when the ball reaches 21 degrees in its angular size.

However, the model is not robust to noise and does not work well for receding objects. In order to overcome the problem here described, a different LGMD neural network was proposed in literature. This model, here named LGMD model 2, will be described in detail and profoundly analyzed in the next sub-chapter.

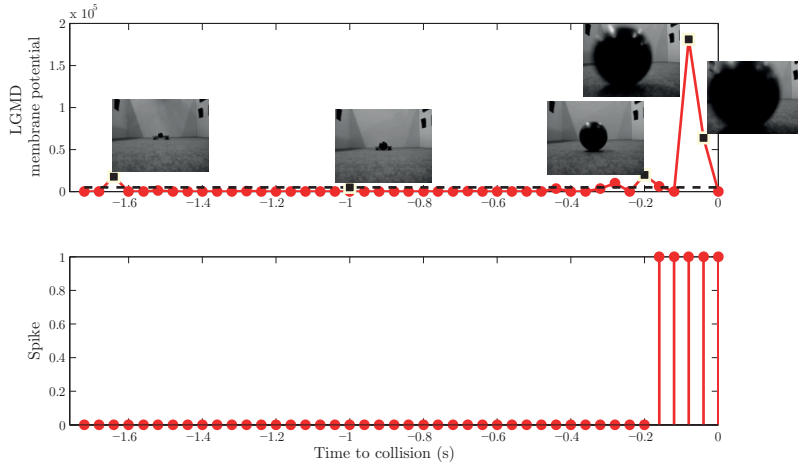


Figure 2.22: LGMD model response when stimulated with a real video sequence. Top: points represent the LGMD membrane potential at each timestep. Dashed line represents the $LGMD_{thresh}$ value. Bottom: the first spike produced, representing the collision alert, occurred at -0.16 seconds, being the simulated object situated at, approximately, 0.19 meters relatively to the camera.

2.5.2.3 LGMD model 2: model evaluation in terms of descriptive adequacy

In the validation step, when evaluating the regression analysis performed with the peak firing rate results obtained with LGMD model 2, in relation to different $l/|v|$ ratios, those can be represented by the following equation: $f_{peak} = -91.68 \log(l/|v|) + 491.8$, $r \simeq 0.88$, in which f_{peak} represents the LGMD model 2 Peak firing rate. The mean difference between f_{peak} values obtained with this model, for $l/|v|$ values between 5 and 50 ms, and the results obtained in biology is 75 spikes, with a standard deviation of 21 spikes.

Comparing these results with the ones obtained with LGMD model 1, we observe that f_{peak} obtained with LGMD model 2, for all $l/|v|$ values tested, is almost the double of the one obtained for model 1. This increment on the LGMD model 2 peak firing rate can result from the decrement on the inhibitory weight contribution for the final value of the $LGMD_{cell}$.

Evaluating the regression line obtained for the correlation between the t_{peak} and the $l/|v|$ ratio ($t_{peak} = -1.8 \cdot l/|v| + 7.1$, $r \simeq 0.9984$), it is concluded that LGMD model 2 peak firing rate always occurred 7.1 ms after the object reached a final angular size of 60 degrees on the camera.

Tests for protocol S_L_I proved that the LGMD model 2 response independence from the visual stimuli shape, texture and approaching angle.

Since model 1 and 2 share a similar architectural basis, the achieved results, for the delineated and same protocols, are similar.

2.5.2.4 LGMD model 2: *biological and robotic model performance evaluation*

In section 2.5.2.2, we verified that, in order to improve the reliability of LGMD model 1 over a wide range of visual scenarios, a new model was proposed in literature. With the integration of new computational processes, it was expected that LGMD model 2 became a more faithful model of the LGMD neural response. Additionally, from a robotic perspective, the improvement on the LGMD model 2 architecture led us to predict that it could be used as an effective collision detector in a wider range of visual scenario's conditions.

To verify the improvement in the performance of the LGMD model 2 to different visual scenarios, this model was submitted to the same simulation protocols described in the section 2.4.1.

Protocol: *S_A_R*

The activity of the LGMD model 2 was evaluated in order to identify the relationship between simulated stimuli and model *FRP* response, which visually is highly similar to the *FRP* verified on the LGMD biological response.

The spike that signals the detection of a collision, was produced at -0.12 seconds (Fig. 2.23, bottom panel, red dots,), when the object was located at $D = 7$ cm relatively to the camera, fulfilling an angular size of 28 degrees. In the second situation tested, $l/|v| = 50$ ms, a collision was correctly detected when the simulated approaching square reached 24 degrees of angular size, being located at $D = 6.1$ cm.

The next step consisted on testing LGMD model 2 to a receding object. When an object is receding and is very close to the camera, it will feed the LGMD neural network with high excitation. This fact can lead the LGMD model 2 to produce false collision alerts. Firstly, we fed LGMD model 2 with a receding square with $l/|v| = 25$ ms.

Figure 2.24 shows that a false collision was detected 0.07 seconds after the object started to recede. This happened because LGMD model 2 responded, with equally high excitation levels, to the approaching and receding object. We also fed the LGMD model 2 with a receding object with $l/|v| = 50$ ms. Likewise the results obtained for the smaller $l/|v|$, a false collision was detected for the new situation tested. Therefore, this model is not able to distinguish movement direction.

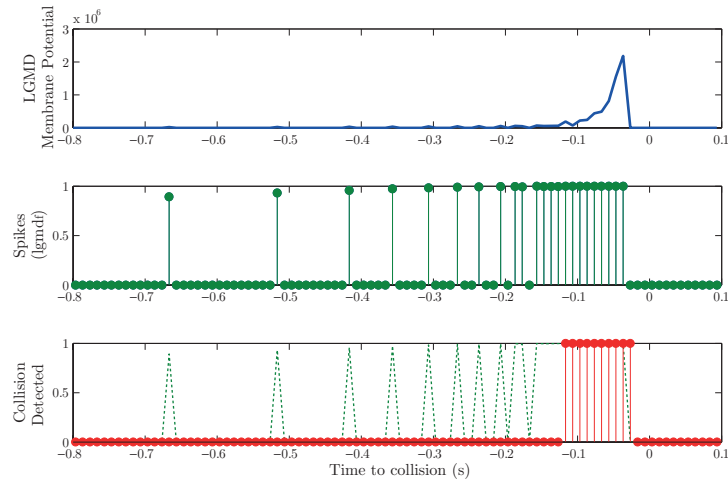


Figure 2.23: LGMD model 2 response to an approaching object, with $l/|v| = 25$ ms. Top panel: continuous line represent the LGMD membrane potential, computed at each time-step. Middle panel: green dots represent the spikes produced before threshold application (T_s and FFI). Bottom panel: dashed line represents all the spikes produced, and red dots are collision alerts, which are the final output of this model. The first collision detected occurred at -0.12 seconds, being the simulated object located at, approximately, 7 cm to the camera.

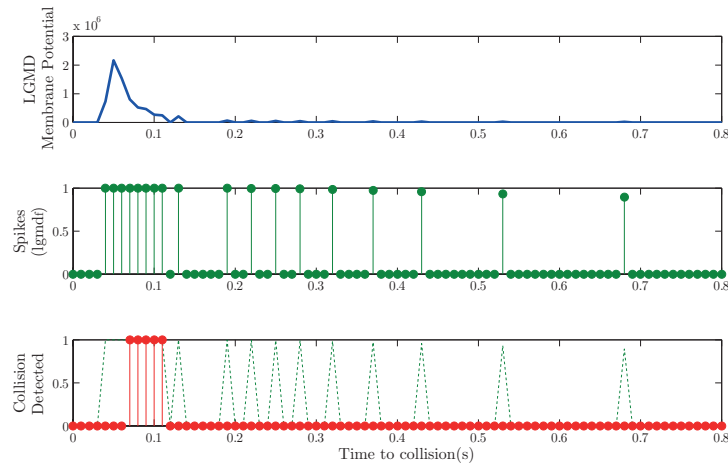


Figure 2.24: LGMD model 2 response to a receding object, with $l/|v| = 25$ ms. The legend is similar to the previous one (see figure 2.23). The first collision detected occurred at -0.07 seconds, being the simulated object located at, approximately, $D = 5.2$ cm to the camera.

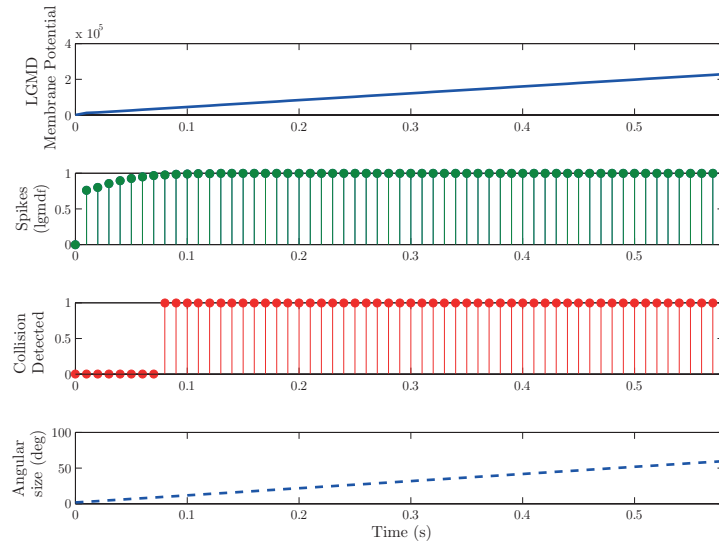


Figure 2.25: LGMD model 2 response to an uniformly approaching object. The object approaches one degree at each time step. The legend is similar to the previous images. Zero time represents the stimuli onset instant.

Protocol: S_U_L

Results obtained to an uniformly approaching object, increasing linearly at one degree per timestep, are shown on figure 2.25.

LGMD model 2 has a different response when compared to LGMD model 1 to this protocol. This happens due to the considerable decrease on the weight given to lateral inhibition in LGMD model 2, when compared to the lateral inhibition weight in LGMD model 1. An almost linear increase in the LGMD membrane potential (Fig. 2.25, top panel) can be directly related to the edge’s linear increase of the captured image. A collision was detected 0.08 seconds after the object started to increase its angular size, corresponding to an object angular size of 9.7 degrees.

In terms of comparison with the biologic response, the results obtained are not similar to the ones verified in the LGMD neuron [181], similarly to model 1.

Protocol: S_N

According to figure 2.26, for a noise percentage between 0.1% and 5%, LGMD model 2 was effectively able to correctly detect collision scenarios (the “collision detection” spikes were produced when the approaching square was near to the camera, at D values between 7 - for $l/|v| = 25$ ms - and 6 cm - for $l/|v| = 50$ ms). For this range of salt-and-pepper noise, the extra excitation produced by noisy pixels was properly eliminated by the new mechanism integrated into the model. However, when the noise

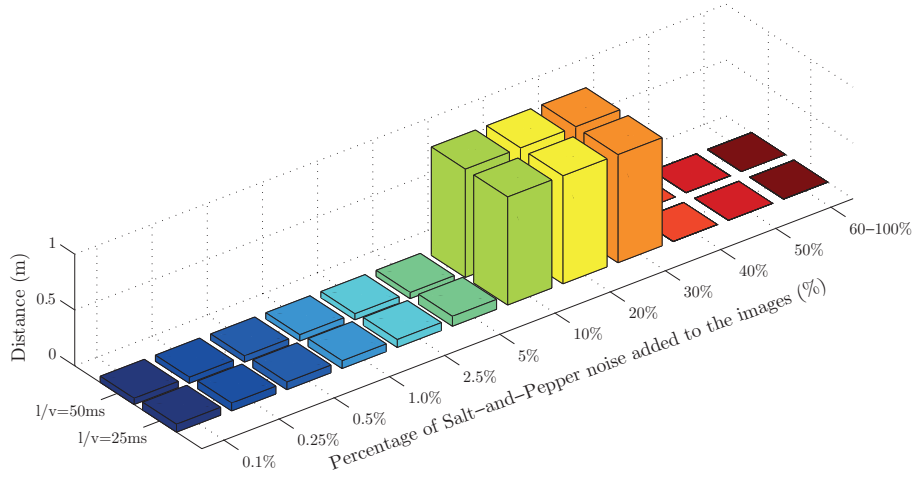


Figure 2.26: Distance at which a collision was detected, by the LGMD model 2, at increasing noise levels, for two different $l/|v|$ ratios tested: 25 and 50 ms.

percentage increased to values between 10 and 30%, the noise reduction mechanism was not able to eliminate all noisy pixels, leading to premature collision detections ($D > 60$ cm). When image corruption level increases to this range, the noisy pixels tend to group in small clusters, leading to a less effective noise reduction by the mechanism proposed. The passing coefficient of clustered pixels (see equation 2.15) tend to increase, leading to a subsequent increment in the summing cells excitation level. Thus, the first spike was produced prematurely when the object was still far away from the camera - located, for both $l/|v|$ values tested, at, approximately, 90 cm to the camera.

For noise levels equal or higher than 40%, LGMD model 2 did not produce any spike. That happened due to the inhibition of the LGMD cell (computed by equation 2.19) by the feed-forward inhibition cell (FFI which was higher than $\text{FFI}_{\text{thresh}}$), which cancel out all the excitation produced, either by the approaching object, either by the noisy pixels.

These simulated environments showed a robustness improvement of the LGMD model 2 over LGMD model 1, as this new model is able to deal with colliding objects, even when the image is corrupted with considerable noise levels.

Protocol: *S_Re*

In order to test the LGMD model 2 capability to detect a collision in a real visual scenario, we fed it with the real image sequence previously described.

Figure 2.27 shows the LGMD model 2 response to a real video sequence. A collision

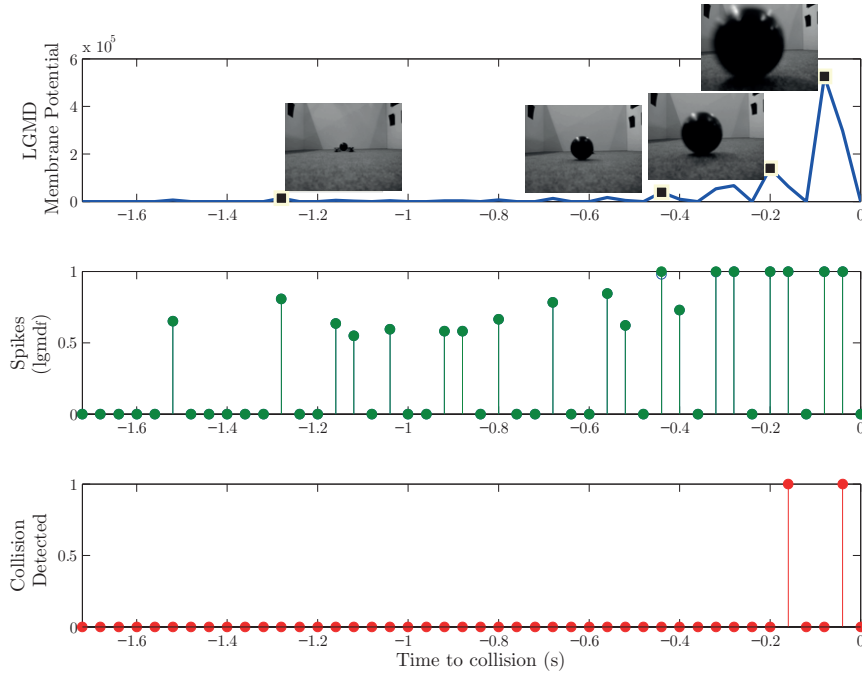


Figure 2.27: LGMD model 2 response to a real video sequence (legend is similar to the one on figure 2.23).

was detected at -0.16 seconds, when the ball was located at, approximately, $D = 19$ cm relatively to the camera (corresponding to a ball angular size of 21 degrees).

2.5.2.5 LGMD model 3: *model evaluation in terms of descriptive adequacy*

The regression analysis performed with the results obtained with LGMD model 3 is represented by the following equation: $f_{\text{peak}} = -44.45 \log(l/|v|) + 253.1$, $r \simeq 0.88$. This regression equation is similar to the one obtained with the previous LGMD model 1 and 2, and consistent with biological results. The mean difference between f_{peak} values obtained with this model, for $l/|v|$ values between 5 and 50 ms, and the biological results (from figure 2.3, left panel), is 37 spikes, with a standard deviation of 35 spikes.

Evaluating the regression line obtained, correlating t_{peak} and $l/|v|$ ratios ($t_{\text{peak}} = -1.8 \cdot l/|v| + 7.1$, $r \simeq 0.99$), it can be conclude that for all values of $l/|v|$, the peak firing rate always occurred 7.1 msec after the object reached a final angular size of 60 degrees on the camera. This result is consistent with the one obtained for the LGMD model 2.

LGMD model 3 shared the independence of its response from the visual stimuli

Table 2.10: Summary of the LGMD model 2 evaluation results obtained for each of the simulation protocols tested. Legend is equal to the one on table 2.9.

Model evaluation: descriptive adequacy												
Model 2	S_L						S_L_I					
	DA_f			DA_t			DA_f			DA_t		
	$\mu(\Delta f_{\text{peak}})$	$\text{std}(\Delta f_{\text{peak}})$		$\Delta\theta_{\text{threshold}}$			$\Delta\theta_{\text{threshold}}$					
	75		21		36°			36°				
	Model evaluation: biological (FRP) and behavioral perspective (CD and D)											
S_A_R			S_U_L			S_N			S_Re			
FRP	CD	D	FRP	CD	D	FRP	CD	D	FRP	CD	D	
A:✓ R:✗	✓✗	✓✗	L:✓ U:✗	✓✗	✓✗	1✓/1✗	1✓/1✗	1✓/1✗	✓	✓	✓	

shape, texture and approaching angle already verified on model 1 and model 2, when subjected to protocol S_L_I .

2.5.2.6 LGMD model 3: *biological and robotic model performance evaluation*

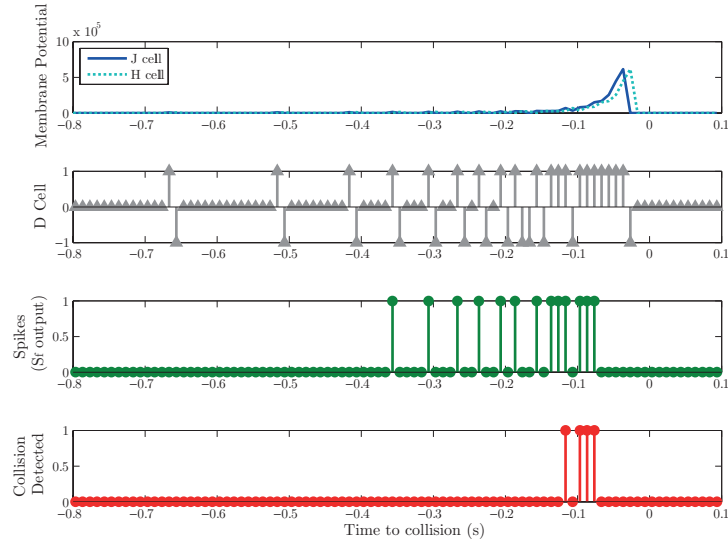
This model has an additional capability to discriminate approaching and receding objects. However, the mechanism introduced in the LGMD model 2 to favor grouped excitations was discarded in the present model. As a consequence, LGMD model 3 is expected to be able to distinguish approaching from receding objects, by producing collision spikes only in the situation of an approaching object. However, it is needed to verify if this capability remains robust even in the presence of noisy environments.

Protocol: S_A_R

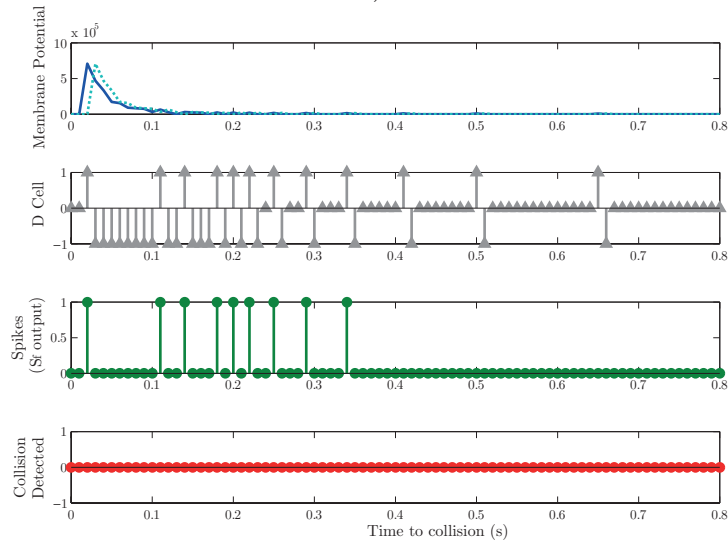
The results obtained for an approaching object, with $l/v = 25\text{ms}$, are represented in figure 2.28, a) panel. According to the results, LGMD model 3 *FRP* is consistent with biology. A collision was detected when the object was located at $D = 7$ (for $l/|v| = 25\text{ms}$, corresponding to an object angular size of 24 degrees) and $D = 5.5$ cm (for $l/|v| = 50\text{ms}$, object angular size equal to 31 degrees) relatively to the camera.

Results on figure 2.28 panel b) show that no collisions were detected when LGMD model 3 was stimulated with an object showing a receding trajectory, with $l/|v| = 25$ ms. The experiment was repeated, but now for an object receding at $l/|v| = 50$ ms. Similarly, no collisions were detected for this second test.

However, analyzing the “D cell” output on figure 2.28, we notice that, in situation a), at some time instants, it takes the value -1 (which is an indicator of a receding trajectory) and, in situation b), assumes value 1 (indicating an approaching trajectory)



a)



b)

Figure 2.28: LGMD model 3 response to an approaching (a) and to a receding object (b), both with $l/|v| = 25$ ms. Membrane Potential: output of the J (continuous line) and H (dashed line) cell. D cell: output of the D cell. 0 - insignificant movement; -1 - receding movement; 1 - approaching movement. Spikes: output of equation 2.31; Collision Detected: red dots represent collision alerts which are the final output of model 3. a) A collision was detected for $t = -0.1833$, being the approaching object located at 5.5 cm to the camera. b) no collisions were detected.

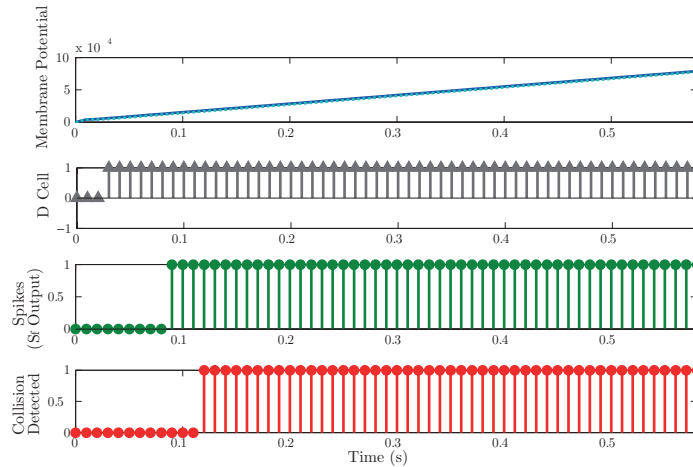


Figure 2.29: LGMD model 3 response to an object approaching at one degree at each time step. Legend similar to figure 2.28.

at, for example, $t = 0.03$ s. This happens because the simulated camera has a limited resolution of 100 pixels, both in vertical and horizontal directions. Consequently, between successive frames, the object’s size does not grow in a continuous and smooth way. The image’s simulation algorithm has to perform an average about the object’s size, computing it in an approximate way. Thus, at some looming instants, H_f becomes higher than J_f (the object keeps its size between successive frames, leading to a decrease in the excitation level).

Despite the previously discussed problem, as a conclusion of the obtained results, we point out the LGMD model 3 capacity in distinguish different directions of movement, by the introduction of a new direction selective system.

Protocol: *S_U_L*

According to this simulation protocol results, LGMD model 3 showed the same *FRP* to an uniformly increasing object, when compared to the LGMD model 2 response. As the object increased linearly one degree per time step, the output of the D cell was kept at “one” during all the experimental course time (see Fig. 2.29, “D cell” graph).

The LGMD model 3 detected a collision 1.2 seconds after the object started to move, corresponding to an angular size of 13.72 degrees.

Through the previous analysis and similarly to the behavior of the LGMD model 1 and 2 when subjected to the same situation, the LGMD model 3 responds too early to an uniformly approaching object.

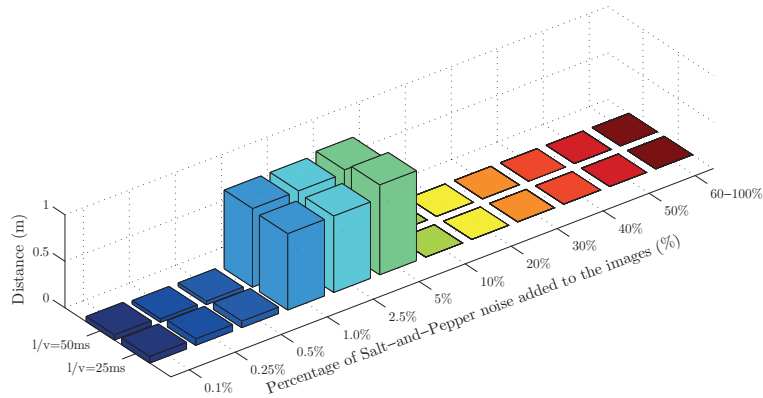


Figure 2.30: Distance at which a collision was detected, by LGMD model 3, at increasing noise levels and for two different $l/|v|$ ratios tested: 25 and 50 ms.

Protocol: S_N

According to figure 2.30, for a noise percentage between 0.1% and 0.5%, LGMD model 3 was effectively able to detect collision scenarios correctly (the “collision detection” spikes were produced when the approaching square was near to the camera). For $l/|v| = 25\text{ms}$, a collision was detected at an average distance of $D = 7\text{cm}$. For $l/|v| = 50\text{ms}$, collisions were detected at an average of $D = 4.3\text{cm}$.

However, for noise percentages between 1 and 5%, the model wrongly detected a collision when the object’s position was far away from the camera (approximately at 86 cm, for both ratios tested). These premature collision detections result from the excitation increment produced by noisy pixels.

For image corruption’s percentages between 10 and 100%, no collisions were detected. That happened due to the inhibition of the LGMD excitation (given by equation 2.26) by the feed-forward inhibition cell (FFI exceeded T_{FFI}).

When compared to LGMD model 2, LGMD model 3 response is highly affected by the presence of noisy synthesized environments.

Protocol: S_Re

After the previous situations tested, the LGMD model 3 was subjected to the real recorded data used to stimulate the previous models.

For the present situation, LGMD model 3 detected a collision at a ball’s position of $D = 19\text{cm}$ relatively to the camera ($t = -0.16\text{ seconds}$), corresponding to the moment when the ball reaches an angular size of 21 degrees.

Observing the obtained results it is concluded that LGMD model 3 works efficiently

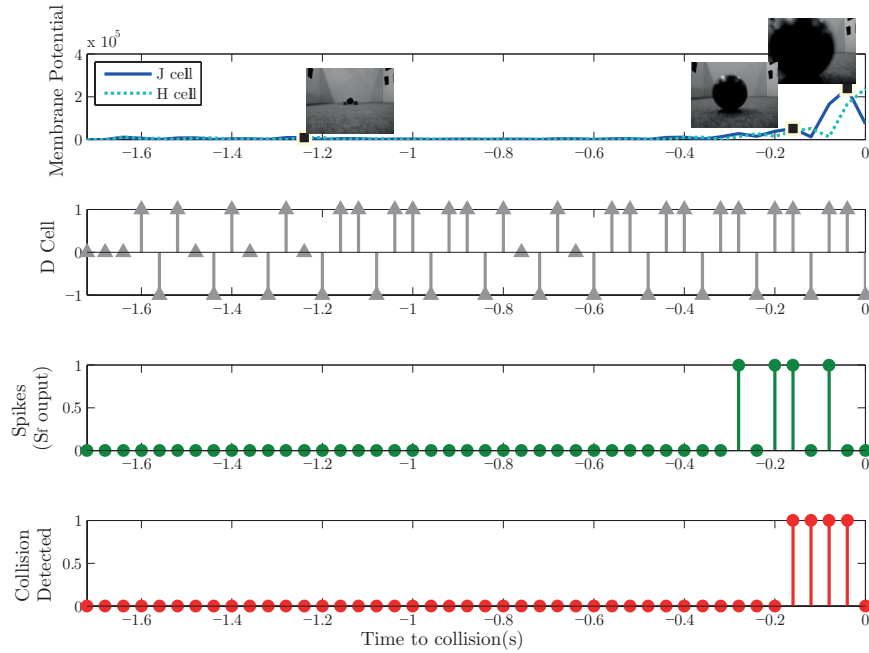


Figure 2.31: LGMD model 3 response to a real image sequence showing an approaching ball (legend is similar to the one on figure 2.28).

in almost all the situations tested. Unfortunately, model 3 is highly affected by images corrupted even with small noise quantities. However, the direction selective system introduced in LGMD model 3 solved the main problem observed in LGMD model 2. This new model is able to distinguish an approaching from a receding object, producing collision alerts only in the first situation.

Table 2.11: Summary of the LGMD model 3 evaluation results obtained for each of the simulation protocols tested. Legend is equal to the one on table 2.9.

Model 3												
Model evaluation: descriptive adequacy												
S_L						S_L_I						
DA_f			DA_t			DA_f			DA_t			
$\mu(\Delta f_{peak})$	std(Δf_{peak})		$\Delta\theta_{threshold}$			$\Delta\theta_{threshold}$			$\Delta\theta_{threshold}$			
37	35		36°			36°						
Model evaluation: biological (FRP) and behavioral perspective (CD and D)												
S_A_R			S_U_L			S_N			S_Re			
FRP	CD	D	FRP	CD	D	FRP	CD	D	FRP	CD	D	
A:✓ R:✗	✓✓	✓✓	L:✓ U:✗	✓✗	✓✗	1✓/4✗	1✓/4✗	1✓/4✗	✓	✓	✓	

2.5.2.7 LGMD connective model: *model evaluation in terms of descriptive adequacy*

Fitting the peak firing rate of the LGMD connective model [15] versus $l/|v|$ stimulus's ratio, the following correlation was obtained: $f_{\text{peak}} = -84.62 \log(l/|v|) + 359.9$, $r \simeq 0.85$. For all $l/|v|$ values tested, the mean difference between the biological and model peak firing rate is 49 spikes, with a standard deviation of 18 spikes.

Relative to the relation between t_{peak} and $l/|v|$ ratio, similarly to what happened with the previous models, a linear correlation was noticed ($t_{\text{peak}} = -3.1 \cdot l/|v| + 7$, $r \simeq 0.99$). According to this, the peak firing rate always occurred 7 ms after the object reached a full angular size of 36 degrees on the camera.

After this first analysis, at protocol *S_L_I*, as the model shown the same linear relationship between the peak firing rate and the $l/|v|$ ratio, it was proved that LGMD connective model responses are largely independent on the stimulus intrinsic variables. So, the extraction of features by the LGMD model proposed by Sergi [15] is highly independent of the image context.

2.5.2.8 LGMD connective model: *biological and robotic model performance evaluation*

In this step, we will evaluate the mathematical equations that integrate the LGMD connective model by analyzing the contribution of each neural layer of the model represented on figure 2.9. The capability to detect an approaching versus a receding object, as well as the detection of an uniformly approaching object will be analyzed. Additionally, the detection of collision scenarios at different noise levels also integrates this analysis. Finally, in order to access the real time properties of this model, we will use the real video sequence showing an approaching ball.

Protocol: *S_A_R*

In order to test the behavior of the LGMD connective model and to compare it with the other models, we subjected this model to the same object trajectories previously described.

In the first experiment, for the sequence showing an approaching square with $l/|v| = 25\text{ms}$, the LGMD model outputs are represented in figure 2.32, top panel.

Applying a $\text{LGMD}_{\text{Meanfiringrate}_{\text{threshold}}} = 50$ to the LGMD mean firing rate output from figure 2.32, a collision was detected when the object was located at 4.6 cm relatively to the camera. In the second experiment, we used an object with a ratio

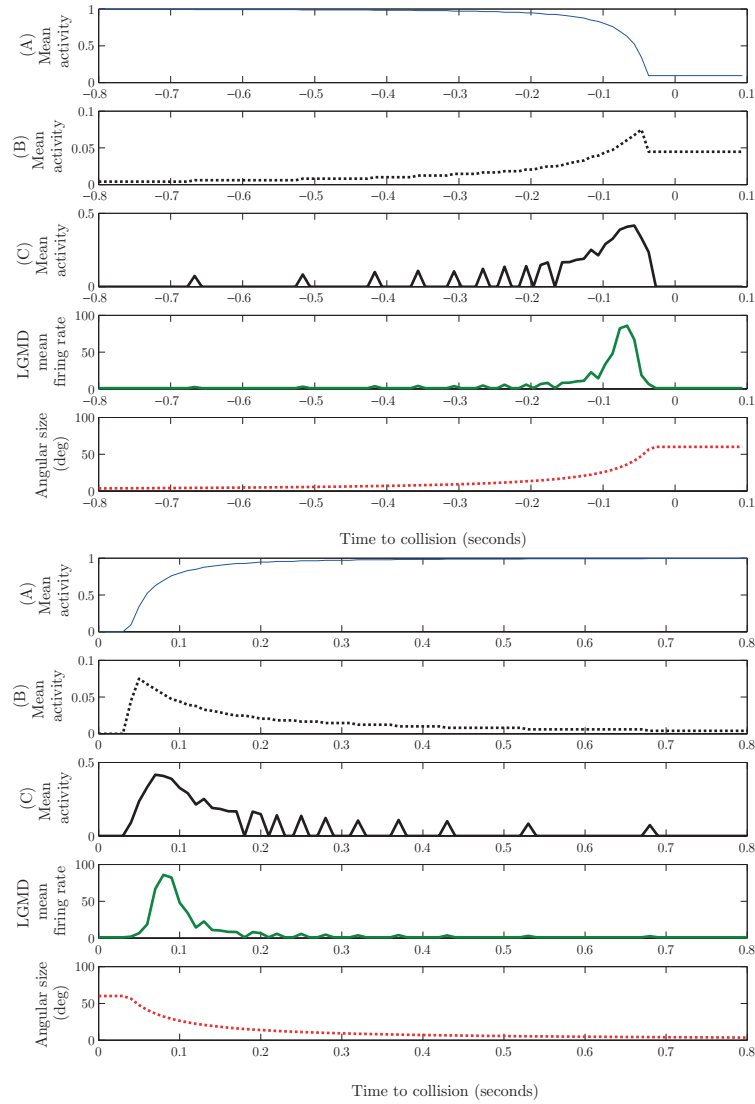


Figure 2.32: LGMD connective model response to an approaching object (top panel) and to a receding object (bottom panel), both with $l/|v| = 25\text{ms}$. (A) mean activity of the Photoreceptive layer; (B) mean activity of the Lamina layer; (C) mean activity of the Medulla layer; Final firing rate of the LGMD model; Object angular size through time.

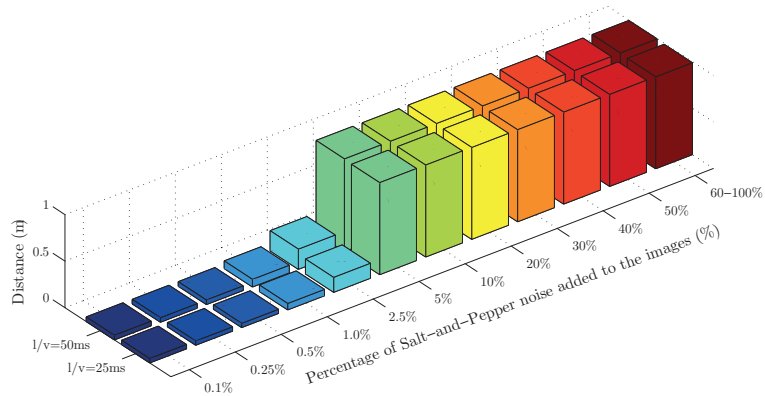


Figure 2.33: Distance at which a collision was detected, by the LGMD connective model, at increasing noise levels and for two different ratios tested: 25 and 50 ms.

$l/|v| = 50$ ms. In this case, and using the same $LGMD_{Meanfiringrate_{threshold}}$ value, a collision was detected exactly when the object was located at the 4.9 cm to the camera.

In relation to the LGMD model stimulation with receding objects ($l/|v| = 25$ and 50 ms), wrong collision scenarios were detected after the object started to recede. We have also noticed that the LGMD firing rate peak, for receding trajectories, depends on the weighting of the post-synaptic inhibition strength.

Protocol: S_U_L

In here, LGMD connective model response was evaluated by using objects showing an uniform size increment, between successive time-steps.

The results obtained for this stimulation protocol showed a peak in the LGMD FRP at the preferred angular size (i.e., when the object reached the angular size threshold, corresponding to 36 degrees). This response profile do not match the biological response for the same simulation protocol.

Protocol: S_N

As observed on figure 2.33, the LGMD connective model correctly detected collision scenarios only for situations when the noise level was inferior than 2.5%. For higher percentages of noise added to the image sequences, premature collisions scenarios were detected by the connective model.

The results obtained for different noise conditions prove the non-robustness of this model to correctly behave in highly corrupted environments.

The nomenclature here used is described on section 2.4.1 and legend is similar to

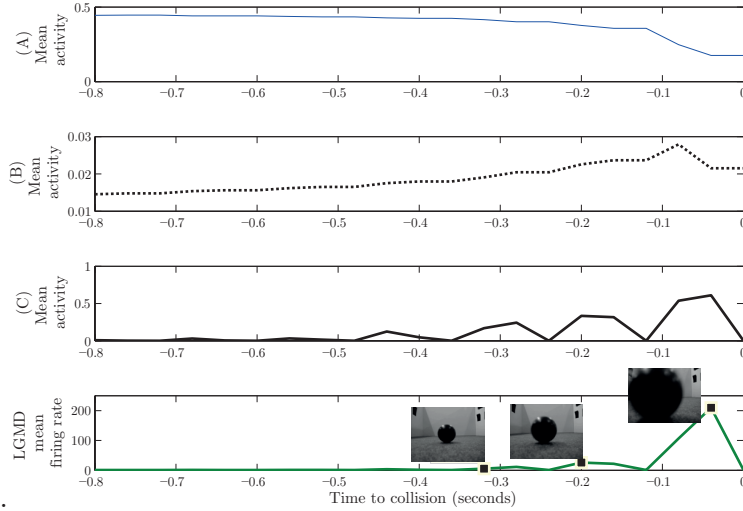


table 2.8.

Figure 2.34: LGMD connective model response to a real image sequence showing an approaching ball (legend is similar to the one on figure 2.32).

Protocol: *S_Re*

In order to evaluate the connective model in a more realistic visual scenario, we used as the visual stimuli, the real recorded video sequence previously described.

For this protocol, the first spike was produced when the ball was located at $D = 9.3$ cm relatively to the camera (for $t = -0.08$ seconds, LGMD mean firing rate is higher than $\text{LGMD}_{\text{Meanfiringrate}_{\text{threshold}}} = 50$ adopted).

Observing the obtained results, it can be concluded that the LGMD connective model works efficiently in almost all the situations tested, but it is highly affected by images corrupted even with small quantities of noise (even below 5%). Besides, this model is not able to distinguish distinct object trajectories (approaching versus receding).

2.6 Model Comparison and Discussion

The analysis described along this chapter, enabled us to test each hypothesis formulated on literature about the LGMD selective mechanism for looming objects, both from a biological and robotic solution perspective. Our main targets are to:

a) compare different hypothesis described on literature about the process behind the LGMD selectivity to looming objects, through computational implementations of different LGMD models, stimulating each model with known visual stimuli, generating

Table 2.12: Summary of the LGMD model 3 evaluation results obtained for each of the simulation protocols tested. Legend is equal to the one on table 2.9.

Model evaluation: descriptive adequacy												
Connective	S_L						S_L_I					
	DA_f			DA_t			DA_f			DA_t		
	$\mu(\Delta f_{\text{peak}})$	$\text{std}(\Delta f_{\text{peak}})$		$\Delta\theta_{\text{threshold}}$			$\Delta\theta_{\text{threshold}}$					
	49	18		12°			12°					
	Model evaluation: biological (FRP) and behavioral perspective (CD and D)											
S_A_R			S_U_L			S_N			S_Re			
FRP	CD	D	FRP	CD	D	FRP	CD	D	FRP	CD	D	
A:✓ R:✗	✓✗	✓✗	L:✓ U:✗	✓✗	✓✗	5✓/7✗	5✓/7✗	5✓/7✗	✓	✓	✓	

outputs and comparing the outputs obtained against our original target specification;

b) to find a good method for generalization in a collision detection recognition system, with its mechanism's source in biology.

However, a central and inherent problem is that drawing any conclusions from this strategy, is not straightforward.

Resultant data from performed stimulations are compacted on tables: 2.8, 2.9, 2.10, 2.11 and 2.12. Unfortunately, data by itself does not directly provide specific and precise information about model's Generalizability (whether the model provides a good indicator of future observations), which is considered as the best criterion on which models should be compared.

In order to compute each of the tested model's Generalizability (Ge) value, a sequence of steps have to be taken.

- The first step consists on computing, for each model, the mean between $\mu(\Delta f_{\text{peak}})$ values and $\Delta\theta_{\text{threshold}}$ obtained (see figure 2.35, top panel), as:

$$\text{GOF}_{1,M} = \frac{\mu(\Delta f_{\text{peak}}) + \Delta\theta_{\text{threshold}}}{2} \quad (2.43)$$

the value obtained corresponds to the Goodness Of Fit ($\text{GOF}_{1,M}$, which M stands for model) between the model and biological data (the lower the difference value, the best is the GOF between the biological and the model output data).

- Compute the Proportion Index of correct choices, through:

$$\text{GOF}_{2,M} = N_{\text{total observations}} - \sum \text{cr} \quad (2.44)$$

where cr stands for the number of correct responses (the lower is the value, the

higher number of situations where the model output was in accordance to the biology - see figure 2.35, middle panel).

- Calculate the complexity of each model, which is directly given by the number of model parameters (MP), which is attractive as a measure of model complexity since it is very easy to calculate (see tables 2.3, 2.4, 2.5 and 2.6, and figure 2.35 - middle panel): the lower the complexity the less sensitive the model is to parameter variations, becoming more flexible.
- Compute model's Ge, through the computation of the adapted Akaike's Information Criterion (AIC, [125]) (see figure 2.35, bottom panel), through:

$$AIC = 2 \times \ln((GOF_1 + GOF_2)/2 \times n) + 2 \times MP + (2 \times MP \times (MP + 1))/(n - MP - 1) \quad (2.45)$$

where n stands for the number of data observations. Results obtained from model comparison can be seen on figure 2.35.

It is important to notice that the AIC is not a model's test in the sense of hypothesis testing; rather it is a tool for model selection. Given a data set, several competing models may be ranked according to their AIC, with the one having the lowest AIC being the best. So, model's Generalizability is estimated such that the lower the AIC value, the better the model is expected to generalize, *ie*, the smaller the AIC value, the closer the model is to the "truth".

According to this, LGMD connective model has the higher Generalizability, followed by Model 1 and Model 3 (which have very similar values), η -function model and, finally, Model 2. In fact, LGMD connective model's working merges principles of both critical race (H1) and feed-forward excitation versus feed-forward inhibition (H2) hypothesis, possibly taking advantages of the processing embedded on the model structure. When compared to the LGMD biological data, this model presented the second lower mean difference value, being also the second lower complex model, which is inferred from its low number of model parameters, as well as the model with the third best overall performance when subjected to protocols S_A_R , S_U_L , S_N and S_Re .

2.7 Conclusion

As evident from this survey, simulations of LGMD neuron responses have a wide-ranging set of goals, from conceptual proof of concept, to biological comparisons, as well as to possible robotic applications.

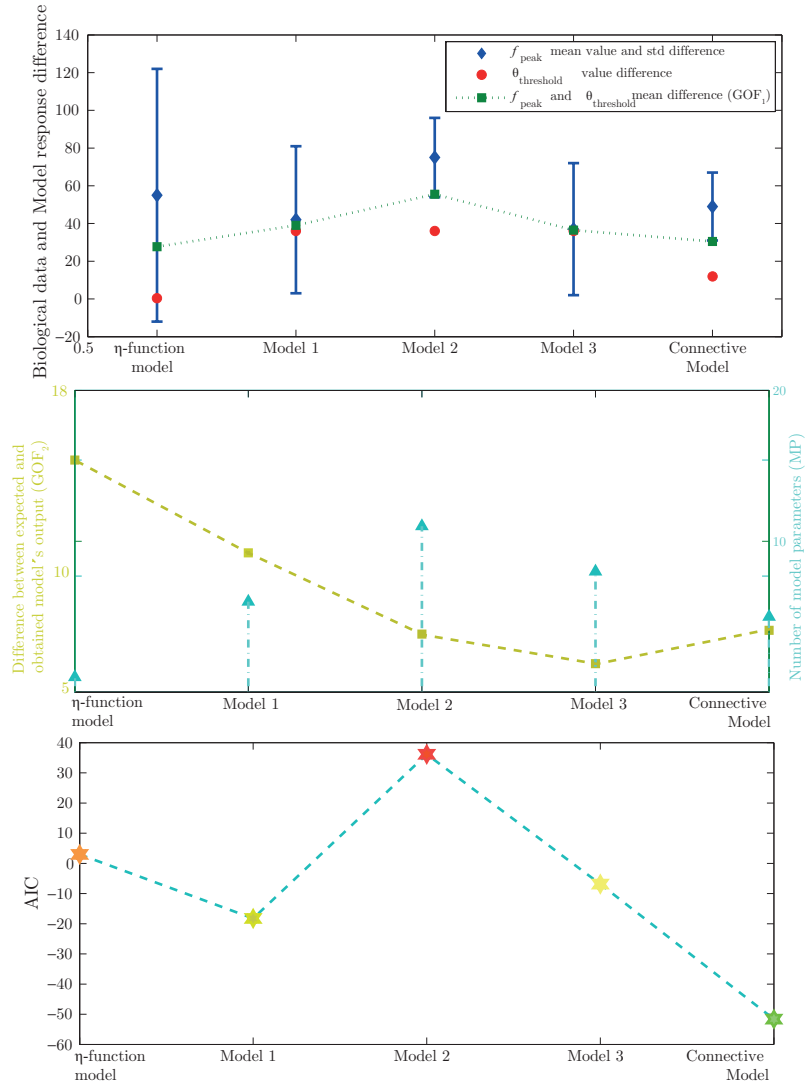


Figure 2.35: Top Panel: Blue diamonds: Mean difference between f_{peak} obtained in biology and with each model tested, averaged over $l/|v|$ values used, and respective standard deviation. Red dots: $\theta_{threshold}$ difference between biological and model data, averaged over all $l/|v|$ values tested. Green squares and dashed line: GOF_1 values, obtained for each model tested. Middle panel: GOF_2 values obtained for each tested model, as well as number of parameters for each model (MP). Bottom panel: Model's Akaike's Information Criterion (AIC). The lower the AIC value, the better the model is expected to generalize.

Along this chapter, a deep analysis of the main neural models of the Lobula Giant Movement Detector (LGMD) neuron proposed in literature was made, covering different hypothesis about theoretical explanations of the neuron functioning. All models here presented have proven to be useful on helping to understand and explain the locust neural response to different visual scenarios.

In order to analyze the difference between selected LGMD models [15, 83, 121, 229, 233] responses to different experimental conditions, five different LGMD models were implemented and tested: the first model is based on the Gabbiani approach [83]; three of them are based on the approach made by Rind [121, 229, 233]; and one based on the model proposed by Sergi [15]. These models were subjected to different visual protocols, consisting in distinct visual scenarios. Through this profound analysis, the limitations and the advantages of each LGMD model have been described and discussed.

The first model analyzed was the one proposed by Gabbiani [83]. According to the results obtained in the validation and stimulation protocols used, this model has proven to be an excellent fit of the LGMD neural responses to looming stimuli. However, the implementation of this model as a real collision detection is quite limited, since the input to this model consists on the angular speed and angular size computation of the approaching object. In a real implementation, the computation of these two variables requires the implementation of complex algorithms to extract the object from its background, and then calculate its the angular speed and size. Accordingly, the logical adequacy of this hypothesis to account for the data, revealed to be incomplete when formalized for modeling.

Two additional and distinct approaches were developed by different research teams [15, 121, 229, 233]. Distinct neural network models have been proposed, along the last years, by Rind and her colleagues [121, 229, 233], in order to explain the LGMD neuron's responses to different visual stimuli. These models take into account all the processing steps done in the different layer of the locust visual system [185], prior to the LGMD neuron itself. Due to its simplicity, the first neural network model - LGMD model 1 [233] - presented some limitations. Model 1 was not able to work in corrupted environments. The noise added to the image sequence worked as an extra excitation, leading the excitation level, in the LGMD neuron, to increase and, consequently, producing premature collision alerts. Besides that, model 1 produced the same excitation level, either for approaching and receding objects. In the case of receding objects, the high excitation of the LGMD neuron lead it to produce false collision alerts.

Due to the limitations presented by the LGMD model 1, two new models were proposed in literature: the LGMD model 2 [229], which has the capability to eliminate noise; and the LGMD model 3 [121], which is able to detect the object's direction of movement. After the computational implementation of these two models, and according to the analysis of their performance to different visual scenarios, the limitation of the LGMD model 2 in distinguish approaching versus receding objects was verified, as well as the limitation of the LGMD model 3 to work within noisy environments. As a future direction, we proposed the integration of these two LGMD models, in order to create a more robust and effective LGMD model [180].

Finally, a new approach was proposed by Sergi[15]. This model goes a step beyond Rind's models [121, 229, 233], making clear anatomical predictions on how specific properties of the LGMD arise, showing that the multiplication between the object's angular size and angular speed is not needed to account for the known properties of the LGMD neuron. This model was able to correctly detect potential collisions in a high range of situations tested, being only negatively affected by noisy environments. Besides that, we also verified a linear relationship between the peak firing time and the $l/|v|$ ratio for objects with different textures, shapes and approaching angles.

According to these results, the three main goals of this chapter were achieved: (1) we were able to provide a critical analysis of the different LGMD models; (2) Along the paper, we highlight the convergence or divergence in results obtained with each one of the models; (3) According to the results obtained with each model when stimulated with a real video sequence, we were able to test the applicability of each model.

As future directions, we propose the application of new simulation protocols, with objects showing complex trajectories (as translation combined with approaching), as biologically tested by [38, 119]. Besides that, the response of these LGMD models in cluttered environments is unknown. Should the LGMD model choose a single object from a cluttered environment? Is the locust able to select a main object from the cluttered environment? There are still many biological questions to answer.

Further, responses of these models to dim light levels is also unknown. In decreasing light levels, both image contrast decreases and image noise increases radically. On these conditions, the reliability of the images is highly corrupted, which can affect the LGMD neural spike rate and, subsequently, the correct detection of potential collisions.

Following this line of thought, as a future work, we should try to predict the biological response to these type of complex visual stimuli when inserted in dynamic environments, for different light levels, using, for that, the principles behind the LGMD models presented and discussed in this chapter, but improved such as to bridge some

limitations.

Chapter 3

LGMD neural responses to complex visual motion with increasing background complexity ¹

Investigation of the principles of visual processing in insects is offering novel, computationally elegant solutions to challenges in machine vision and robot navigation. However, a significant drawback with vision is the complex relationship between the raw signal produced and processed by the sequential neural layers in the insect optic lobe, and the corresponding 3D environmental layout.

While there have been extensive research efforts focused on understanding the response of the LGMD neuron to simple visual stimuli, little attention have been given to comprehend the way this control system works when inserted in more realistic visual scenarios, including different background complexities, multiple approaching objects, as well as objects performing trajectories including translation and approaching components.

This chapter aims at demonstrating how distinct visual pattern's complexities can be directly linked to LGMD neural responses, and how robustly LGMD responses are in different scene's contexts.

Grounded on the results obtained with the experiments described in this chapter, more robust and effective LGMD models could be futurely developed.

¹The work presented in this chapter has been published in: Background complexity affects the response of a looming-sensitive neuron to object motion, by Ana C Silva , Glyn A McMillan , Cristina P. Santos , John R Gray. *Journal of Neurophysiology* Oct 2014, DOI: 10.1152/jn.00478.2014.

3.1 Introduction

Flying animals are continuously challenged with different forms of visual motion, including self-produced flow field motion (self motion in a stationary environment) and motion produced from an object moving within a stationary environment or in a direction opposite to a predicted one. The discrimination between these types of motion is paramount to an animal's survival, for example predator avoidance. Flying through complex visual environments requires the detection of relevant salient visual cues for successful navigation. Looming objects, for example, provide critical information regarding an oncoming collision or perhaps an approaching predator. While stationary, an approaching visual stimulus is clearly interpreted as noxious, thus detection, and subsequent avoidance behaviour, may be relatively straightforward. However, while generating self-generated optic flow during movement or, in the case of swarming animals, surrounded by conspecifics moving at often unpredictable velocities and directions, detection of noxious stimuli is challenging.

The migratory locust, *Locusta migratoria*, is an established neuroethological model system for studying collision avoidance due to its long research history, easily tractable nervous system, and well-identified looming sensitive neurons (LSNs). During flight, a locust's visual environment is dynamic. Within a swarm, individual locusts may fly at ~ 3 m/s and in close proximity with each other, while maintaining flight elevations from 1 – 1000 m above ground [207]. Neighboring locusts approach from different angles and at different velocities while land geography changes below. However challenging the environment, flying locusts are capable of avoiding collisions with conspecifics [211] and aerial attacks of diving birds while swarming [168]. Indeed, experimental studies on free flying [36] and loosely tethered flying locusts [30, 120] show that locusts use a relatively unpredictable range of avoidance behaviours in response to noxious stimuli. Successful navigation within such a complex environment is, in part, related to a well-developed visual network of movement sensitive neurons, specifically and most widely studied are the lobula giant movement detector (LGMD) and its postsynaptic partner the descending contralateral movement detector (DCMD).

Excitation of the LGMD begins when movement within a locust's visual field stimulate retinotopically arranged fibers within the ommatidia, which produce excitatory input to one of the three large dendritic fields of the LGMD [153]. During a looming approach, the number of spikes produced by the LGMD is directly related to an approaching object's angular velocity and subtense angle and is thus referred to as an angular threshold detector [70]. As an object approaches the retina, the LGMD firing rate increases to a peak and then decays once object motion stops and before a

collision would have occurred [38, 68, 70, 71, 77, 80, 119].

Presynaptic lateral inhibition and postsynaptic feed-forward inhibition from the other two dendritic fields control excitation and thus define the peak firing rate of the LGMD [63, 68, 70]. Each LGMD synapses onto a DCMD within the protocerebrum, generating a one-to-one spike ratio [131]; for the ease of access, many studies record from the DCMD axon within the contralateral side of the ventral nerve cord. The LGMD/DCMD pathway is part of a relay system that tracks the approach and signals an impending collision of visual objects to motor centers within the thoracic ganglia [182]. Phases of an avoidance jump have been linked to phases of this pathway's firing rate [58] in addition to a possible role in modifying wing beat rhythm during flight [167]. While the DCMD habituates to repetitive stimuli [77, 84, 134], it remains sensitive to a simple looming stimuli following translatory motion within a locust's field of view and also responds to the transition to and from a looming trajectory [38, 119]. Although it remains unknown if the DCMD is responsible for avoidance behaviours in complex environments (such as those found while flying in a swarm), these studies suggest that the DCMD is capable of responding to important aspects of a complex visual environment (see [151]). The interest in answering the question of complexity reaches beyond neurobiology and into robotics.

Outdoor micro air vehicles (MAVs) and other robotic control systems are often engineered based on the physiology and circuitry of insect models [57, 237, 238]. To understand how visual neurons respond in natural environments, it is important to balance quantifiable stimulus parameters (i.e. object motion) with aspects of complex scenes (i.e. optic flow). In addition to a simple looming stimulus, we presented a combination of bilaterally paired non-looming and looming stimuli (i.e. compound trajectories) at varying velocities. All stimuli were presented in a 3-dimensional environment on a specialized dome projection screen using either a simple white background, a scattered background with hundreds of randomly translating dots to represent a "swarm", or a progressive flow field background representing optic flow produced by forward motion. Consistent with previous work using compound approach trajectories [38, 119], the DCMD responded to a transition to looming with a quantifiable drop in firing rate (valley) that was relatively consistent for all trajectory types, velocities of object approach, and background environment. Response time from transition to DCMD valley was also consistent with previous work [38, 119] and remained relatively invariant across all stimulus combinations. Moreover, within each stimulus background the DCMD firing rate was capable of tracking and responding to the motion of each stimulus. However, many of the measured response parameters of the DCMD response

differed depending on the type of trajectory, velocity, and background. We show that although background complexity affects DCMD responses to looming and transitions to looming stimuli, the collision associated peak response is, in general, remarkably invariant.

3.2 Materials and Methods

Animals

We used 14 adult male *Locusta Migratoria* for experimentation. All animals, at least 3 weeks past the imaginal molt, were obtained from a crowded colony maintained in the Department of Biology at the University of Saskatchewan (25-28°C, 12hr:12hr light:dark). Experiments were carried out at ~25°C during similar times of the animals' light cycle to avoid potential variations in responsiveness when locusts fly at night [74].

Preparation

After the legs were removed and the wings were clipped, a rigid tether was attached to the ventral surface of the thorax using low melting point bee wax. A small patch of ventral cervical cuticle was removed to expose the underlying paired connectives of the ventral nerve cord anterior to the prothoracic ganglia. Locust saline (147 mmol NaCl, 10 mmol KCl, 4 mmol CaCl₂, 3 mmol NaOH, 10 mmol Hepes, pH 7.2) was applied to the exposed tissue (see figure 3.1) and the preparation was moved to the recording stage where two silver wire electrodes were hooked around the left and right ventral nerve connectives; the left and right recording sides are herein referred to as the left and right DCMDs. A mixture of Vaseline and mineral oil was used as an insulator around the recording site once we observed distinct neural responses from each connective to local motion (hand waving). A silver wire was also inserted into the locust's abdomen and connected to ground. Each locust was oriented dorsal-side up and aligned with the azimuthal and elevation axes of the apex of a rear projection dome screen 10 cm away. In this orientation 0° was directly in front of the locust at the dome apex, -90° was the center of the left eye and 90° was the center of the right eye. To allow the animal to acclimate to the experimental setup, the preparation was left for ~10 minutes in front of each background before presenting any visual stimuli. Once experimentation began, we maintained a presentation-to-presentation interval of 3 minutes to prevent confounding effects of neural habituation.

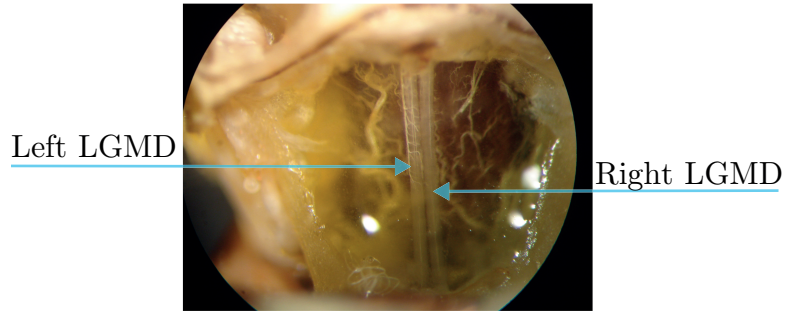


Figure 3.1: Real image of the LGMDs nerve cords, during preparation stage.

Visual Stimuli

The procedure used for visual stimulus generation and data acquisition was similar to that described in [119]. Briefly, visual stimuli were created using Vision Egg [196] on a Python programming platform and represented as 1024 x 1024 pixel portable network graphics (png) files. Each pixel on screen subtended approximately $\sim 0.4^\circ$ of the locust's eye (well below the 1° resolution of individual ommatidia [85]). Two 7 cm diameter black discs traveling at different velocities and trajectories were presented simultaneously to the left and right side of the locust. Expansion properties associated with different velocities were described as a ratio of the half size of the disc ($l = 3.5$ cm) divided by the absolute velocity ($|v|$). All stimuli were scaled in real-time at 85 frames/sec (fps) and projected in 3 dimensions onto a rear projection dome screen using an InFocus Depth Q LCD data projector. A TTL pulse that was included in each video frame and the vertical refresh synchronization pulse from the video card (NVIDIA GeForce4 Ti4200 128 MB) were used to align neuronal recordings with the stimuli (see below).

All primary visual stimuli (7 cm diameter black disc) were presented at 0° elevation and modified within the azimuthal plane. The initial and final approach trajectory within each background type (see below) was a frontal (i.e. 0° azimuth) looming single disc travelling at 3 m/s ($l/|v| = 12$ ms) (figure 3.2A). Following the initial frontal loom, we presented a randomized series of compound trajectory types consisting of two 7 cm black discs that travelled simultaneously along one of three bilaterally-matched trajectories that transitioned from non-looming to looming (Trajectory 1 (T1), Trajectory 2 (T2), and Trajectory 3 (T3)) (figure 3.2A). The compound trajectory discs also travelled at one of three different velocities: 0.875 m/s ($l/|v| = 40$ ms), 0.5833 m/s ($l/|v| = 60$ ms), or 0.4375 m/s ($l/|v| = 80$ ms). Each series of compound approaches was followed by a final frontal loom of a single disc. T1 consisted of a disc

that travelled orthogonal to the long axis of the locust's body 50 cm anterior to the eyes, transitioned at 45° azimuthal angle and loomed toward the eye ipsilateral to the visual field of motion; T2 started in front of the locust, offset from direct center by 5 cm, approached to 90° azimuthal angle and transitioned to a looming approach; and T3 approached from behind the locust and transitioned to a 90° looming approach.

All frontal looms and compound trajectories were presented onto three stimulus backgrounds (figure 3.2B). The simple background (S) was a white background with no other object motion other than the 7 cm disc. The scattered background (SC) was projected over the entire screen and consisted of 600 black discs (0.8 cm diameter; angular size = 4.6°) moving randomly in straight trajectories along a single plane orthogonal to the long axis of the locust at 400 pixels/s (0.028 m/s, or an $l/|v| = 143$ ms). For the flow field background (FF), we used a modified vertical grating pattern that consisted of vertical bars (width of each bar = 2 cm; angular size = 11.42°) moving outwards in the azimuthal plane from the dome apex. Each bar moved at 0.138 m/s across the dome and extended across the entire length of the dome screen before disappearing from the field of view at the edge of the dome screen. Each background, and stimuli presented within each background, maintained a similar contrast ratio, with the exception of the FF, where the edges of the vertical bars faded from black to white. The luminance values and Michelson contrast ratio (0.48) of the white background and black discs were similar to those used previously [38, 80, 119].

Within a randomized background type (S, SC, or FF), each animal was presented with a randomized set of stimuli based on the trajectory (T1, T2, or T3) and stimulus velocity ($l/|v| = 40$ ms, 60 ms, or 80 ms); each different stimulus combination was presented only once per animal. There was a 10-minute interval between each different background and 3-minute interval between each stimulus presentation. We did not randomize background changes with stimulus trajectory and velocity, since we were not concerned with the effect of switching from one background to another. Moreover, with the exception of a few sporadic DCMD spikes, when the only visual stimulus present was the SC or FF backgrounds type, no DCMD responses were generated. In total, there were 11 presentations per background per animal (33 presentations total). For each presentation the 7 cm disc remained on the screen for 1 second before disappearing within one frame and for all presentations with a trajectory change, the change occurred over one frame.

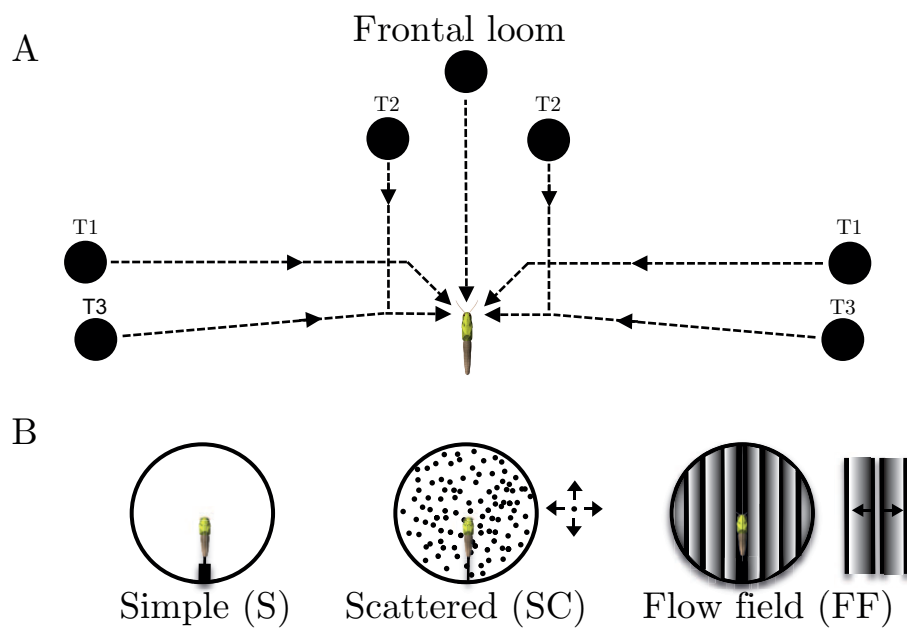


Figure 3.2: Computer-generated stimuli. A) Following an initial and preceding a final frontal looming stimulus using a single 7 cm black disc, each locust was presented, in random order, with 3 compound trajectories (T1, T2, and T3) consisting of a bilateral pair of non-looming transitioning to looming 7 cm black discs traveling at 3 different velocities at two azimuthal angles (T1, 45°; T2 and T3, 90°). B) Each trajectory was presented onto one of three stimulus backgrounds (simple, scattered, or flow field). Arrows in panel A and B represent the relative direction of object motion.

Spike sorting and quantification of DCMD firing properties

For each presentation, neuronal activity from the left and right cervical connective, pulses synchronized with each frame of the stimulus, and vsync pulses from the video card were recorded continuously and stored for future analysis. All neural activity was amplified with a differential AC amplifier (A-M Systems, model No. 1700, gain = 10,000) and sampled at 25 kHz. We used an RP2.1 enhanced real-time processor (Tucker-Davis Technologies, Alachua, FL) with Butterworth filter settings of 100 Hz (high pass) and 5 kHz (low-pass) to store the data. Subsequent neuronal activity was analyzed using Off-line Sorter (Plexon, Dallas, TX) and DCMD activity was isolated using threshold analysis. Spike times were exported to Neuroexplorer (NEX Technologies, Littleton MA) and transformed into peri-stimulus time histograms using a 1-ms bin width and smoothed with a 50 ms Gaussian filter. We used a similar method described in [119] to characterize different DCMD firing properties. These included the firing rate (f) and time (t) of firing rate relative to time of collision (TOC) or time of transition (TOT) associated with each peak (f_p, t_p) or valley (f_v, t_v) firing rate as well as the peak width at 1/2 max firing rate, total spike number during the entire stimulus presentation, the response time (δ) and change in firing rate ($f_{TOT} - f_v$) from each TOT to the associated valley, and durations of the rise and fall phases for each TOC and TOT-associated peak.

The rise phase of each DCMD response was calculated from the point at which the DCMD firing rate exceeded a 99% confidence interval (sampled from data for the entire stimulus presentation) to the peak of the DCMD firing rate (TOC or TOT-associated). The TOC-associated fall phase duration was calculated from the time of the frame when the stimulus stopped expanding to the time of the last spike following when the firing rate decreased to 15% of the peak DCMD firing rate (see [73, 80]). The TOT-associated falling phase duration was marked from the maximum firing rate prior to the time of the valley to the time of the valley; we used this measure rather than the time of TOT to valley since we defined this parameter as δ . We normalized the change in firing rate (f') for our 2D Gaussian fit by dividing the response to a transition (i.e. f_v) by the time of stimulus change (i.e. f_{TOT}), such that values between 0 and < 1 represented a relative decrease in firing rate and values > 1 represented an increase in firing rate (see [119]).

Statistical Analysis

Statistical analysis was performed using SPSS 21.0 (Chicago, IL) and SigmaStat 3.5 and plotted using SigmaPlot 12.5 (Systat Software Inc., Richmond, CA). The statistical treatment of data depended on the number of effects we analyzed and whether the data were parametrically or non-parametrically distributed. In the case of frontal looms, parametric data were tested with one-way repeated measures (RM) ANOVA (reported by F statistic) whereas non-parametric data were tested with Friedman RM ANOVA on ranks (reported by χ^2 statistic). All pairwise multiple comparisons for head on looming data were performed using a Tukey Test and significant results (i.e. $P < 0.05$) were described using the q statistic and difference of ranks. For the 27 compound trajectories, if the data followed a normal distribution, a three-way RM ANOVA was performed (with factors: Trajectory (with levels: initial approach from the side (T1), front (T2), back (T3)); background (with levels: S, SC, FF); and velocity (with levels: $l/|v| = 40$ ms, 60 ms, 80 ms). An aligned rank transformation [223] was applied to the data if it was not normally distributed. In cases where the data failed Mauchly's Test of Sphericity (i.e. $P < 0.05$), the test statistic and d.f. were corrected using the Greenhouse-Geisser estimate of sphericity. All compound trajectory statistics were reported with their F statistic (with subscripted d.f. and error d.f.) and associated P value. To refrain from excessive statistical reporting, only the statistics for the main effects and interaction effects of each factor are described. In all cases, $n = 14$ animals (28 neurons) were sampled and significance was assessed at $P < 0.05$. Descriptive statistics are reported as the mean +/- standard deviation (SD).

There were several instances where no TOT-associated DCMD response was detected so we used the SPSS single imputation method for 7 of the dependent variables ($n = 216/756$ missing values for f_v , t_v , TOC peak rise phase, TOT peak rising and decay phases, δ , and $f_{\text{TOT}} - f_v$). Based on trajectory type, a total of $122/252 = 48\%$, $21/252 = 8\%$, and $73/252 = 29\%$ of recordings in T1, T2, and T3, respectively, did not show TOT-associated responses; FF accounted for most non-responses in T1 and T3.

3.3 Results

Regardless of stimulus background or recording side, DCMDs generated a characteristic rapid rise to a peak firing rate in response to a frontal loom (figure 3.3A). Although the DCMD response from different recording sides within the same animal were variable

(for example, see figure 3.3A), we found no significant differences between the left and right DCMD responses or between the initial and final frontal looms within each background when comparing f_p , number of spikes, peak width at 1/2 max, and t_p ($n = 14$ recordings, 1 presentation per animal, data not shown). Thus, responses were not affected by DCMD location (left or right) or the length of the experiment.

Frontal looms – effects of increasing background complexity

All data were pooled for a total of $n = 56$ recordings per background (14 animals, 2 recording sides, 2 looms per background type). We found a significant effect of background on f_p ($\chi^2 = 18.3$, $P < 0.001$, figure 3.3B) and t_p ($\chi^2 = 40.8$, $P < 0.001$, figure 3.3C). SC and FF resulted in a significantly lower ($q_{27} = 3.6$ and $q_{45} = 6.0$, respectively) and later ($q_{67} = 8.9$ and $q_{25} = 3.3$, respectively) peak relative to S. The peak also occurred significantly later in the presence of FF than SC ($q_{42} = 5.5$) and the median was slightly after time of collision (TOC). The number of spikes were also affected by different backgrounds ($\chi^2 = 8.6$, $P = 0.02$, figure 3.3D) with the highest number occurring in SC, which was significantly higher than in the presence of S ($q_{31} = 4.1$).

Although we found no significant effect of background on peak width at 1/2 max ($F_3 = 2.7$, $P = 0.07$, figure 3.3E), the rise and fall phases of the peak firing rate were strongly affected by the type of background (rise phase: $= 76.1$, $P < 0.001$ and fall phase: $= 59.3$, $P < 0.001$, figure 3.3F).

While SC resulted in a significantly shorter rise phase and longer fall phase relative to S ($q_{59} = 7.9$ and $q_{48} = 6.4$, respectively), FF resulted in the shortest rise phase (FF vs S: $q_{91} = 12.2$; FF vs SC: $q_{32} = 4.3$) and longest fall phase (FF vs S: $q_{81} = 10.8$; FF vs SC: $q_{33} = 4.4$). Overall, these results show that background strongly affected DCMD firing patterns in response to a frontal looming stimulus. More specifically, increasing background complexity resulted in delayed peak firing, lower peak firing rates, higher spike numbers as well as shorter rise and longer fall phases.

Compound trajectories

Similar to the frontal looming results, simultaneously presented bilateral compound stimuli resulted in no differences between individual left and right DCMD responses for the same trajectory. We subsequently pooled the left and right responses for statistical analysis. Following a transition to a looming trajectory, the DCMD exhibited a brief drop in the firing rate that created a local valley followed by a TOC-associated firing

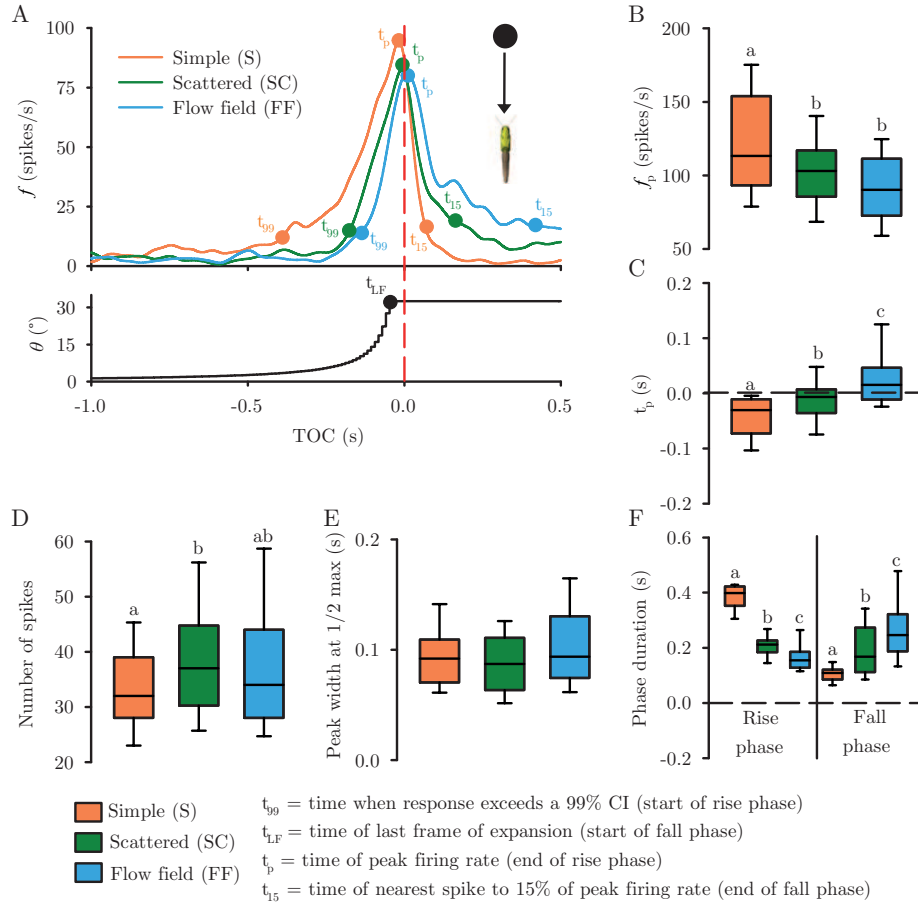


Figure 3.3: Looming disc ($l/|v| = 12$ ms) were presented head on to each locust ($n = 14$) within three background types ($n = 56$ recordings per background). A) Pooled mean DCMD responses (continuous lines) to a looming black disc approaching from the three visual backgrounds (simple [*top*, orange line], scattered [*middle*, green line], and flow field [*bottom*, blue line]), and change in subtense angle aligned to the time of collision (TOC; dashed, red vertical line). Labeled points on the mean DCMD response panels (t_{99} , t_p and t_{15}) and t_{LF} on the subtense angle panel represent specific times used for the LF calculation of the rise and fall phases (see figure legend and Methods). B-F represent, respectively, the statistical comparisons of the TOC-associated firing rate (f_p), time of peak firing (t_p), number of spikes, peak width at 1/2 max, and phase duration for each background type. Different letters above bars represent significant differences between parameters. Significance assessed at $P < 0.05$.

rate increase (figure 3.4), which occurred regardless of background type and approach velocity and is consistent with previous findings (see [119] and [38]). We also observed lower peak amplitudes, later peak times, shorter rise and longer fall phases in the more complex backgrounds (figure 3.4). In some trajectories (such as T1 - FF, figure 3.4), TOT-associated responses were masked by the presence of a flow field. Statistical comparisons can be found in Table 3.1 and valuations of effect weight were based on the resulting F statistic. All TOC-associated parameters are summarized in figure 3.5, TOT-associated parameters in figure 3.6, and the rise and fall phases in figure 3.7.

Table 3.1 summarizes the statistical analysis of all 13 response variables for all three factors and their interactions ($n = 28$). Trajectory affected all measured DCMD response variables, changes in stimulus velocity affected all variables except the peak width at 1/2 max, δ , and TOT fall phase whereas the background type affected all variables except the $f_{\text{TOT}-v}$, t_v , and δ . Interactions between stimulus variables also affected DCMD responses. The interaction between trajectory and velocity affected all variables except f_p , the interaction between trajectory and background affected all variables except peak width at 1/2 max and δ , and the interaction between velocity and background affected all variables except peak width at 1/2 max, f_{TOT} , and the TOC fall phase. The combined effect of all three factors (trajectory, velocity and background) resulted in significant differences in all variables except peak width at 1/2 max, f_p , f_{TOT} , and t_v .

TOC-associated response parameters are affected by trajectory, velocity, and background

Regardless of trajectory or background, higher $l/|v|$ values (lower velocities) evoked a higher number of spikes (80 ms > 60 ms > 40 ms, figure 3.5A). For T1, more spikes were evoked depending on the background (SC > S > FF). The background type had variable effects on responses to the different trajectory types, where there was little effect of trajectory type in S, while in SC and FF there was an effect of trajectory type (T1 > T3 > T2). Overall, velocity had the strongest effect on the number of spikes produced; however the interaction between trajectory and background had the strongest interaction (Table 3.1). With the exception of trajectory (where T3 > T1 > T2) and background (where S > SC and FF), we found few differences in peak width at 1/2 max (figure 3.5B).

Table 3.1 shows that the type of trajectory had the greatest effect on peak width at 1/2 max followed by the type of background. Although changes in velocity did not

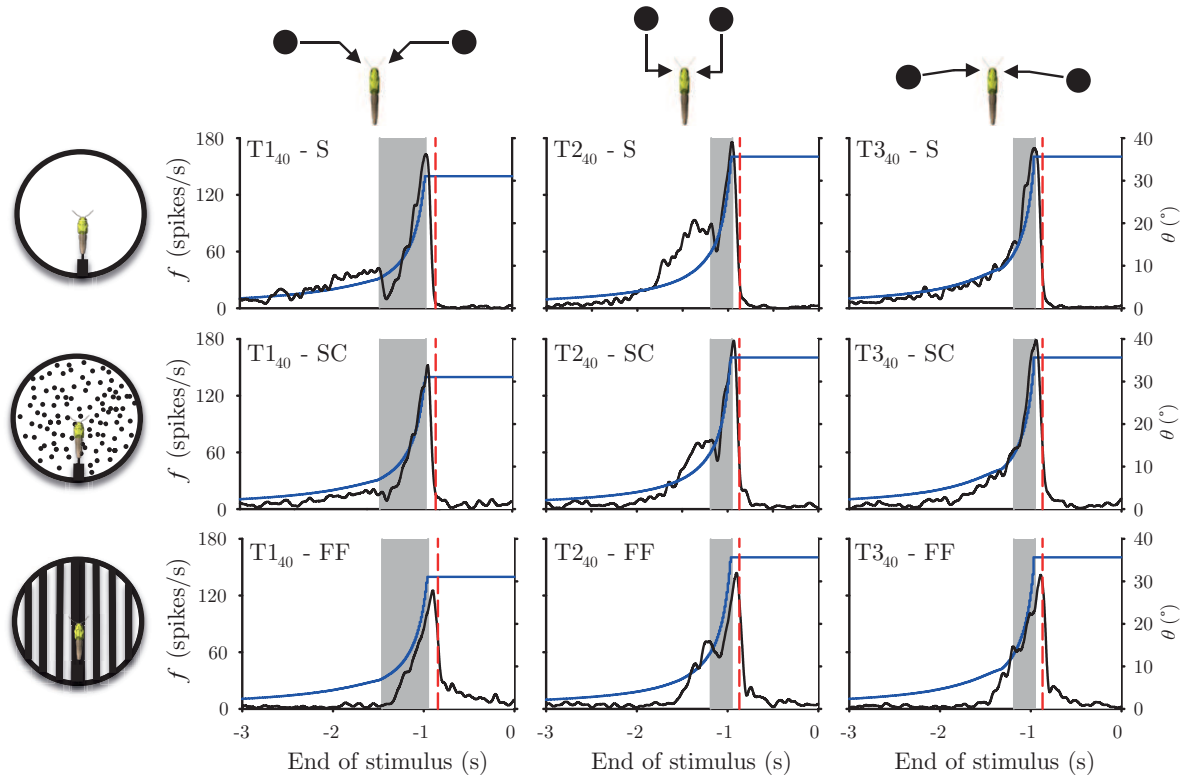


Figure 3.4: Example DCMD responses (pooled left and right) to three compound trajectory types (columns: *left*, T1; *middle*, T2; and *right*, T3) at an $l/|v| = 40$ ms presented in three visual backgrounds (rows: *top*, simple (S); *middle*, scattered (SC); and *bottom*, flow field (FF)). The grey shading in each panel represents the looming phase of the stimulus. The blue line in each panel represents the change in subtense angle, relative to the eye of the locust, over each frame and three seconds prior to the end of stimulus. The vertical red dotted line in each panel represents TOC. Each DCMD response was averaged from $n = 28$ recordings. With but a few exceptions (see RESULTS), transitions to looming caused a valley in the firing rate followed by a TOT-associated rise and peak firing around the time of collision. Irrespective of background, the most robust response was found for T2, when the non-looming component of the moving disc travelled in the opposite direction, the DCMD response to a transition was quite subtle (i.e. T1). In general, DCMD peak firing rates were diminished and delayed in the presence of either SC or FF. In addition, the rise and fall phases were greatly affected by background in all trajectories.

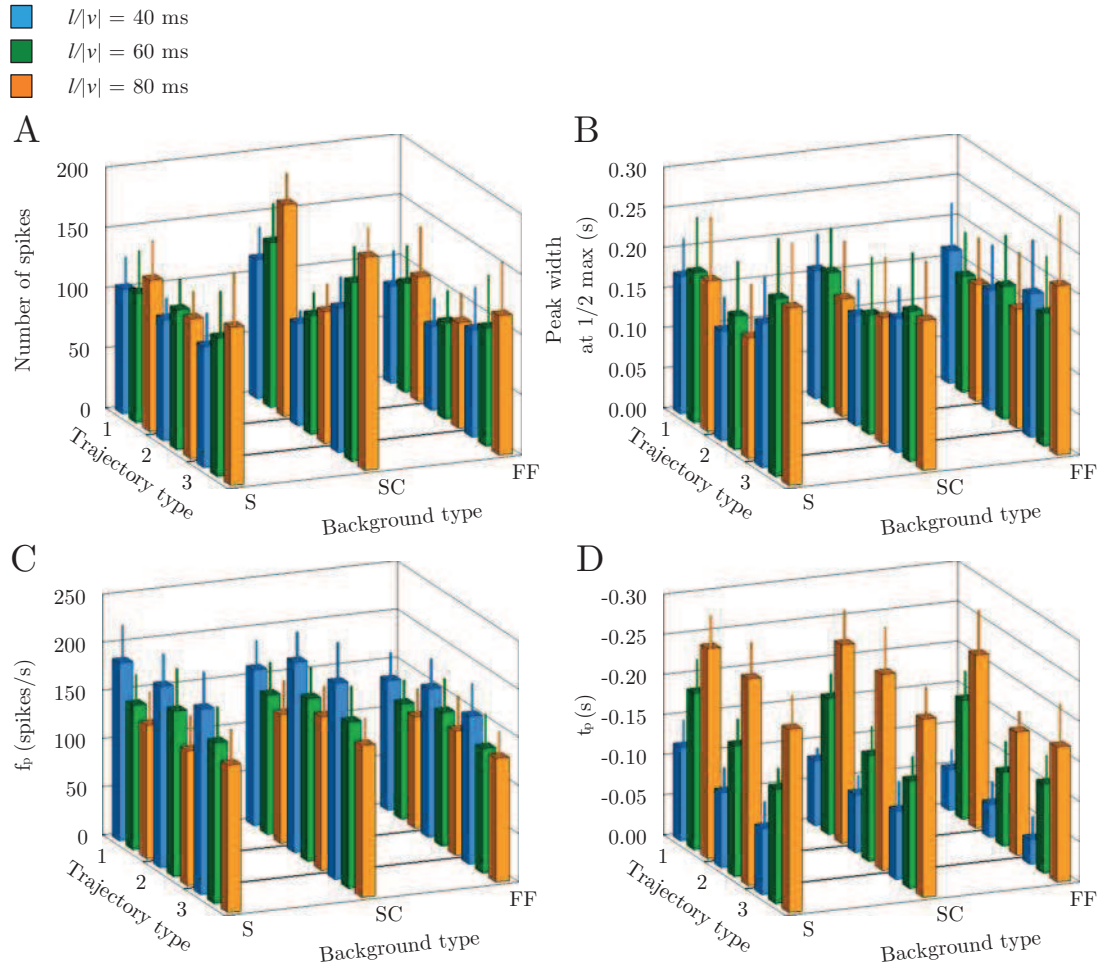


Figure 3.5: Associated peak response variables. A) Higher number of spikes were present in the SC and lower numbers in FF relative to S. Higher $l/|v|$ values also generated more spikes, as did T1 and T3. B) The peak width at half 1/2 max was generally unaffected by trajectory type, velocity, or background. C) Higher peak firing rates (f_p) were observed at lower $l/|v|$ values, in S, and in T2 and T3. D) Delays in the time of peak (t_p) were observed in FF, at higher $l/|v|$ values, and for T2 and T3. Each column represents the mean (+SD) for each response ($n = 28$ recordings) to one of 27 stimulus combinations (see METHODS)). The bars are colour coded based on the velocity of the 7 cm disc (blue ($l/|v| = 40$ ms), green ($l/|v| = 60$ ms), and orange ($l/|v| = 80$ ms)) and grouped based on trajectory type (1, 2 and 3) on the z-axis and background (S = simple, SC = scattered, and FF = flow field) on the x-axis. See Table 3.1 and Results for statistical comparisons.

affect the peak width at 1/2 max, we did find an interaction effect with trajectory, which is likely related to the strong effect of trajectory.

Generally, regardless of trajectory or background, lower $l/|v|$ values (higher velocities) evoked a higher f_p (40 ms > 60 ms > 80 ms, figure 3.5C). The type of background also affected f_p within each trajectory and velocity (S > SC > FF). Although there was not as great of an effect, trajectory type also influenced f_p (T2 and T3 > T1). Regardless of trajectory type FF resulted in the lowest f_p . The main effects of velocity and background appear to have caused the greatest change in f_p (Table 3.1).

For any given trajectory or background, higher $l/|v|$ values (lower velocities) evoked an earlier t_p (80 ms > 60 ms > 40 ms, figure 3.5D) and for any given trajectory or velocity, FF generated the latest t_p . We also found that trajectory had some effect on t_p occurring earlier for T1, relative to T2 and T3. The velocity of approach had the greatest effect on the time of t_p , although all main effects and their interactions influenced t_p (Table 3.1). In summary, we found that more spikes were produced in response to T1 and T3 relative to T2, at lower velocities, and for SC. Increasing stimulus velocity evoked a higher f_p and earlier t_p . Relative to S, the SC and FF backgrounds caused lower f_p and later t_p . In general, T2 and T3 evoked a higher f_p and earlier t_p relative to T1. With the exception of T1 generating a wider peak width at 1/2 max relative to T2 and T3, we found little other differences in peak width.

TOT-associated response parameters are affected by trajectory, velocity, and background

Different stimulus trajectories evoked clearly different f_{TOT} (T2 > T3 > T1, figure 3.6A) and higher $l/|v|$ values (lower velocities) evoked lower f_{TOT} (80 ms < 60 ms < 40 ms, figure 3.6A). Overall, background had a strong effect on f_{TOT} (FF < SC < S), although several recordings showed no TOT-associated response, specifically when the stimulus followed T1 within FF, and the data were quite variable (see error bars in figure 3.6A). Although there was an effect of velocity and significant interactions, the type of trajectory and background had the greatest effects on f_{TOT} (Table 3.1).

Trajectory (T1 < T2 and T3), velocity (80 ms < 60 ms < 40 ms), background (FF < SC < S), and their interactions affected f_v (figure 3.6B). Trajectory and velocity were the strongest main effects on f_v and their interaction yielded the strongest interaction effect (Table 3.1).

Different trajectories significantly affected f_{TOT-v} (T2 and T3 > T1, figure 3.6C). Although there was a significant effect of velocity, no clear trends were observed.

Table 3.1: Statistical comparison of measured variables for all TOC and TOT-associated DCMD responses. Trajectory type, velocity of object motion, and background type were the three major factors compared. Shaded cells indicate a non-significant effect and each cell contains the corresponding F statistic, with degrees of freedom and associated P value, generated by a three-way RM ANOVA (see METH-ODS).

Response variable	Trajectory	Velocity	Background	Trajectory \times Velocity	Trajectory \times Background	Velocity \times Background	Trajectory \times Velocity \times Background
No. of spikes	$F_{(2,54)} = 42.9$ $P < 0.001$	$F_{(1.4,40.4)} = 135.6$ $P < 0.001$	$F_{(2,54)} = 34.9$ $P < 0.001$	$F_{(4,108)} = 8.4$ $P < 0.001$	$F_{(2.8,77.7)} = 21.6$ $P < 0.001$	$F_{(4,108)} = 18.1$ $P < 0.001$	$F_{(8,216)} = 3.12$ $P < 0.001$
Peak width at 1/2 max	$F_{(2,54)} = 25.9$ $P < 0.001$	$F_{(1.4,39.3)} = 2.5$ $P = 0.106$	$F_{(2,54)} = 4.2$ $P = 0.02$	$F_{(4,108)} = 3.2$ $P = 0.02$	$F_{(4,108)} = 1.855$ $P = 0.124$	$F_{(4,108)} = 2.2$ $P = 0.076$	$F_{(8,216)} = 1.1$ $P = 0.407$
f_p	$F_{(1.6,42.3)} = 17.1$ $P < 0.001$	$F_{(1.6,44.4)} = 118.2$ $P < 0.001$	$F_{(2,54)} = 58.9$ $P < 0.001$	$F_{(4,108)} = 1.3$ $P = 0.244$	$F_{(4,108)} = 3.7$ $P = 0.006$	$F_{(4,108)} = 4.2$ $P = 0.003$	$F_{(8,216)} = 1.6$ $P = 0.124$
t_p	$F_{(2,54)} = 68.3$ $P < 0.001$	$F_{(2,54)} = 1361.1$ $P < 0.001$	$F_{(2,54)} = 175.1$ $P < 0.001$	$F_{(4,108)} = 7.1$ $P < 0.001$	$F_{(4,108)} = 7.1$ $P < 0.001$	$F_{(4,108)} = 4.6$ $P = 0.002$	$F_{(8,216)} = 3.3$ $P < 0.001$
f_{TOT}	$F_{(2,54)} = 125.6$ $P < 0.001$	$F_{(1.4,40.4)} = 14.6$ $P < 0.001$	$F_{(1.6,44.3)} = 24.6$ $P < 0.001$	$F_{(2.9,79.3)} = 2.9$ $P = 0.04$	$F_{(2.9,78.6)} = 4.1$ $P = 0.01$	$F_{(4,108)} = 0.4$ $P = 0.793$	$F_{(4.8,128.2)} = 2.1$ $P = 0.080$
f_v	$F_{(2,54)} = 426.5$ $P < 0.001$	$F_{(2,54)} = 205.2$ $P < 0.001$	$F_{(2,54)} = 113.4$ $P < 0.001$	$F_{(4,108)} = 94.4$ $P < 0.001$	$F_{(4,108)} = 63.9$ $P < 0.001$	$F_{(4,108)} = 29.9$ $P < 0.001$	$F_{(8,216)} = 17.3$ $P < 0.001$
f_{TOT-v}	$F_{(2,54)} = 113.6$ $P < 0.001$	$F_{(2,54)} = 25.5$ $P < 0.001$	$F_{(2,54)} = 0.3$ $P = 0.681$	$F_{(4,108)} = 9.3$ $P < 0.001$	$F_{(4,108)} = 36.1$ $P < 0.001$	$F_{(4,108)} = 10.4$ $P < 0.001$	$F_{(8,216)} = 9.4$ $P < 0.001$
t_v	$F_{(2,54)} = 873.3$ $P < 0.001$	$F_{(2,54)} = 4038.4$ $P < 0.001$	$F_{(2,54)} = 0.3$ $P = 0.696$	$F_{(4,108)} = 620.9$ $P < 0.001$	$F_{(4,108)} = 4.6$ $P = 0.002$	$F_{(4,108)} = 4.2$ $P = 0.003$	$F_{(8,216)} = 1.1$ $P = 0.341$
δ	$F_{(2,54)} = 41.6$ $P < 0.001$	$F_{(2,54)} = 0.4$ $P = 0.662$	$F_{(2,54)} = 2.1$ $P = 0.133$	$F_{(4,108)} = 8.7$ $P < 0.001$	$F_{(4,108)} = 2.1$ $P = 0.087$	$F_{(4,108)} = 4.3$ $P = 0.003$	$F_{(8,216)} = 2.3$ $P = 0.03$
TOT peak rise phase	$F_{(2,54)} = 133.3$ $P < 0.001$	$F_{(2,54)} = 452.6$ $P < 0.001$	$F_{(2,54)} = 439.6$ $P < 0.001$	$F_{(4,108)} = 72.5$ $P < 0.001$	$F_{(4,108)} = 135.3$ $P < 0.001$	$F_{(4,108)} = 48.7$ $P < 0.001$	$F_{(8,216)} = 54.1$ $P < 0.001$
TOT peak fall phase	$F_{(2,54)} = 27.9$ $P < 0.001$	$F_{(2,54)} = 1.4$ $P = 0.250$	$F_{(2,54)} = 95.1$ $P < 0.001$	$F_{(4,108)} = 9.9$ $P < 0.001$	$F_{(2.9,77.8)} = 42.1$ $P < 0.001$	$F_{(2.9,80.2)} = 3.5$ $P = 0.019$	$F_{(8,216)} = 2.9$ $P = 0.004$
TOC peak rise phase	$F_{(1.5,39.8)} = 838.3$ $P < 0.001$	$F_{(2,54)} = 2561.2$ $P < 0.001$	$F_{(2,54)} = 70.5$ $P < 0.001$	$F_{(4,108)} = 179.9$ $P < 0.001$	$F_{(4,108)} = 3.5$ $P = 0.01$	$F_{(4,108)} = 9.2$ $P < 0.001$	$F_{(5.7,154.9)} = 2.8$ $P = 0.02$
TOC peak fall phase	$F_{(1.6,43.2)} = 37.8$ $P < 0.001$	$F_{(2,54)} = 5.7$ $P = 0.006$	$F_{(2,54)} = 438.9$ $P < 0.001$	$F_{(4,108)} = 4.7$ $P < 0.001$	$F_{(4,108)} = 34.3$ $P < 0.001$	$F_{(4,108)} = 2.3$ $P = 0.066$	$F_{(8,216)} = 5.1$ $P < 0.001$

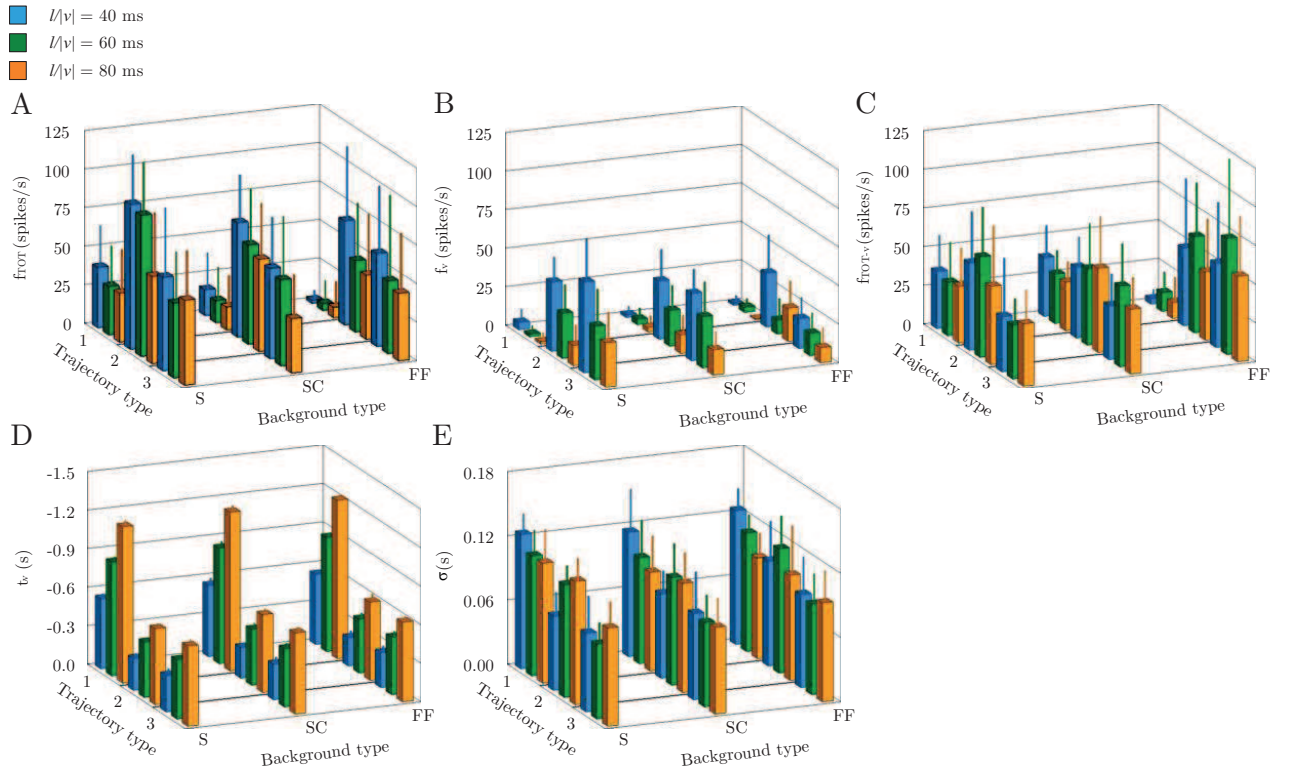


Figure 3.6: TOT-associated peak and valley response variables. The firing rate at TOT (f_{TOT}) (A) and at the valley (f_v) (B) were higher for lower $l/|v|$ values, in S, and for T2 and T3. C) The change in firing rate from TOT to valley (f_{TOT-v}) was unaffected by background type, although the smallest change was observed for T1 FF. Although individually significant differences were found, no trend was observed for the effect of trajectory type or velocity. D) The time of valley (t_v) was clearly related to when the disc transitioned to looming in each trajectory; higher $l/|v|$ values and T1 had earlier times. E) Although variation existed between the different trajectories (particularly for T1), the response time (δ) was relatively invariant of background and velocity. Similar labeling and colouring scheme as in Fig. 3.5.

We found very similar $f_{\text{TOT}-v}$ for different backgrounds ($S = 43 \pm 27$, $SC = 42 \pm 21$, and $FF = 44 \pm 32$ spikes/s), although T1 in FF showed very little change, likely contributing to this result as T2 and T3 in FF had the highest $f_{\text{TOT}-v}$. All interactions affected $f_{\text{TOT}-v}$ with the interaction between trajectory and background resulting in the greatest effect. Overall, it was the type of trajectory that resulted in the greatest differences in $f_{\text{TOT}-v}$ (Table 3.1).

Regardless of velocity or background, T1 evoked an earlier t_v than T2 and T3 (figure 3.6D). Higher $l/|v|$ values (lower velocities) also evoked earlier t_v ($80 \text{ ms} > 60 \text{ ms} > 40 \text{ ms}$). Velocity and trajectory had the greatest effect on t_v followed by the interaction between trajectory and velocity (Table 3.1).

We found that δ was only affected by trajectory ($T1 > T2 > T3$, figure 3.6E). However, we also found significant interactions between velocity and background, trajectory and velocity and a three way interaction (Table 3.1). For stimuli that followed T1, the highest velocity ($l/|v| = 40 \text{ ms}$) generated the longest δ relative to T2 and T3, where as for T2 and T3, the longest δ was at an $l/|v| = 60 \text{ ms}$. Moreover, in T1 only, lower velocities caused shorter δ . Thus, although we did find significant interaction effects, trajectory type appears to be the greatest determining factor in affecting δ (Table 3.1).

In summary, we found that T2 and T3 generated a higher f_{TOT} , f_v , and $f_{\text{TOT}-v}$ relative to T1. The t_v also occurred later in T2 and T3 relative to T1 and the δ was longest in T1, followed by T2 and then T3. Lower velocities evoked lower f_{TOT} and f_v amplitudes and earlier t_v in all trajectories. Background only affected f_{TOT} and f_v with S and FF resulting in the highest and lowest amplitudes, respectively.

TOT- and TOC-associated DCMD peak rise and fall phases depend on the trajectory and velocity of object approach and type of background

Trajectory type significantly affected TOT peak rise phase ($T1 > T3 > T2$, except for FF, figure 3.7A) and fall phase ($T1 > T2 > T3$ in S and SC, Fig. 3.7B). Generally, faster object velocities resulted in shorter TOT peak rise phases (particularly for T1 and T3, S and SC), but did not affect the fall phases. FF resulted in shorter TOT peak rise and fall phases regardless of trajectory or velocity. Although the type of background and velocity of object motion had the greatest effect on the rise phase of the TOT peak, all interactions showed an effect (Table 3.1). For the TOT fall phase, the type of background had the greatest effect followed by the type of trajectory and

interaction between the trajectory and background (Table 3.1).

Regardless of background or velocity, T1 evoked a much longer TOC peak rise phase than T2 and T3 and slightly longer TOC peak fall phase relative to T2 and T3 in FF (figure 3.7C, D). Within each trajectory and background, higher $l/|v|$ values caused longer TOC peak rise phases (80 ms > 60 ms > 40 ms). Regardless of trajectory or velocity, background affected both the TOC peak rise phase (FF > SC > S) and TOC peak fall phase (FF > SC > S). Whereas velocity and trajectory most strongly affected the TOC rise phase, the strongest effect on TOC fall phase was background type (Table 3.1).

In summary, changes in trajectory, velocity, and background strongly affected TOT- and TOC-associated peak rise and fall times. T1 typically had the longest TOT and TOC peak rise and fall phases of all three trajectories. While T2 and T3 shared similar TOC peak rise and fall phases, T2 resulted in shorter TOT peak rise phases and longer TOT peak fall phases. Slower stimulus velocities caused longer TOT and TOC peak rise phases and shorter TOC fall phases. In general, S caused the longest TOT peak rise phase and shortest TOC fall phase, while FF caused the shortest TOT peak rise phase and longest TOC fall phase; SC evoked intermediate values.

Expansion properties at the time of transition predict changes in the DCMD firing rate

Transitions to looming causes a decrease in firing rate (i.e. $f' < 1$) that is correlated to unique expansion properties of the stimulus ([38, 119]). During a transition to looming, there is an increase in subtense angle velocity (ϑ') and decrease in leading edge velocity (ψ') (figure 3.8A). This decrease in ψ' (which is related to where the transition occurs in 3-dimensional space and speed of approach) ([38, 119]) is responsible for the observed TOT response. However, DCMD responses to approaching objects are better matched to changes in angular acceleration of the image rather than velocity ([119, 151]). To confirm that a decrease in f' is correlated to a positive change in the acceleration of the subtense angle (ϑ'') and a negative change in the acceleration of the leading edge (ψ''), data were pooled from ([119]) and ([38]) and those presented here. Data failed to converge when we attempted to fit our data set to predetermined constraints from the previous model (i.e. ([38, 119])), and thus the data did not satisfy tolerances of the 2D Gaussian model. Given that this current data set only included transitions to looming and the original model included values from transition to and away from looming,

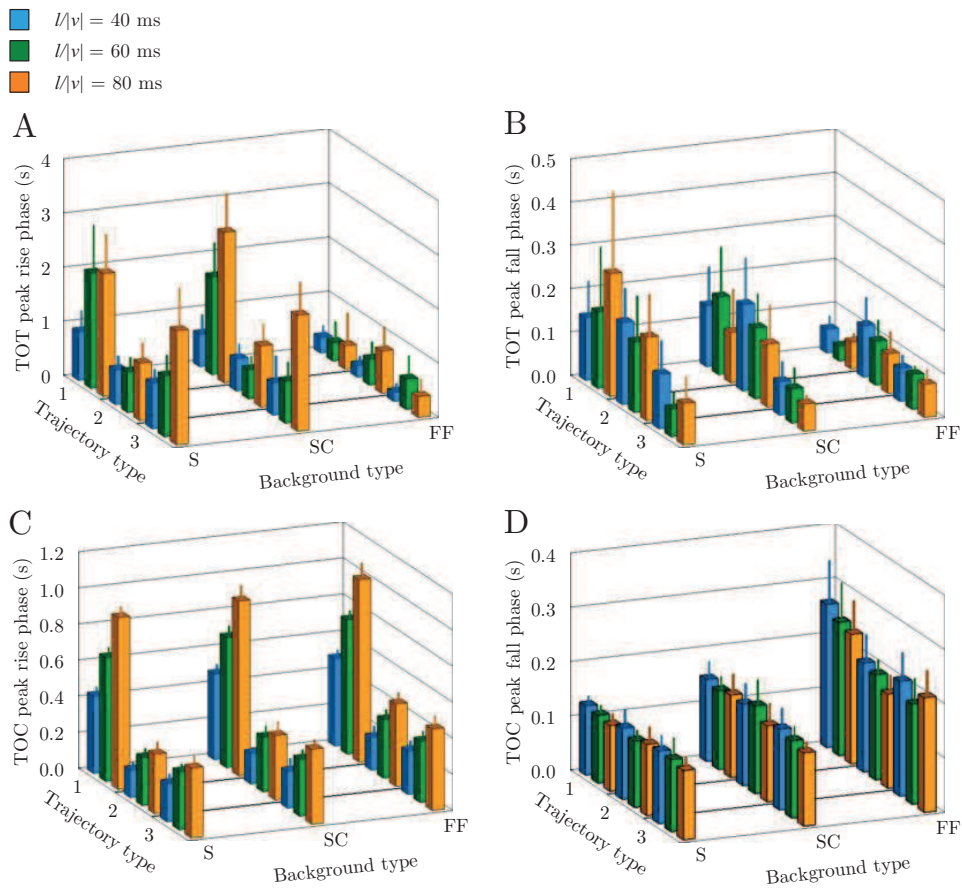


Figure 3.7: Rise and fall phases of the TOT and TOC-associated peak firing rates. A) Longer TOT peak rise phases were observed in T1 and for higher $l/|v|$ values, while the FF caused significantly shorter TOT rise phases. B) The FF also caused shorter TOT fall phases, as did T3. C) The TOC peak rise phase was longest in T1 and for higher $l/|v|$ values. D) The FF and SC resulted in significantly longer TOC peak fall phases, while the trajectory and velocity had little effect. Similar labeling and colouring scheme as in Fig. 3.5.

there could be a weighted effect of data points falling below a $f' = 1$. Subsequent fitting of an unconstrained 2D Gaussian model resulted in a good fit to the pooled data ($r^2 = 0.75$, Equation 3.1, figure 3.8B):

$$f' = 3.0e^{-0.5 \left[\left(\frac{\theta'' + 6.6}{-32.3} \right)^2 + \left(\frac{\psi'' + 157.7}{136.1} \right)^2 \right]} \quad (3.1)$$

While the mean normalized f' evoked by S (0.31 0.18), SC (0.27 0.16), and FF (0.27 0.17) backgrounds were relatively invariant for each background, we wanted to determine if there was an effect of background using the new constraints established in equation 3.1. When isolating the data based on background but using previous data we found that all backgrounds had similar r^2 values (S = 0.77, SC = 0.75, FF = 0.73), suggesting that background type does not have an effect on f' at TOT for the same values of ϑ'' and ψ'' . Although f' changed according to unique stimulus parameters (velocity, angle of transition, and also stimulus background), the response time (δ) was relatively invariant and weakly fit a 2D Gaussian model using the same stimulus parameters (ϑ'' and ψ'') with an $r^2 = 0.24$ (Equation 3.2, figure 3.8C):

$$f' = 0.1e^{-0.5 \left[\left(\frac{\theta'' + 4.0}{43.2} \right)^2 + \left(\frac{\psi'' - 378.1}{728.7} \right)^2 \right]} \quad (3.2)$$

With the addition of background complexity, unique stimulus trajectories and velocities to previous data, we confirm that at TOT an increase in ϑ'' and decrease in ψ'' correlates to a decrease in f' . The relative changes in ϑ'' and ψ'' are related to the point of transition in 3- dimensional space ([119]) and velocity of approach ([38]) but, as our results suggest, not background complexity. Consistent with previous work, we also confirm that δ remains relatively invariant regardless of stimulus complexity and is only weakly correlated to changes in ϑ'' and ψ'' (however, see above regarding the effect of trajectory on δ).

3.4 Discussion

We show that the type of visual background influences DCMD responses to different object motion. We characterize typical TOT-associated drops in firing rate and subsequent rises to peak firing prior to TOC that are affected by the object's velocity, trajectory, and type of presentation background. Irrespective of trajectory or background, increasing stimulus velocity generally evoked higher spike numbers, larger peak firing rates, later peak firing and longer TOT- and TOC-associated peak rise

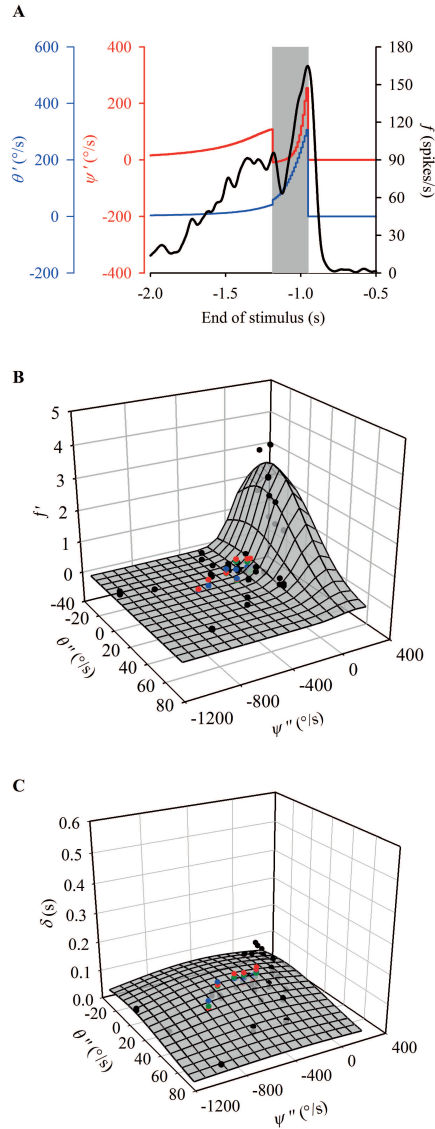


Figure 3.8: Correlation of DCMD firing modulation with selected expansion parameters of a disc during a transition to looming. A) An example illustrating the relationship between a decrease in subtense angular velocity (ϑ' , blue line), increase in rotational velocity of the leading edge of the disc (ψ' , red line) and resulting drop in DCMD firing rate (f , black line) at the time of transition; sample data represents a 7-cm disc travelling along Trajectory 2 at an $l/|v| = 40$ ms within a simple background (see Fig. 3.2). The grey shaded area indicates when the disc is on a looming trajectory; the first transition from white to grey represents TOT and the second transition represents when object motion stops. B) 3-dimensional scatter plot representing simple (blue), scattered (green), and flow field (red) data plotted with previous data (black; [119] and [38]) and fit to a 2D Gaussian equation (mesh plot). Data represent the mean firing rate change (f') in response to a transition plotted against the subtense angular acceleration (ϑ'') and the rotational acceleration of the leading edge (ψ''); data fit with an $r^2 = 0.75$. C) Correlation of mean response time (δ) to ϑ'' and ψ'' ; data weakly fit to a Gaussian equation with an $r^2 = 0.24$ (mesh plot).

phases. Although each trajectory was unique, T2 and T3 shared identical looming components, which accounts for similarities in some response parameters. Overall, the type of trajectory had a large, and varying, impact on both TOT and TOC-associated responses. More complex backgrounds delayed peak firing, evoked lower peak firing rates and generated shorter TOT-associated peak rise phases and longer TOC-associated peak fall phases. The strong correlation between relative increases in ϑ , decreases in ψ , and decreases in f' at TOT (figure 3.8) was invariant to background types. Moreover, δ remained relatively invariant to all stimulus parameters. Although we attribute no biophysical mechanism by which this process operates, our data support the hypothesis that the LGMD/DCMD pathway is capable of conveying information regarding unique expansion properties of a moving object ([38, 119]) regardless of background complexity.

Although our stimuli and background environments were relatively slow when considering the natural flight speed of *Locusta migratoria* or predatory bird attacks ([168]), they were designed to increase the level of visual complexity compared to our previous studies ([38, 119]) and to coincide with background velocities used in a developing computational ([180]) and real world robot ([180]) model of object motion detection. Additionally, although the LGMG/DCMD pathway responds preferentially to monocularly presented small objects ([62, 151]), we simultaneously presented all compound stimuli bilaterally, a situation which locusts could conceivably encounter in a swarm or during flight ([62]). However, contralateral DCMD stimulation may affect ipsilateral responses; an affect which may originate from the optic lobe or within the thoracic ganglia ([62]). Thus, each DCMD may have produced a different response if presented with unilateral stimuli. Given the relatively small area of stereoscopic overlap in locusts ([163]), in the case of the compound trajectories, the discs would have moved out of the contralateral eye's field of view before affecting ipsilateral DCMD responses, with any overlap early on (such as in T2, figure 3.3) only marginally affecting the responses. However, in the case of our frontal looming presentation, object expansion would spread equally across each eye. [78], who recorded the activity from each DCMD simultaneously, also reported relatively low peak firing rates to head-on looms but attributed the weaker response to relatively low ommitidial density in the anterior portion of the eye.

Based on comparisons with previous work (i.e. [119] and [38]), we found no qualitative evidence to suggest that simultaneous bilateral stimulation greatly affects unilateral and contralateral responses. For example, the looming component of our T2 (a lateral loom) generated comparable TOC-associated peak firing rates as did the 40 ms

lateral loom used in [38]. Moreover, our intention was not to compare the effect of one side of the pathway on the other but to test more complex stimuli based on previously used types of stimuli within the working confines of a robot model. Our progressive FF pattern reliably suppressed DCMD responses (see also [72]) regardless of recording side, our compound and frontal looming stimuli generated DCMD responses that are similar to those previously described. We did not compare the putative effect of switching backgrounds that, in the case of the FF, would occur as the animal begins moving forward. However, [155] found no response to the start of motion of their drifting grating stimuli. Moreover, we were primarily concerned with comparing differences between the same type of object motion within a different background and not direct comparisons of the backgrounds themselves (although we anecdotally noted more spiking in the SC background). We also did not provide any feedback from the locust, which may have altered the perceived approach of the object (or motion of the background, such as a turn).

Whereas previous studies have tested the locust LGMD/DCMD pathway to compound approaches [119] varying in velocity [38], looming approaches combined with optic flow [71, 151], other moving periodic patterns [63, 132, 140], or examined steering torques using pseudo-swarm and progressive flow field stimuli [143], this study is unique in a few ways. First, we used bilaterally presented stimuli and recorded from both ventral nerve cords (isolated right and left DCMD axonal responses), which allowed us to test the effect of simultaneous DCMD stimulation spiking between opposite sides: a situation that a locust may experience while flying in a swarm. Second, during forward motion, a more realistic flow field would have motion parallax with translating motion in a single, predictable direction, and stationary objects expanding at different rates and directions [226]. Our compound approach trajectories traveled at different velocities and were presented in multiple background environments, including a progressive flow field. Finally, we had the advantage of presenting in virtual 3-dimensional space, encompassing a large area of the visual field (270°). [143] presented simulated gratings and spotted patterns to the longitudinal body axis of *Schistocerca gregaria*, yet their stimuli did not cover the entire visual field. [151] used moving gratings presented laterally to a single eye and [71] used a background flow that consisted of constantly expanding concentric rectangles presented 2-dimensionally and perpendicular to a single eye. Our stimuli further represented motion in depth that simulated translational gaze shift and rotational gaze shift [46].

Although typical LSN responses show little to no activity within optic flow, they remain sensitive to objects that approach the eye ([71, 72, 151, 197, 225]). However,

the responses are generally suppressed [63, 71, 72, 151]. Figure 3.5 A illustrates that relatively fewer spikes are generated in response to FF, which has been shown to be related to the velocity of a flow field [151]. While some studies have indicated that flow fields have little effect on time of peak firing [151], other findings and ours reported here, showed a slight delay in peak firing time [71, 225]. In the FF background, longer lasting feed-forward inhibition would delay the build up of excitation, thus delaying peak firing. We also found a significantly shorter TOT-associated peak rise phase and longer TOC-associated fall phase in the presence of a flow field (figure 3.7 A and D). Without the presence of a background, feed-forward inhibition terminates the DCMD response to object approach [149] by controlling excitation [72]. Although [151] did not measure DCMD peak firing rise and fall phases, their Figure 8A is consistent with our results, where the rise phase is shorter in the presence of a flow field. However, their fall phase is not longer. In addition, [71] also found a shorter rise phase, although the fall phase seemed unaffected. This result, however, is likely related to differences in our visual background stimuli, since our FF covered a larger field of view. Several studies have shown that higher velocity looming stimuli result in fewer spikes, and narrower, larger amplitude peak firing rates that occur later [38, 68, 70, 77, 78, 80, 117, 149, 156], which is consistent with our findings in all backgrounds.

Activation and termination of the DCMD response is strongly affected by the kinematics of the stimuli. For example, higher $l/|v|$ values (slower velocities) may cause a longer and weaker activation of excitation that is overcome earlier by feed-forward inhibition [72], since the edges of the approaching object are increasing more slowly. Indeed, we found that higher $l/|v|$ stimuli resulted in longer rise phases (TOT and TOC) and shorter TOC peak fall phases (figure 3.7). Differences in the trajectory leading up to a transition also affected some TOT and TOC response parameters. For example, T2 was the shortest trajectory and thus had the fewest spikes. T2 also contained the greatest change in angle of transition, which occurred closer to the animal and from the anterior, thus generating the highest level of excitation and the largest drop in firing rate (i.e. f_v); this result may be related to the relative optical density across [107] the retina in addition to the relative differences in object expansion at TOT. Consistent with [38] who reported little difference between their f_{TOT} and f_v for any angle or $l/|v|$ they tested (see their figure 3.7), we found similar results with the exception of the FF background, which generated the largest f_{TOT-v} (except for T1).

Optic flow direction is known to affect LSN responses in pigeons; when flow and direction of object motion are opposite, no looming response is detected [225]. In

our study, the non-looming, translational component of the compound trajectories originated from different locations around the locust and the presence of FF decreased DCMD responses to the translational component in all trajectories. However, the reduction was much more pronounced in the trajectories where object motion traveled opposite to the flow field (overall, T2 generated the highest f_{TOT}). Moreover, the looming component of all compound trajectories traveled in a different direction of FF and all peak firing rates were substantially reduced. In fact the most robust translational response was from T2 (figure 3.4), where translational motion was in the same direction as FF.

The different rates of object expansion (i.e. relative and values) at TOT for each trajectory affected the relative timing and amplitude of DCMD responses. Although δ was relatively variable among all animals and stimuli, they are consistent and within the range of δ in previous studies using different compound trajectories, object sizes, and object velocities [38, 119].

The LGMD/DCMD pathway responds to more than simple looming objects/shapes: directionality [119, 138], near-miss trajectories [38, 78, 96, 119], compound shapes [80], proximity and direction of non-looming, translatory trajectories, and changes to and from a direct collision course [119], and different stimulus velocities during a transition to looming [38]. Locusts, particularly in flight and in a swarm, are not likely to only encounter simple objects that move in a predictable direction and whose edges expand uniformly across the retina. Moreover, locusts generate collision avoidance behaviours in response to objects that approach along non-looming trajectories [162] and thus an object does not need to approach on a direct collision course to be important in collision detection. Although our backgrounds do not replicate all aspects of complex natural motion within a swarm, DCMD responses within our SC and FF backgrounds still provide valuable insights into how it may encode aspects of an emulated swarm or during forward flight. We found that the DCMD was still remarkably responsive to object motion (both to transitions and to a loom) within SC and FF, even though the LGMD receives wide field inhibition [132] and habituates to stimuli repeatedly presented in the same area of the retina [77, 84, 134]. However, the DCMD is not suppressed during walking [163], which would produce a progressive flow field and is only strongly suppressed during a saccade in the optomotor response [236]. The optic flow generated from rotation (such as a saccade) and translation (such as objects moving in the context of a single reference point, i.e. the moving animal) is quite different. The LGMD is inhibited if the entire field of view shifts at once, such is the case in a rotational gaze shift which would cause all objects to appear to move at the same

angular velocity, whereas during straight flight, objects in the flight path would expand at different rates [105]. Since the LGMD/DCMD response is related to a balance between excitation and lateral inhibition [63], during forward flight with translational optic flow, the DCMD may remain sensitive since the objects in the flight path have varying expansion rates, thus the spread of excitation is faster than the corresponding inhibition. Indeed, the DCMD response to a moving object is suppressed with an increase in temporal frequency of periodic vertical bars [63, 155]. The LGMD remains responsive to new movements since recovery from habituation is not only rapid, but it is localized to the area on the retina that was repetitively stimulated [132]. Thus, an habituated DCMD is still responsive to the approach of the same object on a different approach trajectory (i.e. different part of the visual field) or a larger object on the same trajectory [77]. This would explain how the DCMD was still able to respond to trajectory changes within the complex backgrounds and generate a relatively large peak firing rate. Interestingly, although we found a lower f_p in the SC relative to the S background, there were higher overall spike numbers. Perhaps the lower f_p within SC is simply related to a reduced number of stimulated ommatidia, since part of the visual field would expectedly be shadowed by the moving dots. Meanwhile, the moving dots in other parts of the visual field would be stimulating corresponding ommatidia in that particular region, leading to a higher spike number over a wider time window.

Considering edge expansion alone may explain why we observed lower f_p in both complex backgrounds. Thus, with similar contrasts, when a looming object exceeds the size of moving objects around it (in this case, the subtense angle of the dots in SC ($\sim 5^\circ$) or bars in FF ($\sim 12^\circ$)) we should observe a DCMD response. Indeed, relative to S and SC where the TOT- associated rise phase of the DCMD response begins before the 7 cm disc subtends either 5° or 12° (figure 3.4), the FF background resulted in a much later TOT-associated rise phase that began closer to 12° . The lateral inhibition network presumably prevents fatigue of individual small- field elements [63], thus during the SC background, more spikes were produced and the DCMD was still able to respond robustly to the moving visual stimuli while in the FF background, fewer spikes were produced due to relatively larger cover area of the bars. Summation of responses to multiple looming stimuli are sublinear [80] and controlled by postsynaptic mechanisms, such as the absolute refractory period within the LGMD spike initiating zone (see [80]), that compensate for the afferent inputs onto the LGMD [106]. Regardless of the background we used, the type of trajectory, and thus the motion of the disc and not the background, had the largest main effect on DCMD response parameters, significantly affecting all 13 measured variables (Table 3.1 and figs 4, 5, and 6). Thus,

one of our major findings is that while DCMD responses are sensitive to background complexity, they are more sensitive to object motion complexity, i.e. trajectory changes and velocity.

We found that DCMD responses within FF had a delay in peak firing. As suggested regarding pigeons [225], locusts would benefit from a timing delay since in flight they need to react faster to avoid a predator. Moreover, while in flight (emulated, in part, by our FF) and potentially surrounded by conspecifics (emulated, in part, by our SC), locusts would have difficulty isolating approaching visual stimuli and may respond later to ensure that the predator is on a collision course and that the animal does not continually perform emergency avoidance responses to conspecifics. However, the DCMD may also assist in subtle course deviations while in swarming flight, which may be related to the relatively lower firing rates in the presence of FF compared to S. Yet the importance of peak firing remains unclear, since it often occurs after the initiation of behavioural responses during flight [24, 78, 117, 120] and before looming-evoked jumps [82]. The DCMD response leading up to the peak is likely quite important and has been related to phases in an avoidance jump [58, 155, 167]. However, if this was the case for avoidance responses during flight, our observed short rise phase within the FF relative to S also suggests that locusts would still need to respond more rapidly to an approaching predator while flying.

We show how responses of a single neuron are modulated by approach velocity, trajectory, and background type. Since relative object motion can represent different visual stimuli, the rapid detection and performance of appropriate responses are paramount. Many animal groups use different aspects of the same sensory stimuli to extract behaviourally relevant information, such as velocity, contrast, texture, and more [101]. For example, flies use flow field motion to provide cues regarding self motion, discriminate objects from background and estimate the relative distance of objects [199]. Nevertheless, it is likely that several LSNs in the locust's visual system (e.g. LDCMD [79]) are also involved in detecting salient stimuli and responsible for producing appropriate avoidance responses. In fact, in studies where the DCMD neuron has been ablated, animals are still capable of performing avoidance responses [82, 167].

Chapter 4

LGMD model development and responses to complex object motion in increasing complex backgrounds

In this chapter, we explore the way the type of visual background influences LGMD/DCMD model responses to different object motion.

On Chapter 3, the proposed approach used additional stimulation protocols, which were able to independently manipulate different motion parameters (e.g. angular size, speed, trajectory changes and background complexities). These experiments provided new data on more realistic, dynamic environments, which could be seen as a first step to build a more flexible model able to deal with more realistic visual environments.

A new insect-based model is here proposed, emphasizing the different processing layers that build up the hierarchical locust visual system. This model will try to achieve similar results to the ones obtained in biology, by proving its robustness when subjected to complex environments. For that, the conclusions achieved with the biological results from the previous chapter will be included in the model.

4.1 Introduction

Nowadays, unmanned vehicles, as mobile robots, offer great perspective in a high range of different applications, as industrial, search and rescue, surveillance, agricultural automation, among others [171]. In all the potential applications cited, navigation involves a range of common problems, being collision avoidance the most universally needed [88]. In fact, collision avoidance still remains a focus of active research in the

autonomous navigation research field [13, 50, 61, 238]. For an autonomous vehicle to operate properly in an uncontrolled environment, safety must be ensured under a broad range of conditions. Reliably recognizing objects approaching on a collision course is extremely important, which becomes a more difficult task when the presence of dynamic environments.

Concerning the perception of the surrounding, information can be provided by active and passive sensors. Active sensors, as laser, sonar, infra-red, have significant drawbacks as their need to send energy into the environment, their vulnerability to be interfered by other radiation sources as well as the complicated analysis required to extract salient information. On the other hand, passive sensors, as cameras, do not need to send energy into the environment, have low electrical power requirements, have a smaller size and, typically, are less costly [177, 238]. However, real-time collision detection in dynamic scenarios is a hard task if the algorithms used are based on conventional techniques of computer vision, based on a sequence of pre-processing, segmentation, object extraction, and pattern recognition of each captured frame, since these are computationally complex and, consequently, time-consuming techniques [88, 238]. On the other hand, bio-inspired visual sensors are suitable candidates for mobile robot navigation in unknown environments, since biological systems are highly efficient, reliable and refined. Distinct animals, as mammals, birds or even insects, have been pressured by natural selection to obtain very complex behaviors while using simple, local motion control rules [59].

In fact, research performed at the robotic navigation field has been finding much inspiration from biological systems, with a particular focus in insects. Insects are a perfect example of complex behaviors allied with a relatively simple nervous system, making them very attractive as sources of inspiration. As previously mentioned on chapter 2 and 3, locusts have been seen as an important animal model by researchers seeking to comprehend collision-avoidance neural responses. The neural structure that responds vigorously to a looming object, the LGMD neuron, has been the basis of the development of different models (chapter 2, table 2.2).

While extensive research efforts have been focused on understanding and modeling the response of the LGMD neuron to simple visual stimuli [68, 96, 151, 156], little attention has been given to comprehend the way this control system behaves when inserted in more dynamic and realistic visual scenarios, as would happen in real world situations. Experiments described on chapter 3 provided additional LGMD data on more realistic environmental conditions. Given the presence of continuous background movements, the fundamental task of detecting object's approaching motion within a

scene becomes a significant computational problem. Thus, the way that colliding objects are filtered out by the neural structure is still not well understood. In fact, one of the central questions that neuroscience tries to explain is how particular computations, or tasks, are implemented by neural networks to generate a specific output: are translation components filtered out by directionally selective neurons? How is this filtering process achieved? Does it adapt to different types of translation movements?

The combination of several feature selective neurons may be in the basis of a robust collision detection system, as the one found at the locust visual system, for example. In fact, it is believed that different specialized visual neurons act together to extract and fuse distinct cues from dynamic scenes. Besides looming detecting neurons, as the LGMD neuron, directionally selective neurons constitute a type of visual neurons specialized in the response to certain direction motion cues (up, down, left and right movement), which have been found in different animals, including both vertebrates and insects [56, 135].

In order to find out how this directional selectivity is achieved at the neural level, in a first stage it has been demonstrated that spatial asymmetries have important roles in creating basis building blocks of neural processing [11]. Particularly, in [65], it was found that asymmetric inhibition is on the basis of the direction selectivity verified in the rabbit's retina ganglion cells. Additional research has demonstrated that inhibition is stronger for movements that happen in a particular direction, being itself directionally selective [227]. Physically, this asymmetry could be implemented at the structural level, in the wiring of the direction-selectivity circuitry, or could result from unequal synaptic strengths in an otherwise structurally symmetric circuit. In order to unveil the asymmetric origin, [21] work enabled to conclude that a structural asymmetry between neurons contributes to the direction selectivity. In fact, the suppression of non-approaching stimuli responses only occurs if asymmetric inhibition acts sufficiently fast to cancel out excitation [124]. However, the way that looming neurons act together with directional selective neurons to extract relevant information, remains a subject of speculation.

Seen as a research tool, modelling may provide chances to explore possible mechanisms of information processing at and between motion sensitive neurons, belonging to the locust visual system.

According to literature, a possible technical use of a model is, in fact, understanding a physical system by using knowledge of its inputs and outputs in order to infer about the system characteristics. In the present work, the physical system being modeled is the entire LGMD neural structure, by using information about the visual stimuli

characteristics (input) and the neural response (output). The proper connectivity between model's neurons is essential for the implementation of the algorithms used in the neural computations that lead to the detection of approaching obstacles when in the presence or absence of other types of movement. So, by using a modeling strategy, we expect to understand how information is processed at the different layers of the locust optic lobe, by exploring several possible organizations of the directional selective neurons in order to produce the responses obtained in biology. These could also be used as a robust collision detection system for robotic applications

The model is expected to respond to imminent collisions in dynamic scenes, but not to respond to objects performing translational movements.

4.2 Methods and Materials

At insect level, it is known that the interneurons that process visual information are arranged in a serie of neuropiles, distributed beneath the compound eye, making up the optic lobe [185]. The visual information flows within and through different layers in the optic lobe, either sequentially (forward or feedforward) or laterally (through lateral connections). Based on that and similarly to previous studies [228, 230, 232, 234], in this work an innovative model is proposed as an artificial neural network. This model merges principles of direction-selective and approach sensitive neurons. Four types of direction-selective neurons, including left, right, up and down, were included in the model. Asymmetrical lateral inhibition yields the directional selectivity of these four neuron types. For example, the right selective neuron spreads lateral inhibition to the neighbor neurons located on its right direction, being sensitive to all movement directions excluding the inhibited right direction.

The model here proposed is insect based and, consequently, includes several processing steps performed at the different layers of the insect visual system. It is composed by seven different groups of neurons: Photoreceptor neurons (P layer), Lamina neurons (L layer), Medulla neurons (M layer, witch includes the four direction-selective neurons) and by one single neuron: the LGMD neuron.

Simulations were performed on a set of computer generated stimuli.

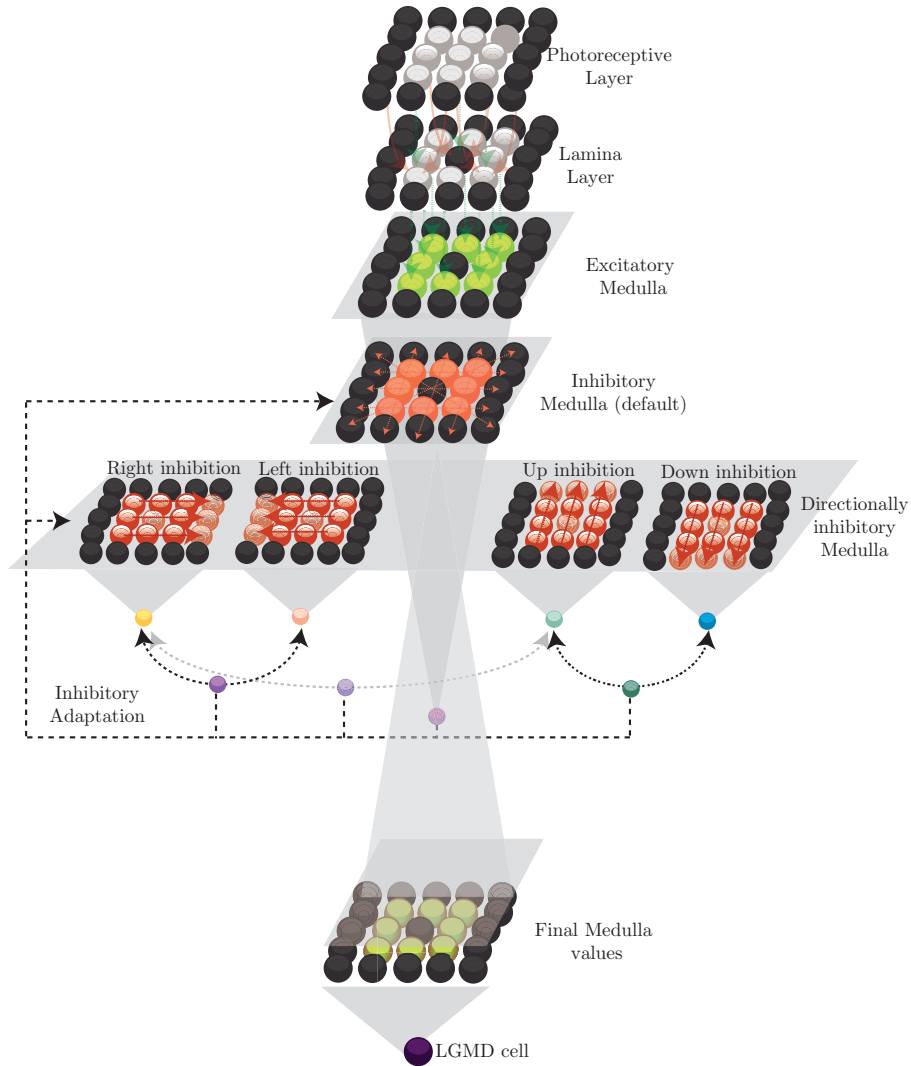


Figure 4.1: LGMD model: schematic illustration of the different layers that make up the model here proposed.

4.2.1 The LGMD model

The Photoreceptive layer (P)

The first processing in the locust visual system is done by photoreceptors, which convey a representation of the environment[222] to the first neuropile, Lamina.

A grayscale image of the camera current field of view, represented as a matrix of values (from 0 to 255), is the input to a matrix of photoreceptor units (P layer), being represented as:

$$P_f(x, y) = I_f(x, y) \quad (4.1)$$

$P_f(x, y)$ is the output from the Photoreceptor cell at position (x, y) for frame f and $I_f(x, y)$ is the intensity of each pixel in the input image, at position (x, y) , for frame f .

Lamina layer (L)

Based on [89, 190], the role of early sensory processing, performed by neurons located in the lamina, is to reduce redundancy and recode the sensory input into an efficient form. This should be done because natural signals are highly redundant, due to the tendency towards spatial and temporal uniformity of these signals[86]. So, a neural direct representation of the raw image would be inefficient. An important way to achieve this goal is to perform predictive coding. According to this approach, neural networks learn the statistical distributions inherent in images and reduce redundancy by removing the predictable components of the input, transmitting just what is not predictable [186]. This is a possible explanation to the centre-surround antagonism in the receptive fields of visual interneurons found in very different animals species [190]. The antagonistic surround takes a weighted mean of the signal in the neighboring receptors to generate a statistical prediction of the signal at the center. Then, the predicted value is subtracted from the actual center signal, minimizing the range of outputs transmitted. This process decorrelates the input signals by flattening the spatial and temporal power spectra, leading to a reduction of the output redundancy[89]. This kind of inhibition in sensory system is known as lateral inhibition. Difference of Gaussians (DoG) filter is usually used to simulate such process [15]

Based on this, lamina cells receive the output of the photoreceptive cells and, as previously mentioned, model the spatial predictive coding strategy, through:

$$L_f(x, y) = \sum_{i=-3}^3 \sum_{j=-3}^3 |P_f(x+i, y+j) \cdot \text{DoG}(i, j)| \quad (4.2)$$

where $L_f(x, y)$ represents the absolute activity of the lamina neuron at position (x, y) , at frame f . DoG is a difference of Gaussians kernel, being mathematically represented as:

$$\text{DoG}(i, j) = \frac{1}{2\pi\sigma_e} \exp\left(-\frac{i^2 + j^2}{2\sigma_e}\right) - \frac{1}{2\pi\sigma_i} \exp\left(-\frac{i^2 + j^2}{2\sigma_i}\right) \quad (4.3)$$

where $\sigma_e = \text{Filter Size}/18$ and $\sigma_i = \text{Filter Size}/9$ represent the excitatory and inhibitory distributions widths, respectively. The DoG filter size adopted, by trial and error, holds 7 pixels. The result of this mathematical operation leads to an edge

detection and enhancement.

Medulla layer (M)

The output from the L cells form two types of inputs to the cells in the Medulla layer, which is composed by two sequential computations.

One type of Medulla cells are excitatory (*Me*), whose excitation value is received directly from the retinotopically arranged counterpart cells in the *L* layer, at each frame *f*, being represented as:

$$Me_f(x, y) = L_f(x, y) \quad (4.4)$$

The other type of Medulla cells are inhibitory (*Mi*). For simplicity, *Mi* directionally selective cells can be divided in four types: left, right, up and down inhibitory cells. As an example, in relation to the left directional inhibitory cell, the excitation from a L cell passes to its retinotopic counterpart's on the *Mi* directionally layer, being directly converted into inhibition which is spread to its left side neighboring cells. In this situation, this neuron will be less sensitive to left-moving edges.

The directionally selective cells serve to evaluate and adapt the inhibitory filter set by default, by varying inhibition strength and spreading area accordingly to the spatial and temporal frequency contents captured by the camera.

Mathematically, left directionally selective inhibitory neurons transmit inhibition to its retinotopic counterpart's left side neighbouring cells, through:

$$Mi_{\text{left},f}(x, y) = \sum_{i=1}^{n_{\text{inh left},f}} L_f(x + i, y)w_I(i) \quad (4.5)$$

where $Mi_{\text{left},f}(x, y)$ is the inhibition that will be combined with the excitatory $Me_f(x, y)$, $n_{\text{inh left},f}$ is the spread of lateral inhibition to the left direction, $w_I(i) = 1$ is the local inhibition weight, controlling the neighboring inhibition strength. When inhibition is strong (for example, $w_I(i, j) = 1$) from the right side, excitation produced by left moving edges will be eliminated or highly attenuated. For example, for this directionally selective cell, with a lateral inhibition spread = 10 pixels, the vision system can deal with image motion slower than 5 pixels per frame, being equivalent to 100 degrees/second, using a camera acquisition frequency of 100 frames/second, with a resolution of 300×300 pixels and 60 degrees field of view.

Additionally to the spatial dimension, adaptations to different types of environment can lead to substantial changes in the temporal response function of the medulla cells.

Thus, at the final processing at the Medulla level, each neuron combines the actual excitatory level with a weighted linear combination of the past inhibitory history of each pixel. So, for each frame f , the value of each Medulla neuron is given by:

$$M_{\text{left},f}(x,y) = h_0 \cdot Me_f(x,y) + \sum_{a=1}^{f-b} h_a \cdot Mi_{\text{left},f-a}(x,y) \quad (4.6)$$

where f indicates the current sample and the set of temporal coefficients is $\{h_a : a = 0, 1, f - b\}$, being $(f - b + 1)$ the number of samples included in the filter, which was set to 10, by trial and error. $Mi_{\text{left},f-a}$ are the values of left Lamina inhibitory neurons during the last $(f - b + 1)$ frames. The temporal coefficients are modeled through a Gaussian function, being computed through:

$$h_a = \frac{1}{\sigma_{\text{et}} \sqrt{2\pi}} \exp\left(-\frac{a}{2\sigma_{\text{et}}}\right) - \frac{1}{\sigma_{\text{it},f} \sqrt{2\pi}} \exp\left(-\frac{a}{2\sigma_{\text{it},f}}\right) \quad (4.7)$$

where σ_{et} is the temporal spread of excitation, being constant and equal to 0.5. $\sigma_{\text{it},f}$ is the temporal spread of inhibition and can be variable, accordingly to the temporal characteristics of the visual stimuli. Adaptation to one environment or the other can produce substantial changes in the temporal response function of the Medulla cells, becoming more or less biphasic (see figure 4.2).

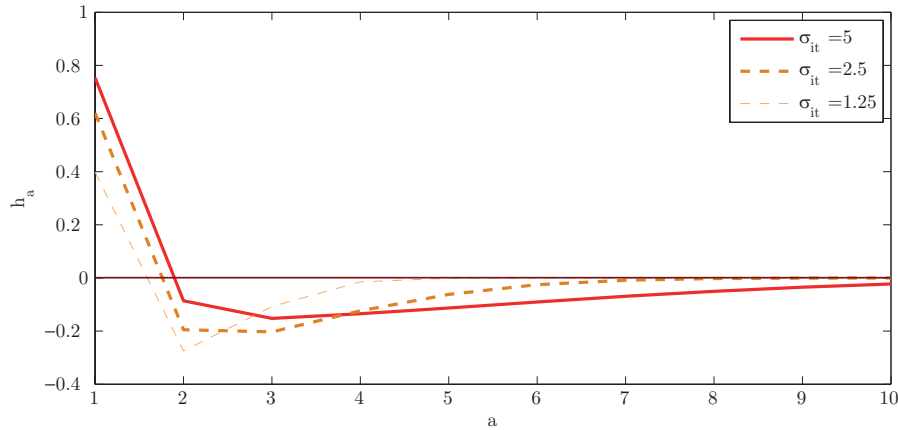


Figure 4.2: Temporal coefficients used in the modelation of the Medulla layer.

However, due to the direct relationship between the number of frames taken for temporal inhibition and the increment of the computational cost, during these experiments, $\sigma_{\text{it},f}$ was kept low and constant (figure 4.2, $\sigma_{\text{it},f} = 1.25$).

The final excitations from the Medulla directionally selective cells ($M_{\text{left},f}(x,y)$) that exceed a threshold (set to zero), are averaged by the $\overline{M}_{\text{left},f}$ cell, and the negative

excitations will be ignored by the summing operation. This process is mathematically defined as:

$$\overline{M}_{\text{left},f} = \frac{\sum_{x=30}^{n_h-30} \sum_{y=30}^{n_v-30} \Theta(M_{\text{left},f}(x, y))}{2 * (n_h - 30) + 2 * (n_v - 30)} \quad (4.8)$$

where n_h and n_v are the number of cells counted in a row and a column, respectively. Cells located in the edge of a layer (within a neighborhood of 30) have been discarded due to the border distortions resultant from the convolutions performed in the layers above. In this work, the input images were 300 by 300 pixels. Therefore, $n_h = n_v = 300$. Θ denotes the threshold operation, being defined as:

$$\Theta = \begin{cases} 1 & \text{if } M_{\text{left},f}(x, y) > 0 \\ 0 & \text{others} \end{cases} \quad (4.9)$$

Additionally, the remainder right, up, and down movement detecting neurons share the same working principles as the left moving detecting neurons. These four direction selective neuron's output is then combined and the information extracted is used as a feedback to adapt the inhibition spreading area (n_{inh} value), as well as to decide which, if any, directionally selective neurons will be active (figure 4.3).

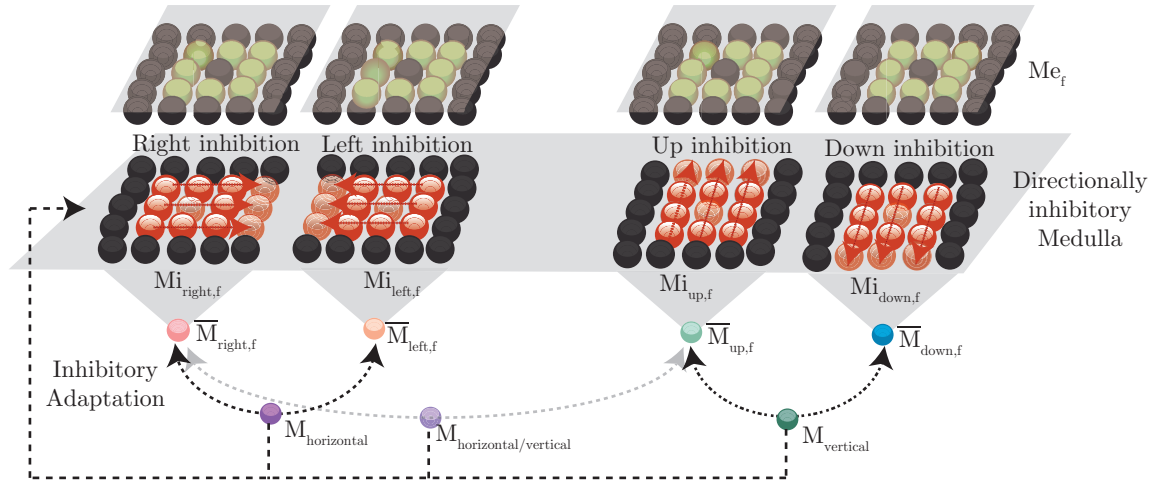


Figure 4.3: Directionally selective neuron and respective connections between them.

First, a comparative analysis will be performed between left and right selective neurons, as well as between up and down selective neurons. For right and left the

procedure is:

$$M_{\text{horizontal},f} = \left| \frac{\overline{M}_{\text{left},f} - \overline{M}_{\text{right},f}}{\overline{M}_{\text{left},f} + \overline{M}_{\text{right},f}} \right| \quad (4.10)$$

In the case that $M_{\text{horizontal},f} \geq 0.1$, (0.1 was taken as a significant difference value) it means that the activity of the right detecting and the left detecting neuron is significant.

If the activity of the right detecting neuron is lower than the left detecting neuron, the inhibition should be spread into the right direction (for an example, see figure 4.4), through:

$$n_{\text{inh right},f} = \begin{cases} n_{\text{inh right},f-1} + 1 & \text{if } (M_{\text{horizontal},f} \geq 0.1 \wedge \\ & \overline{M}_{\text{right},f} < \overline{M}_{\text{left},f}) \\ 0, & \text{if } M_{\text{horizontal},f} < 0.1 \end{cases} \quad (4.11)$$

When the left detecting neuron activity is significantly lower than the right detecting neuron, the inhibitory spreading of the left detecting neurons will be increased.

Following the same line of thought, a comparative analysis between the up and down selective neurons will also be performed. That determines $M_{\text{vertical},f}$.

However, in the particular situation where no significant horizontal ($M_{\text{horizontal},f}$) and vertical ($M_{\text{vertical},f}$) differences are found (both are < 0.1), an extra comparative analysis will be performed between, for example, the right and the up detecting neurons, through:

$$M_{\text{horizontal/vertical},f} = \left| \frac{\overline{M}_{\text{right},f} - \overline{M}_{\text{up},f}}{\overline{M}_{\text{right},f} + \overline{M}_{\text{up},f}} \right| \quad (4.12)$$

If, for example, the activity of the right detecting neuron is lower than the up detecting neuron, the inhibition should be spread into the left and right direction, through:

$$n_{\text{inh right},f}, n_{\text{inh left},f} = \begin{cases} n_{\text{inh right},f-1} + 1, & \text{if } (M_{\text{horizontal/vertical},f} \geq 0.1 \wedge \\ n_{\text{inh left},f-1} + 1 & \overline{M}_{\text{right},f} < \overline{M}_{\text{up},f}) \\ 0, & \text{if } M_{\text{horizontal/vertical},f} < 0.1 \end{cases} \quad (4.13)$$

The same though is applied when the activity of the up detecting neuron is lower than the left detecting neuron.

The second type of inhibitory cells, the medullar uniformly lateral inhibitory cells (Mi , which is non-directional), receive excitation from the L cells, convert it into inhibition, which is spread to all its neighboring cells. The way that inhibition is passed to the retinotopic counterpart's neighbouring cells, in terms of space dimension, is dynamically adaptable to the environment, depending on the directionally selective values previously computed. There is a spatially uniform inhibitory kernel, set by default ($Mi_{\text{def},f}$), that spreads inhibition into the nearest neighboring cells, being defined as:

$$Mi_{\text{def},f}(x, y) = \left(\sum_{i=-n_{\text{inh},f}/2}^{n_{\text{inh},f}/2} \sum_{j=-n_{\text{inh},f}/2}^{n_{\text{inh},f}/2} L_f(x+i, y+j) w_{I,\text{def}}(i, j) \right) \quad (4.14)$$

where $L_f(x, y)$ is the excitation that comes from the Lamina layer, $n_{\text{inh},f}$ is the spread of the non-directionally lateral inhibition, which by default is set to be 3. $w_{I,\text{def}}(i, j) = 1$ is the local inhibition weight, controlling the neighboring inhibition strength.

In case no significant differences are found on the horizontal, vertical and horizontal/vertical directions, but \overline{M} excitation value of the directionally selective neurons is >5 , the default uniformly spreading inhibition, n_{inh} (equation 4.14), is increased at each time step through: $n_{\text{inh},f} = n_{\text{inh},f-1} + 1$, leading to an increment on the uniformly spread inhibition, until the resultant excitation is decreased to a minimum value. When the \overline{M} excitation value of the directionally selective neurons is <5 (value considered as low enough to not produce any significant response, by trial and error), the adaptation process stops and the values found are used during the next frames, until a sudden variation on the captured image happens and all the inhibitory adaptation process restarts again. However, this restart process was not considered in the present work.

The total inhibition on the medulla layer becomes:

$$Mi_f(x, y) = Mi_{\text{def},f}(x, y) + Mi_{\text{left},f}(x, y) + Mi_{\text{right},f}(x, y) + Mi_{\text{up},f}(x, y) + Mi_{\text{down},f}(x, y) \quad (4.15)$$

Based on this, we expect that when driven by multiple spatially uniform stimuli (SC environment), the receptive field of inhibition (Mi_f) strengths into all directions of its surround, suppressing sensitivity to any translational movement. When driven by a vertical grating (FF environment), the receptive field is expected to develop a left

horizontal spreading that will suppress sensitivity to translational moving bars. When driven by an uncorrelated stimulus (S), the receptive field would become uniformly attenuated.

Thus, and similarly to the directionally uniformly cells, the resultant excitation in each neuron of the Medulla layer is computed as:

$$M_{,f}(x, y) = h_0.Me_f(x, y) + \sum_{a=1}^{f-b} h_a.Mi_{f-a}(x, y) \quad (4.16)$$

where the temporal coefficients ($\{h_a : a = 0, 1, f - b\}$) are computed as represented on equation 4.7.

LGMD cell

Finally, the LGMD cell value is given by:

$$\text{LGMD}_f = \frac{\sum_{x=30}^{n_h-30} \sum_{y=30}^{n_v-30} \Theta(M_f(x, y))}{2 * (n_h - 30) + 2 * (n_v - 30)} \quad (4.17)$$

where the threshold operator, Θ , is computed as indicated by equation 4.9. n_h and n_v are the same constants used on equation 4.8.

Additionally, a temporal summation is performed, being modeled as a temporal Gaussian integration. This temporal summation depends on the activity verified on the output of equation 4.2. The more activity on the Lamina layer, the more inhibition will be applied on the medulla layer and, consequently, it will be needed to apply a temporal integration in order to reach similar peak LGMD_f values. Thus, the temporal integration will be modeled as[5]:

$$\Delta t_a = \exp\left(-\frac{a}{2\sigma_{\text{ti},f}}\right) \quad (4.18)$$

where $\{\Delta t_a : a = 0, 1, f - b\}$, being $(f - b + 1)$ the number of samples included in the filter, which was set to 10, by a trial and error process. $\sigma_{\text{ti},f}$ is the temporal integration extent, being variably dependent on the mean activity of the lamina layer.

For simplification, $\sigma_{ti,f}$ can take three distinct values, being defined as:

$$\sigma_{ti,f} = \begin{cases} 10/8, & \text{if } \left(\frac{\sum_{x=1}^{300} \sum_{y=1}^{300} L_f(x,y)}{300*300} \right) \leq 83 \\ 10/6, & \text{if } 83 < \left(\frac{\sum_{x=1}^{300} \sum_{y=1}^{300} L_f(x,y)}{300*300} \right) \leq 166 \\ 10/4, & \text{if } 166 < \left(\frac{\sum_{x=1}^{300} \sum_{y=1}^{300} L_f(x,y)}{300*300} \right) \leq 250 \end{cases} \quad (4.19)$$

These three discrete stages of temporal integration were chosen using multiple simulation experiments. This division in three discrete stages can lead to an inappropriate summation extent for Lamina excitation mean values close to the limits here used.

Using this strategy, the temporally integrated LGMD excitation becomes:

$$\text{LGMD}_{t,f}(x, y) = \sum_{a=0}^{f-b} \Delta t_a \cdot \text{LGMD}_{f-a} \quad (4.20)$$

where $\text{LGMD}_{t,f}(x, y)$ is the LGMD value after temporal integration and Δt_a defines the temporal integration coefficient values.

Directional selective cells: information extraction and adaptive processing example

As mentioned previously, the output of the four directional selective neurons is combined in order to extract information about the movement of the visual stimuli captured by the camera. A square located at 1 meter to the camera, performing a translation route in relation to the camera (moving from left to right), at 2 m/s, is equivalent to a square moving at $\simeq 6$ pixels/frame. Using that visual stimuli, the output of the four directional selective neurons, for a spreading of lateral inhibition equivalent to 4 pixels to each of the directions tested, is depicted on figure 4.4.

Using the \overline{M}_f values obtained for each directional selective neurons type, it is noticeable that, for the right directional selective neuron (figure 4.4, b) panel, red dashed line), the excitation value obtained at each time step is significantly different from that of the remainders selective neurons (left, right and up, respectively). For this situation, $M_{\text{horizontal},f}$ was close to 0.15. However, when computing $M_{\text{vertical},f}$, it is null. Therefore, one can infer which type of movements are happening on the captured image and use this visual information for further processing.

In order to achieve a complete adaptation of the visual system to this type of translational square, so that the collision detector output, LGMD_f , would produce its

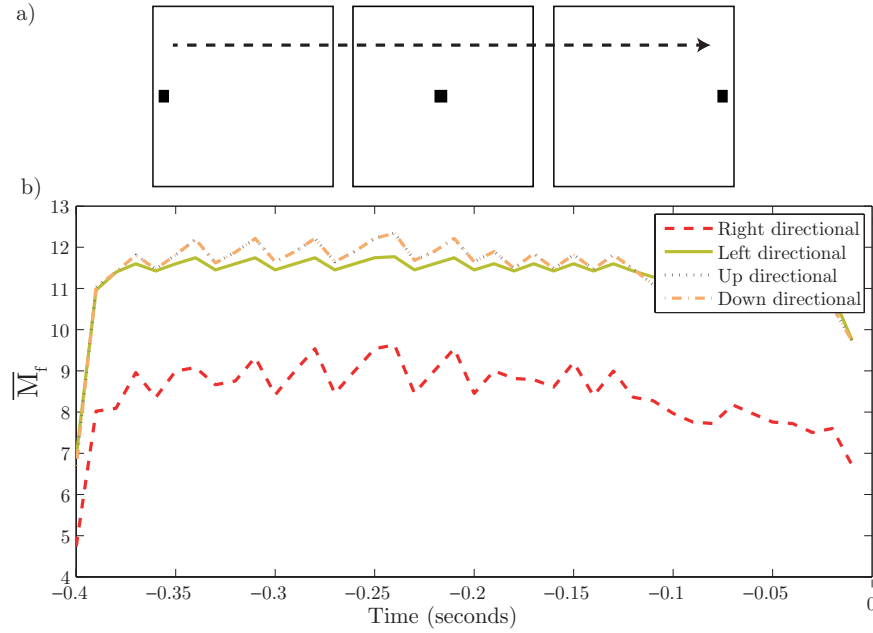


Figure 4.4: a) Sample images of the computer generated visual stimuli, with a 300 by 300 pixels and 60 degrees of field of view. The black square (20×20 pixels), with a translating speed of 4 pixels per frame to the right, showing different frames of the square performing a translation route (the arrow is indicating the visual stimuli moving direction). b) $\overline{M}_{\text{right},f}$ (red dashed line), $\overline{M}_{\text{left},f}$ (green solid line), $\overline{M}_{\text{up},f}$ and $\overline{M}_{\text{down},f}$ (back dotted and orange dot-dashed lines, respectively) computed at each frame of the image sequence shown above.

minimum value ($\simeq 0$) when stimulated with this type of visual stimuli, the right detection neuron's inhibition should be extended into more neighboring neurons. Through an iterative process of minimizing the $M_{\text{right},f}$ value through an increment on the right inhibition spreading, we found that the vision system can eliminate the image motion when using a right lateral inhibition that is spread to 8 or more pixels ($n_{\text{inh right},f} = 8$).

4.2.2 Materials

Visual stimuli

In order to reproduce some of the conditions described in the previous chapter, a simulated visual environment was developed using Vision Egg [196] on a Python programming platform, merged with Matlab software [118]. Objects were simulated according to their movement and the corresponding data was acquired by a simulated camera and processed by the proposed model. Image sequences were generated by a simulated camera with a field of view of 60° in both x and y axis, a sampling frequency of 100

Hz, and a resolution of 300 by 300 pixels.

Three different environments were created. One of the environments (Simple, S) is composed by a simple white background. The second environment (SC) is composed by multiple black discs (40 discs, each covering 10 pixels, corresponding to an angular size = 2 degrees), moving randomly in translation trajectories (at $\simeq 4$ pixels/frame, corresponding to 400 pixels/second, for a frame rate of 100 frames/second). The third visual scenario (FF) is composed by a vertical sinusoidal grating (each bar covering approximately 10 degrees), moving at 600 pixels/second (corresponding to 120 degrees/second).

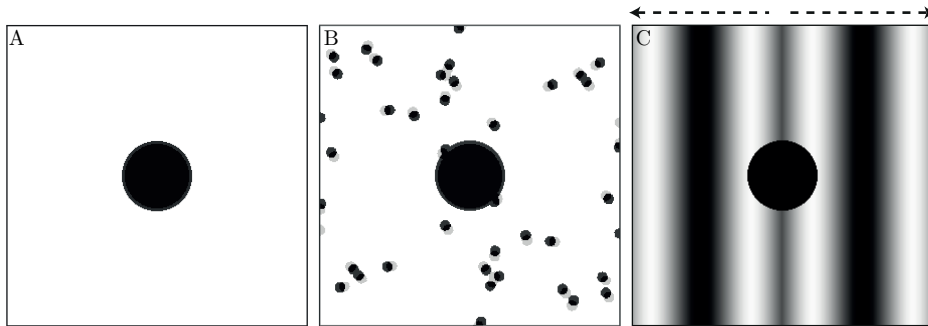


Figure 4.5: Computer-generated stimuli samples of the three distinct environments created. A) Simple environment (S). B) Scattered environment (SC). Black dots: position of the gray dots, in the preceding frame. C) Flow-field environment (FF). The top arrows indicate the direction of the flow field motion.

After a period of adaptation to the environmental condition (S, CS or FF), a single 7 cm looming disc, moving at 3 m/s ($l/|v| = 12$ ms) was superimposed to the static (figure 4.5, A) and moving (figure 4.5, B and C) backgrounds. The disk continuously approaches the camera, until it reaches a final angular size of 40 degrees.

The model output ($\text{LGMD}_{t,f}$, equation 4.20) was analyzed in terms of: $\text{LGMD}_{t,f}$ peak firing rate, time of peak firing rate (t_p) and phase duration (rise phase and fall phase, respectively). The rise phase of the model response was calculated from the point at which the $\text{LGMD}_{t,f}$ firing rate exceeded a 99% confidence interval (sampled from data for the entire stimulus presentation) until the $\text{LGMD}_{t,f}$ peak. The associated fall phase duration was calculated from the time of the frame when the stimulus stopped expanding to the time of the last spike following when the firing rate decreased to 15% of the peak firing rate.

4.3 Results

Simple Environment (S): Frontal Looming and effects on the LGMD_f response

In the first stage of this analysis, we presented our model with a simple white background. During this condition, all the photoreceptor cells and, subsequently, the neurons located below, are being stimulated with a spatially uniform white stimulus. Consequently, the LGMD_f values obtained for this white background are zero when activating sequentially each of the directional selective cells (by default, we have started with $n_{\text{inh},f} = 3$, leading to an uniform inhibition spreading). Due to the nonexistence of LGMD_f excitation when presented with the uniform and static white background, the default kernel applied in the inhibitory layer ($M_{\text{def},f}$) was a 3×3 kernel, fulfilled with 1 values.

Then, the looming black object ($l/|v| = 12$ ms) was inserted on the image sequence feeding the model here proposed. The output obtained is represented on the top panel of figure 4.6.

Relatively to the temporal integration, due to the low activity on the Lamina layer (computed as represented on equation 4.19), the minimum temporal summation took place.

Following the results obtained in biology (see previous chapter, results section), LGMD_{t,f} generated a characteristic rapid rise to a peak firing rate in response to the frontal loom (figure 4.6, top panel).

Scattered Environment (SC): Frontal Looms and effects on the LGMD_f response

In the second stage, a scattered background, with dots moving into all directions, feeded the model here presented. On this condition, all the photoreceptors cells, as well as the neurons from the lamina and medulla layers, are being stimulated with multiple stimuli, moving in randomly translation routes. Consequently, in order to suppress the excitation produced by all this moving stimuli, the inhibition at the Medulla cells should be spread uniformly until the excitation produced by the movement of those multiple dots is minimum.

In fact, observing the top panel on figure 4.7, we can verify that \overline{M}_f responses obtained for each directional selective cell are quite similar (as previously done, we have started with directional $n_{\text{inh right},f} = n_{\text{inh left},f} = n_{\text{inh up},f} = n_{\text{inh down},f} = 3$). By comput-

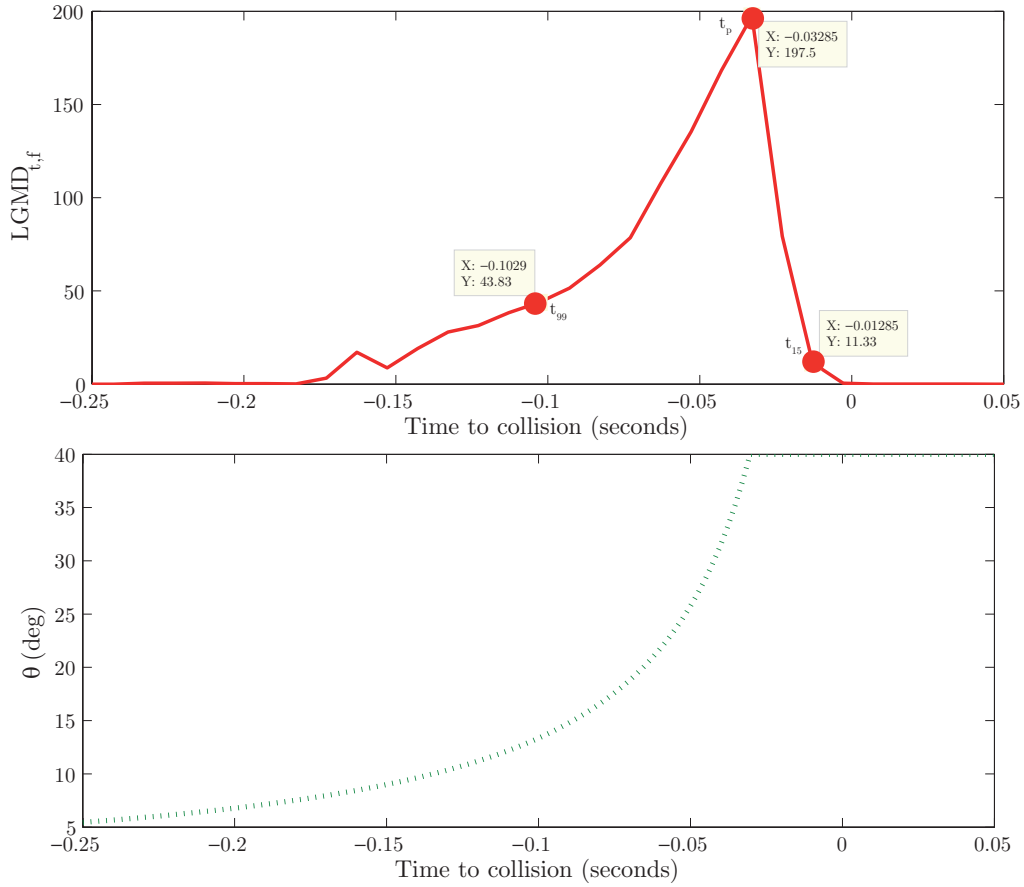


Figure 4.6: Top panel: $LGMD_f$ responses (continuous line) to a looming black disc approaching from the white visual background. Labeled points on the LGMD response panels (t_{99} , t_p and t_{15}) represent: t_{99} : time when response exceeds a 99% confidence interval (start of rise phase); t_p : time of peak firing rate (end of rise phase); t_{15} : time of nearest spike to 15% of peak firing rate (end of fall phase). Bottom panel: change in subtense angle during object approach.

ing the $M_{horizontal,f}$ (using the values of the right and left directional detectors, plotted on figure 4.7, top panel), a value of $\simeq 0.04$ was obtained. On the other hand, $M_{vertical,f}$, was $\simeq 0.03$. As both differences were smaller than 0.1, $M_{horizontal/vertical,f}$ was computed and the result was also lower than the significance value considered. This fact leads us to the conclusion that, in fact and as previously predicted, inhibition should be spread uniformly in order to decrease excitation produced by those multiple moving dots.

According to this, a $n_{inh,f}=5$, spreading inhibition uniformly into all directions, was considered optimal to suppress the excitation produced by the moving dots. By using this non-directional inhibition spread, the $LGMD_{t,f}$ spike rate profile, represented on the bottom panel of figure 4.7, was obtained.

In terms of temporal integration, as the mean activity of the Lamina layer (computed as represented on equation 4.19) was lower than 83, the minimum temporal summation was activated.

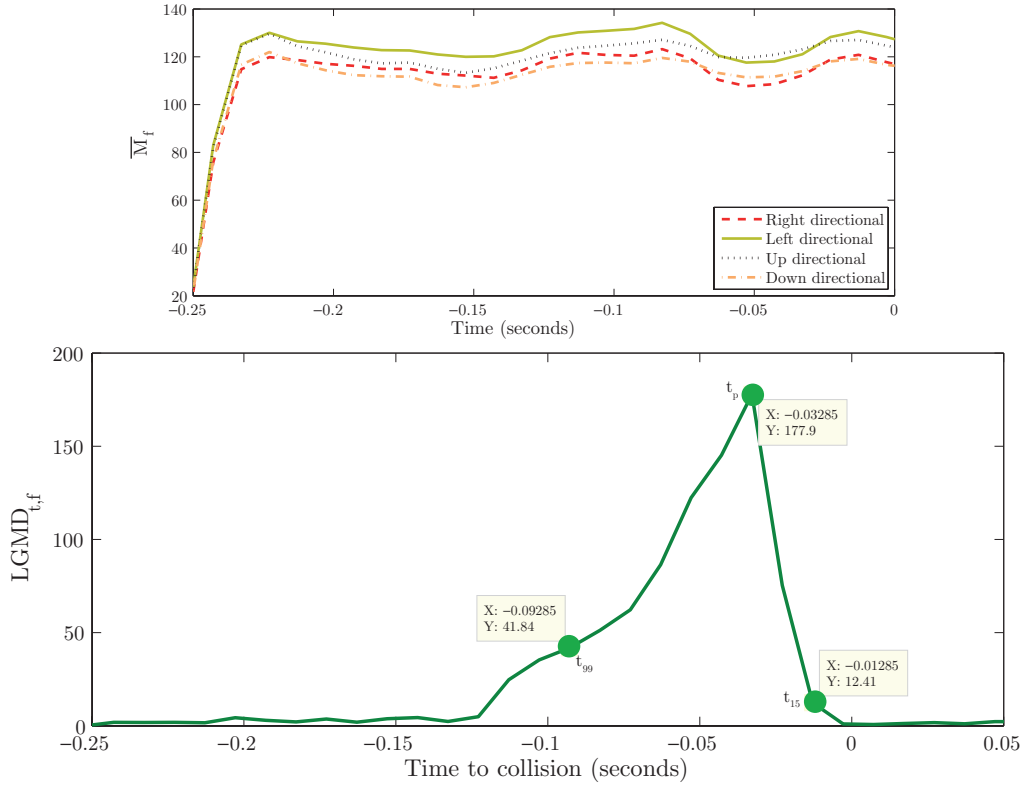


Figure 4.7: Top panel: Output of the $\overline{M}_{right,f}$ (red dashed line), $\overline{M}_{left,f}$ (green solid line), $\overline{M}_{up,f}$ and $\overline{M}_{down,f}$ (back dotted and orange dot-dashed lines, respectively) during adaptation to the scattered environment, for each of the directional selective cells. Bottom: $LGMD_{t,f}$ response (continuous green line) to a looming black disc approaching, when inserted in a dynamic scattered environment, after inhibitory adaptation. Legend is similar to the one of figure 4.6.

Flow Field Environment (FF): Frontal Looms and effects on the $LGMD_f$ response

In the third stage, our model was stimulated with the moving flow field background. During this condition, all the photoreceptor cells and, subsequently, the neurons located below, are being stimulated with a vertical grating, moving horizontally, both to the left (the left half of the image) and to the right direction (the other half of the image). Consequently, at the medulla inhibitory layer, an horizontally oriented

inhibition should be developed, suppressing sensitivity to those horizontally moving bars.

As previously done, by default, we have started with $n_{inh\ right,f} = n_{inh\ left,f} = n_{inh\ up,f} = n_{inh\ down\ f} = 3$, leading to an inhibition of 3 pixels/frame in right, left, up and down direction, respectively. Due to the movement of the bars to both horizontal directions (see figure 4.5, C), right and left selective neurons shared the same mean values ($\simeq 70$), as well as the up and down selective neurons ($\simeq 222.17$). Despite the mean difference between left and right ($M_{horizontal,f}$), up and down ($M_{vertical,f}$) selective neurons being close to zero, the mean difference between right and up selective neurons ($M_{horizontal/vertical,f}$), was $\simeq 0.52$. This led to an increment on the right and left inhibition spread extension ($n_{inh\ right,f} = n_{inh\ left,f} = 7$), in order to bring the excitation close to zero, inducing a total adaptation to the horizontally moving sinusoidal gratings.

Additionally, temporal integration was increased too. As the mean activity of the Lamina layer (computed as represented on equation 4.19) was higher than 200, the maximum temporal summation was activated.

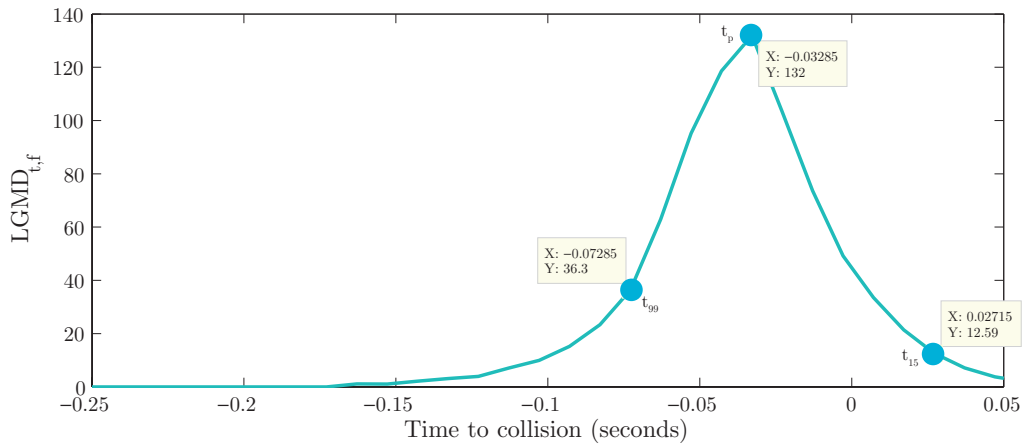


Figure 4.8: $LGMD_{t,f}$ responses (continuous blue line) to a looming black disc approaching, when inserted in a dynamic flow field environment. Legend is similar to the one of figure 4.6.

Adaptation to different environments: spatial and temporal model parameter's summary

The best spatial and temporal parameters, found for each of the environments tested, are listed on table 4.1. Using these model parameter's values, at the different condi-

tions tested, the model is capable of distinguish between real collisions from those of non-directional rapid translations (SC) and directional translations (FF).

Table 4.1: Summary of the optimal spatial and temporal parameters found for each environment tested (S, SC and FF, respectively).

Environment	Spatial inhibition									Temporal inhibition	Temporal integration	
	Horizontal				Vertical				Uniformly distributed	σ_{it}	σ_{ti}	
	Left	n_{inh} left	Right	n_{inh} right	Up	n_{inh} up	Down	n_{inh} down	n_{inh}			
Simple (S)	✗	0	✗	0	✗	0	✗	0	✓	3 × 3, default	$\sigma_{it} = 1.25$	$\sigma_{ti} = 10/8$
Scattered (SC)	✗	0	✗	0	✗	0	✗	0	✓	5 × 5	$\sigma_{it} = 1.25$	$\sigma_{ti} = 10/8$
Flow Field (FF)	✓	7	✓	7	✗	0	✗	0	✓	3 × 3, default	$\sigma_{it} = 1.25$	$\sigma_{ti} = 10/4$

Comparative analysis between the model and the biological data

In chapter 3 We have presented the biological LGMD responses obtained in the presence of similar similar situations. Similarly, we have decide to evaluate the model here proposed according to three main distinct characteristics: the peak of the LGMD $_t$, and both the rise and fall phases of the peak firing rate. According to the results shown on figure 4.9, panel A), the LGMD peak was affected by the image background. Peaks obtained at the SC and FF backgrounds were lower relative to S.

The rise phase duration was also affected (figure 4.9, B) by the background characteristics. S has the higher rise phase duration, followed by the SC and, finally, the FF background. On the other hand, the fall phase duration (figure 4.9, C), was larger for the FF condition, being equal for both S and SC backgrounds.

When comparing these results with the ones obtained in biology, we conclude that there is a high degree of accordance between the model output and the insect responses.

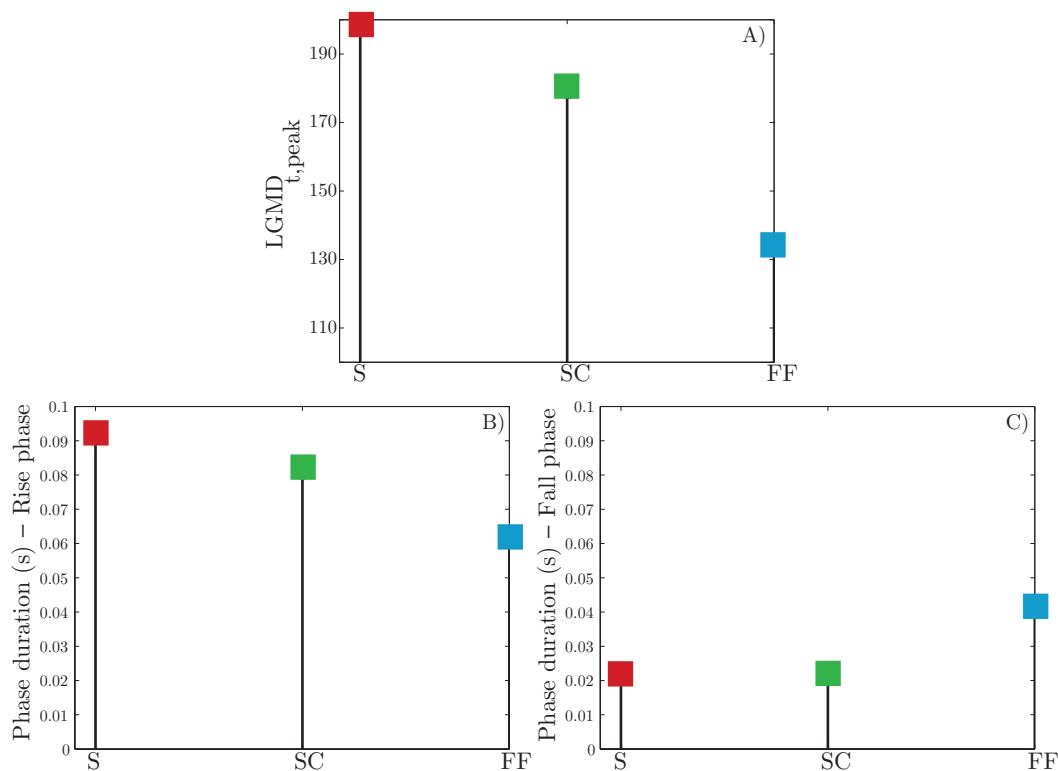


Figure 4.9: A) Comparisons of the LGMD peak values obtained for each of the conditions tested (S: simple, SC: scattered; FF: flow-field). B) Rise phase duration and C) Fall phase duration obtained for each background type.

4.4 Discussion

LGMD model here presented, structured as a neural network, has proven to be a very useful tool in linking the biological theory and the data recorded and analyzed in the previous chapter. However, as a model it should be kept in mind it provides for a simplification and approximation of the real LGMD neuron.

Taking into account the obtained results, the LGMD model provided non-trivial insights in the multitudes of experimental observations previously done, link seemingly unrelated data to each other.

The way that the different visual backgrounds influences the model response to approaching objects has been presented, leading to a possible explanation for the biological results obtained at the same visual conditions. In order to achieve that goal, a systematic characterization of the model output, for each of the backgrounds used, has been performed, leading to a series of conclusions that will be described in the following.

Approach sensitivity relies upon a rapid and effective inhibition

We analyzed the effect that adaptable inhibitory neurons (both directional and non-directional ones) have on reducing and even eliminating the excitation caused by moving non-looming stimuli at the Lamina layer (verified on conditions SC and FF). At SC condition, the multiple dots, moving randomly in all translation directions relatively to the camera, lead to an initial increment on the excitation of the Medulla excitatory cells. This high excitation level (figure 4.7, top panel) could even be considered as a “false positive” signal of a potential collision scenario. However, after adaptation, and due to an uniform increment on inhibitory spreading area at the Medulla inhibitory layer, all the excitation produced by the moving dots was eliminated. However, LGMD model keeps its sensitivity to the looming object, producing a very similar response to the one obtained for the same looming object approaching over a white static background.

Using the FF condition, we have tried to replicate the flow field typically produced by the forward movement of, for example, a locust or a robot moving in an environment. Similarly to the inhibitory adaptation verified in the SC condition, the adapted directionally inhibitory neurons (left and right, respectively) were able to eliminate the excitation produced by those laterally moving bars. Consequently, the LGMD model was able to reliably detect the approaching object.

Based on these experiments, we can conclude that inhibition prevents model responses to undesired stimuli, such as lateral moving stimuli or others.

A key-aspect of the approach sensitivity mechanism pertains to dynamics: suppression of the response to non-approach stimuli occurs if inhibition acts sufficiently rapidly to cancel out excitation.

Adaptation to different background complexities: a network plasticity hypothesis

The three environments here tested differ substantially in their spatial frequency content (figure 4.5). Subsequently, the medulla directionally inhibitory neurons will be driven differently by those three background conditions, leading to the hypothesis that, probably, these local neurons need to adapt their receptive field in the neural circuit to prevent false collision detections.

In fact, the qualitative function of the model here proposed has a simple interpretation: one can view each directionally selective medulla cell as “trying to predict” the response of the lamina cell in the next time instant, from stimulus information in its own directionally spatial receptive field. Those neurons that are successful get “rewarded” with a highly spread inhibitory receptive field. As a result, the successful predictions are subtracted from the lamina cell’s output and, by a continuous adaptation of its spreading inhibitory area, the model literally performs a dynamic version of predictive coding.

Filtering behaviorally relevant stimuli

Biological organisms continuously select and sample information used by their neural structures for perception and action, and for creating coherent cognitive states guiding their autonomous behavior.

In fact, and based on the results obtained, the goal of the visual system is not to reconstruct internally a veridical reproduction of the intensity pattern that falls on the insect retina. Instead, the system must reduce the onslaught of raw visual information and extract the few bits of information that are relevant for behavior. In this case study, visual information related with collision detection and avoidance have been successfully extracted. The remainder information, related with background movement, has been eliminated in an effective way, showing the effectiveness and possible applicability of this model as, for example, a collision detector that could be use to drive generic actuators in the robotic area.

Chapter 5

Statistics of Motion

Approaches described so far are based on a progressive reconstruction of the visual input from local computations, successively integrated into different layers of increasing complexity, in order to extract salient information of the captured scene.

In contrast, some experimental studies have suggested that world scene's recognition may be initiated from the encoding of the global configuration, ignoring most of the object information and details.

In the present chapter, a different approach, based on the study of image statistics, is addressed.

5.1 Introduction

The ecological approach to visual perception developed, at first, by Gibson [76] and then defended by Duchon et al. [42], “*views animals and their environments as “inseparable pairs” that should be described at a scale relevant to the animal’s behavior*”, being named as Direct Perception. According to this view, the animals perceive the layout of surfaces and not the coordinates of points in space, as well as not merely the three-dimensional structure but what the layout affords for action. A main dogma of the ecological approach is that the pattern of light reflected from the surrounding surfaces, provides adequate information for controlling behavior without further inferential processing or model construction.

The impression of a deterministic connection between perception and environment is an illusion [75, 206]. Most perceptual capabilities depend upon a combination of many different sources of stimulus information - as lighting/shading, texture, occlusion, motion, among others - each of which is merely probabilistically predictive in the task the organism is performing. Besides, all visual measurements are inher-

ently noisy, due to the randomness of both light absorption and phototransduction's chemical events. Consequently, the appropriate way to characterize visual stimuli is through a statistical approach [75, 205]. In fact, a very promising and recent approach for solving some difficult problems in vision, is based on the study of image statistics [90].

Even from a casual inspection of natural images, which are image scenes captured in a natural environment, it can be noticed that neighboring spatial locations are strongly correlated in intensity. According to literature [186], the standard measurement for summarizing these dependencies is the intensity autocorrelation function, which computes the correlation of the image pixel's intensity at two locations as a function of their spatial separation. A closely related measurement is its Fourier transform, in particular, the Image Power Spectrum. Expressing the autocorrelation function by its Fourier transform is convenient for several reasons. It connects the statistics of images with linear systems models of image processing.

Furthermore, the two-dimensional image power spectrum can be reduced to a one-dimensional function of spatial frequency, through a rotational average on the two-dimensional Fourier plane [200]. Extensive experimental analysis has led researchers to find out that the power spectrum of natural images falls with frequency of $1/f^\alpha$. The slope of the energy spectrum α , provides a description of the spatial correlation found in natural images [52, 53, 208]. Additional research has shown that different environmental types exhibit distinctive power spectrum slopes [3, 129, 198], being 1.0, 1.4, 1.8 and 2.3 for sky, road, vegetation and man-made scenes, respectively. [164] has argued that it is the particular distribution of sizes and distances of objects on images that governs the spectral falloff.

In fact, during the last years, there has been a great deal of interest on the images statistic's study, both from a computational and biological vision perspective. Considering the computational perspective, this interest emerged from: 1) the need for better redundancy reduction/image compression and image/video coding strategies [22]; 2) the pursuit for better image restoration algorithms (including denoising, inpainting, among others) [127]; 3) the necessity to estimate surfaces (depth map) from stereo, texture, motion, shading [202]. From a biological perspective, most research has been focused on studying how neural properties (from photoreceptors to higher level's neurons) are adapted to the statistics of the visual environment [33, 75]. Additionally, artificial models of biological image processing have been developed and used to verify the influences of ecological niches on the characteristics of neural receptive fields [9, 39, 52].

While the majority of the research in this scientific field has been focused in evaluating the spatial frequency of images, a full consideration of image statistics must certainly include time [40, 210]. Images falling on the retina have important temporal structures arising from self-motion of the observer, as well as from the motion of objects in the world [18, 48, 49, 172]. Despite the complexity of daily image sequences captured by the biological systems, natural vision systems appear to work well in complex 3D scenes. Many fast moving animals, either simple as flies and bees, or more complex biological systems as birds, seem to have little trouble navigating through the environments. A biological system provided with vision needs to be able to survive within a dynamical world, one that appears to be constantly changing when viewed over extended periods of time.

Looking at these findings from an engineering point-of-view, in this chapter it is illustrated how simple statistics of simulated and real images vary as a function of the interaction between the world and the observer. A methodology that highlights those changes on the statistical properties, being successfully implemented in a simple robotic platform, is here proposed. Results show how simple image statistics can be used to predict the presence or absence of colliding objects in the scene, before exploring the image/environment.

5.2 Related work

The statistical properties of static images, consisting on a frame taken from a film, have been studied for many years [27], seeking to describe the spatial regularities and correlations of such images. However, during those years, the regularities in time-varying images had been studied in a very limited way, mainly due to the high cost associated with the technology to capture and analyze motion pictures on computers, by then.

Posteriorly, in 1992, van Hateren [209] directed the first research aiming to characterize, indirectly, the spatio-temporal structure of visual stimuli. This was determined by the spatial power spectrum of the natural images, combined with the distribution of velocities perceived by the visual system, when moving in the environment. Through this, van Hateren was able to infer about the joint spatio-temporal spectrum obtained for the situations tested and, subsequently, about the optimal neural filter which maximized the information rate in the photoreceptive channels of the eye. This analysis enabled van Hateren to verify the high correlation between the temporal response properties of biological visual neurons and the optimal neural filter derived from this

study.

In 1995, Dong and Attick [40] measured the spatio-temporal correlations for a group of motion pictures segments, through the computation of the three-dimensional Fourier transform on these movie segments and then by averaging together their power spectra. In Dong and Attick work [40], it was shown that the slope of the spatial power spectrum becomes more flat at higher temporal frequencies. At the temporal frequency spectrum domain, the slope becomes more flat at higher spatial frequencies. These results had shown that the dependence between spatial and temporal frequencies is, in general, non-separable. A theoretical derivation of this scaling behavior was proposed, being demonstrated that it emerges from objects appearing at a variety of depths and moving at different velocities relative to the observer. Additionally, and similarly to the methodology implemented by van Hateren [209], Dong and Attick computed the optimal temporal filter to remove time correlations. The filter proposed was proved to closely match the lateral geniculate neurons' frequency response function.

Some years later, Rivait and Langer [161] examined the spatiotemporal power spectra of image sequences depicting dense motion parallax, namely the parallax seen by an observer moving laterally in a cluttered environment. A parametrized set of synthesized image sequences were used and the structure of its spatiotemporal spectrum was analyzed in detail. This work specifically addressed lateral translation. However, the proposed analysis could be generalized to more complex types of motion, including components of rotation or forward translation [161].

Controversially to the results obtained by Dong and Attick [40], in 2008 Tversky and Geisler [205] measured scene spatiotemporal statistics from real and artificial movies of first-person translation through a forest environment. Power spectrum obtained at higher temporal or lower spatial frequencies differed dramatically from the translational model's predictions proposed by [40]. A possible explanation is that the expansion motion present in the used scenes breaks the Dong and Attick model's scaling behavior. Conclusions had shown that the dynamic power spectrum of first-person motion is, in fact, not scale invariant [204, 205] (meaning that we should be able to zoom in and out of an image, or travel through a natural scene, and expect that the statistics will not remain roughly constant), as previously though).

In order to summarize related works that have been developed in the computer vision field, in [200] a deep and detailed review relative to the state of the art of image statistics was performed. Additionally, its potential applications on the computer graphics field, as well as in related areas, was also addressed in the cited paper [200].

Looking at the potential use of the image power spectra in a different perspective,

Dror et al. [41] and Wu et al. [224] addressed the problem of motion/velocity estimation, by coupling the output of the well-known bio-inspired Elementary Motion Detector (EMD) [20, 147] with a real-time computed image power spectra. According to the results obtained with this methodology [224], the real-time reliability of velocity estimation was highly improved with a real-time response look-up table based on the input signal's power spectral analysis.

Recently, [172] performed a systematical analysis of the spatiotemporal statistics of image sequences generated during the two distinct behavioral strategies performed by flying insects [48]: saccadic and intersaccadic behaviours, when inserted on cluttered environments. Results have shown that rotational movements of the environment, obtained during saccades, elicit high fluctuations on image parameters, as brightness, contrast and spatial frequency (measured in terms of α). On the other hand, during intersaccadic intervals, which result in translational movements on the insect retina, similar fluctuations on image parameters are only caused by nearby objects. Consequently, those changes could be the basis for the detection of behaviorally relevant objects on the surrounding environment, without any need for further image segmentation.

As mentioned so far, image statistics have attracted the attention in a high and different variety of research fields, ranging from biology processing comprehension to computer vision purpose, leading to very important conclusions on both research fields.

Giving specifically attention to the fact that:

a) the dynamic power spectrum of first-person motion is not scale invariant, as previously thought [40];

b) in fact, the expansion motion present in the scenes used on [204, 205] breaks the Dong and Attick model's scaling behaviour;

c) during flying insect's forward translation, spatiotemporal statistical fluctuations are caused by nearby objects, probably leading to the detection of relevant objects [172];

a new methodology, based on a sequential real-time computation of the image's power spectra, is here proposed. Through a direct image's spatiotemporal analysis, we expect it to give an indication about the proximity of obstacles on the captured images. The methodology will be tested in a variety of distinct visual scenarios before being applied in a robotic platform, as a collision detection system.

5.3 Methods and Materials

Figure 5.1 summarizes the algorithm proposed in this chapter and depicts the connection among the different parts that integrate it. It is mainly composed by two distinct parts, I and II, which will be described in detail in the following.

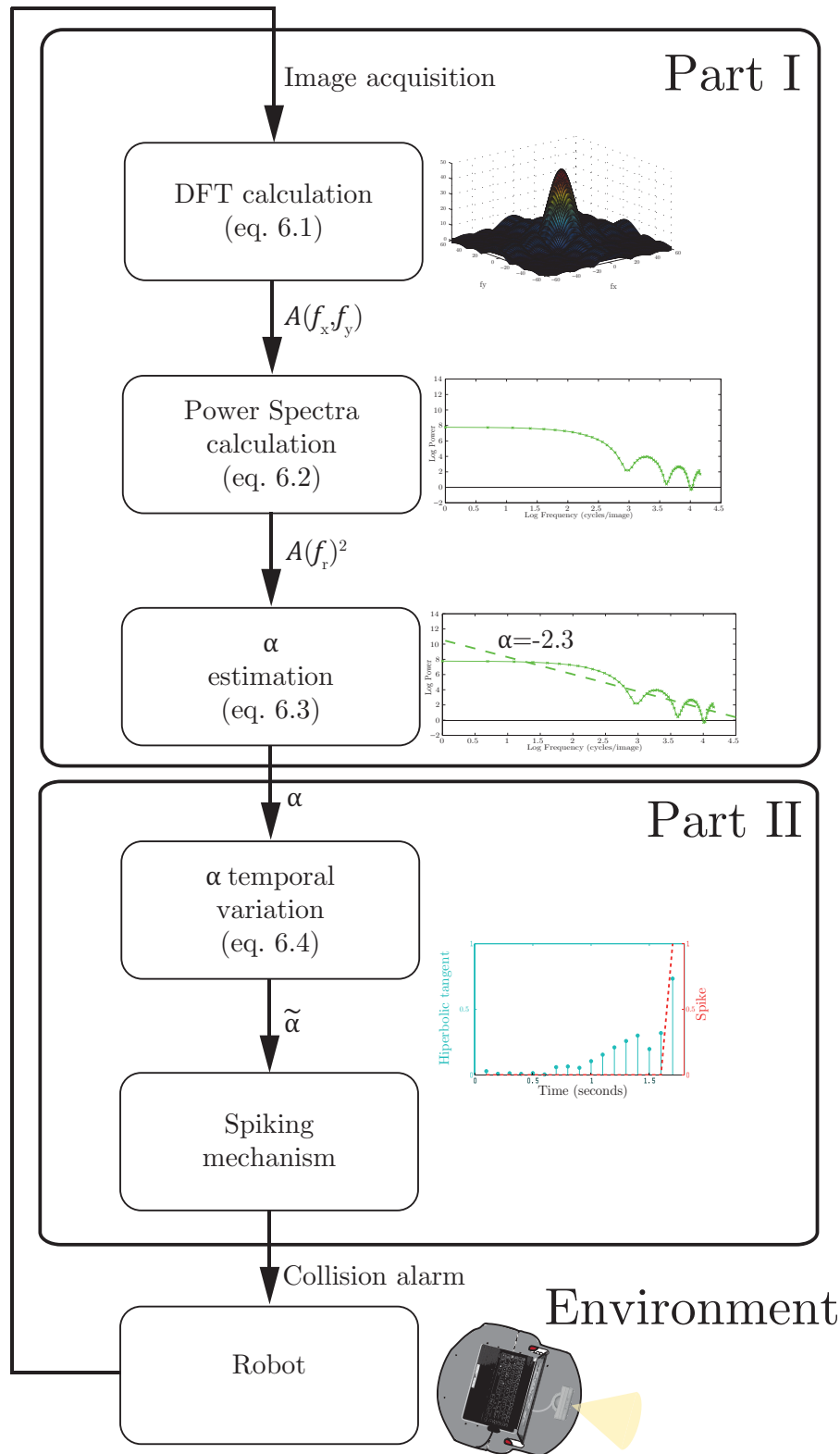


Figure 5.1: Schematic illustration of the proposed algorithm divided in the different parts that integrate it.

5.3.1 Part I: Power spectrum estimation through polynomial curve fitting

At first, an image is acquired, converted to a gray scale, and the algorithm here proposed starts by computing the Discrete Fourier Transform (DFT) of each image (which should previously be set squared through zero pad if needed), through:

$$\begin{aligned} \text{DFT}_t(f_x, f_y) &= \sum_{x=0}^{N-1} \sum_{y=0}^{N-1} I_t(x, y) g(x, y) e^{-j\frac{2\pi}{N^2}(f_x x + f_y y)} \\ &= A(f_x, f_y) e^{j\Phi(f_x, f_y)} \end{aligned} \quad (5.1)$$

where $I_t(x, y)$ denotes the intensity of the pixel in the (x, y) position, at time instant t ; f_x and f_y denote the spatial frequencies in x and y directions; $g(x, y)$ is a Gaussian window used to reduce boundary effects. $N \times N$ indicates the image size.

The complex function $\text{DFT}(f_x, f_y)$ is the discrete Fourier transform that can be decomposed into two real terms: $A(f_x, f_y) = |\text{DFT}_t(f_x, f_y)|$, the amplitude spectrum of the image, and $\Phi(f_x, f_y)$ is the phase function of the discrete Fourier transform. $\Phi(f_x, f_y)$ represents the information relative to the local properties of the image, containing information about the form and position of image components. On the other hand, $A(f_x, f_y)$ contains unlocalized information about the image structure, representing the spatial frequencies spread all over the image. Information about smoothness, length, orientation and width of the contours contained on the image scene is given by $A(f_x, f_y)$.

The squared magnitude of the DFT, or power spectrum (PS), gives the distribution of the energy of the signals at different spatial frequencies, being represented as:

$$\text{PS}_t(f_x, f_y) = A(f_x, f_y)^2 \quad (5.2)$$

providing a scene representation invariant to object arrangements or object identities. PS encodes only information about the dominant structural patterns on the image [1, 9].

By unfolding the square amplitude of the DFT from Polar to Cartesian coordinates, and performing a rotational average within the two-dimensional Fourier plane, the PS from equation 5.2 is reduced to a one-dimensional function of spatial frequencies, $f_r = \sqrt{f_x^2 + f_y^2}$. Then, using the polyfit function, from MATLAB®[118] curve fitting toolbox, the relationship between the power obtained for each spatial frequency can be approximated by a polynomial function, of degree one, that minimizes the sum of the squares of the difference between the observed data and the fitting function obtained.

The fitting obtained can be described as:

$$\log(\text{PS}_{t,r}) \approx \log(O) - \alpha_t \log(f_r) \quad (5.3)$$

where PS_t is computed by a least square fit of a linear function to $\log(f_r)$, with slope equal to $-\alpha$, and offset O , which is an arbitrary constant that depends on scene log contrast [169].

According to literature, α value depends on many factors, as image depth, image blurring, sparseness of local structures, among other characteristics [54, 114, 164, 203]. In some situations tested, the function that describes the relationship between the power spectra for each spatial frequency is not perfectly linear. The overall quality of the linear fit, measured through the correlation coefficient R , was calculated for all the experiments here described. Notice that R was superior to 0.7 for the entire set of experiments performed.

5.3.2 Part II: Processing α -value and Information Extraction

Image's power spectra is expected to vary during movement on the scenery, over time.

In order to understand how the power spectrum varies in time in the scenery, the power spectrum slope α is observed and processed as follows.

To extract α -value variations, the bias must be removed through:

$$\tilde{\alpha}_t = \left| \alpha_t - \frac{1}{n} \sum_{i=t-n}^{t-1} \alpha_i \right| \quad (5.4)$$

where n is the number of samples used to compute the α mean value over n time steps, being set as: $n = \text{camera frame rate}/5$ (value computed by a trial and error process).

The $\tilde{\alpha}_t$ value is then transformed into a spiking (or pulse) output using an Hyperbolic Tangent transformation, through:

$$ht_f = \tanh(W_I \times \tilde{\alpha}_t) \quad (5.5)$$

in which W_I is the weight factor for the α -value computed at each frame, and is set to 5, by trial and error, in our experiments. Since $\tilde{\alpha}_t$ is always greater than, or equal to zero, the Hyperbolic Tangent $ht_f \in [0, 1]$.

The spiking mechanism¹ output works as a collision alarm. If the Hyperbolic

¹spiking mechanism could be replaced by pulse mechanism, but due to the biological mechanisms

Tangent transformation value ht_f exceeds the threshold T_s , a spike is produced:

$$s_f = \begin{cases} 1 & \text{if } ht_f \geq T_s \\ 0 & \text{if } ht_f < T_s \end{cases} \quad (5.6)$$

If a spike is produced, a collision alarm will be triggered. For instance, in case of a collision detection mechanism for a robot, the collision alarm would result in a motor command to control the robot, making it to stop. In the experiments, T_s is 0.7.

5.3.3 Experimental setup

Both simulated and real image sequences have been used in this work. For simplification, we have decided to divide the experiments performed on three different sets, being named as condition 1, 2 and 3. In all conditions, the computer used is a Laptop (Toshiba Portégé R830-10R) with 4 GHz CPUs and Windows 7 operating system.

Condition 1 (C1): Artificial image sequences captured by an artificial camera

In a first stage, artificial image sequences were created using MATLAB® [118]. The simulated environment created enables the adjustment of several parameters, such as: image noise level; number, size, shape, texture, distance of objects; contrast; among other characteristics. Additionally, movement (at different speeds), as well as trajectories with different complexity levels could be added to the objects present on the artificial image sequences created. Image sequences were captured by a simulated camera with 60° field of view in both vertical and horizontal direction, an image size of 100 × 100 pixels and a sampling frequency of 100 frames per second.

A looming object, with a specific half length l and moving at a constant speed v , shows a typical rate of expansion, with a slow initial angular speed that rapidly increases as the object is getting closer to the camera. The angular size subtended at the camera by an approaching object is given by:

$$\theta(t) = 2 \cdot \tan^{-1}(l/vt) \quad (5.7)$$

in which t denotes the Time-To-Collision (TTC) of the object in relation to the camera, conventionally chosen to be negative prior to collision. Velocity is negative for an object approaching and positive to an object receding. In a looming approach, typical in collision scenarios, both the angular size ($\theta(t)$) and the angular expansion rate are non-linear functions of time, whose temporal dynamics solely depend on $l/|v|$

involved we kept this nomenclature

ratio. Based on this physical principle, looming, receding and translating trajectories were created, for different $l/|v|$ ratios of the visual stimuli.

Each frame of the video sequence created is read on MATLAB® [118], where all the operations described on subsections 5.3.1 and 5.3.2 were sequentially performed.

In a first stage (*C1-1*), it was analyzed how α value depends on the size that the object occupies on the image. A simulated approaching square, moving at a speed (v) of 2 m/s, was created.

In a second stage (*C1-2*), using artificial images, we aim to verify α value immunity to: image contrast (ranging from 0.1 (low contrast) to 0.9 (high contrast)) and image noise level (ranging from 1 to 50% of image salt-and-pepper noise pixels). Salt-and-pepper noise was chosen due to its intensity spiking characteristic, which may lead to the production of false collision alarms. Considering a robotic perspective, this is a commonly verified noise form, caused by malfunctioning camera's sensor cells, by memory cell failure or by synchronization errors in the image digitization and transmission. For that, a sequence showing a looming square, approaching at two different $l/|v|$ ratios (25 and 50ms) was used. Then, increasing percentages of salt-and-pepper noise (here named No), ranging from 1% to 50% of figure pixels were added to the images sequence. A combined noise level increment and subsequent image contrast (named Co) decrement, as what happens when light level on the environment decreases, was used to prove the effectiveness of the proposed algorithm to work at different light intensities.

Then, keeping a high contrast ($Co = 1$) and a low noise level ($No = 0\%$), and by using distinct object's approaching speed (1, 2 and 5 m/s) and sizes (4 and 6 degrees of object initial angular size), through a trial and error iterative process, n , W_I and T_s parameter's values, able to fit all situations tested, were obtained.

Condition 2 (C2): Realistic artificial image sequences and real image sequences captured by a simulated and a real camera

In order to analyze the variation of parameters $\tilde{\alpha}$, ht and s in more realistic visual scenarios, in an initial phase (*C2-1*), shadow effects, as well as a 3D perspective view was added to the simulated video sequence. But in stage *C2-1*, image sequences were only composed by foreground objects, being the background uniform.

In a second phase (*C2-2*), a complex background was added to one of the image sequences developed on *C2-1*. The background complexity (c_t) was measured in terms of the standard deviation of the brightness of all pixels on the image, through:

$$c_t = \sqrt{\frac{1}{N^2} \sum_{(x,y)} (I_t(x,y) - \frac{1}{N^2} \sum_{(x,y)} I_t(x,y))^2} \quad (5.8)$$

that results in a value of 39.2. Additionally, in this situation, the camera moves on the environment, approaching the static object (foreground) over a complex environment (background). The video sequence generated was captured by an artificial camera with an original 320×180 resolution, and a sampling rate of 30 frames/s.

In order to analyze the variations on the algorithm parameters $\widetilde{\alpha}_t$, ht and s , as well as the time of computation required, in *C2-3* both simulated (*C2-3-1*) and real video sequences (*C2-3-2*) of collision scenarios were projected on a screen (LG Fatron E2441), being captured by the PlayStation Eye camera, located at 5 cm away from the screen, at 10 frames/s (see figure 5.2).

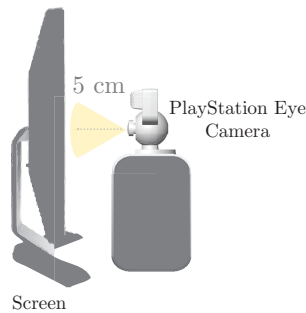


Figure 5.2: Setup used on condition *C2-3*.

Condition 3 (C3): Camera mounted on the robot captures images of the real environment

Using robotic experiments, we wanted to determine if the method here proposed could serve as a useful collision avoidance system for a robot running autonomously. For that, a Pioneer 3-DX robot was placed in a real lab environment. A PlayStation Eye digital camera was used to capture the visual information from the environment. The resolution of the captured images was 320×240 pixels, a field of view of 75 degrees, with an acquisition frequency of 10 frames per second. Each captured image was read on MATLAB [118], in real time. According to the final output value, s_f , a respective command was sent to the Pioneer robot's wheels via a serial port through an RS232 cable: if $s_f = 0$ the robot keeps its linear velocity; if $s_f = 1$, the linear velocity is set to zero, and the robot stops immediately.

Table 5.1 summarizes all the conditions previously described.

Table 5.1: Summary of the conditions created to test the proposed algorithm.

Condition	Nomenclature	Visual scenery	Goal	Part
1	<i>C1</i>	Artificial image sequences captured by an artificial camera	Analyze how α value varies according to the image sequence.	I, II
	<i>C1-1 + C1-2</i>	A simulated approaching square moving at 2 m/s	α value dependence on square size.	I
		Different noise levels (No)	α value immunity to noise (No) and image contrast (Co).	
		Different image contrast (Co)	Find values for parameters: n , W_I and T_s .	II
2	<i>C2</i>	More realistic and real image scenarios captured by a static and a moving artificial and real camera.		
	<i>C2-1</i>	Only foreground objects artificial camera		
	<i>C2-2</i>	Add complex backgrounds moving artificial camera	Verify if the methodology can work as a collision detection mechanism in a high range of different scenarios.	I and II
	<i>C2-3-1</i>	Use artificial images captured by a static real camera		
	<i>C2-3-2</i>	Use real images captured by a real camera		
3	<i>C3</i>	Camera mounted on a real robot, capturing online visual scenes.	Test the methodology as a collision detector applied to a real robot.	I and II

5.4 Results and Discussion

Results to Condition 1:

In order to analyze how α -value changes as an object approaches to the camera, stimulus *C1-1* was used.

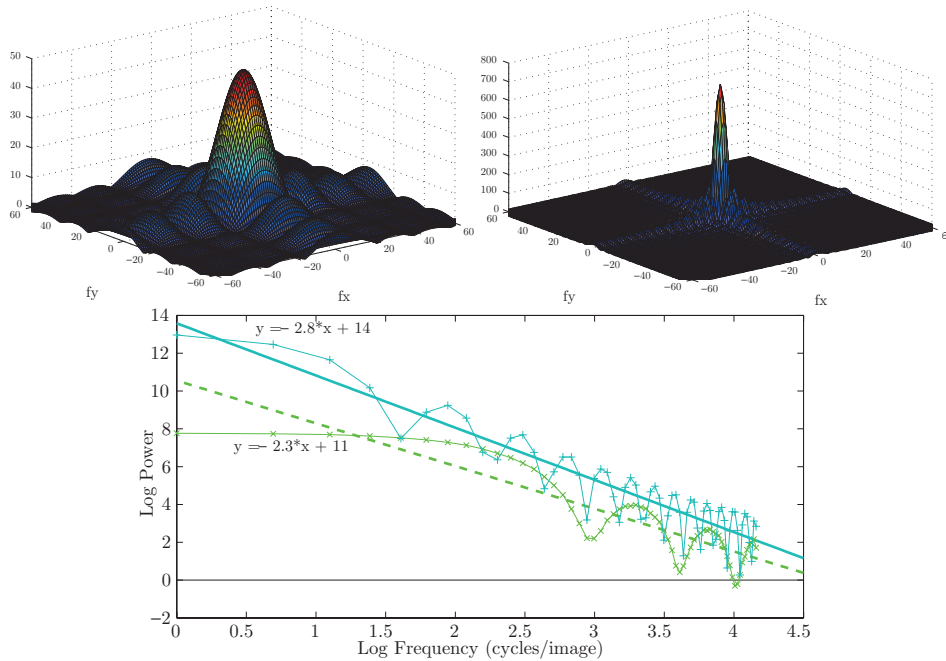


Figure 5.3: Spectral analysis of a looming square, when its dimension is 7 by 7 pixels (top, left) and 27 by 27 pixels (top, right). Bottom graph: Plus signal blue line: results from the 27×27 pixels object size, fitted with the linear function $\log(\text{PS}) = -2.8 \times \log(f_r) + \log(14)$, with $\alpha = -2.8$, and a correlation coefficient $R=0.8626$; Crossed green line: results from the 7×7 pixels object size, fitted with the linear function $\log(\text{PS}) = -2.3 \times \log(f_r) + \log(11)$, with $\alpha = -2.3$ and $R=0.8092$.

Analyzing figure 5.3, we verify that the absolute value of the averaged power spectra (α) follows the increment on the angular size of the visual stimuli, taking absolute higher values as the object approaches the camera ($|\alpha| = 2.3$ for object area equal to 7×7 pixels and $|\alpha| = 2.8$ when the object covers an area of 27×27 pixels).

Additionally to the approaching situation, objects performing receding and translation trajectories have been created. According to the obtained results, α -value tends to increase as the object approaches, being an indicator of object proximity. On the other hand, for the receding situation tested, α value tends to decrease, directly following the decrement on object angular size.

Finally, a square performing a translation was created. The simulated object performed a translational trajectory at 1 meter to the camera, moving at a speed of 1m/s. Results show that, the α -value's standard deviation across the entire translation was $\simeq 0.0078$, being much more constant for a translation than for an approaching (standard deviation $\simeq 0.19$), as expected.

At condition *C1-2*, attention was focused in verifying if the algorithm here proposed is capable of correctly detecting an approaching object, when the images are corrupted by salt-and-pepper noise with increasing noise ratios and decrements on image contrast. Results on figure 5.4 shows that absolute α values are highly immune to noise increment and contrast decrements, following the object approach by an increment on α value, being highly similar to the results obtained for the maximum contrast ($C=1$) and when no noise is present on the image sequence ($N=0\%$) (figure 5.4, green continuous line).

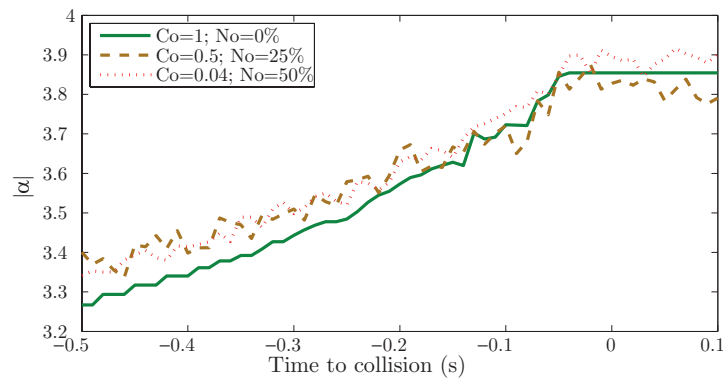


Figure 5.4: Absolute slope value $|\alpha|$ obtained for each frame of the image sequence, at condition *C1-2*, as the object is approaching the camera. Green continuous line: α value obtained, at each time step, for the square approaching the camera, at 2 m/s (*C1-1*), when image contrast $Co=1$ and when noise is absent in the entire image ($No=0\%$), representing, respectively, the optimal conditions of contrast and noise. Yellow dashed line: same configuration, but Co decreased to half (0.5) and 25% of the image is composed by noisy pixels. Red pointed line: same configuration, but Co decreased to very low values (0.04) and noise increased to 50% of the image pixels.

Based on the results obtained for the simulated images, we conclude that, in fact, α value is a good indicator of object proximity.

Results to Condition 2:

C2-1: One approaching ball was introduced in the green visual scene, with a 5 cm size, and approaching at 0.36 m/s, approximately (fig. 5.5, top snapshots).

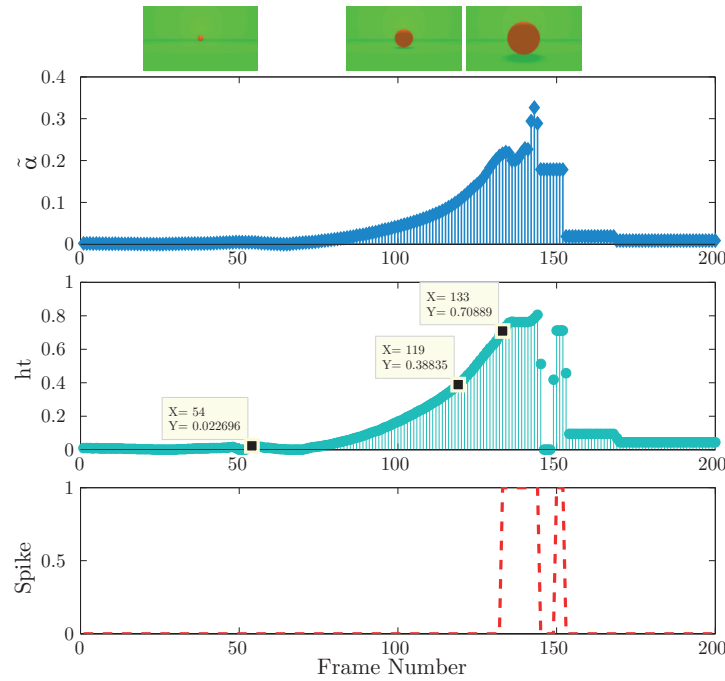


Figure 5.5: Slope variation value ($\tilde{\alpha}_t$, top graph), hyperbolic tangent transformation value (ht , middle graph) and spike output (s , bottom graph) obtained for each frame of the C2-1 image sequence. Three important frame numbers are pointed out on the graph, and the correspondent video frames are sequentially disposed on the image top.

Figure 5.5 shows the obtained values of $\tilde{\alpha}_t$, ht and s for each frame of the image sequence previously described. Important time instants were highlighted in the hyperbolic tangent transformation output graph. As observed on the first two graphs, the increment on object size as it approaches the camera leads to a subsequent increment on both $\tilde{\alpha}_t$ and ht values. The bottom graph shows us that a spike was produced for frame $f = 133$, signaling the moment at which the approaching ball was already close to the camera (third video frame, on figure 5.5).

Then, all values suddenly decreased (for $f \geq 153$) when the ball passed the camera virtual position, disappearing from its field of view. The results obtained enabled us to verify the feasibility of the proposed algorithm, as a good indicator of the proximity of the objects in more realistic scenery (shadow inclusion).

C2-2: Two conditions were modified: motion of the artificial camera and background complexity (fig. 5.6).

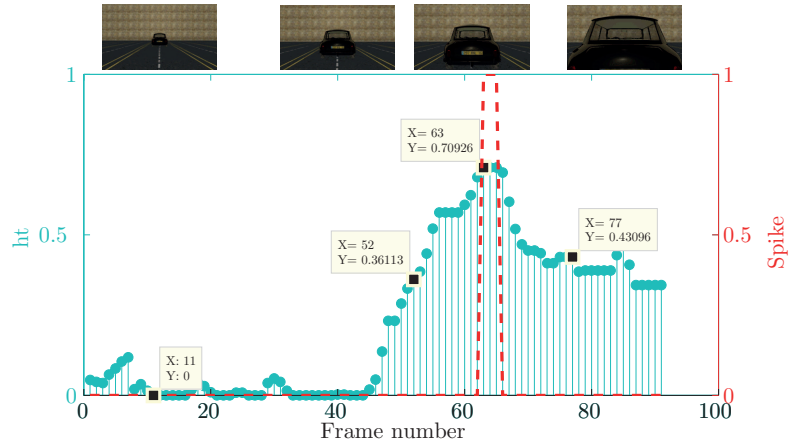


Figure 5.6: Hyperbolic Tangent transformation (ht , left axis, blue dots) and spike (s , right axis, dashed red line) values obtained for the images captured by a camera approaching a car located inside a complex environment (C2-2). Four important frame instants are pointed out on the graph, and the correspondent video frames are sequentially disposed on the image top.

Figure 5.6 shows, that even when movement type (the environment is static and the camera is moving) and complexity conditions were changed (inclusion of a non-uniform background), a spike is produced (at frame 63) when the moving camera position is very close to the stationary car.

C2-3-1: This condition verifies acquisitions with a real camera. Images were captured at 10 frames per second (fps), meaning that a frame is captured within 0.1 seconds after the previous frame had been obtained. In this case, all computations required for the collision estimation must also be completed within 0.1 seconds.

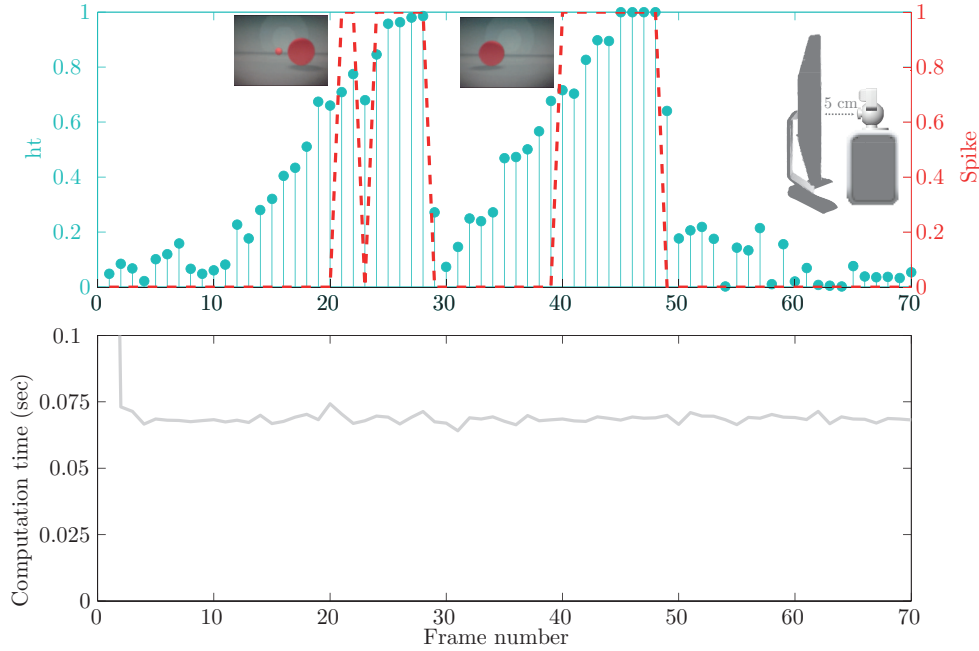


Figure 5.7: Top Panel: Hyperbolic Tangent transformation (ht , left axis, blue dots) and spike (s , right axis, dashed red line) values obtained for the images projected on a screen and captured by the PlayStation Eye camera, showing two balls approaching the camera (C2-3-1). The video frames relative to the moments when the first spikes ($f = 21$ and 40) for the first and second approaching ball, were produced, are shown. The illustration presented on the right side of the top panel represents the experimental setup used on the experiment. Bottom panel: representation of the computation time required to run the proposed algorithm at each frame of the video sequence.

Top panel of figure 5.7 shows the effectiveness of the proposed method in detecting collision of both approaching balls (at $f = 21$ and $f = 40$). Additionally, the computation times of the operations computed for each frame are presented on the bottom panel of figure 5.7. As the computation time required is always lower ($\simeq 0.075$ seconds) than the camera acquisition frequency, the proposed algorithm is able to run in real-time.

C2-3-2: In a second stage, the real image sequence showing a car approaching to the camera, was recorded by the PlayStation Eye camera, with the configuration previously used and represented on figure 5.8.

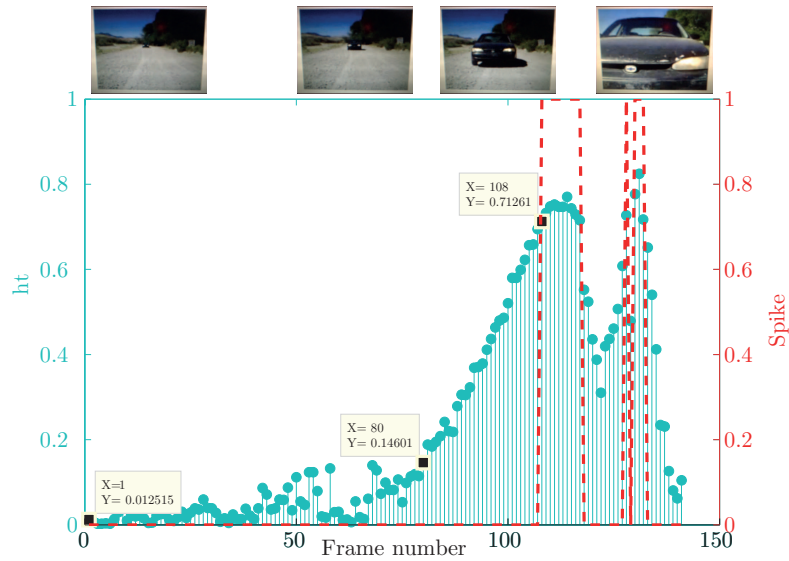


Figure 5.8: Hyperbolic Tangent transformation (ht , left axis, blue dots) and spike (s , right axis, dashed red line) values obtained for the real images projected on a screen and captured by the PlayStation Eye camera, showing a real car approaching the stationary camera (C2-3-2). The first spike was produced at frame 108.

Observing figure 5.8, the first spike was produced at frame 108, when the moving car reached an angular size of 29 degrees on the camera image, being a good indicator of an eminent collision.

This experiment proves the efficiency of the algorithm here proposed to work in a real environment, at real time.

Results to Condition 3:

The environment where the robot was placed was relatively simple, composed by a uniform wall where three different paper squares, with different textures (striped and uniformly colored) and colors, were attached. Figure 5.9 shows the results obtained for the mentioned situation.

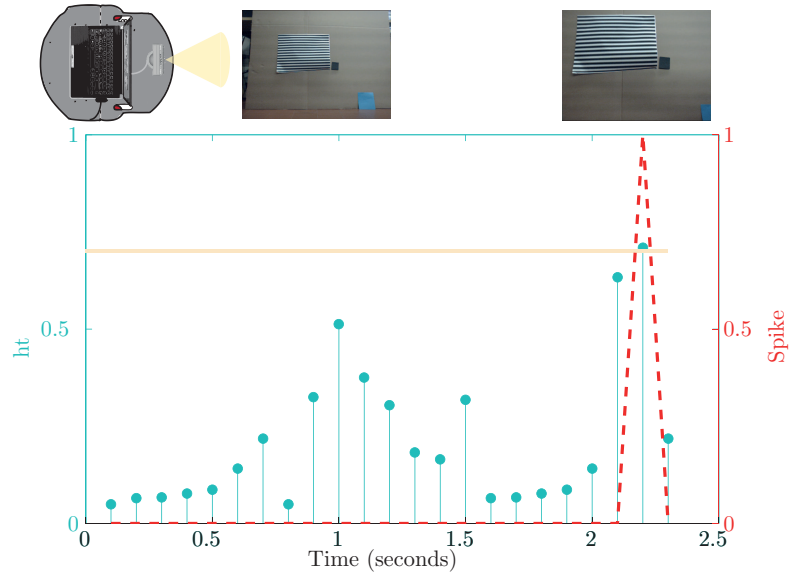


Figure 5.9: Hyperbolic Tangent transformation (ht , left axis, blue dots) and spike (s , right axis, dashed red line) obtained for the images captured by a camera placed on a Pioneer robot, moving forward in a real lab environment. The continuous line represents the T_s value (0.7). On the top of the graph, two instantaneous frames represent the images captured at 0.1 and 2.2 seconds, respectively. A spike was produced at 2.2 seconds, when the object was located at approximately 10 cm to the wall, leading the robot to stop. The illustration presented on the left side of the top panel represents the experimental setup used on the experiment.

Similarly to previous results, figure 5.9 shows that the hyperbolic tangent transformation value, and the subsequent spike output, is a good indicator of a potential collision. Along the time interval between 0 and 1 seconds, ht amplitude (equation 5.5) started to slowly increase as the robot was getting closer to the objects attached on the viewing wall. For time instants between 1 and 1.5 seconds, there is a small decrement on the ht value, because the blue object located initially inside the camera field-of-view, started to continuously laying outside the camera visual range as the robot was moving forward. Then, for time instants superior to 2 seconds, the ht amplitude started to increase rapidly as the robot was getting closer to the objects attached on the wall. Finally, a spike was produced when the robot was located at, approximately, 10 cm away from the wall. Subsequently, the robot linear velocity was immediately set to zero, being sent to the robot wheels, making it to stop at a safe distance from the obstacle.

Besides the robotic experiment performed inside a relatively simple environment,

an additional experiment was performed. In this second situation, the robot was located inside a completely random environment.

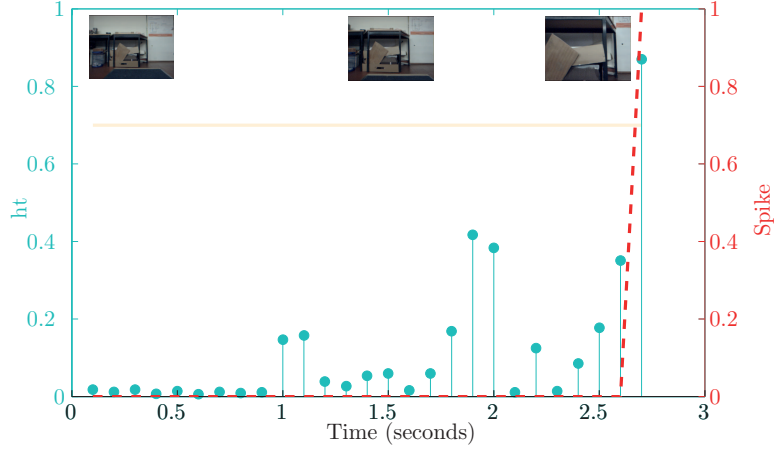


Figure 5.10: Hyperbolic Tangent transformation (ht , left axis, blue dots) and spike (s , right axis, dashed red line) obtained for the images captured by a camera placed on a Pioneer robot, moving forward in a real complex environment. The continuous line represents the T_s value (0.7). On the top of the graph, two instantaneous frames represent the images captured at 0.1 and 1.5 and 2.7 seconds, respectively. A spike was produced at 2.7 seconds, when the object was located at approximately 15 cm to the objects.

Figure 5.10 shows the effectiveness of the proposed algorithm in avoiding collisions, even in situations where the complexity of the experiment is clearly high. In the present experiment, the robot was moving directly to a table with multiple and non-uniform objects located below it. Despite the non-uniformity of the objects, as well as the high complexity on its shapes, a collision was correctly detected when the robot was located at 15 cm to the obstacle.

According to these results, the method proposed in this work can be definitely useful in providing information about the safety of the robot trajectory path.

5.5 Conclusions

In this chapter, a simple method of visual sensory processing is proposed and described, being easily applied to a mobile platform. For that, a detailed analysis of the spatiotemporal variation of the image's power spectra, computed for a high range of different image sequences, have been performed. Distinct visual scenarios were

constructed - simulation - and recorded - in real environments. Based on the results obtained, we have demonstrated that our approach is able to correctly detect any obstacle or approaching object, regardless of the color, shape or physical characteristics of these objects. The algorithm is very general and when applied to a real robot demonstrated its capability to work in real-time and to correctly decide when the robot should stop.

As future work, we will continue to investigate the response of the method proposed for a range of robot speeds, environment complexities and objects moving inside the camera's field of view. Additionally, we will try to enlarge the robot behavioral adaptations, by controlling the robot speed accordingly to the Hyperbolic Tangent Transformation values. Finally, we would like to integrate the algorithm here proposed in different fields of research, as car safety, exploratory mission, among others.

Chapter 6

Vision at low light intensity

As a neural pathways specialized in the detection of potential collisions, it is highly important to maintain its reliability apart of the environmental conditions, or at least for a certain niche. Thus, it is especially important for its function to remain undisrupted by noise increment, as it happens when day light decreases. The LGMD is an integrating neuron, which output depends on the signals produced at each layer of the locust optic lobe: the photoreceptive layer, the lamina layer, and the medulla layer. When corrupted, signals produced at different neural stages can affect and compromise the final response of the LGMD neuron.

As locusts have apposition compound eyes, highly tuned to activity during day light, one should expect these insects to be inactive at low light levels. The scarcity of light and consequent increment of visual noise, would make locust vision unreliable. As a consequence, the detection of potential collisions or obstacles would be highly fallible at night. However, it was found that locusts are able to perform migrations at low level intensities, taking advantages of the benefits of night foraging . As a consequence, an inevitable question arose: How are locusts able to improve their visual capabilities in dim light? In order to function efficiently at low light levels, the visual signal captured has to be maximized and, simultaneously, the noise necessarily needs to be minimized.

A deep research focused on insect vision adaptation to lighting conditions[214] found that, to see at night, the visual system should capture as much light as possible. In order to accomplish this, two strategies can be performed. Optical apparatus adaptations, which enables the collection of more photons within the eye. Unfortunately, this solution alone is not sufficient for improving the reliability of vision at very low light conditions. The ultimate solution is to optimize sensitivity at low light intensities via neural adaptations.

Being interested in the development of a real-time light adaptation system, and

taking into consideration that actual digital cameras still rely on a single exposure time, as well as on image sensors with photo elements of uniform sensitivity, the second strategy should be adopted. However, since there is not a well-established paradigm for this light adaptation mechanism via neural adaptations, verified in some flying insect, behavioral experiments/assessment should be performed in order to establish it.

However, due to the difficult problem of performing behavioral tests with animals as inconstant as locusts, a different animal model, having similar physiological and neural characteristics, was chosen: bumblebees. In fact, bumblebees *Bombus Terrestris* have become increasingly common as a model organism in behavioral studies. Particularly because it is easier to train these insects to fly in a specific and controlled environment, and, subsequently, to relate the environmental conditions to their flying characteristics and, through this, infer about potential adaptations at the neural level.

6.1 Introduction

It is well known that diurnal, as well as nocturnal insects, use information from self-induced image motion, or optic flow, to control ground speed and position during flight [7, 12, 43, 48, 141, 193]. When flying in an enclosed space, bees tend to fly through the center by balancing the rate of image motion perceived by each one of the compound eyes, . This “centering response” acts to guide the bee down a safe path in, for example, a narrow flight tunnel [103, 173, 191, 193].

In bumblebees, the precision of this centering response is dependent on the spatial frequency of the visual stimulus [43]. At low spatial frequencies, bees that are allowed to fly through a tunnel with one wall lined with a black and white, sinusoidal pattern of a specific spatial frequency, and the other wall lined with a gray uniform pattern, will fly closer to the gray wall. However, as the spatial frequency is increased, the bias towards the gray wall decreases, probably because the bees can no longer resolve the gratings [43].

As the light intensity decreases, the precision of the centering response in bumblebees will be negatively affected and the bees can be observed to slow down. The decrease in flight speed is most likely a behavioral adaptation that allows them to fly in dim light. However, the decreased centering performance suggests that a lower flight speed is not sufficient to support a faultless flight in dim light [145].

The transition to a dim-light environment is a complex phenomenon for insects with apposition compound eyes that typically has a low absolute sensitivity to light.

The decreased photon capture rate experienced at lower light levels will unconditionally result in a noise level increment, reducing the ability to resolve contrast [214, 215]. However, the sensitivity of the system can be increased by increase in photon-catch area [221]. Therefore, nocturnal insects feature larger ommatidial facets compared to their diurnal relatives of similar size [92, 99, 100, 122, 123]. These differences also exist within a single species: large individuals of the bumblebee *Bombus Terrestris* have larger eyes with wider facets and wider rhabdoms compared to their small conspecifics and also forage at lower light levels [98]. However, this documented difference in optical lens and rhabdom diameter cannot fully account for the higher light sensitivity observed in bigger individuals. It has therefore been suggested that neuronal modifications should also be present, enabling day active bumblebees to extend their activity to low light conditions [212, 214].

A neural solution to enhance sensitivity of an eye is to extend the integration time, during which a sample of photons is counted by the visual system. This neuronal process, termed “temporal summation” acts to increase the signal-to-noise ratio of lower temporal frequencies, but comes at a price: it reduces the capacity of the animals to detect fast moving objects. A recent study shows that bumblebees compensate for this by a reduction in flight speed as the light level falls, making the world to move more slowly across the retina of the bee [145].

A second neural possible solution to extend the sensitivity of the visual system is to sum output of neighboring ommatidia [128, 201, 212, 214]. This process termed “spatial summation” increases photon capture and image brightness, but will unavoidably make the visual scene blurrier and coarser. The higher the spatial summation, the lower the spatial resolution. For maximum sensitivity at each light intensity level, the relative amount of spatial and temporal summation depends, at least theoretically, on the image velocity experienced by the animal [104].

For example, increased image motion decreases the gain from temporal summation, and to counteract this, the eye has to sum more extensively in space, and vice versa. Thus, at each light level, it appears to be a trade-off between spatial and temporal summation, which depends on the spatial (pattern) and temporal (speed) characteristics of the captured images. However, nothing is known about the relative contributions of spatial and temporal integration at different light levels. According to this, the aim of this investigation is to infer the trade-offs between spatial and temporal neural summation strategies, applied by the visual flight-control system of the day-active bumblebee *Bombus Terrestris*.

6.2 Materials and Methods

Animals and Environment

A bumblebee hive (*Bombus Terrestris*), from a commercial breeder (Natupol Beehive, Koppert B.V., The Netherlands) was placed close to the entrance of a 200 cm long, 30 cm wide and 30 cm high flight tunnel, covered with insect netting (see fig.6.1). The walls and the floor of the tunnel were dressed with black and white sinusoidal gratings of different spatial frequencies (0.05, 0.1, 0.4, 0.8, 1.2 and 1.6 cycles/cm) or with uniform gray patterns (corresponding to a spatial frequency of 0 cycles/cm). For a bee flying through the center of the tunnel, the spatial frequency of the sinusoidal gratings would appear as 0.01, 0.03, 0.1, 0.21, 0.31 and 0.42 cycles/deg, respectively.

The bees were kept in a 18h:7h light:dark cycle in a controlled laboratory environment (22° C, 44% air humidity, 994 hPa ambient pressure) and trained to fly through the tunnel to a sugar and pollen feeder at the end of the tunnel (indicated on figure 6.1).

Each bee was marked with a numbered and colored tag, which was attached to their thorax, for identification. This enabled us to identify the individuals in the experiments, as well as to count the number of individual bees recorded during a specific combination of light intensity and spatial frequency pattern.

Dimmable fluorescent lamps (BIOLUX[®], OSRAM GmbH, Munich, Germany) covered with white diffusion filters (LEE 252 Eight White Diffusion, LEE Filters, UK) illuminated the tunnel from above. All experiments were performed under three light conditions: 600, 60 and 6 lux (as measured from the center of the tunnel). In order to reach the lowest light intensity (6 lux), the lamps were fitted with a neutral density filter (210 0.6 ND, LEE filters, UK). Each experimental trial lasted for one hour, and before recording commenced, the bumblebees were allowed to adapt to the test light intensity for 30 minutes. Bumblebee flight towards the feeder were recorded at 60 Hz (1281 × 306 pixels) with a high-speed digital video camera (MotionBLITZ EoSens[®] mini, Miktron GmbH, Unterschleisheim, Germany), mounted above the tunnel. At 6 lux, two infrared illuminators (IR Illuminator silver, TV6700, Abus, Elfa Distraltec AB, Järfälla, Sweden) were used to improve the signal to noise ratio in the images captured by the camera.

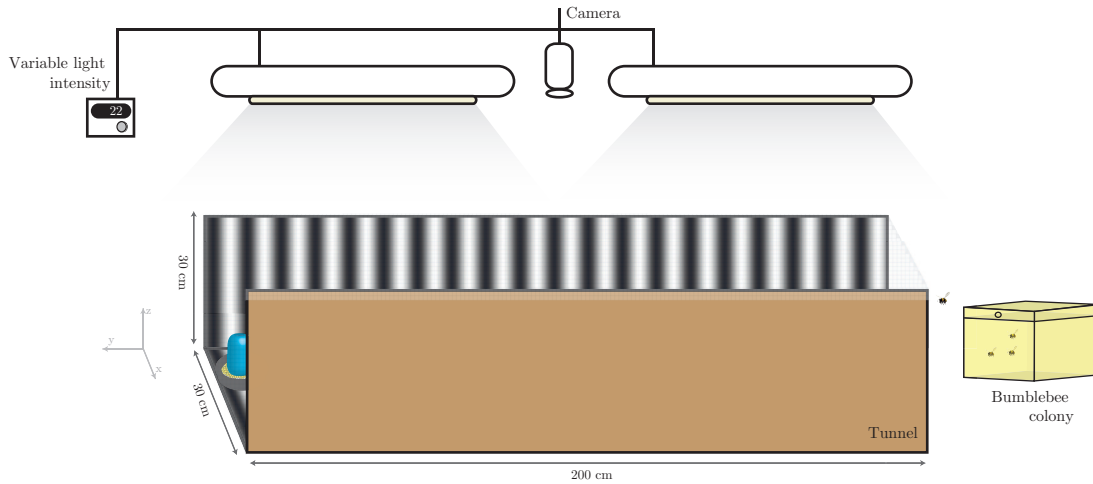


Figure 6.1: Experimental setup.

Experimental procedures

Experiment 1: To analyze the effect of light intensity and spatial frequency on ground speed control, we recorded bumblebees flying in a tunnel (see above) with walls and floor lined with sinusoidal grating patterns of different spatial frequencies (ranging from 0.05 to 1.6 cycles/cm). In each condition, the same pattern lined both walls and the floor.

Experiment 2: To analyze the effect of light intensity and spatial frequency on position control, we recorded bumblebees flying in a tunnel (see above), in which one of the walls (left or right) was lined with a black and white sinusoidal grating pattern of a specific spatial frequency (ranging from 0.05 to 1.6 cycles/cm). The other wall and the floor were covered with uniform gray patterns (corresponding to a spatial frequency of 0 cycles/cm).

All experimental conditions in experiment 1 and 2 were presented at three different light intensities (ranging from 6 to 600 lux), being randomized over the days to avoid circadian influences on the results.

Data analysis

In each video frame, the centre of mass (in x- and y- coordinates) of the bumblebee was determined using an automated tracking program [113].

The flight trajectories were analyzed over a distance of 80 cm: 40 cm before and 40 cm after the midsection of the tunnel. Position data was converted from pixels

to millimeters using a reference pattern placed at 15 cm above the tunnel floor (the approximate height of the flight trajectories). Ground speed was calculated by dividing the two dimensional distance traveled between successive frames (including the forward and lateral components) by the frame duration (1/60 s). The centering response was analyzed by finding the distance from the midline of the bee in each frame. For both ground speed and centring, an average value or standard deviation for each flight of each bee was calculated and used in the analyzes.

All statistical tests were performed in Matlab® [118]. The Shapiro-Wilk test [175] verified that the data was normally distributed. Parametric one-way and two way ANOVA comparisons with light intensity (three levels) and spatial frequency (six levels) as two factors and flights (evaluated in terms of speed and position) as repeated measurements were carried out to determine the effect of these two factors on speed and position control. The Tukey-Kramer method was used to perform multiple comparisons between experimental trials. A linear regression of the mean ground speed against spatial frequency was performed (Curve Fitting Toolbox™ [118]).

The comparison between the response, in terms of speed, and an Elementary Motion Detector (EMD) model output was made taking into account the mean-square error (MSE, [118]).

Estimation of angular spatial frequency, image angular velocity and temporal frequency

It was of interest to estimate the angular spatial frequency (in cycles/deg), the angular velocity of the image (the speed of the image on the retina) and the temporal frequency (Hz) of the periodic stimulus conditions here used. First, we estimated the apparent spatial frequencies, in the lateral field of view (90 degrees) through:

$$f_{\text{ang}} = \arctan\left(\frac{1}{2d}\right) \times f \quad (6.1)$$

where f_{ang} is the angular spatial frequency (in cycles/deg), f is the spatial frequency in cycles/cm and d is equal to the distance between the bee's position and the tunnel wall (left or right) (in cm).

The image angular velocity (ν , in deg/s) was computed using the following relationship:

$$\nu = \left(\frac{360}{2\pi}\right) \times \left(\frac{V_x}{d}\right) \quad (6.2)$$

where V_x is the linear ground speed of the bee (in cm/s), and d is the variable previously described.

The temporal frequency (cycles/s or Hz) is then computed through:

$$\omega = \nu \times f_{\text{ang}} \quad (6.3)$$

giving the information of how many complete stimulus periods have been seen by the bumblebee, for each second.

6.3 Results

Experiment 1: effect of light intensity and spatial frequency on bumblebee ground speed and position

To analyze the effect of light intensity and spatial frequency on ground speed control, we recorded bumblebees flying through a narrow tunnel at three different light intensities: 6, 60 and 600 lux. The walls and the floor of the tunnel were lined with patterns of different spatial frequencies (ranging from 0.05 to 1.6 cycles/cm). In each condition, the same pattern lined both walls and floor (see Methods, experiment 1).

In the first stage of this experiment, we compared the position and ground speeds of bees flying in the experimental tunnel, with the configuration shown on the left panel of figure 6.7, when its walls and floor were covered with sinusoidal patterns with spatial frequencies ranging from 0 to 1.6 cycles/cm, at the maximum light intensity level (600 lux). The number of flights (n), as well as the number of different bees (N) for the conditions tested are summarized on table 6.1.

For the tunnel configuration used on Experiment 1 (figure 6.7, left panel), we would expect bumblebees to fly through the center of the tunnel, independently of the pattern's spatial frequency. However, for the highest light intensity tested, our results show a statistical difference ($F=12.15$, $P<0.0001$) of the mean centering position according to the tunnel's spatial frequency. For $0.8 < f \leq 1.2$ cycles/cm, bumblebees tend to deviate from the tunnel center, probably due to the difficulty on seeing the high frequency of visual patterns covering the tunnel wall, leading them to deviate to a preferred side (figure 6.2). Following this strategy, and as the apparent spatial frequency is inversely proportional to the distance to the tunnel walls (see equation 6.1), bumblebees will be able to decrease the apparent spatial frequency of the wall they tend to fly closer, restoring the visual information to the insect so that it is able to control its flight in a more precise way. This shift to one preferred wall side can be

Table 6.1: Number of animals, per experimental condition.

Spatial frequency (f) (cycles/cm)		Light intensity (lux)					
		600		60		6	
		Flights (n)	N ^o bees (N)	Flights	N ^o bees	Flights	N ^o bees
Experiment 1	0 (gray)	23	9	13	5	9	7
	0.05	39	27	28	20	7	7
	0.1	36	25	44	22	15	5
	0.4	33	17	42	18	17	9
	0.8	26	15	29	18	2	1
	1.2	15	11	19	9	2	2
	1.6	37	18	30	16	2	2
Experiment 2	0.05	29	10	23	9	4	4
	0.1	18	7	16	3	8	5
	0.4	36	10	22	15	3	3
	0.8	16	9	12	5	22	7
	1.2	35	10	23	11	9	7
	1.6	22	7	20	3	24	5

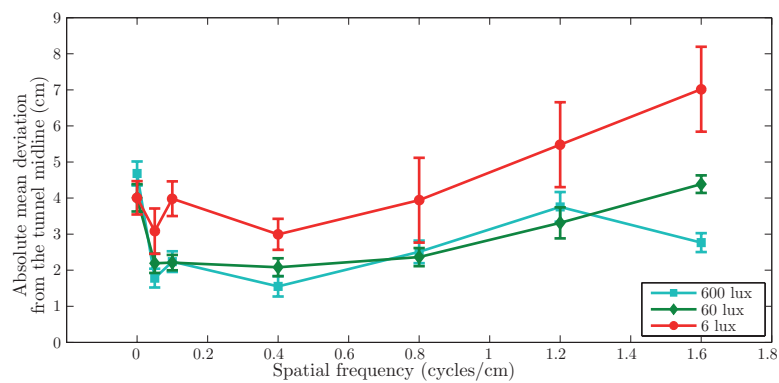


Figure 6.2: Effect of spatial frequency and light intensity on lateral position. The mean position at 600 lux (blue squares), 60 lux (green diamonds) and 6 lux (red dots) is plotted against spatial frequency. Error bars indicate mean standard errors.

the result of some type of visual lateralization, already reported on literature as being present on some invertebrate animals ([112]).

Similarly, for the other two light intensities tested, the mean lateral distance to the tunnel midline of flying bumblebee dependence on the tunnel spatial frequency is also statistically significant ($P < 0.0001$ for 60 lux and $P = 0.008$ for 6 lux), probably as a result of the large deviation verified for spatial frequency values superior than 0.8 cycles/cm. Additionally, we verified that, for each tunnel's spatial frequency configuration of 0.05, 0.1, 0.4 and 1.6 cycles/cm, decrements on light intensity does affect significantly bumblebee's mean centering position ($P < 0.02$). On the other hand, the effect is not statistically significant for spatial frequencies of 0, 0.8 and 1.2 cycles/cm ($P > 0.05$).

Due to the lateral deviation verified, the apparent spatial frequencies seen by bumblebee's left and right eye are different, being computed using equation 6.1.

As previously seen, individual flies seem to deviate from the tunnel midline (see figure 6.3, both panels). The standard deviation of each bumblebee gives an indication of how straight individual bees are flying for a given combination of spatial frequency and light intensity. According to the results obtained for the spatial frequencies represented on figure 6.3, individual bees flight straighter for the higher light intensities (the standard deviation is lower at 600 lux). As light intensity decreases, a higher number of distinct positions are taken by individual bees across flight. This leads to the conclusion that bees tend to decrease its position control at lower light levels.

Additionally, individual flies seem to have a preferred range of speed (see figure 6.4) in specific spatial and light intensity tunnel's characteristics. This mean preferred ground speed varied to a larger extent between individuals for higher tunnel's spatial frequency (figure 6.4, bottom panel).

Our results also show that ground speed is affected by the spatial frequency of the patterns covering the tunnel walls ($N = 113$, $F = 9.94$, $P < 0.0001$), but not in such a way that simply decreases or increases with a rise in spatial frequency (figure 6.5).

We also find that the ground speed for each spatial frequency decreases with decreasing light intensity. This result is consistent with the results of earlier studies [8, 145]. Interestingly, the effect of light intensity on ground speed strongly depended on the spatial frequency presented to the bee ($F = 4.67$, $P < 0.0001$, multi-way ANOVA, see figure 6.5).

Based on these results, we were able to compute the temporal frequencies experienced by the flying bumblebees (using equation 6.3), at each experimental condition of combined tunnel's spatial frequency and light intensity. For 600 lux, temporal

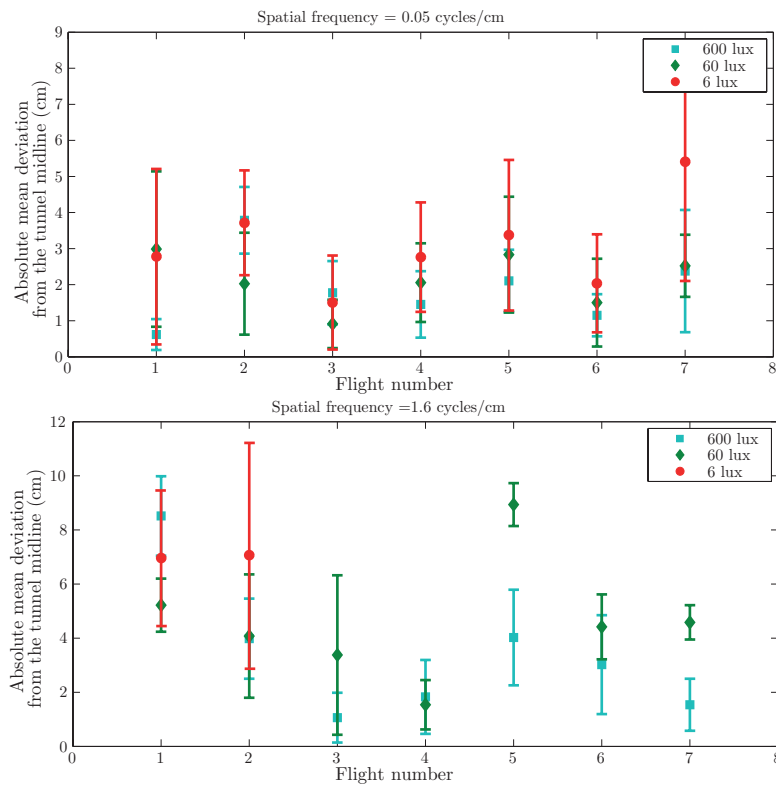


Figure 6.3: Examples of absolute mean (\pm standard deviation) deviation from the tunnel midline, for a tunnel's spatial frequency of 0.05 cycles/cm (top panel) and 1.6 cycles/cm (bottom panel), at: Blue squares: 600 lux; Green diamonds: 60 lux; Red dots: 6 lux.

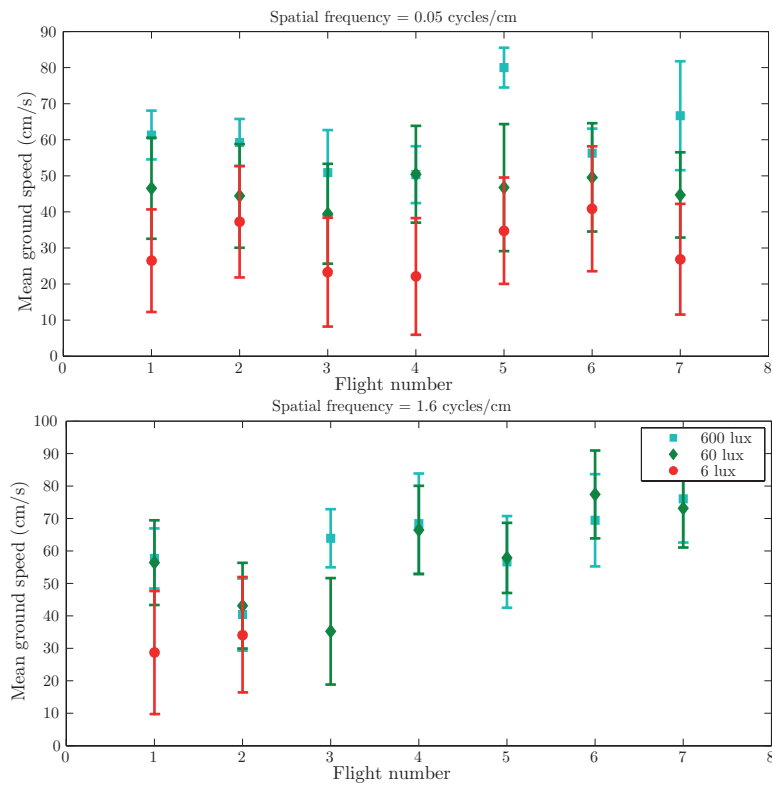


Figure 6.4: Examples of absolute mean (\pm standard deviation) ground speed, for a tunnel's spatial frequency of 0.05 cycles/cm (top panel) and 1.6 cycles/cm (bottom panel), at: Blue squares: 600 lux; Green diamonds: 60 lux; Red dots: 6 lux.

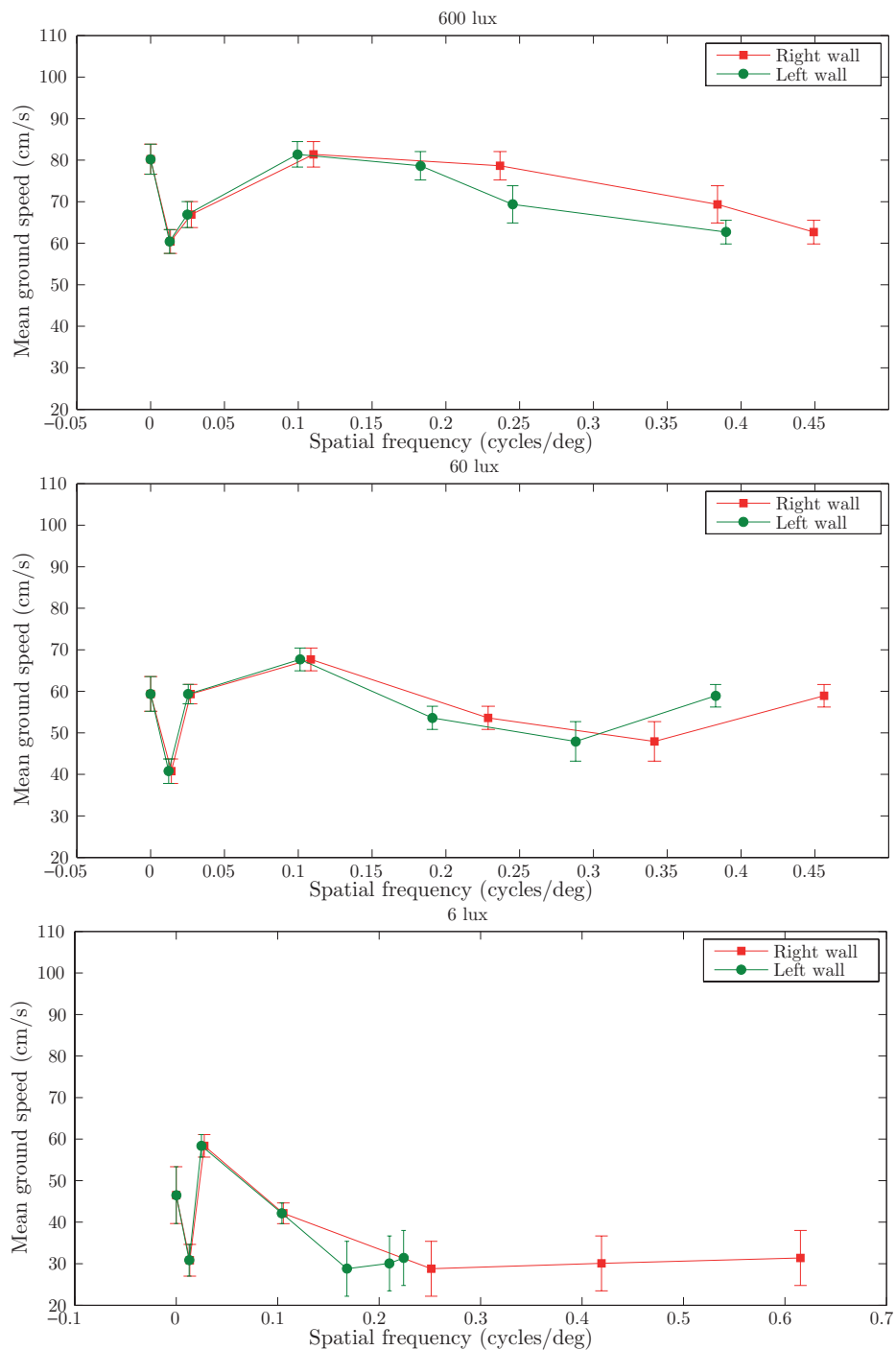


Figure 6.5: The effect of spatial frequency on bumblebee flight speed, at 600 (top), 60 (middle) and 6 lux (bottom). Red squares: mean ground speed, for spatial frequencies seen by the bumblebee's right eye. Green dots: mean ground speed, for spatial frequencies seen by the bumblebee's left eye. Error bars indicate mean standard errors.

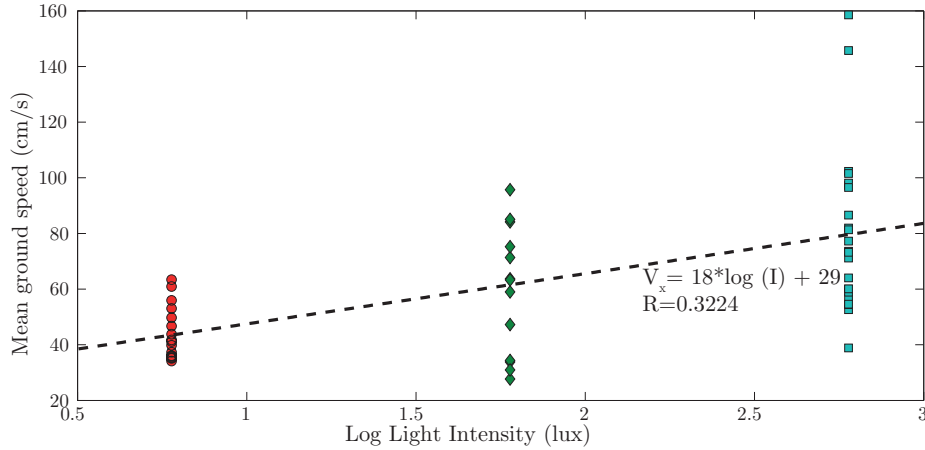


Figure 6.6: The effect of light intensity on mean ground speed, when both tunnel walls and floor are covered with uniform gray patterns.

frequency (ω) values ranged between 3 ($f = 0.05$ cycles/cm) and 100 Hz ($f = 1.6$ cycles/cm). For 60 lux, $2 \leq \omega \leq 95$ Hz and, for the lowest light intensity tested, $1.5 \leq \omega \leq 50$ Hz.

To understand how light intensity affects ground speed in the absence of visual cues, we recorded bumblebees when flying along tunnels with gray patterns on the walls and floor. Even in the absence of strong visual cues, the flight speed of bumblebees was affected by light intensity (figure 6.6).

For an object moving with an angular velocity ν (deg/s, equation 6.2), during one integration time Δt (s), the image is displaced an angular distance of $\nu\Delta t$ degrees on the retina [188, 214]. Assuming that the temporal response function of the bumblebee's photoreceptors is modeled as a Gaussian of half width $\nu\Delta t$, and considering the results when the tunnel was lined with gray patterns (figure 6.6), where the application of spatial summation strategies will not compromise the spatial properties of the tunnel (it is null), the spatio-temporal resolution of the bumblebee's visual system can be uniquely modeled by the temporal summation applied. Taking into consideration that, through a behavioral adaptation, bumblebee's are trying to keep the image displaced on its retina constant at different light intensity levels, and, knowing that for a normal light intensity level the bee acquisition frequency is ≈ 100 Hz (leading to a temporal integration of $\Delta t = 1/100 = 0.01$ seconds), then:

$$\begin{aligned}
 (\nu\Delta t)_{600} &= (\nu\Delta t)_{60} \Leftrightarrow \\
 \Leftrightarrow 306 \times 0.01 &= 122.23 \times \Delta t_{60} \Leftrightarrow \\
 \Leftrightarrow \Delta t_{60} &= 0.014 \text{ seconds}
 \end{aligned}$$

The same procedure was repeated for the 6 lux, resulting in $\Delta t_6 = 0.025$ seconds. Through a combination of flying speed adaptation, merged with the application of temporal summation strategies, bumblebees are able to keep the level of image blur constant at the different light levels here tested.

Experiment 2: effect of light intensity and spatial frequency on bumblebee centering response and speed

In Experiment 2, we recorded the flight trajectories of bumblebees flying through the experimental tunnel when only one wall displayed a sinusoidal pattern (ranging from 0.05 to 1.6 cycles/cm, depending on experimental condition). The other wall and the floor were uniform gray. When the sinusoidal pattern displayed low spatial frequencies, the bees flew closer to the uniform gray wall, a result that is consistent with earlier investigations into bumblebee centring behaviour [43] ($N=54$, $F=4.92$, $P<0.0001$, see figure 6.7). Furthermore, this response was consistent across all three light intensities. At higher spatial frequencies, the bees flew closer to the midline of the tunnel. This is what we expect if the bees can no longer resolve the gratings due to the limitation of the spatial resolution of their eyes [109, 115] and thus perceive the grating pattern as being uniformly gray [43]. This provides us with a tool to investigate the resolution limit of the visual system of the flying bees under different light intensities.

Following this line of thought, results plotted on figure 6.8 were used to compute the resolution of the bee's eyes at different light levels. By computing the higher angular spatial frequency (f_{sang}) that can be accurately detected by the mosaic of photoreceptors, through:

$$f_{sang} = \frac{1}{2 \times \Delta\phi} \quad (6.4)$$

where $\Delta\phi$ represents the interommatidial angle (angle between two photoreceptors), we conclude that, for different light intensities, the resolution limit of the bee visual system for flight control decrease with falling light levels. For 600 lux, the lowest difference value plotted on figure 6.8, being directly correlated to f_{sang} , is located for apparent spatial frequency values between 0.2 and 0.4 cycles/deg, resulting in $1.2 \leq \Delta\phi \leq 2.5$. At 60 lux, $0.1 \leq f_{sang} \leq 0.3$, resulting in $1.7 \leq \Delta\phi \leq 5$ and, finally, for 6 lux $0.04 \leq f_{sang} \leq 0.1$, leading to $5 \leq \Delta\phi \leq 12.5$.

Through this behavioral performance at different light intensities, we can infer that the applied spatial summation does affect the spatial characteristics of the visual scene viewed by flying bumblebees.

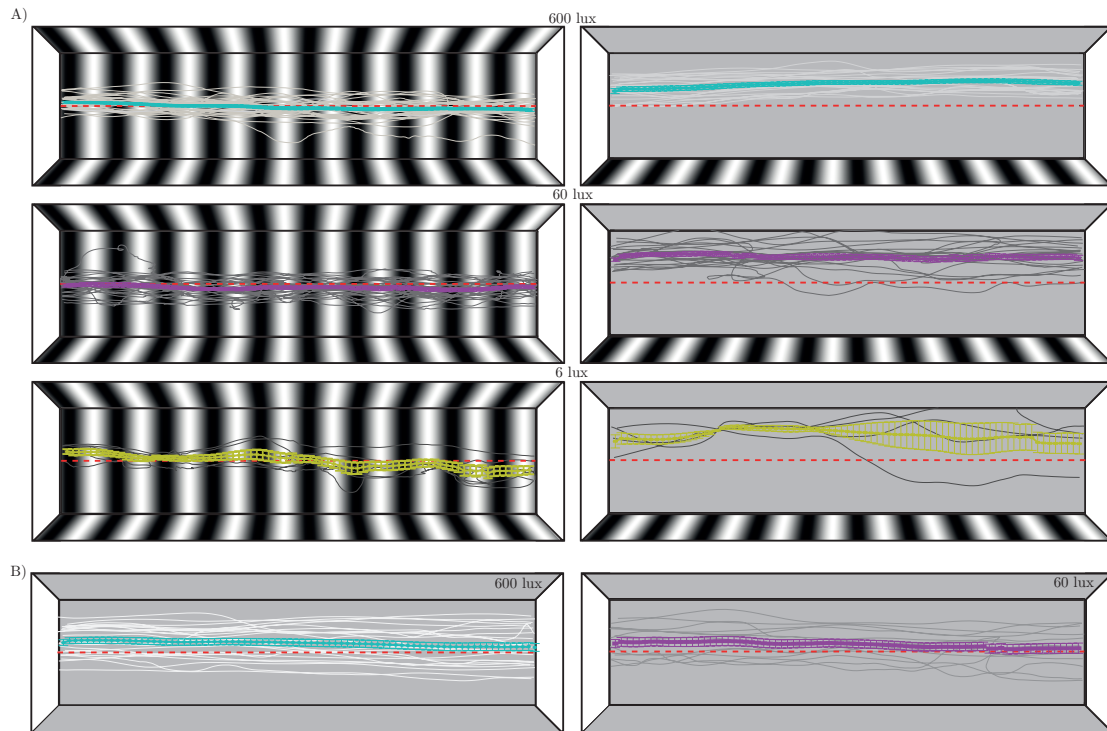


Figure 6.7: Representations of distinct tunnel configurations on: Panel A) Experiment 1 (Left panel) and Experiment 2 (Right panel). Flight trajectories when the tunnel walls and floor are covered with 0.05 cycles/cm sinusoidal gratings (left panel - Experiment 1) and when the tunnel floor and one of the walls are covered with uniform gray patterns (right panel - Experiment 2), recorded at three different light intensities (top-down: 600, 60, and 6 lux, respectively). Panel B) Flight trajectories recorded when tunnel walls and floor were covered with uniform gray patterns, at 600 lux (left) and 60 lux (right), respectively.

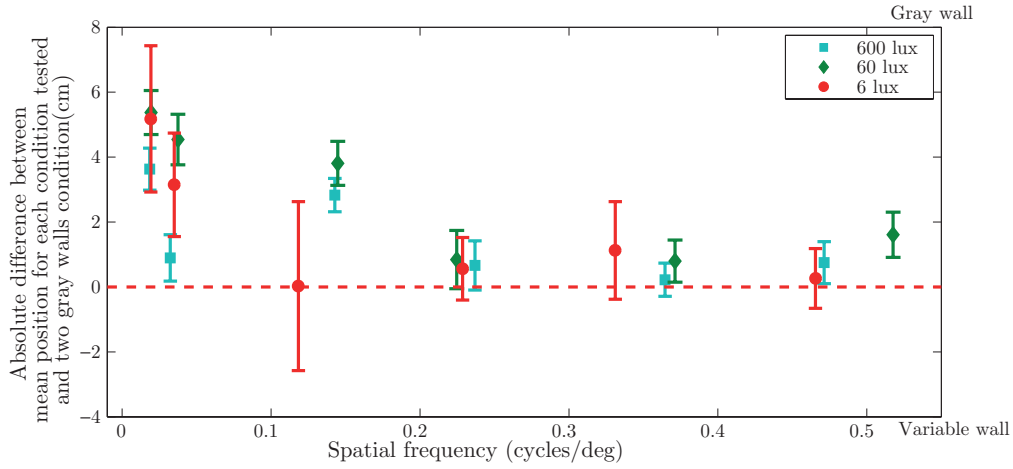


Figure 6.8: The effect of spatial frequency on lateral position. The absolute difference between the mean position for each condition of spatial frequency and light intensity, and mean position obtained when both walls were lined with uniform gray patterns, recorded at the each of the light intensities tested, are plotted. Error bars indicate mean standard errors.

On the other hand, different tunnel spatial frequencies had no significant effect on the mean ground speed of flying bumblebees (see figure 6.9, $P > 0.05$), at the different light intensities tested, when subjected at Experiment 2.

Modeling the effect of light intensity and spatial frequency on bumblebee flight control

There is strong evidence that biological motion detectors function by correlating the time-delayed outputs of adjacent photoreceptors [19]. The outputs of these detectors, while motion sensitive, are generally dependent on the spatial and temporal frequency of the stimulus.

In fact, the average response, R , of an Elementary Motion Detector (EMD) or Reichardt correlator [147], which is a motion sensitive detector present on the insect's visual system, is a function of the input pattern's angular velocity (ν , degrees/s) and spatial wavelength ($\lambda = 1/f_{\text{ang}}$, degrees), and three detector variables: the angular separation of input elements ($\Delta\phi$, degrees), the width of the angular sensitivity ($\Delta\rho$, degrees) of the input elements, and the time constant (τ , seconds) [23, 44, 81, 147]:

$$R \approx \frac{1}{\sqrt{(1 + (2\pi\tau\nu/\lambda)^2)}} \times \sin\left(\arctan\left(\frac{2\pi\tau\nu}{\lambda}\right)\right) \times \sin\left(\frac{2\pi\Delta\phi}{\lambda}\right) \times \frac{1}{\sqrt{(1 + (\Delta\rho/\lambda)^2)}} \quad (6.5)$$

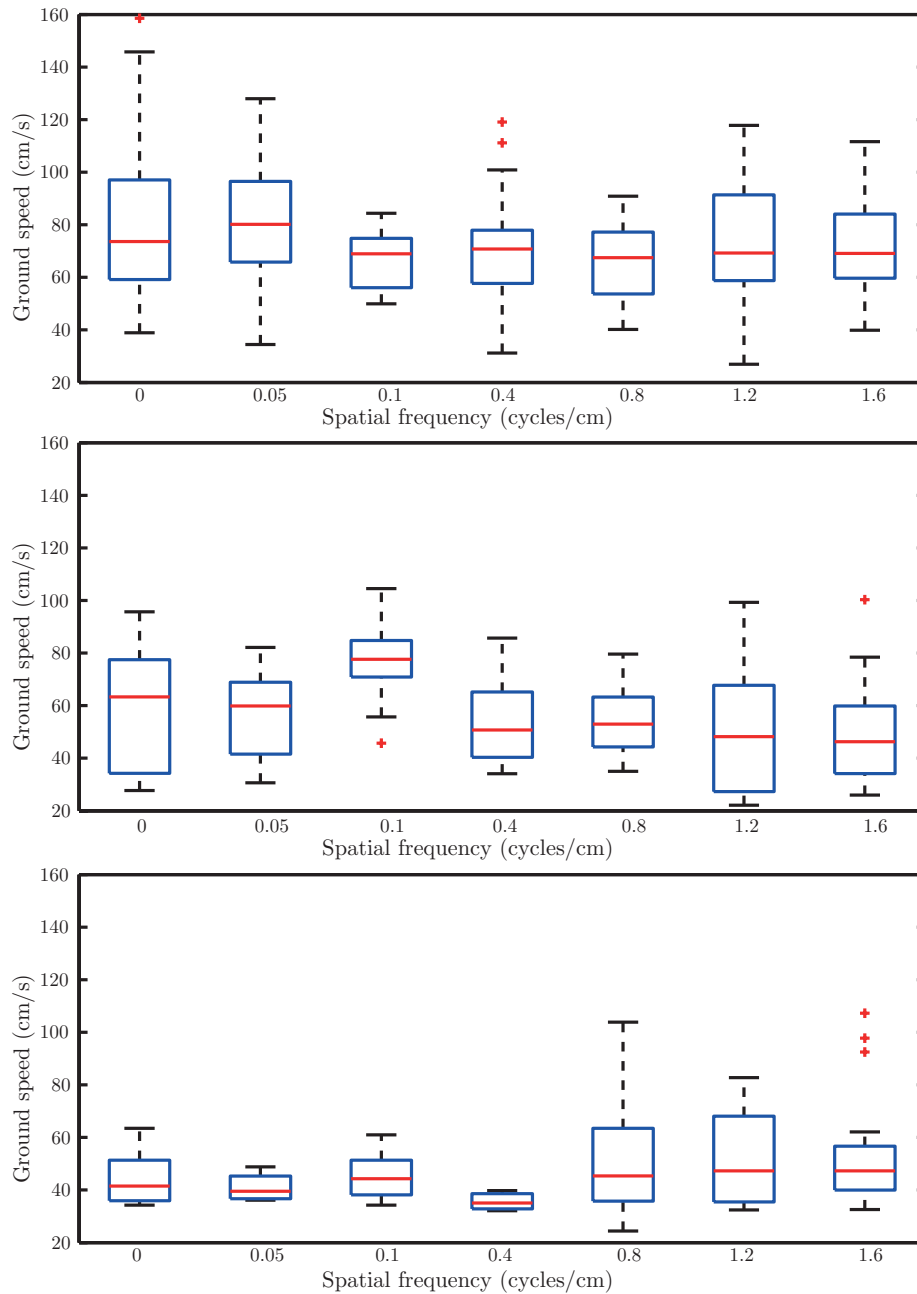


Figure 6.9: Median ground speed in tunnels with Experiment 2 configuration, for light intensities of 600 lux (top), 60 lux (middle) and 6 lux (bottom).

The first term of the equation represents the amplitude factor of the EMD first-order low-pass filter, which depends on the temporal frequency (ω) of the input signal, *i.e.*, the number of luminance cycles that pass an EMD input element, per second: $\omega = \nu/\lambda$. $\sin(\arctan(\frac{2\pi\tau\nu}{\lambda}))$ is the temporal frequency term, being responsible for tuning the EMD to an optimal temporal frequency. The interference term, $\sin(\frac{2\pi\Delta\phi}{\lambda})$, provides a quantitative prediction of the EMD response variation with λ . When patterns have wavelengths in the range $\Delta\phi < \lambda < 2\Delta\phi$, the sign of the EMD response will be inverted, being referred as spatial aliasing (or geometric interference). The last term, $\frac{1}{\sqrt{(1+(\Delta\rho/\lambda)^2)}}$ is a spatial low-pass filter, being responsible to modulate the EMD response.

First, we have tried to determine the temporal and spatial properties of the bumblebees visual system, at the highest light intensity tested. In relation to the spatial properties, the model response R represents a low-pass filtered version of the geometric interaction between the bumblebee's sampling array and the periodic sinusoidal pattern. By varying the angular separation $\Delta\phi$ between the range values previously indicated through the results obtained on Experiment 2 ($1.2 \leq \Delta\phi \leq 2.5$, increment steps of 0.1 degrees), using angular sensitivity values determined by: $\Delta\rho = 2\Delta\phi$, and, finally, through a comparison of the model output with the biological responses (figure 6.5), the spatial parameters which output gives the best fitting to the biological results, were found (see table 6.2).

The temporal terms of the EMD model (equation 6.5), which together generate a characteristic output, resembling a symmetric band-pass filter, with a maximum amplitude at a specific temporal frequency whose value depends on the time constant τ , were then analyzed. The τ value was systematically varied, in steps of 1 millisecond, until the response optimum corresponded to that of the maximum biological response, obtained for the highest light intensity tested.

As represented in figure 6.10, the biological response is best fitted by: $\Delta\phi = 1.4$ degrees, $\Delta\rho = 2.8$ degrees and $\tau = 10$ ms, values that are consistent with values that have previously been proposed [81, 115].

We then performed the same procedure for the data at 60 lux. Figure 6.11 shows that, in this condition, the model values that best fit the biological response, are different. As expected [104, 213, 214], both "optimal" spatial and temporal parameters increased leading to an increment on the ommatidial acceptance angle, $\Delta\rho = 5.6$ degrees and a higher integration time $\tau = 15$ ms.[81, 115].

At the lowest light intensity, spatial and temporal parameters increased even more when compared to the values obtained at 600 and 60 lux: the acceptance angle in-

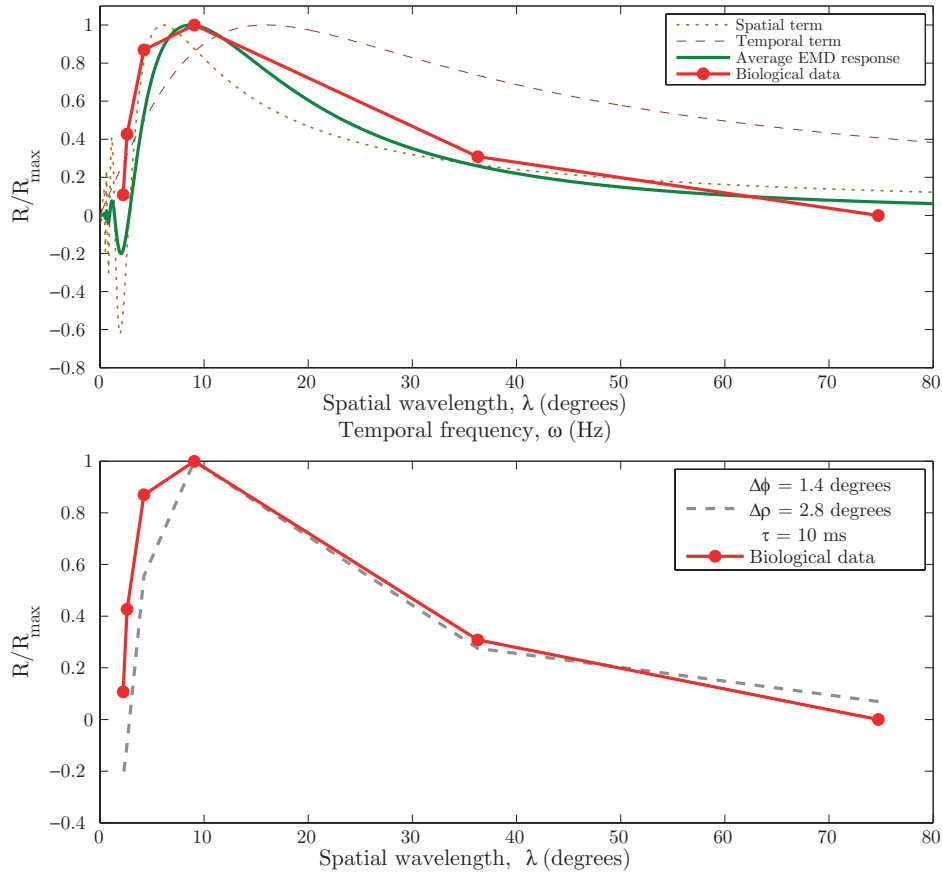


Figure 6.10: Experimental biological data, recorded at 600 lux, and predicted EMD model response (R), as a function of: Top: spatial wavelength (λ) and temporal frequency (ω). Bottom: spatial wavelength (λ). In both graphs, R model output, as well as mean ground speed values - biological data - have been normalized. Top panel: both λ and ω values, used to find the model parameters ($\Delta\phi$, $\Delta\rho$ and τ) that best fits the biological response, ranged from 0.02 to 100, in steps of 0.1 degrees (λ) or Hz (ω). Bottom panel: both λ and ω values used to compute model response (R) were computed using the data from the biological experiments (using equations 6.1, 6.2 and 6.3). Mean square error (MSE) between model response (R) and biological data is 0.0441.

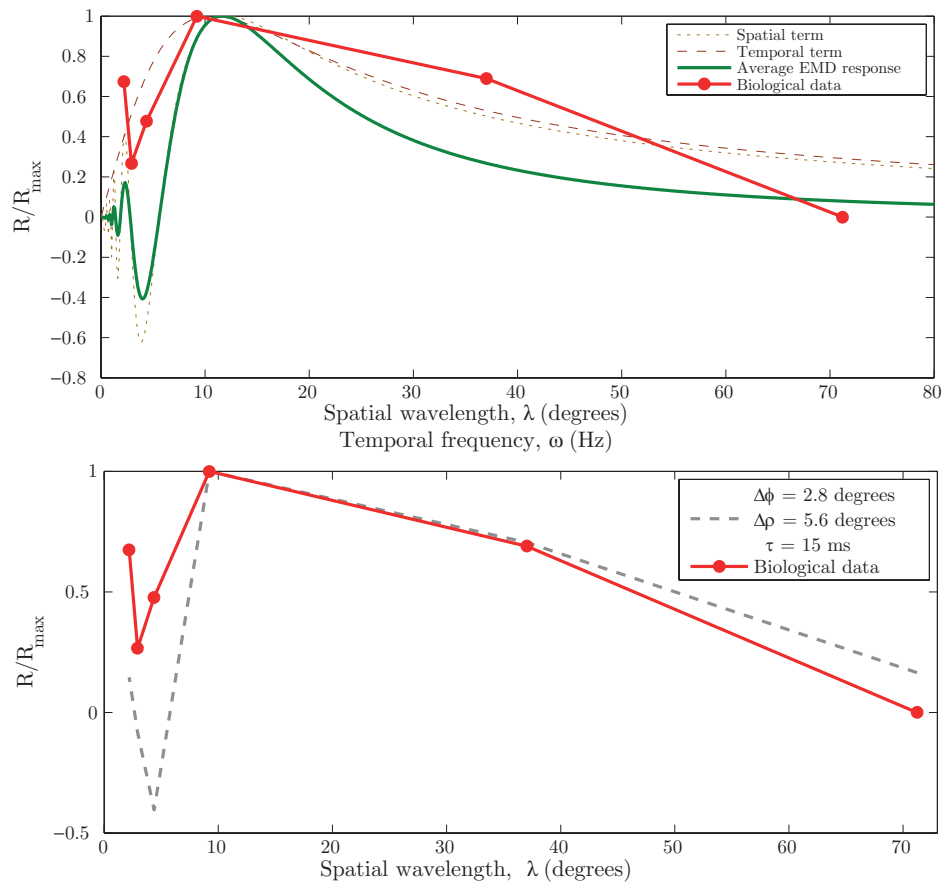


Figure 6.11: Experimental biological data, recorded at 60 lux, and EMD model response (R), as a function of: Top: spatial wavelength (λ) and temporal frequency (ω). Bottom: spatial wavelength (λ). Legend similar to the one of figure 6.10. MSE=0.1096.

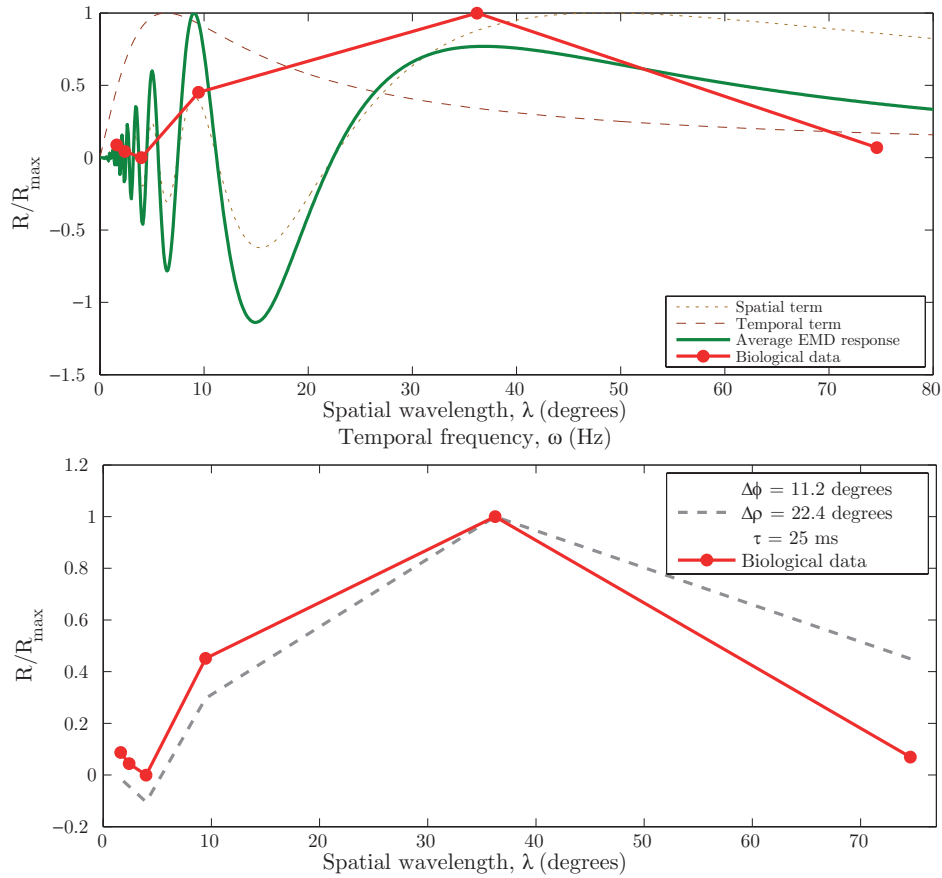


Figure 6.12: Experimental biological data, recorded at 6 lux, and EMD model response (R), as a function of: Top: spatial wavelength (λ) and temporal frequency (ω). Bottom: spatial wavelength (λ). Legend similar to the one of figure 6.10. MSE=0.0180.

creased to $\Delta\rho = 24.2$ degrees, and the integration time to $\tau = 25$ ms.[81, 115] (figure 6.12).

These results provide evidence that both spatial and temporal summation are exponentially related to the logarithmic decrement on light intensity.

6.4 Discussion

Many flowers accumulate nectar and pollen during the night. Consequently, bees that are able to forage early in the morning can gather larger nectar and pollen loads while only needing to visit a small number of flowers [34]. Additionally, by becoming more nocturnal, bees would be able to avoid day-active predators [99]. However, two main environmental factors limit the behavioral capabilities of bees: ambient air temperature and, the main focus of the present research, light availability [98]. Even

Table 6.2: Best parameters achieved by comparing the Biological response with the EMD model output.

Light Intensity (lux)	$\Delta\phi$ (degrees)	$\Delta\rho$ (degrees)	τ (ms)
600	1.4	2.8	10
60	2.8	5.6	15
6	11.2	22.4	25

in poor light conditions, bees require visual information to navigate through their environment [8] and this is made more difficult by their apposition compound eyes, which are poorly suited for vision in dim light due to their low sensitivity. In order to overcome this problem, it has been suggested that diurnal bees must use neuronal modifications to extend their activity into low light conditions [213, 214].

In this work, we have presented an experimental analysis of bumblebee’s flight behavior, in terms of speed (Experiment 1) and position with respect to nearby obstacles (Experiment 2), for different combinations of environmental spatial frequency and light intensity. Using this strategy, we were able to infer about the neural summation strategies applied by bumblebee’s visual system to improve vision reliability, at declining light levels.

The bumblebee’s ground speed tuning to spatial frequency

Experiment 1 indicates that speed, and by extension the underlying optic flow system, depends on the spatial frequency of the surrounding environment. In previous studies, it has been observed that bees use optic flow information from both lateral and ventral visual fields [6, 141]. Particularly, in [141] it has been demonstrated and highlighted the role and importance of ventral optic flow in the control of ground speed. Unlike the experiments performed by Dyhr in [43], where a blank white pattern was used to line the tunnel floor leading to a weak measure of the perceived optic flow through the bumblebee’s flying speed response, the tunnel configuration used in experiment 1 does effectively affect the bumblebee’s mean speed.

The structure of the Elementary Motion Detector (EMD) allows one to predict several aspects of behavioral reactions to wide-field image motion, as the ones experienced by the bumblebees in the experiments addressed in the present work. The limit of the spatial resolution is merely dependent on the EMD sampling base ($\Delta\phi$) and on the width of the angular sensitivity function of the input elements ($\Delta\rho$), determin-

ing the EMD response's dependency on the spatial configuration of the surroundings. Additionally, the EMD response peaks at a certain temporal frequency of the moving stimulus, independently on the spatial wavelength of the pattern. So, the optimum velocity of the EMD response is related to the spatial sampling base and the time constant of the temporal filter. By measuring the goodness of fit, through an iterative process, between the model output (R , equation 6.5) and biological data (V_x), we were able to find the spatial and temporal parameters that best fit the results obtained for different spatial frequencies tested, and that are in accordance with the results obtained on experiment 2. For the highest light level, the result of modeling the behavioral response measured on *Bombus Terrestris* suggest that the sampling base ($\Delta\phi$) must lie close to 1.4 deg and the width of the angular acceptance function of the input elements ($\Delta\rho$) must be 2.8 deg. In what concerns the temporal response of the input elements, results suggest that it must be close to 10 milliseconds. This level of spatial and temporal resolution is consistent with that of most insects [108, 115, 187].

The bumblebee's ground speed tuning to light intensity

By analyzing the speed of flying bumblebees, in particular the case where spatial details are absent (gray tunnel configuration), at decreasing light levels, we found that flying speed decreased almost linearly in response to a logarithmic decrease in light intensity (figure 6.6). This effect was in accordance with recent findings described in [145].

Using a mathematical analysis, we found that, by decreasing flight speed, bumblebees are able to decrease image motion on the retina, which enables the application of a higher temporal integration τ without sacrificing and losing important temporal information. τ values obtained are also in accordance with values cited in [104, 187].

The bumblebee's position adaptation at different light intensity levels

Experiment 2 indicates that the bumblebee's centering response is dependent on the spatial frequency of the stimulus. These results are in agreement with conclusions of previous studies [43].

We also attempted to identify the resolution limit of the optic flow system, as well as the way it was affected by light intensity. The first stage of the analysis was done by comparing different sinusoidal gratings to a uniform gray pattern. Results obtained suggest that the maximum spatial frequency that can be reliably transmitted

by an array of input elements is located in the range 0.2-0.4 cycles/deg. EMD model simulations (equation 6.5, figure 6.10) enabled us to find the sampling base value of the detector, leading to the conclusion that the higher spatial frequency resolvable by the bumblebee visual system is ≈ 0.357 cycles/deg. Higher spatial frequencies will suffer from spatial aliasing. A previous study [115] reported that the best angular acuity of bumblebees, for vertical gratings, was 0.36 cycles/deg, which is consistent with our results.

By decreasing the light intensity, we predicted that bumblebee's vision system would apply neural strategies to improve the signal-to-noise ratio of the visual signal. However, the improvement of visual reliability comes by sacrificing the signal-to-noise ratio at higher frequencies. By increasing the amount of spatial summation, we expected that the cut-off frequency would be shifted towards lower spatial frequencies, and this was supported by our results. The higher spatial frequency resolvable by the bumblebee visual system, at 60 lux, is ≈ 0.18 cycles/deg and, at the lowest light level tested, ≈ 0.045 cycles/deg.

Inferring the extent of spatial and temporal summation at decreasing light levels

Our behavioral results, taken together with the implementation and analysis of an EMD model, raise a number of relevant hypothesis about the extent of spatial and temporal summation strategies applied by a day-active insect, the bumblebee *Bombus Terrestris*. We found that the spatial and temporal summation applied is strongly influenced by the light intensity. Decreases in light intensity led to increases in both spatial and temporal summation.

The application of spatial and temporal summation reduces both spatial and temporal resolution. To avoid decreasing temporal resolution, bumblebees compensate behaviorally by flying slower as light intensity decreased. Decreasing image velocity at low light levels enables a strong increase of temporal integration (10 ms (600 lux), 15 ms (60 lux) and 25 ms (6 lux)).

The application of spatial summation strategies lead to an unavoidable decrement on spatial resolution which was also reflected on the obtained results (0.357 (600 lux), 0.18 (60 lux) and 0.045 (6 lux) cycles/deg). Finer details (higher spatial frequencies) will be lost due to spatial summation. In fact, in typical biological environments, as forests, behaviorally relevant objects, as tree trunks, are defined by lower spatial frequencies [172], being preserved even when spatial summation strategies are applied.

Therefore, the trade-off between spatial and temporal summation extent must be influenced both by behavioral and ecological constraints.

Chapter 7

Conclusions

The research addressed in this dissertation is multidisciplinary, gathering expertise and knowledge from different fields, such as neurophysiology, behavioral analyses, computer vision, robotics, and both theoretical and experimental approaches.

LGMD–DCMD network is well adapted for mediating an efficient escape response. Earlier work on this topic has proposed several artificial models to explain the selective response of the LGMD neuron to approaching objects. Firstly, existent models [15, 70, 121, 176, 233] were computationally implemented and results were compared with real, bio-experimental data.

Further, it was needed to learn more about the properties of the LGMD firing system, in particular in response to different stimuli, such as compound trajectories (non-looming transitioning to looming) and dynamic backgrounds. Thus, in the second stage of this work, neural recordings were performed from locusts (*Locusta Migratoria*) and it has been researched how these stimuli properties are coded by the LGMD firing rate.

In the third stage, taking into account the results obtained in this work, an innovative model has been proposed. This model is innovative in its ability to self-adapt to different dynamic environments, by the introduction of directional and non-directional selective neurons, eliminating the excitation produced by non-approaching visual stimuli that could lead to false collision detections. We have experimentally shown, by implementing the model under the same conditions used on the second stage, the performance and effectiveness of a biologically-based collision detection model in dynamic environments.

An additional and innovative approach, based on simple measurements of variations of image statistics, was addressed in this fourth stage of this dissertation. Simulations and real experiments proved the effectiveness of this new approach on collision

detection.

A limiting factor of any visual system is its dependence on lighting conditions. Since low lighting conditions may impact the collision detection model performance, in the fifth stage we used behavioral analyses to investigate how insects adapt their flight at different light levels. Using a behavioral approach, we intent to infer the neural strategies applied by those insects to improve image reliability at the different light levels.

Unfortunately, one of the problems about locusts is the unpredictability of their behavior. Thus, it is difficult to correlate the environmental conditions with the effect that it has on the insect behavior. In order to overcome this problem, bumblebees (*Bombus Terrestris*) were used as our second model animal. These are easily trained, are readily obtained and use visual information to flight control even in dim light conditions [8].

This chapter summarizes the contributions of this thesis and future directions of research.

7.1 Summary of contributions

In order to achieve our final goals, we have started this dissertation by describing, implementing, testing and analyzing three representative collision avoidance models: the Gabbiani [70], Rind [121, 176, 233] and Sergi [15] based models. More specifically, we provided: A description and critical analysis of selected LGMD model's response to specific stimulation protocols used in biology; An analysis of each model applicability in the robotic field; And the main reasons behind model's failure in the different collision scenarios used were pinpointed.

However, the computational properties of LGMD neurons have mainly been characterized in tethered locusts with simplistic visual stimuli, so far. Simple, artificial stimuli have been crucial tools for identifying the neural computations in the visual motion pathway of collision detection in locusts, but for a number of reasons, they do not easily allow to predict and model the performance of this collision detection neuron in more natural, dynamic contexts.

Some insects, as locusts, have the capacity to detect and track small approaching objects, often against cluttered moving backgrounds. Determining how this task is performed is an intriguing challenge, both from a physiological and from a computational perspective.

Recent studies [38, 119], where locusts were presented with compound visual stim-

uli, suggested that firing properties of the LGMD neurons were more complex than previously thought, not only signaling a potential collision, but also codifying changes in the object trajectory. Despite this important finding, it remained unclear how this collision detection visual system copes with highly dynamic stimuli, as encountered, for instance, by the locust during free flight. It is by no means easy to predict the signals of the LGMD neuron under such natural conditions. Another problem is that LGMD neuron cannot be expected to be sensitive to optic-flow components induced by movements that are their own preferred self-motion. Which computational strategies allow these insects to perform so extraordinarily well in visually guided collision detection when inserted in complex and dynamic environments?

In order to answer this biological research question, in chapter 3 of this thesis, new visual stimuli were built up and computationally developed. Those integrated three types of visual backgrounds: simple (uniform white), a moving flow-field and a moving scattered background, over which different foreground stimuli were superimposed. Those were compound visual stimuli, combining translation trajectories with transitions to looming.

Regardless of stimulus background, DCMD responses to looming were characteristic and related to previously described effects of azimuthal approach angle and velocity of object expansion. However, increasing background complexity caused reduced firing rates, delayed peaks, shorter rise phases and longer fall phases, responding to the first research question (RQ1) stated on chapter 1. DCMD responded to transitions to looming with a characteristic drop in a firing rate that was relatively invariant across most stimulus combinations and occurred regardless of stimulus background (answer to RQ2). We show that DCMD response time to a transition depends on unique expansion parameters of the moving stimulus irrespective of background complexity. Our results show how background complexity shapes DCMD responses to looming stimuli, proving that neuronal codification depends on their contextual significance.

However, a fundamental question remained open: how are these higher-order sensory neurons (ie, the LGMD/DCMD) able to generate looming selectivity from their complex inputs?

Focused on answering this research question, as well as to propose an innovative computational model for collision detection in dynamic environments, that could be implemented in an autonomous robot, a neural network was developed from the electrophysiological results previously described.

The model, proposed on chapter 4, was tested in specially designed computer simulations, replicating the visual conditions created for the experiments with real

locusts. Using this strategy, we were able to identify: which components of the visual scene are important for collision detection; which components are filtered out; and the way this is achieved at the neural level. The integration, in the model, of self-adaptable inhibitory neurons, both directional and non-directional ones, have reduced and even eliminated the excitation caused by moving non-looming stimuli. This model was able to extract visual information related with the approaching stimuli, being able to respond to the RQ 3 formulated. Model results have also shown the effectiveness and possible applicability of this model as a collision detector for autonomous robotic navigation.

A distinct approach to collision detection was addressed on Chapter 5. A new methodology, based on a sequential real-time computation of the image's power spectra, is here proposed. It has been implemented in a real robotic platform, showing that distant dependent variations on image statistics are likely to be functional significant. Thus, RQ 4 has been answered

In the fourth stage, a deep characterization of the statistics of motion that occur when navigating in distinct environments, as well as the study of the implications of those statistics for collision detection have been performed. Based on simple measurements of image statistics' variations (α), and through the implementation of the methodology developed as a reliable collision detector in a real robotic platform, we can conclude that α variations can have a behavioral role, signaling the presence of potential hazard situations.

For autonomous robots moving at twilight or at night levels, collision avoidance is not a trivial problem, as vision and visually based control systems become less reliable and more noisy the darker it gets. Interesting solutions to how this loss in precision can be avoided by modelling the remarkably light sensitive visual system adaptations of a diurnal bumblebee able to forage even in low light conditions.

Following this line of thought, we set up a controlled environment, where environmental conditions, as spatial frequency and light intensity of the environment, could be changed. Real behavioral experiments were performed using bumblebees (*Bombus Terrestris*). The effect of spatial frequency and light intensity on bumblebee's position and speed control was analyzed. These behavioral results, taken together with the implementation and analysis of an EMD model, raised a relevant hypothesis about the extent of spatial and temporal summation strategies applied by these day-active insects at decreasing light levels. We inferred that the spatial and temporal summation applied at bumblebee's neural level is strongly influenced by the light intensity available, leading to the conclusion that decreases in light intensity lead to increases

in both spatial and temporal summation. These results constitute the answer to RQ5.

The inclusion of this light adaptive system within the LGMD model here proposed is hoped to improve the performance of this collision detection model, by introducing spatial and temporal summation strategies, making the detection of potential collisions more reliable in dim light conditions.

Overall, the work developed in this dissertation represents an important step in the development of bio-inspired visual strategies, addressing concepts of collision detection and light adaptation. Such an approach is duly justified with biological evidences, which show that, the combination of both these approaches seems to be required in order to achieve robotic vision systems capable of dealing with several situations of the real world. Analyses at both the neuronal and behavioral levels enabled us to unveil some principles behind particular extraordinary capabilities of insects. In fact, one of the most exciting developments in modern biology has been the vigorous and renewed interest in studying complex problems, such as visual information processing, by using approaches that integrate different research methods, as electrophysiological and behavioral recordings. Additionally, combining the results from multiple insect model systems is likely to yield critical insights into the function of vision systems.

7.2 Future directions

Even if the experiments provided promising results, there are still some aspects that need to be uncovered, modeled and improved .

Due to the interdisciplinarity of the work addressed in this dissertation, it has future implications in a number of distinct research areas. Thus, this section will divide the future work in four different areas: electrophysiological investigation of the collision avoidance behavior; Behavioral studies; Modeling strategies and hardware development; and image statistics.

7.2.1 Electrophysiological investigation of the collision avoidance behavior

There are several interesting electrophysiological experiments suggested by the results from chapter 3 of this dissertation.

Since our moving disc and dots in scattered and vertical gratings in flow-field backgrounds were similar in contrast, it is possible that there was a shadowing effect of the moving disc each time it overlapped with the background. In addition, although

the FF and the 7 cm looming disc were distinct stimuli, looming objects should contribute to increased translational flow, if the object travelled in the same direction and irrespective of its velocity. Therefore, it would be interesting to determine how DCMD responds to a disc traveling slower or at the same velocity as the flow field. The relative velocity and trajectory of objects in an animal's visual environment may represent very different things. If the looming object was designed to travel slower than the flow field it would appear to the locust that it was catching up to a slower moving object and we would expect a weakened DCMD response compared to an object that was traveling faster than the flow, which may indicate the trajectory of a predator. Conversely, we would expect that no response would be detected if the disc was traveling the same velocity, as it would appear as a stationary part of the flowing environment. In addition, we only presented a flow in one direction, so it would be interesting to see what happens if presented in opposite direction or if the flow stopped during the approach of an object. Visual gratings that simulate progressive motion causes landing responses in flies when the change in expansion velocity of the pattern occupies a large enough area of the retina [45], which has also been suggested to occur in locusts [2]. Categorizing the LGMD/DCMD pathway as being simply looming sensitive may underestimate what this and potentially other similarly responding neurons encode.

Ultimately, an interesting future experiment would be to record, simultaneously, the locust wing kinematics, electromyographic recordings from the locust's flight motor neuron and the correspondent DCMD responses, to these types of stimuli. This will elucidate the importance of different aspects of complex stimulus environments. Using this strategy, it would help to identify many important features of the visual environments that affect behavioural responses. How does the change in object trajectory, from translation to looming, affect the behavior of a flying locust? Does it hold any behavioral implication?

7.2.2 Behavioral studies

There are a variety of possible future research extending the behavioral analysis from Chapter 6, in which bumblebee's flight speed was found to decrease with decreasing light intensity levels. One incremental research project would be to unveil how bumblebee's flight is controlled within environments containing even weaker, noisier or subthresholded visual stimuli, combined with different odor stimuli concentration gradients. In fact, the sensory input from different sensory modalities can be integrated in order to improve the performance of the flight control in an insect. Does the

bumblebee's brain integrate multisensory information by weighting each modality in proportion to its reliability?

This knowledge could lead to the development of a better way to achieve bio-inspired solutions in the robotic control field, by placing information from various sensory modalities into context, or learning to substitute one stimulus for another in guiding a specific action.

7.2.3 Modeling strategies and hardware development

Chapter 6 provide us with information about how behavioral adaptations can reflect the neural strategies applied by day-active insects to improve image reliability at night. Hereafter, and taking inspiration from these behavioral adaptations, an innovative dynamic computational model of temporal and spatial summation could be proposed.

For each combination of light intensity, spatial frequency of the sinusoidal grating and image motion, the spatio-temporal filter would evolve in order to give the best denoised image for that particular condition.

Further, it would be of interest to implement, on hardware, an analog VLSI chip, integrating both the data acquisition sensor, as well as the processing circuitry in the same die. Using this strategy, problems of data communication and analog-to-digital conversion are avoided, making the neuromorphic system faster and more power efficient.

7.2.4 Image statistics

Chapter 5 examined extensively the time variations of the Fourier power spectra for different image sequences. Image sequences used were either developed artificially, as well as real recordings of movements in indoor environments. Future analyses should include measurements of the spatiotemporal statistics of image sequences as the ones captured during the translatory displacement of flying insects (as bumblebees), when moving in natural environments. Then, by stimulating tethered bumblebees with those image sequences, while recording the correspondent behavioral response, a correlation could be performed between image statistical variations and the effect that it has on bumblebee's behavior. Using this strategy, we might be able to verify if pattern and distant dependent spatiotemporal fluctuations have a functional meaning for insect flying control.

References

- [1] A. Torralba and A. Oliva. Statistics of natural image categories. *Network: Comput. Neural Syst*, 14:391–412, 2003.
- [2] Andreas Baader. Simulation of self-motion in tethered flying insects: an optical flow field for locusts. *Journal of Neuroscience Methods*, 38:193 – 199, 1991. ISSN 0165-0270. doi: [http://dx.doi.org/10.1016/0165-0270\(91\)90169-Z](http://dx.doi.org/10.1016/0165-0270(91)90169-Z).
- [3] R Baddeley, L F Abbott, M C Booth, F Sengpiel, T Freeman, E A Wakeman, and E T Rolls. Responses of neurons in primary and inferior temporal visual cortices to natural scenes. *Proceedings. Biological sciences / The Royal Society*, 264(1389):1775–1783, 1997. ISSN 0962-8452.
- [4] S. Bermudez I Badia and P.F.M.J. Verschure. A collision avoidance model based on the Lobula giant movement detector (LGMD) neuron of the locust. *2004 IEEE International Joint Conference on Neural Networks (IEEE Cat. No.04CH37541)*, 3, 2004. ISSN 1098-7576. doi: 10.1109/IJCNN.2004.1380872.
- [5] Wyeth Bair and J Anthony Movshon. Adaptive temporal integration of motion in direction-selective neurons in macaque visual cortex. *The Journal of neuroscience : the official journal of the Society for Neuroscience*, 24(33):7305–7323, 2004.
- [6] Emily Baird, Mandyam V Srinivasan, Shaowu Zhang, and Ann Cowling. Visual control of flight speed in honeybees. *The Journal of experimental biology*, 208: 3895–3905, 2005. ISSN 0022-0949. doi: 10.1242/jeb.01818.
- [7] Emily Baird, Torill Kornfeldt, and Marie Dacke. Minimum viewing angle for visually guided ground speed control in bumblebees. *The Journal of experimental biology*, 213:1625–1632, 2010. ISSN 0022-0949. doi: 10.1242/jeb.038802.

-
- [8] Emily Baird, Eva Kreiss, William Weislo, Eric Warrant, and Marie Dacke. Nocturnal insects use optic flow for flight control. *Biology letters*, 7(February): 499–501, 2011. ISSN 1744-9561. doi: 10.1098/rsbl.2010.1205.
- [9] Rosario M. Balboa and Norberto M. Grzywacz. Power spectra and distribution of contrasts of natural images from different habitats. *Vision Research*, 43:2527–2537, 2003. ISSN 00426989. doi: 10.1016/S0042-6989(03)00471-1.
- [10] H Barlow. Redundancy reduction revisited. *Network*, 12:241–253, 2001. ISSN 0954-898X. doi: 10.1088/0954-898X/12/3/301.
- [11] H B BARLOW and R M HILL. Selective sensitivity to direction of movement in ganglion cells of the rabbit retina. *Science (New York, N.Y.)*, 139:412–414, 1963. ISSN 0036-8075.
- [12] Andrew Barron and Mandyam V. Srinivasan. Visual regulation of ground speed and headwind compensation in freely flying honey bees (*apis mellifera* l.). *Journal of Experimental Biology*, 209(5):978–984, 2006. doi: 10.1242/jeb.02085.
- [13] S. Bermúdez i Badia, P. Pyk, and P. F.M.J. Verschure. A fly-locust based neuronal control system applied to an unmanned aerial vehicle: the invertebrate neuronal principles for course stabilization, altitude control and collision avoidance. *The International Journal of Robotics Research*, 26:759–772, 2007. ISSN 0278-3649. doi: 10.1177/0278364907080253.
- [14] Sergi Bermúdez i Badia, Pawel Pyk, and Paul F M J Verschure. A biologically based flight control system for a blimp-based UAV. In *Proceedings - IEEE International Conference on Robotics and Automation*, volume 2005, pages 3053–3059, 2005.
- [15] Sergi Bermúdez i Badia, Ulysses Bernardet, and Paul F M J Verschure. Non-linear neuronal responses as an emergent property of afferent networks: a case study of the locust lobula giant movement detector. *PLoS computational biology*, 6(3), 2010. ISSN 15537358. doi: 10.1371/journal.pcbi.1000701.
- [16] Mark Blanchard, F. Claire Rind, and P. F M J Verschure. Collision avoidance using a model of the locust LGMD neuron. *Robotics and Autonomous Systems*, 30:17–38, 2000. ISSN 09218890. doi: 10.1016/S0921-8890(99)00063-9.

- [17] Mark J. Blanchard, F. Claire Rind, and Paul F. M. J. Verschure. Using a mobile robot to study locust collision avoidance responses. *International Journal of Neural Systems*, 9(5):405–410, 1999.
- [18] N Boeddeker, J P Lindemann, M Egelhaaf, and J Zeil. Responses of blowfly motion-sensitive neurons to reconstructed optic flow along outdoor flight paths. *Journal of comparative physiology. A, Neuroethology, sensory, neural, and behavioral physiology*, 191:1143–1155, 2005. ISSN 0340-7594. doi: 10.1007/s00359-005-0038-9.
- [19] a Borst and M Egelhaaf. Principles of visual motion detection. *Trends in neurosciences*, 12(8):297–306, August 1989. ISSN 0166-2236.
- [20] Alexander Borst, Juergen Haag, and Dierk F Reiff. Fly motion vision. *Annual review of neuroscience*, 33:49–70, January 2010. ISSN 1545-4126. doi: 10.1146/annurev-neuro-060909-153155.
- [21] Kevin L Briggman, Moritz Helmstaedter, and Winfried Denk. Wiring specificity in the direction-selectivity circuit of the retina. *Nature*, 471(7337):183–188, 2011. ISSN 0028-0836. doi: 10.1038/nature09818.
- [22] R.W. Buccigrossi and E.P. Simoncelli. Image compression via joint statistical characterization in the wavelet domain. *Image Processing, IEEE Transactions on*, 8(12):1688–1701, Dec 1999. ISSN 1057-7149. doi: 10.1109/83.806616.
- [23] E. Buchner. Elementary movement detectors in an insect visual system. *Biological Cybernetics*, 24(2):85–101, 1976. ISSN 03401200.
- [24] M. Burrows. *The Neurobiology of an Insect Brain*. Oxford University Press, 1996. ISBN 9780198523444.
- [25] M. Burrows and C.H. Fraser Rowell. Connections between descending visual interneurons and metathoracic motoneurons in the locust. *Journal of comparative physiology*, 85(3):221–234, 1973. ISSN 0340-7594. doi: 10.1007/BF00694231.
- [26] M. Burrows, a. H. D. Watson, and D. E. Brunn. Physiological and Ultrastructural Characterization of a Central Synaptic Connection between Identified Motor Neurons in the Locust. *The European journal of neuroscience*, 1(2):111–126, 1989. ISSN 1460-9568.

- [27] G. J. Burton and Ian R. Moorhead. Color and spatial structure in natural scenes. *Applied Optics*, 26(1):157–170, 1987.
- [28] Gwyneth Card and Michael H. Dickinson. Visually Mediated Motor Planning in the Escape Response of *Drosophila*. *Current Biology*, 18:1300–1307, 2008. ISSN 09609822. doi: 10.1016/j.cub.2008.07.094.
- [29] Gwyneth M. Card. Escape behaviors in insects. *Current Opinion in Neurobiology*, 22(2):180–186, 2012. ISSN 09594388. doi: 10.1016/j.conb.2011.12.009.
- [30] R. WM. Chan and F. Gabbiani. Collision-avoidance behaviors of minimally restrained flying locusts to looming stimuli. *The Journal of Experimental Biology*, 216(4):641–655, 2013. doi: 10.1242/jeb.077453.
- [31] R. F. Chapman. *The Insects - Structure and Function*. 2012. ISBN 9780521113892.
- [32] T.A. Christensen. *Methods in insect sensory neuroscience*. Frontiers in neuroscience. CRC Press, 2005.
- [33] Richard Clarke and R. Beau Lotto. Visual processing of the bee innately encodes higher-order image statistics when the information is consistent with natural ecology. *Vision Research*, 49(11):1455–1464, 2009. ISSN 00426989. doi: 10.1016/j.visres.2009.02.021.
- [34] S. a. Corbet, N. M. Saville, M. Fussell, O. E. Prys-Jones, and D. M. Unwin. The competition box : a graphical aid to forecasting pollinator performance. *Journal of applied ecology*, 32(4):707–719, 1995. ISSN 0021-8901. doi: 10.2307/2404810.
- [35] H. Cuntz, M.W.H. Remme, and B. Torben-Nielsen. *The Computing Dendrite: From Structure to Function*. Springer Series in Computational Neuroscience. Springer New York, 2013. ISBN 9781461480945.
- [36] J.W. Dawson, W. Kutsch, and R.M. Robertson. Auditory-evoked evasive manoeuvres in free-flying locusts and moths. *Journal of Comparative Physiology A*, 190(1):69–84, 2004. ISSN 0340-7594. doi: 10.1007/s00359-003-0474-3.
- [37] Richard B. Dewell and Fabrizio Gabbiani. Escape behavior: Linking neural computation to action. *Current Biology*, 22(5):R152–R153, 2012. ISSN 09609822. doi: 10.1016/j.cub.2012.01.034.

- [38] Paul C. Dick and John R. Gray. Spatiotemporal stimulus properties modulate responses to trajectory changes in a locust looming-sensitive pathway. *Journal of Neurophysiology*, 111(9):1736–1745, 2014. ISSN 0022-3077. doi: 10.1152/jn.00499.2013.
- [39] Eizaburo Doi, Jeffrey L Gauthier, Greg D Field, Jonathon Shlens, Alexander Sher, Martin Greschner, Timothy a Machado, Lauren H Jepson, Keith Mathieson, Deborah E Gunning, Alan M Litke, Liam Paninski, E J Chichilnisky, and Eero P Simoncelli. Efficient coding of spatial information in the primate retina. *The Journal of neuroscience : the official journal of the Society for Neuroscience*, 32(46):16256–64, 2012. ISSN 1529-2401. doi: 10.1523/JNEUROSCI.4036-12.2012.
- [40] Dawei Dong and Joseph Atick. Statistics of natural time-varying images. *Network: Computation in Neural Systems*, 6:345–358, 1995. ISSN 0954-898X. doi: 10.1088/0954-898X/6/3/003.
- [41] Ron O. Dror, David C. O’Carroll, and Simon B. Laughlin. The role of natural image statistics in biological motion estimation. In Seong-Whan Lee, Heinric H. Balthoff, and Tomaso Poggio, editors, *Biologically Motivated Computer Vision*, volume 1811 of *Lecture Notes in Computer Science*, pages 492–501. Springer Berlin Heidelberg, 2000. ISBN 978-3-540-67560-0. doi: 10.1007/3-540-45482-9_50.
- [42] Andrew P. Duchon, William H. Warren, and Leslie Pack Kaelbling. Ecological robotics. *Adaptive Behavior*, 6, 1994.
- [43] Jonathan P Dyhr and Charles M Higgins. The spatial frequency tuning of optic-flow-dependent behaviors in the bumblebee *Bombus impatiens*. *The Journal of experimental biology*, 213:1643–1650, 2010. ISSN 0022-0949. doi: 10.1242/jeb.041426.
- [44] Jonathan P. Dyhr and Charles M. Higgins. Non-directional motion detectors can be used to mimic optic flow dependent behaviors. *Biological Cybernetics*, 103(6):433–446, 2010. ISSN 03401200.
- [45] Hendrik Eckert. The vertical-horizontal neurone (vh) in the lobula plate of the blowfly, *phaenicia*. *Journal of comparative physiology*, 149(2):195–205, 1982. ISSN 0340-7594. doi: 10.1007/BF00619213.

- [46] Dennis Eckmeier, Roland Kern, Martin Egelhaaf, and Hans-Joachim Bischof. Encoding of naturalistic optic flow by motion sensitive neurons of nucleus rotundus in the zebra finch (*taeniopygia guttata*). *Frontiers in Integrative Neuroscience*, 68(7):195–205, 2013. ISSN 1662-5145. doi: 10.1007/BF00619213.
- [47] M.D.D.C.A.L.J.J.V. Edited by Robert E. Armstrong. *Bio-inspired Innovation and National Security*. NDU Press, 2012.
- [48] Martin Egelhaaf, Norbert Boeddeker, Roland Kern, Rafael Kurtz, and Jens P Lindemann. Spatial vision in insects is facilitated by shaping the dynamics of visual input through behavioral action. *Frontiers in neural circuits*, 6(December): 108, 2012. ISSN 1662-5110. doi: 10.3389/fncir.2012.00108.
- [49] Martin Egelhaaf, Roland Kern, and Jens Peter Lindemann. Motion as a source of environmental information: A fresh view on biological motion computation by tiny brains. *Frontiers in Neural Circuits*, 8(127), 2014. ISSN 1662-5110. doi: 10.3389/fncir.2014.00127.
- [50] Farbod Fahimi, C. Nataraj, and Hashem Ashrafiun. Real-time obstacle avoidance for multiple mobile robots. *Robotica*, 27(May):189, 2009. ISSN 0263-5747. doi: 10.1017/S0263574708004438.
- [51] Olivier Faivre and Mikko Juusola. Visual coding in locust photoreceptors. *PLoS ONE*, 3(5), 2008. ISSN 19326203. doi: 10.1371/journal.pone.0002173.
- [52] D J Field. Relations between the statistics of natural images and the response properties of cortical cells. *Journal of the Optical Society of America. A, Optics and image science*, 4(12):2379–2394, 1987. ISSN 0740-3232. doi: 10.1364/JOSAA.4.002379.
- [53] David J. Field. *What Is the Goal of Sensory Coding?*, 1994.
- [54] David J. Field and Nuala Brady. Visual sensitivity, blur and the sources of variability in the amplitude spectra of natural scenes. *Vision Research*, 37(23): 3367–3383, 1997. ISSN 00426989. doi: 10.1016/S0042-6989(97)00181-8.
- [55] Leo J Fleishman and Adam C Pallus. Motion perception and visual signal design in Anolis lizards. *Proceedings. Biological sciences / The Royal Society*, 277(June):3547–3554, 2010. ISSN 1471-2954. doi: 10.1098/rspb.2010.0742.

- [56] Monica Hoyos Flight. Visual system: Mapping motion detection. *Nature Reviews Neuroscience*, 14:3590, 2013.
- [57] Dario Floreano and Jean-Christophe Zufferey. Insect vision: A few tricks to regulate flight altitude. *Current Biology*, 20(19):R847 – R849, 2010. ISSN 0960-9822. doi: <http://dx.doi.org/10.1016/j.cub.2010.08.022>.
- [58] Haleh Fotowat and Fabrizio Gabbiani. Relationship between the phases of sensory and motor activity during a looming-evoked multistage escape behavior. *The Journal of Neuroscience*, 27(37):10047–10059, 2007. doi: 10.1523/JNEUROSCI.1515-07.2007.
- [59] Haleh Fotowat and Fabrizio Gabbiani. Collision detection as a model for sensory-motor integration. *Annual review of neuroscience*, 34:1–19, 2011. ISSN 0147-006X. doi: 10.1146/annurev-neuro-061010-113632.
- [60] Haleh Fotowat, Amir Fayyazuddin, Hugo J Bellen, and Fabrizio Gabbiani. A novel neuronal pathway for visually guided escape in *Drosophila melanogaster*. *Journal of neurophysiology*, 102(May 2009):875–885, 2009. ISSN 0022-3077. doi: 10.1152/jn.00073.2009.
- [61] J. C. Fraile, J. Perez-Turiel, J. L. Gonzalez-Sanchez, E. Baeyens, and R. Perez. Comparative analysis of collision-free path-planning methods for multi-manipulator systems. *Robotica*, 24(May):711, 2006. ISSN 0263-5747. doi: 10.1017/S0263574706002888.
- [62] C.H. Fraser Rowell and Michael O’Shea. Modulation of transmission at an electrical synapse in the locust movement detector system. *Journal of comparative physiology*, 137(3):233–241, 1980. ISSN 0340-7594. doi: 10.1007/BF00657118.
- [63] C.H. Fraser Rowell, Michael O’Shea, and J.L.D. Williams. Neuronal basis of a sensory analyser, the acridid movement detector system. iv. the preference for small field stimuli. *Journal of Experimental Biology*, 68:157–185, 1977.
- [64] Rikard Frederiksen and Eric J Warrant. The optical sensitivity of compound eyes: theory and experiment compared. *Biology letters*, 4(December):745–747, 2008. ISSN 1744-9561. doi: 10.1098/rsbl.2008.0467.
- [65] Shelley I Fried, Thomas a Münch, and Frank S Werblin. Mechanisms and circuitry underlying directional selectivity in the retina. *Nature*, 420:411–414, 2002. ISSN 0028-0836. doi: 10.1038/nature01179.

- [66] Barrie J. Frost and Hongjin Sun. Chapter 2 The biological bases of time-to-collision computation. *Advances in Psychology*, 135:13–37, 2004. ISSN 01664115. doi: 10.1016/S0166-4115(04)80004-9.
- [67] F. Gabbiani, G. Laurent, N. Hatsopoulos, H. G. Krapp, F. C. Rind, and P. J. Simmons. The many ways of building collision-sensitive neurons [2] (multiple letters). *Trends in Neurosciences*, 22(10):437–438, 1999. ISSN 01662236. doi: 10.1016/S0166-2236(99)01478-2.
- [68] F. Gabbiani, C. Mo, and G. Laurent. Invariance of angular threshold computation in a wide-field looming-sensitive neuron. *The Journal of neuroscience : the official journal of the Society for Neuroscience*, 21:314–329, January 2001.
- [69] Fabrizio Gabbiani and Holger G Krapp. Spike-frequency adaptation and intrinsic properties of an identified, looming-sensitive neuron. *Journal of neurophysiology*, 96(March 2006):2951–2962, 2006. ISSN 0022-3077. doi: 10.1152/jn.00075.2006.
- [70] Fabrizio Gabbiani, Holger G. Krapp, and Gilles Laurent. Computation of object approach by a wide-field, motion-sensitive neuron. *The Journal of Neuroscience*, 19:1122–1141, 1999.
- [71] Fabrizio Gabbiani, Holger G. Krapp, Christof Koch, and Gilles Laurent. Multiplicative computation in a visual neuron sensitive to looming. *Nature*, 420: 320–324, November 2002.
- [72] Fabrizio Gabbiani, Holger G. Krapp, Nicholas Hatsopoulos, Chun-Hui Mo, Christof Koch, and Gilles Laurent. Multiplication and stimulus invariance in a looming-sensitive neuron. *Journal of Physiology-Paris*, 98:19 – 34, 2004. ISSN 0928-4257. doi: <http://dx.doi.org/10.1016/j.jphysparis.2004.03.001>. Representation of 3-D Space Using Different Senses In Different Species.
- [73] Fabrizio Gabbiani, Ivan Cohen, and Gilles Laurent. Time-dependent activation of feed-forward inhibition in a looming-sensitive neuron. *Journal of Neurophysiology*, 94(3):2150–2161, 2005. ISSN 0022-3077. doi: 10.1152/jn.00411.2005.
- [74] Edward Gaten, Stephen J. Huston, Harold B. Dowse, and Tom Matheson. Solitary and gregarious locusts differ in circadian rhythmicity of a visual output neuron. *Journal of Biological Rhythms*, 27(3):196–205, 2012. doi: 10.1177/0748730412440860.

- [75] Wilson S Geisler. Visual perception and the statistical properties of natural scenes. *Annual review of psychology*, 59:167–192, 2008. ISSN 0066-4308. doi: 10.1146/annurev.psych.58.110405.085632.
- [76] J.J. Gibson. *The ecological approach to visual perception.*: Houghton Mifflin, 1979. ISBN 9780395270493.
- [77] John R. Gray. Habituated visual neurons in locusts remain sensitive to novel looming objects. *Journal of Experimental Biology*, 208(13):2515–2532, 2005. doi: 10.1242/jeb.01640.
- [78] John R Gray, Jessica K. Lee, and R. Meldrum Robertson. Activity of descending contralateral movement detector neurons and collision avoidance behaviour in response to head-on visual stimuli in locusts. *Journal of Comparative Physiology A*, 187:115–129, March 2001.
- [79] JohnR. Gray, Eric Blincow, and R.Meldrum Robertson. A pair of motion-sensitive neurons in the locust encode approaches of a looming object. *Journal of Comparative Physiology A*, 196(12):927–938, 2010. ISSN 0340-7594. doi: 10.1007/s00359-010-0576-7.
- [80] B. B. Guest and J. R. Gray. Responses of a looming-sensitive neuron to compound and paired object approaches. *Journal of neurophysiology*, 95(3):1428–1441, March 2006.
- [81] J Haag, W Denk, and a Borst. Fly motion vision is based on Reichardt detectors regardless of the signal-to-noise ratio. *Proceedings of the National Academy of Sciences of the United States of America*, 101(46):16333–16338, 2004. ISSN 0027-8424. doi: 10.1073/pnas.0407368101.
- [82] Reid R. Harrison Haleh Fotowat and Fabrizio Gabbiani. Multiplexing of motor information in the discharge of a collision detecting neuron during escape behaviors. *Neuron*, 69(1):147 – 158, 2011. ISSN 0896-6273. doi: <http://dx.doi.org/10.1016/j.neuron.2010.12.007>.
- [83] Nicholas Hatsopoulos, Fabrizio Gabbiani, and Gilles Laurent. Elementary computation of object approach by a wide-field visual neuron. *Science*, 270:1000–1003, 1995.

- [84] G. Horn and C. H. Fraser Rowell. Medium and long-term changes in the behaviour of visual neurones in the tritocerebrum of locusts. *Journal of Experimental Biology*, 49(1):143–169, 1968.
- [85] G. A. Horridge. The separation of visual axes in apposition compound eyes. *Philosophical Transactions of the Royal Society of London B: Biological Sciences*, 285(1003):1–59, 1978. ISSN 0080-4622. doi: 10.1098/rstb.1978.0093.
- [86] Toshihiko Hosoya, Stephen A. Baccus, and Markus Meister. Dynamic predictive coding by the retina. *Nature*, 436(7047):71–77, July 2005. ISSN 1476-4687. doi: 10.1038/nature03689.
- [87] Jonathon Howard. Temporal resolving power of the photoreceptors of *Locusta migratoria*. *Journal of Comparative Physiology A*, 144:61–66, 1981. ISSN 03407594. doi: 10.1007/BF00612798.
- [88] Michael Hoy, Alexey S. Matveev, and Andrey V. Savkin. Algorithms for collision-free navigation of mobile robots in complex cluttered environments: a survey. *Robotica*, 33:463–497, 3 2015. ISSN 1469-8668. doi: 10.1017/S0263574714000289.
- [89] Yanping Huang and Rajesh P. N. Rao. Predictive coding. *WIREs Cogn Sci*, 2(5):580–593, 2011. doi: 10.1002/wcs.142.
- [90] A. Hyvriinen, J. Hurri, and P. O. Hoyer. *Natural Image Statistics: A Probabilistic Approach to Early Computational Vision*. Springer Publishing Company, Incorporated, 1st edition, 2009.
- [91] a C James and D Osorio. Characterisation of columnar neurons and visual signal processing in the medulla of the locust optic lobe by system identification techniques. *Journal of comparative physiology. A, Sensory, neural, and behavioral physiology*, 178:183–199, 1996. ISSN 0340-7594. doi: 10.1007/BF00188161.
- [92] Ursula Jander and Rudolf Jander. Allometry and resolution of bee eyes (Apoidea). *Arthropod Structure and Development*, 30(3):179–193, 2002.
- [93] P. W. Jones and F. Gabbiani. Impact of neural noise on a sensory-motor pathway signaling impending collision. *Journal of Neurophysiology*, 107(November 2011):1067–1079, 2012. ISSN 0022-3077. doi: 10.1152/jn.00607.2011.

- [94] P. W. Jones and F. Gabbiani. Logarithmic Compression of Sensory Signals within the Dendritic Tree of a Collision-Sensitive Neuron. *Journal of Neuroscience*, 32(14):4923–4934, 2012. ISSN 0270-6474. doi: 10.1523/JNEUROSCI.5777-11.2012.
- [95] Peter W. Jones and Fabrizio Gabbiani. Synchronized neural input shapes stimulus selectivity in a collision-detecting neuron. *Current Biology*, 20(22):2052–2057, 2010. ISSN 09609822. doi: 10.1016/j.cub.2010.10.025.
- [96] S Judge and F Rind. The locust dcmd, a movement-detecting neurone tightly tuned to collision trajectories. *The Journal of Experimental Biology*, 200(16):2209–16, 1997.
- [97] M Juusola, R O Uusitalo, and M Weckström. Transfer of graded potentials at the photoreceptor-interneuron synapse. *The Journal of general physiology*, 105 (January):117–148, 1995. ISSN 0022-1295. doi: 10.1085/jgp.105.1.117.
- [98] a. Kapustjanskij, M. Streinzer, H. F. Paulus, and J. Spaethe. Bigger is better: Implications of body size for flight ability under different light conditions and the evolution of alloethism in bumblebees. *Functional Ecology*, 21:1130–1136, 2007. ISSN 02698463. doi: 10.1111/j.1365-2435.2007.01329.x.
- [99] Almut Kelber, Eric J. Warrant, Michael Pfaff, Rita Wallén, Jamie C. Theobald, William T. Wcislo, and Robert a. Raguso. Light intensity limits foraging activity in nocturnal and crepuscular bees. *Behavioral Ecology*, 17(November):63–72, 2006. ISSN 10452249. doi: 10.1093/beheco/arj001.
- [100] William B. Kerfoot. Correlation between Ocellar Size and the Foraging Activities of Bees (Hymenoptera; Apoidea), 1967.
- [101] R. Kern, M. Lutterklas, and M. Egelhaaf. Neuronal representation of optic flow experienced by unilaterally blinded flies on their mean walking trajectories. *Journal of Comparative Physiology A*, 186(5):467–479, 2000. ISSN 0340-7594. doi: 10.1007/s003590050445.
- [102] F. Killmann, H. Gras, and F.-W. SchÄCermann. Types, numbers and distribution of synapses on the dendritic tree of an identified visual interneuron in the brain of the locust. *Cell and Tissue Research*, 296(3):645–665, 1999. ISSN 0302-766X. doi: 10.1007/s004410051325.

- [103] W. H. Kirchner and M. V. Srinivasan. Freely flying honeybees use image motion to estimate object distance. *Naturwissenschaften*, 76:281–282, 1989. ISSN 00281042. doi: 10.1007/BF00368643.
- [104] Andreas Klaus and Eric J Warrant. Optimum spatiotemporal receptive fields for vision in dim light. *Journal of vision*, 9:18.1–16, 2009. ISSN 1534-7362. doi: 10.1167/9.4.18.
- [105] Jan J. Koenderink. Optic flow. *Vision Research*, 26(1):161 – 179, 1986. ISSN 0042-6989. doi: [http://dx.doi.org/10.1016/0042-6989\(86\)90078-7](http://dx.doi.org/10.1016/0042-6989(86)90078-7).
- [106] Holger G. Krapp and Fabrizio Gabbiani. Spatial distribution of inputs and local receptive field properties of a wide-field, looming sensitive neuron. *Journal of Neurophysiology*, 93(4):2240–2253, 2005. ISSN 0022-3077. doi: 10.1152/jn.00965.2004.
- [107] Holger G. Krapp, Bärbel Hengstenberg, and Roland Hengstenberg. Dendritic structure and receptive-field organization of optic flow processing interneurons in the fly. *Journal of Neurophysiology*, 79(4):1902–1917, 1998. ISSN 0022-3077.
- [108] M F Land. Visual acuity in insects. *Annual review of entomology*, 42(46):147–177, 1997. ISSN 0066-4170. doi: 10.1146/annurev.ento.42.1.147.
- [109] M.F. Land and D.E. Nilsson. *Animal Eyes*. Oxford animal biology series. Oxford University Press, 2002. ISBN 9780198509684.
- [110] S B Laughlin and P G Lillywhite. Intrinsic noise in locust photoreceptors. *The Journal of physiology*, 332:25–45, 1982. ISSN 0022-3751.
- [111] Simon B. Laughlin. Form and function in retinal processing. *Trends in Neurosciences*, 10(11):478–483, 1987. ISSN 01662236. doi: 10.1016/0166-2236(87)90104-4.
- [112] Pinar Letzkus, Norbert Boeddeker, Jeff T Wood, Shao-Wu Zhang, and Mandyam V Srinivasan. Lateralization of visual learning in the honeybee. *Biology letters*, 4(February 2008):16–18, 2008. ISSN 1744-9561. doi: 10.1098/rsbl.2007.0466.
- [113] Jens Lindemann. *Visual navigation of a virtual blowfly*. PhD thesis, Bielefeld University, 2005.

- [114] Renting Liu, Zhaorong Li, and Jiaya Jia. Image partial blur detection and classification. *26th IEEE Conference on Computer Vision and Pattern Recognition, CVPR*, 2008. ISSN 1063-6919. doi: 10.1109/CVPR.2008.4587465.
- [115] T Macuda, R J Gegear, T M Laverty, and B Timney. Behavioural assessment of visual acuity in bumblebees (*Bombus impatiens*). *The Journal of experimental biology*, 204:559–564, 2001. ISSN 0022-0949. doi: 10.1002/cne.22011.
- [116] Henrik Malm, Magnus Oskarsson, Eric Warrant, Petrik Clarberg, Jon Hasselgren, and Calle Lejdfors. Adaptive enhancement and noise reduction in very low light-level video. *Proceedings of the IEEE International Conference on Computer Vision*, 2007. ISSN 1550-5499. doi: 10.1109/ICCV.2007.4409007.
- [117] Thomas Matheson, Stephen M. Rogers, and Holger G. Krapp. Plasticity in the visual system is correlated with a change in lifestyle of solitary and gregarious locusts. *Journal of Neurophysiology*, 91(1):1–12, 2004. ISSN 0022-3077. doi: 10.1152/jn.00795.2003.
- [118] MATLAB. *version 7.10.0 (R2010a)*. The MathWorks Inc., Natick, Massachusetts, 2010.
- [119] Glyn A. McMillan and John R. Gray. A looming-sensitive pathway responds to changes in the trajectory of object motion. *Journal of Neurophysiology*, 108(4): 1052–1068, 2012. ISSN 0022-3077. doi: 10.1152/jn.00847.2011.
- [120] Glyn A. McMillan, Vicky Loessin, and John R. Gray. Bilateral flight muscle activity predicts wing kinematics and 3-dimensional body orientation of locusts responding to looming objects. *The Journal of Experimental Biology*, 216(17): 3369–3380, 2013. doi: 10.1242/jeb.087775.
- [121] Hongying Meng, Kofi Appiah, Shigang Yue, Andrew Hunter, Mervyn Hobden, Nigel Priestley, Peter Hobden, and Cy Pettit. A modified model for the Lobula Giant Movement Detector and its FPGA implementation. *Computer Vision and Image Understanding*, 114:1238–1247, 2010. ISSN 10773142. doi: 10.1016/j.cviu.2010.03.017.
- [122] R. Menzel and R. Wehner. Augenstrukturen bei verschieden gro\en Arbeiterinnen von *Cataglyphis bicolor* Fabr. (Formicidae, Hymenoptera). *Zeitschrift f??r Vergleichende Physiologie*, 68(4):446–449, 1970.

- [123] J C Moser, J D Reeve, J M S Bento, T M C Della Lucia, R S Cameron, and N M Heck. Eye size and behaviour of day- and night-flying leafcutting ant alates. *Journal of Zoology*, 264:69–75, 2004. ISSN 0952-8369.
- [124] Thomas a Münch, Rava Azeredo da Silveira, Sandra Siegert, Tim James Viney, Gautam B Awatramani, and Botond Roska. Approach sensitivity in the retina processed by a multifunctional neural circuit. *Nature neuroscience*, 12(10):1308–1316, 2009. ISSN 1097-6256. doi: 10.1038/nn.2389.
- [125] Ji Myung, Y Tang, and Ma Pitt. Evaluation and comparison of computational models. *Methods in enzymology*, 6879(08):1–31, 2009. ISSN 0076-6879. doi: 10.1016/S0076-6879(08)03811-1.Evaluation.
- [126] Hideki Nakagawa and Kang Hongjian. Collision-Sensitive Neurons in the Optic Tectum of the Bullfrog , *Rana catesbeiana* Collision-Sensitive Neurons in the Optic Tectum of the Bullfrog , *Rana catesbeiana*. *Journal of Neurophysiology*, (September 2010):2487–2499, 2011. ISSN 0022-3077. doi: 10.1152/jn.01055.2009.
- [127] Mads Nielsen and Martin Lillholm. What do features tell about images? In Michael Kerckhove, editor, *Scale-Space and Morphology in Computer Vision*, volume 2106 of *Lecture Notes in Computer Science 2106*, pages 39–50. Springer Berlin Heidelberg, 2001. ISBN 978-3-540-42317-1. doi: 10.1007/3-540-47778-0_4.
- [128] D.-E. Nilsson and A.-I. Ro. Did neural pooling for night vision lead to the evolution of neural superposition eyes? *Journal of Comparative Physiology A*, 175(3):289–302, 1994. ISSN 0340-7594. doi: 10.1007/BF00192988.
- [129] Aude Oliva, Antonio Torralba, Anne Guerin Dugue, and Jeanny Herault. Global semantic classification of scenes using power spectrum templates, 1999.
- [130] Damián Oliva, Violeta Medan, and Daniel Tomsic. Escape behavior and neuronal responses to looming stimuli in the crab *Chasmagnathus granulatus* (Decapoda: Grapsidae). *The Journal of experimental biology*, 210:865–880, 2007. ISSN 0022-0949. doi: 10.1242/jeb.02707.
- [131] Michael O’Shea and J.L.D. Williams. The anatomy and output connection of a locust visual interneurone; the lobular giant movement detector (lgmd) neurone.

- Journal of comparative physiology*, 91(3):257–266, 1974. ISSN 0340-7594. doi: 10.1007/BF00698057.
- [132] Rowell O’Shea, Michael and C. H. Fraser. Protection from habituation by lateral inhibition. *Nature*, 254:53–55, 1975. doi: <http://dx.doi.org/10.1038/254053a0>.
- [133] D. Osorio. Directionally selective cells in the locust medulla. *Journal of Comparative Physiology A*, 159:841–847, 1986. ISSN 03407594. doi: 10.1007/BF00603737.
- [134] John Palka. An inhibitory process influencing visual responses in a fibre of the ventral nerve cord of locusts. *Journal of Insect Physiology*, 13(2):235 – 248, 1967. ISSN 0022-1910. doi: [http://dx.doi.org/10.1016/0022-1910\(67\)90151-5](http://dx.doi.org/10.1016/0022-1910(67)90151-5).
- [135] T Pasternak, J E Albano, and D M Harvitt. The role of directionally selective neurons in the perception of global motion. *The Journal of neuroscience : the official journal of the Society for Neuroscience*, 10(9):3079–3086, 1990. ISSN 0270-6474.
- [136] Simon Peron and Fabrizio Gabbiani. Spike frequency adaptation mediates looming stimulus selectivity in a collision-detecting neuron. *Nature neuroscience*, 12(3):318–326, 2009.
- [137] Simon P Peron, Holger G Krapp, and Fabrizio Gabbiani. Influence of electrotonic structure and synaptic mapping on the receptive field properties of a collision-detecting neuron. *Journal of neurophysiology*, 97:159–177, 2007. ISSN 0022-3077. doi: 10.1152/jn.00660.2006.
- [138] Simon P. Peron, Peter W. Jones, and Fabrizio Gabbiani. Precise subcellular input retinotopy and its computational consequences in an identified visual interneuron. *Neuron*, 63(6):830 – 842, 2009. ISSN 0896-6273. doi: <http://dx.doi.org/10.1016/j.neuron.2009.09.010>.
- [139] Simon Peter Peron and Fabrizio Gabbiani. Role of spike-frequency adaptation in shaping neuronal response to dynamic stimuli. *Biological Cybernetics*, 100: 505–520, 2009. ISSN 03401200. doi: 10.1007/s00422-009-0304-y.
- [140] ROBERT B. PINTER. Visual discrimination between small objects and large textured backgrounds. *Nature*, 270:429–431, 1982.

- [141] Geoffrey Portelli, Franck Ruffier, Frédéric L. Roubieu, and Nicolas Franceschini. Honeybees' speed depends on dorsal as well as lateral, ventral and frontal optic flows. *PLoS ONE*, 6(5), 2011. ISSN 19326203. doi: 10.1371/journal.pone.0019486.
- [142] Ruben Portugues and Florian Engert. The neural basis of visual behaviors in the larval zebrafish. *Current Opinion in Neurobiology*, 19:644–647, 2009. ISSN 09594388. doi: 10.1016/j.conb.2009.10.007.
- [143] R. Preiss and P. Spork. Flight-phase and visual-field related optomotor yaw responses in gregarious desert locusts during tethered flight. *Journal of Comparative Physiology A*, 172(6):733–740, 1993. ISSN 0340-7594. doi: 10.1007/BF00195398.
- [144] Frederick R. Prete. *Complex worlds from simpler nervous systems*. 2004. ISBN 0262162237.
- [145] Therese Reber, Antti Vähäkainu, Emily Baird, Matti Weckström, Eric Warrant, and Marie Dacke. Effect of light intensity on flight control and temporal properties of photoreceptors in bumblebees. *The Journal of Experimental Biology*, 2015. doi: 10.1242/jeb.113886.
- [146] D. Regan and K.I. Beverley. Looming detectors in the human visual pathway. *Vision Research*, 18(4):415–421, January 1978. ISSN 00426989. doi: 10.1016/0042-6989(78)90051-2.
- [147] W. Reichardt. Movement perception in insects. *Processing of Optical Data by Organisms and by Machines*, pages 465–493, 1969.
- [148] Heinrich Reichert and Jeffrey J. Wine. Coordination of lateral giant and non-giant systems in crayfish escape behavior. *Journal of Comparative Physiology* ??? A, 153:3–15, 1983. ISSN 03407594. doi: 10.1007/BF00610337.
- [149] F. C. Rind. Intracellular characterization of neurons in the locust brain signaling impending collision. *Journal of Neurophysiology*, 75(3):986–995, 1996. ISSN 0022-3077.
- [150] F C Rind and D I Bramwell. Neural network based on the input organization of an identified neuron signaling impending collision. *Journal of neurophysiology*, 75(3):967–985, 1996. ISSN 0022-3077.

- [151] F. C. Rind and P. J. Simmons. Orthopteran dcmd neuron: a reevaluation of responses to moving objects. i. selective responses to approaching objects. *Journal of Neurophysiology*, 68(5):1654–1666, 1992. ISSN 0022-3077.
- [152] F C Rind and P J Simmons. Seeing what is coming: building collision sensitive neurons. *Trends in Neurosciences*, in press(1989):215–220, 1999.
- [153] F. Claire Rind. A chemical synapse between two motion detecting neurones in the locust brain. *Journal of Experimental Biology*, 110:143–167, 1984.
- [154] F. Claire Rind. Motion detectors in the locust visual system: From biology to robot sensors. *Microscopy Research and Technique*, 56(December 2000):256–269, 2002. ISSN 1059910X. doi: 10.1002/jemt.10029.
- [155] F. Claire Rind and Roger D. Santer. Collision avoidance and a looming sensitive neuron: size matters but biggest is not necessarily best. *Proceedings of the Royal Society of London B: Biological Sciences*, 271(Suppl 3):S27–S29, 2004. ISSN 0962-8452. doi: 10.1098/rsbl.2003.0096.
- [156] F. Claire Rind and Peter J. Simmons. Signaling of object approach by the dcmd neuron of the locust. *Journal of Neurophysiology*, 77(2):1029–1033, 1997. ISSN 0022-3077.
- [157] F. Claire Rind and Peter J. Simmons. Local circuit for the computation of object approach by an identified visual neuron in the locust. *Journal of Comparative Neurology*, 395(February):405–415, 1998. ISSN 00219967. doi: 10.1002/(SICI)1096-9861(19980808)395:3<405::AID-CNE9>3.0.CO;2-6.
- [158] F Claire Rind, Roger D Santer, and Geraldine a Wright. Arousal facilitates collision avoidance mediated by a looming sensitive visual neuron in a flying locust. *Journal of neurophysiology*, 100:670–680, 2008. ISSN 0022-3077. doi: 10.1152/jn.01055.2007.
- [159] Fc Rind. A Directionally Selective Motion-Detecting Neurone in the Brain of the Locust: Physiological and Morphological Characterization. *J Exp Biol*, 19: 1–19, 1990. ISSN 00220949.
- [160] F.Claire Rind, Mark Blanchard, and Paul F.M.J. Verschure. Collision avoidance in a robot using looming detectors from a locust. In Paul S. Schenker and Gerard T. McKee, editors, *Proceedings of SPIE the international society for optical engineering*, volume 4196, page 147. SPIE, Bellingham WA, 2000.

- [161] Derek Rivait and Michael S. Langer. Spatiotemporal power spectra of motion parallax: the case of cluttered 3d scenes. *In IS T-SPIE Symp. on El. Imaging*, 2007.
- [162] R. M. Robertson and A. G. Johnson. Collision avoidance of flying locusts: Steering torques and behaviour. *Journal of Experimental Biology*, 183(1):35–60, 1993.
- [163] C. H. FRASER ROWELL. Variable responsiveness of a visual interneurone in the free-moving locust, and its relation to behaviour and arousal. *Journal of Experimental Biology*, 55(3):727–747, 1971.
- [164] Daniel L. Ruderman. Origins of scaling in natural images. *Vision Research*, 37: 3385–3398, 1997.
- [165] G. L. Ruskell. *Biology of Sensory Systems*, volume 197. 2000. ISBN 9780470694374. doi: 10.1046/j.1469-7580.2000.1973051313.x.
- [166] Roger D. Santer, Peter J. Simmons, and F. Claire Rind. Gliding behaviour elicited by lateral looming stimuli in flying locusts. *Journal of Comparative Physiology A: Neuroethology, Sensory, Neural, and Behavioral Physiology*, 191: 61–73, 2005. ISSN 03407594. doi: 10.1007/s00359-004-0572-x.
- [167] Roger D. Santer, F. Claire Rind, Richard Stafford, and Peter J. Simmons. Role of an identified looming-sensitive neuron in triggering a flying locust's escape. *Journal of Neurophysiology*, 95(6):3391–3400, 2006. doi: 10.1152/jn.00024.2006.
- [168] Roger D. Santer, F. Claire Rind, and Peter J. Simmons. Predator versus prey: Locust looming-detector neuron and behavioural responses to stimuli representing attacking bird predators. *PLoS ONE*, 7(11):e50146, 11 2012. doi: 10.1371/journal.pone.0050146.
- [169] a Van Der Schaaf, a Van Der Schaaf, J H, and J H. van Hateren, "Modelling the power spectra of natural images: Statistics and information,". *Vision Research*, 28(17):pp2759–2770, 1996.
- [170] G. R. Schlotterer. Response of the locust descending movement detector neuron to rapidly approaching and withdrawing visual stimuli. *Canadian Journal of Zoology*, 55(8):1372–1376, 1977. doi: 10.1139/z77-179.

- [171] D.A. Schoenwald. Auvs: In space, air, water, and on the ground. *Control Systems, IEEE*, 20(6):15–18, Dec 2000. ISSN 1066-033X. doi: 10.1109/MCS.2000.887445.
- [172] Alexander Schwegmann, Jens Peter Lindemann, and Martin Egelhaaf. Temporal Statistics of Natural Image Sequences Generated by Movements with Insect Flight Characteristics. *PLoS ONE*, 9(10):e110386, 2014. ISSN 1932-6203. doi: 10.1371/journal.pone.0110386.
- [173] Julien R. Serres, Guillaume P. Masson, Franck Ruffier, and Nicolas Franceschini. A bee in the corridor: Centering and wall-following. *Naturwissenschaften*, 95: 1181–1187, 2008. ISSN 00281042. doi: 10.1007/s00114-008-0440-6.
- [174] Kristen Eileen Severi. Contributions of zebrafish descending motor control neurons to visually-guided locomotor behaviors. 2011.
- [175] S. S. Shapiro and M. B. Wilk. An analysis of variance test for normality (complete samples). *Biometrika*, 3(52), 1965.
- [176] Yue Shigang and F. Claire Rind. A collision detection system for a mobile robot inspired by the locust visual system. *Proceedings - IEEE International Conference on Robotics and Automation*, 2005(April):3832–3837, 2005. ISSN 10504729. doi: 10.1109/ROBOT.2005.1570705.
- [177] B. Siciliano and O. Khatib. *Springer Handbook of Robotics*. Gale virtual reference library. Springer, 2008. ISBN 9783540239574.
- [178] Ana C Silva, Glyn A McMillan, Cristina P. Santos, and John R Gray. Background complexity affects the response of a looming-sensitive neuron to object motion. *Journal of Neurophysiology*, 2014. ISSN 0022-3077. doi: 10.1152/jn.00478.2014.
- [179] Ana Carolina Silva and Cristina P. Santos. A time-analysis of the spatial power spectra indicates the proximity and complexity of the surrounding environment. In *Informatics in Control, Automation and Robotics (ICINCO), 2014 11th International Conference on*, volume 02, pages 148–155, Sept 2014.
- [180] Ana Carolina Silva, Jorge Silva, and Cristina Peixoto Santos. A modified lgmd based neural network for automatic collision detection. In Jean-Louis Ferrier,

- Alain Bernard, Oleg Gusikhin, and Kurosh Madani, editors, *Informatics in Control, Automation and Robotics*, volume 283 of *Lecture Notes in Electrical Engineering*, pages 217–233. Springer International Publishing, 2014. ISBN 978-3-319-03499-7. doi: 10.1007/978-3-319-03500-0_14.
- [181] P J Simmons and F C Rind. Orthopteran DCMD neuron: a reevaluation of responses to moving objects. II. Critical cues for detecting approaching objects. *Journal of neurophysiology*, 68(5):1667–1682, 1992. ISSN 0022-3077.
- [182] PETER SIMMONS. Connexions between a movement-detecting visual interneurone and flight motoneurons of a locust. *The Journal of Experimental Biology*, 86(1):87–97, 1980.
- [183] Peter J. Simmons and F. Claire Rind. Responses to object approach by a wide field visual neurone, the LGMD2 of the locust: Characterization and image cues. *Journal of Comparative Physiology - A Sensory, Neural, and Behavioral Physiology*, 180:203–214, 1997. ISSN 03407594. doi: 10.1007/s003590050041.
- [184] Peter J. Simmons, F. Claire Rind, and Roger D. Santer. Escapes with and without preparation: The neuroethology of visual startle in locusts. *Journal of Insect Physiology*, 56(8):876–883, 2010. ISSN 00221910. doi: 10.1016/j.jinsphys.2010.04.015.
- [185] P.J. Simmons and D. Young. *Nerve Cells and Animal Behaviour*. Cambridge University Press, 2010.
- [186] Eero P Simoncelli and Bruno A Olshausen. Natural image statistics and neural representation. *Annual Review of Neuroscience*, 24(1):1193–1216, 2001. doi: 10.1146/annurev.neuro.24.1.1193. PMID: 11520932.
- [187] Peter Skorupski and Lars Chittka. Differences in photoreceptor processing speed for chromatic and achromatic vision in the bumblebee, *Bombus terrestris*. *The Journal of neuroscience : the official journal of the Society for Neuroscience*, 30(11):3896–3903, 2010. ISSN 0270-6474. doi: 10.1523/JNEUROSCI.5700-09.2010.
- [188] Allan W. Snyder. Acuity of compound eyes: Physical limitations and design. *Journal of Comparative Physiology ??? A*, 116:161–182, 1977. ISSN 03407594. doi: 10.1007/BF00605401.

- [189] M Srinivasan, S Zhang, M Lehrer, and T Collett. Honeybee navigation en route to the goal: visual flight control and odometry. *The Journal of experimental biology*, 199:237–44, 1996. ISSN 1477-9145. doi: 10.1006/anbe.1998.0897.
- [190] M. V. Srinivasan, S. B. Laughlin, and A. Dubs. Predictive coding: a fresh view of inhibition in the retina. *Proceedings of the Royal Society of London. Series B, Containing papers of a Biological character. Royal Society (Great Britain)*, 216(1205):427–459, November 1982. ISSN 0080-4649.
- [191] M. V. Srinivasan, M. Lehrer, W. H. Kirchner, and S. W. Zhang. Range perception through apparent image speed in freely flying honeybees. *Visual Neuroscience*, 6:519–535, 5 1991. ISSN 1469-8714. doi: 10.1017/S095252380000136X.
- [192] Mandyam V Srinivasan. Honeybees as a model for the study of visually guided flight, navigation, and biologically inspired robotics. *Physiological reviews*, 91: 413–460, 2011. ISSN 0031-9333. doi: 10.1152/physrev.00005.2010.
- [193] Mandyam V Srinivasan and Shaowu Zhang. Visual motor computations in insects. *Annual review of neuroscience*, 27(Wehner 1981):679–696, 2004. ISSN 0147-006X. doi: 10.1146/annurev.neuro.27.070203.144343.
- [194] MandyamV. Srinivasan. A visually-evoked roll response in the housefly. *Journal of comparative physiology*, 119(1):1–14, 1977. ISSN 0340-7594. doi: 10.1007/BF00655868.
- [195] Richard Stafford, Roger D. Santer, and F. Claire Rind. A bio-inspired visual collision detection mechanism for cars: Combining insect inspired neurons to create a robust system. *BioSystems*, 87:164–171, 2007. ISSN 03032647. doi: 10.1016/j.biosystems.2006.09.010.
- [196] Andrew D Straw. Vision egg: an open-source library for realtime visual stimulus generation. *Frontiers in Neuroinformatics*, 2(4), 2008. ISSN 1662-5196. doi: 10.3389/neuro.11.004.2008.
- [197] Hongjin Sun and Barrie J Frost. Computation of different optical variables of looming objects in pigeon nucleus rotundus neurons. *Nat Neuroscience*, 1(4): 296–303, 1998. ISSN 1097-6256. doi: <http://dx.doi.org/10.1038/1110>.
- [198] E Switkes, M J Mayer, and J A Sloan. Spatial frequency analysis of the visual environment: anisotropy and the carpentered environment hypothesis. *Vision research*, 18(10):1393–1399, 1978. ISSN 00426989.

- [199] Lance F. Tammero and Michael H. Dickinson. The influence of visual landscape on the free flight behavior of the fruit fly *Drosophila melanogaster*. *Journal of Experimental Biology*, 205(3):327–343, 2002.
- [200] Erik Reinhard Tania Pouli, Douglas W. Cunningham. Image Statistics and their Applications in Computer Graphics. *Eurographics State of the Art Report (STAR)*, pages 83–112, 2010.
- [201] Jamie Carroll Theobald, Birgit Greiner, William T. Wcislo, and Eric J. Warrant. Visual summation in night-flying sweat bees: A theoretical study. *Vision Research*, 46:2298–2309, 2006. ISSN 00426989. doi: 10.1016/j.visres.2006.01.002.
- [202] a. Torralba and a. Oliva. Depth estimation from image structure. *IEEE Transactions on Pattern Analysis and Machine Intelligence*, 24(9):1–13, 2002. ISSN 0162-8828. doi: 10.1109/TPAMI.2002.1033214.
- [203] Antonio Torralba and Aude Oliva. Depth estimation from image structure. *IEEE Transactions on Pattern Analysis and Machine Intelligence*, 24:2002, 2002.
- [204] T. Tversky and The University of Texas at Austin. Computer Science. *Motion Perception and the Scene Statistics of Motion*. University of Texas at Austin, 2008. ISBN 9780549705055.
- [205] Tal Tversky, Tal Tversky, Risto Miikkulainen, Risto Miikkulainen, Wilson S Geisler, and Wilson S Geisler. *Motion Perception and the Scene Statistics of Motion*. PhD:125, 2008.
- [206] W.R. Uttal. *Mind and Brain: A Critical Appraisal of Cognitive Neuroscience*. MIT Press, 2011. ISBN 9780262015967.
- [207] B.P. Uvarov, B.P. Uvarov, and Anti-Locust Research Centre (Great Britain). *Grasshoppers and locusts: a handbook of general acridology*. Number v. 2 in Grasshoppers and Locusts: A Handbook of General Acridology. published for the Anti-Locust Research Centre [by] Cambridge U.P., 1966. ISBN 9780851350721.
- [208] A. van der Schaaf and J.H. van Hateren. Modelling the power spectra of natural images: Statistics and information. *Vision Research*, 36(17):2759 – 2770, 1996. ISSN 0042-6989. doi: [http://dx.doi.org/10.1016/0042-6989\(96\)00002-8](http://dx.doi.org/10.1016/0042-6989(96)00002-8).
- [209] J. H. van Hateren. A theory of maximizing sensory information. *Biological Cybernetics*, 68(1):23–29, 1992. ISSN 03401200.

- [210] J. H. Van Hateren. Spatiotemporal contrast sensitivity of early vision. *Vision Research*, 33(2):257–267, 1993. ISSN 00426989. doi: 10.1016/0042-6989(93)90163-Q.
- [211] Z. Waloff. Orientation of flying locusts, *schistocerca gregaria* (forsk.), in migrating swarms. *Bulletin of Entomological Research*, 62:1–72, 7 1972. ISSN 1475-2670. doi: 10.1017/S0007485300003771.
- [212] E. Warrant, T. Porombka, and W. H. Kirchner. Neural Image Enhancement Allows Honeybees to See at Night. *Proceedings of the Royal Society B: Biological Sciences*, 263:1521–1526, 1996. ISSN 0962-8452. doi: 10.1098/rspb.1996.0222.
- [213] Eric Warrant and Marie Dacke. Vision and visual navigation in nocturnal insects. *Annual review of entomology*, 56:239–254, 2011. ISSN 0066-4170. doi: 10.1146/annurev-ento-120709-144852.
- [214] Eric J. Warrant. Seeing better at night: Life style, eye design and the optimum strategy of spatial and temporal summation. *Vision Research*, 39:1611–1630, 1999. ISSN 00426989. doi: 10.1016/S0042-6989(98)00262-4.
- [215] Eric J. Warrant and Sönke Johnsen. Vision and the light environment. *Current Biology*, 23(22):R990–R994, 2013. ISSN 09609822. doi: 10.1016/j.cub.2013.10.019.
- [216] B Webb. Can robots make good models of biological behaviour? *The Behavioral and brain sciences*, 24(6):1033–1050; discussion 1050–1094, 2001. ISSN 0140-525X.
- [217] Barbara Webb. Robots in invertebrate neuroscience. *Nature*, 417:359–363, 2002.
- [218] Barbara Webb. Robots in invertebrate neuroscience. *Nature*, 417:359–363, 2002. ISSN 0028-0836. doi: 10.1038/417359a.
- [219] Barbara Webb. Validating biorobotic models. *Journal of neural engineering*, 3(3):R25–R35, 2006.
- [220] Barbara Webb. Chapter 1 using robots to understand animal behavior. volume 38 of *Advances in the Study of Behavior*, pages 1 – 58. Academic Press, 2008. doi: [http://dx.doi.org/10.1016/S0065-3454\(08\)00001-6](http://dx.doi.org/10.1016/S0065-3454(08)00001-6).

- [221] David S. Williams. Changes of photoreceptor performance associated with the daily turnover of photoreceptor membrane in locusts. *Journal of Comparative Physiology* ??? A, 150:509–519, 1983. ISSN 03407594. doi: 10.1007/BF00609577.
- [222] M Wilson, P Garrard, and S McGinness. The unit structure of the locust compound eye. *Cell and tissue research*, 195:205–226, 1978. ISSN 0302-766X. doi: 10.1007/BF00236720.
- [223] Jacob O. Wobbrock, Leah Findlater, Darren Gergle, and James J. Higgins. The aligned rank transform for nonparametric factorial analyses using only anova procedures. In *Proceedings of the SIGCHI Conference on Human Factors in Computing Systems*, CHI '11, pages 143–146, New York, NY, USA, 2011. ACM. ISBN 978-1-4503-0228-9. doi: 10.1145/1978942.1978963.
- [224] Haiyan Wu, Ke Zou, Tianguang Zhang, Alexander Borst, and Kolja Kühnlenz. Insect-inspired high-speed motion vision system for robot control. *Biological cybernetics*, 106(8-9):453–63, October 2012. ISSN 1432-0770. doi: 10.1007/s00422-012-0509-3.
- [225] Qian Xiao and Barrie J. Frost. Looming responses of telencephalic neurons in the pigeon are modulated by optic flow. *Brain Research*, 1305(0):40 – 46, 2009. ISSN 0006-8993. doi: <http://dx.doi.org/10.1016/j.brainres.2009.10.008>.
- [226] Qian Xiao and Barrie J. Frost. Motion parallax processing in pigeon (*columba livia*) pretectal neurons. *European Journal of Neuroscience*, 37(7):1103–1111, 2013. ISSN 1460-9568. doi: 10.1111/ejn.12115.
- [227] Keisuke Yonehara, Kamill Balint, Masaharu Noda, Georg Nagel, Ernst Bamberg, and Botond Roska. Spatially asymmetric reorganization of inhibition establishes a motion-sensitive circuit. *Nature*, 469(7330):407–410, 2011. ISSN 0028-0836. doi: 10.1038/nature09711.
- [228] Shigang Yue and F. Claire Rind. Visual motion pattern extraction and fusion for collision detection in complex dynamic scenes. *Computer Vision and Image Understanding*, 104:48–60, 2006. ISSN 10773142. doi: 10.1016/j.cviu.2006.07.002.
- [229] Shigang Yue and F. C. Rind. Collision detection in complex dynamic scenes using an LGMD-based visual neural network with feature enhancement. 17(3): 705–716, 2006. doi: 10.1109/TNN.2006.873286.

- [230] Shigang Yue and F. Claire Rind. A synthetic vision system using directionally selective motion detectors to recognize collision. *Artificial life*, 13(0044):93–122, 2007. ISSN 1064-5462. doi: 10.1162/artl.2007.13.2.93.
- [231] Shigang Yue and F. Claire Rind. Visually stimulated motor control for a robot with a pair of LGMD visual neural networks. *International Journal of Advanced Mechatronic Systems*, 4(X):237, 2012. ISSN 1756-8412. doi: 10.1504/IJAMECHS.2012.052219.
- [232] Shigang Yue and F. Claire Rind. Postsynaptic organisations of directional selective visual neural networks for collision detection. *Neurocomputing*, 103:50–62, 2013. ISSN 09252312. doi: 10.1016/j.neucom.2012.08.027.
- [233] Shigang Yue, F. Claire Rind, Matthais S. Keil, Jorge Cuadri, and Richard Stafford. A bio-inspired visual collision detection mechanism for cars: Optimisation of a model of a locust neuron to a novel environment. *Neurocomputing*, 69:1591–1598, 2006. ISSN 09252312. doi: 10.1016/j.neucom.2005.06.017.
- [234] Shigang Yue, Roger D. Santer, Yoshifumi Yamawaki, and F. Claire Rind. Reactive direction control for a mobile robot: A locust-like control of escape direction emerges when a bilateral pair of model locust visual neurons are integrated. *Autonomous Robots*, 28:151–167, 2010. ISSN 09295593. doi: 10.1007/s10514-009-9157-4.
- [235] J M Zanker. On the elementary mechanism underlying secondary motion processing. *Philosophical transactions of the Royal Society of London. Series B, Biological sciences*, 351:1725–1736, 1996. ISSN 0962-8436. doi: 10.1098/rstb.1996.0154.
- [236] M Zaretsky. Quantitative measurements of centrally and retinally generated saccadic suppression in a locust movement detector neurone. *The Journal of Physiology*, 328(1):521–533, 1982. ISSN 1469-7793. doi: 10.1113/jphysiol.1982.sp014281.
- [237] J.-C. Zufferey and D. Floreano. Fly-inspired visual steering of an ultralight indoor aircraft. *Robotics, IEEE Transactions on*, 22(1):137–146, Feb 2006. ISSN 1552-3098. doi: 10.1109/TRO.2005.858857.
- [238] J.C. Zufferey. *Bio-inspired Flying Robots: Experimental Synthesis of Autonomous Indoor Flyers*. Engineering sciences: Microtechnology. EFPL Press, 2008. ISBN 9781439808115.